STUDIES ON ELECTRONIC PROPERTIES OF FUNCTIONAL POLYMERS AND RELATED MATERIALS

HIROKI AGO

Division of Molecular Engineering
Graduate School of Engineering
Kyoto University

1996

PREFACE

Our life of these days is supported by a large number of electronic devices made of inorganic semiconductors, such as silicon and germanium crystals. This highly-developed semiconductor technology, however, has reached the limits of the fabrication, and an alternative device which controls behavior of electrons with nano or angstrom scale has become required.

For a long time, organic compounds had been believed to be insulator owing to the tightly bound σ-electrons and, hence, used only for the passive aims in the industry. However, the appearance of high electrically conducting organic materials originating in delocalized π-electrons, such as polyacetylene and a complex of tetrathiafulvalene (TTF) and tetracyano-*p*-quinodimethane (TCNQ), overthrown the traditional conception of organic materials. These new findings have stimulated the following investigation into the functional organic materials which form a novel field named "synthetic metals", and the research has now been bearing fruits. Among organic materials, a polymer and a pyrolyzed polymer are the most promising targets for applications because of their high processibility, stability, and easiness of mass production.

The purpose of this thesis is to search for the functional polymeric materials with attractive electronic properties or advanced functionality from the both experimental and theoretical points of view. The author hopes that the studies in this thesis will contribute to further progress in this developing area of material science.

ACKNOWLEDGMENTS

The thesis is a summary of the author's studies from 1992 to 1996 at the Division of Molecular Engineering, Graduate School of Engineering, Kyoto University. The author would like to express his greatest gratitude to Professor Tokio Yamabe for his suggestive discussions and constant encouragement. He is extremely grateful to Professor Kazuyoshi Tanaka for his precious guidance, stimulating discussion, and sincere encouragement. Acknowledgment must be expressed to Dr. Kazunari Yoshizawa for his valuable discussions and unsparing advice.

The author wishes to thank Dr. Shizukuni Yata, Mr. Nobuo Ando, and other members of Kanebo Ltd. for valuable discussions on the polyacenic semiconductor materials. He also acknowledges Professor Mitsuo Ishikawa, Professor Atsutaka Kunai, and Dr. Johji Ohshita of the Department of Applied Chemistry, Hiroshima University for their suggestive discussions and the sample offering of organosilicon polymers. The author is grateful to Professor Takehiko Terao, Associate Professor Kiyonori Takegoshi, and Mr. Toshikazu Miyoshi of Department of Chemistry, Kyoto University for their stimulating discussion, valuable suggestion, and the NMR measurements. Thanks are due to Professor A. K. Bakhshi of Punjab University for his valuable comment on the polymer calculation. The author is indebted to Mr. Masahiro Sakai of Institute for Molecular Science for his kind instructions in the ESR measurements.

The author is grateful to Associate Professor Akitomo Tachibana and Dr. Yohji Misaki for their valuable suggestions and kind encouragement. He wishes to express appreciation to Dr. Yukihito Matsuura, Mr. Hiroo Aoki, Miss. Takako Kuga, Mr. Koji Nagata for their collaboration. Acknowledgment is also made to Dr. Satoru Nishio, Mr. Akira Takata, Dr. Akihiro Ito, Mr. Tohru Sato, Mr. Hideki Fujiwara, Mr. Yoshiaki Oshima, Mr. Masashi Hatanaka, Mr. Takeshi Saito, Mr. Yoshimasa Ono, and Mr. Motoki Katoh for their kind suggestions and help for performing his work. He would like to thank other members of Professor Yamabe's laboratory for stimulating discussion in various seminars. Thanks are due to the members of Institute for Fundamental Chemistry, in particular, Dr. Mayumi Okada, Dr. Kenji Okahara, Dr. Yoichi Yamaguchi, Mr. Keizo Nakajima, and Mr. Yoichi Matsuzaki. He also expresses his appreciation to Mrs. Chunyan Li, secretary of Prof. Yamabe, for her official work.

A part of the numerical calculations were carried out at Data Processing Center of Kyoto University, and a part of cryogenic experiments were carried out at Instrumental Center of Institute for Molecular Science.

He would also like to express his gratitude to Miss. Maki Ago, Miss. Masami Kita, and Mr. Ichiro Takagi and his family for their heart felt kindness and continuous encouragement.

Finally, the author wishes to appreciate his parents Mitsunori Ago and Teruko Ago for their support, understanding, and encouragement.

Kyoto, December 1996

Hiroki Ago

LIST OF PUBLICATIONS

(1) Electronic structures of organosilicon polymers containing thienylene units
K. Tanaka, H. Ago, T. Yamabe, M. Ishikawa, and T. Ueda
Organometallics, **13**, 3496 (1994).

(2) Design of ferromagnetic polymers involving organosilicon moieties
K. Tanaka, H. Ago, and T. Yamabe
Synthetic Metals, **72**, 225 (1995).

(3) Electronic properties of polymers based on thienothiadiazole and thiophene
A. K. Bakhshi, H. Ago, K. Yoshizawa, K. Tanaka, and T. Yamabe
The Journal of Chemical Physics, **104**, 5528 (1996).

(4) Electronic property of polyacene in a constant magnetic field perpendicular to the condensed aromatic-rings plane
K. Tanaka, H. Aoki, H. Ago, and T. Yamabe
Synthetic Metals, **79**, 145 (1996).

(5) ESR study of alkali-doped polyacenic semiconductor (PAS) materials prepared by thermal decomposition of azides
H. Ago, T. Kuga, T. Yamabe, K. Tanaka, S. Yata, Y. Hato, and N. Ando
Carbon, in press.

(6) Electronic properties of p-type doped copolymers consisting of oligothienylene and disilanylene units
H. Ago, T. Kuga, T. Yamabe, K. Tanaka, A. Kunai, and M. Ishikawa
Chemistry of Materials, submitted.

(7) ESR study of Li-doped polyacenic semiconductor (PAS) materials
K. Tanaka, H. Ago, Y. Matsuura, T. Kuga, S. Yata, Y. Hato, and N. Ando
Synthetic Metals, submitted.

(8) ^{7}Li NMR study of Li-doped polyacenic semiconductor (PAS) materials
H. Ago, K. Tanaka, T. Yamabe, K. Takegoshi, T. Terao, S. Yata, Y. Hato, and N. Ando
Physical Review B, submitted.

(9) Structural analysis of polyacenic semiconductor (PAS) materials with ^{129}Xe NMR Measurements
H. Ago, K. Tanaka, T. Yamabe, T. Miyoshi, K. Takegoshi, T. Terao, S. Yata, Y. Hato, and N. Ando
Carbon, submitted.

(10) Theoretical study of Li-doped amorphous carbon materials
H. Ago, K. Nagata, K. Yoshizawa, K. Tanaka, and T. Yamabe
Carbon, submitted.

Other papers not included in this thesis.

(1) Polymeric organosilicon systems. 22: synthesis and photochemical properties of poly[(disilanylene)oligophenylenes] and poly[(silylene) biphenylenes]
J. Ohshita, T. Watanabe, D. Kanaya, H. Ohsaki, M. Ishikawa, H. Ago, K. Tanaka, and T. Yamabe
Organometallics, **13**, 5002 (1994).

(2) An ESR analysis of $C_{60}S_{16}$
K. Tanaka, H. Ago, T. Yamabe, J. Li, and K. Kitazawa
Chemical Physics Letters, **235**, 217 (1995).

(3) Structure and properties of deeply Li-doped polyacenic semiconductor (PAS)
T. Yamabe, K. Tanaka, H. Ago, K. Yoshizawa, and S. Yata
Synthetic Metals, in press.

(4) Bond alternation in carbon nanotubes including σ-electrons
K. Tanaka, H. Ago, T. Yamabe, K. Okahara, and M. Okada
International Journal of Quantum Chemistry, in press.

(5) Interlayer interaction of two graphene sheets as a model of double-layer carbon nanotube
K. Tanaka, H. Aoki, H. Ago, T. Yamabe, and K. Okahara
Carbon, in press.

(6) Magnetic properties of 1,3,5-tris[bis(*p*-methoxyphenyl)amino]benzene cation radicals
K. Yoshizawa, M. Hatanaka, H. Ago, K. Tanaka, and T. Yamabe
Bulletin of the Chemical Society of Japan, **69**, 1417 (1996).

(7) Design of novel donor-acceptor polymers with low band gaps
A. K. Bakhshi, Y. Yamaguchi, H. Ago, and T. Yamabe
Synthetic Metals, **79**, 115 (1996).

(8) Electronic structures of donor-acceptor polymers based on polythiophene, polyfuran, and polypyrrole
A. K. Bakhshi, Y. Yamaguchi, H. Ago, and T. Yamabe
Molecular Engineering, **6**, 239 (1996).

CONTENTS

PART II

Electronic Properties of Narrow-Gap Polymers

PART III

Electronic Structure and Li-Storage Mechanism of Polyacenic Semiconductor (PAS) Material

GENERAL INTRODUCTION

We human beings have tried to find and understand the rules which govern the world and have created the useful substances and technologies for ourselves. Among many scientific fields, solid state physics which mainly describes motion and state of electrons in solid has attracted a great deal of interest, because electrons in solid bring about very fascinating phenomena and, at the same time, they are closely related to our life. For example, we can enumerate some fascinating properties associated with electrons in solid as follows,

i) Electronic property: metallic, semiconducting, and superconducting states
ii) Magnetic property: ferro, ferri, and antiferromagnetic states
iii) Optical property: emission or absorption of light, photoexcitation
iv) Surface property: catalytic reaction

By making use of these properties, a great many innovative applications and technologies have been made and, as a result, our life has become very comfortable and convenient.

In particular, present-day life greatly owes to electric appliances which effectively handle electricity, in more precisely, electrons in solid material. Transistor, integrated circuit (IC), very large scale integration (VLSI), solar cell, magnetic memory, and so on have been created and improved based on the understanding of the electronic structure of materials. In these functional substances, inorganic materials such as silicon and germanium crystals have been playing a crucial role. However, pursuit of reduction of the size has reached limits of manufacturing. Hence, like a quantum device, an alternative material which works with a distinct concept from that used so far has been energetically searched. In addition, environmental pollution caused

by heavy (transition) metals used in appliances like Ni-Cd batteries, has emerged as the serious problem.

As one of the promising candidates to overcome the above problems, the functional organic materials, so called "synthetic metals" which appeared in the late 1970's, have become the subject of increased interest. Synthetic metals overturned the traditional view on organic materials which had been considered to be insulator and used only for passive aims. Functions of these new kinds of materials are based on behavior of electrons (mainly π-electrons) in molecules or polymers. Solid state physics as well as quantum chemistry has played a significant role for the evaluation of the functionality. Functions expected from synthetic metals can be classified into the following four groups: (I) electrically conducting property, (II) magnetic property, (III) optical property, and (IV) application to devices.

I. Electrically conducting property

Semiconducting property in organic material was first reported in 1954 for charge-transfer (CT) complex of perylene and iodine with the conductivity of 10^{-1} S/cm [1]. Through the CT from the electron donor (D) to the acceptor (A), unpaired π-electrons are formed and become conduction carriers. At that time, the CT theory was developed to explain the new absorption peak appeared at visible region based on the resonance structure between DA and D^+A^- [2]. These findings brought us the new insight that an electron is not always confined in a molecule, and this new insight has promoted the study of organic conductors. In 1973, metallic conductor was discovered in the CT complex consisting of tetrathiafulvalene (TTF) and tetracyano-p-quinodimethane (TCNQ) with 1:1 ratio, and its conductivity reaches 10^4 S/cm at 60 K [3]. In addition, this complex showed the metal-insulator (semiconductor) transition, and this phenomenon has been

confirmed in terms of the Peierls transition which is a characteristic of one-dimensional (1D) metallic system [4]. The segregated column structure of TTF-TCNQ complex forms a peculiar 1D metallic system and, hence, the distortion in the periodicity of the geometry and the electronic state occurs through the electron-phonon coupling, resulting in charge density wave (CDW). A partial CT (the degree of CT is 0.59) is known to be the origin of the high conductivity. From the fact that the Peierls transition deteriorates the metallic state, it has been confirmed that the increase of the dimensionality is necessary for stabilization of the metallic state.

The first "organic superconductor", $(TMTSF)_2PF_6$ complex (T_c=0.9 K at P=1.2 kbar, Type II superconductor) where TMTSF is tetramethyl-tetraselenafulvalene, was discovered in 1980 [5]. The pressure applied has been found to suppress a metal-insulator antiferromagnetic ordering transition (spin density wave, SDW) which is also a characteristic feature of a 1D system. In succession, an organic superconductor under ambient pressure, the complex of bis(ethylenedithio)tetrathiafulvalene (BEDT-TTF) and I_3 (T_c=1.2 K) was reported in 1983 [6]. Studies for preparing new superconducting CT complex have been energetically performed and over 50 of superconductors have been reported so far. It should be emphasized that alkali-doped C_{60} (A_3C_{60}) becomes superconductor at the highest temperature (T_c=33 K for $Rb_1Cs_2C_{60}$ [7]) among organic superconductors.

Another approach to realize electrically conducting material is polymerization. The success in polymerization of acetylene into film-shaped polyacetylene (PA) [8] has realized highly conducting state with the conductivity of 40 S/cm in 1977 by adding electron acceptor (p-type doping) [9]. Improvement of the preparation technique has enabled to prepare the highly-oriented and defect-free PA film which showed metallic nature with the conductivity of 10^5 S/cm comparable with copper [10]. The high

conductivity of PA originates in the π-conjugation along the chain or, in other words, delocalization of π-electrons. The observed change in the absorption and electron spin resonance (ESR) spectra have been explained in terms of "soliton" and "polaron" [11,12]. The neutral PA is insulating due to the bond-alternation shown in Fig. 1, which stems from the Peierls distortion reflecting the peculiar 1D structure [4]. The defect in the bond-alternation is called neutral soliton which can be confirmed by the ESR spectrum. It is considered this neutral soliton changes to a charged soliton which becomes a conduction carrier. Further doping causes the coupling of a neutral soliton and a charged soliton, resulting in polaron possessing a charge as well as a spin. It should be noted that the theoretical prediction on the very high T_c superconducting π-conjugated polymer proposed by Little has encouraged the study of conducting polymers [13].

After the discovery of highly conducting state in the doped PA, a number of π-conjugated polymers have been synthesized and some of them have shown metallic nature with the conductivity of ~10^5 S/cm. The typical polymers are polythiophene (PT) [14], polypyrrole (PPy) [15], poly(*p*-phenylene) (PPP) [16], poly(*p*-phenylenevinylene) (PPV) [17], polyaniline (PAn) [18], and poly(*p*-phenylenesulfide) (PPS) [19]. Their chemical structures are shown in Fig. 1. Because they have non-degenerate ground state, the conduction mechanism was considered to be different from that in PA and is explained by polaron and "bipolaron" which are generated at the low and high doped levels, respectively [20,21]. The former is the same as that of PA and the latter is the state in which two charged solitons couple accompanying with the lattice distortion into the quinoid form. These polymers are more favorable to applications because of their higher stability in air compared with PA, and indeed they have been examined for various purposes as will be mentioned later.

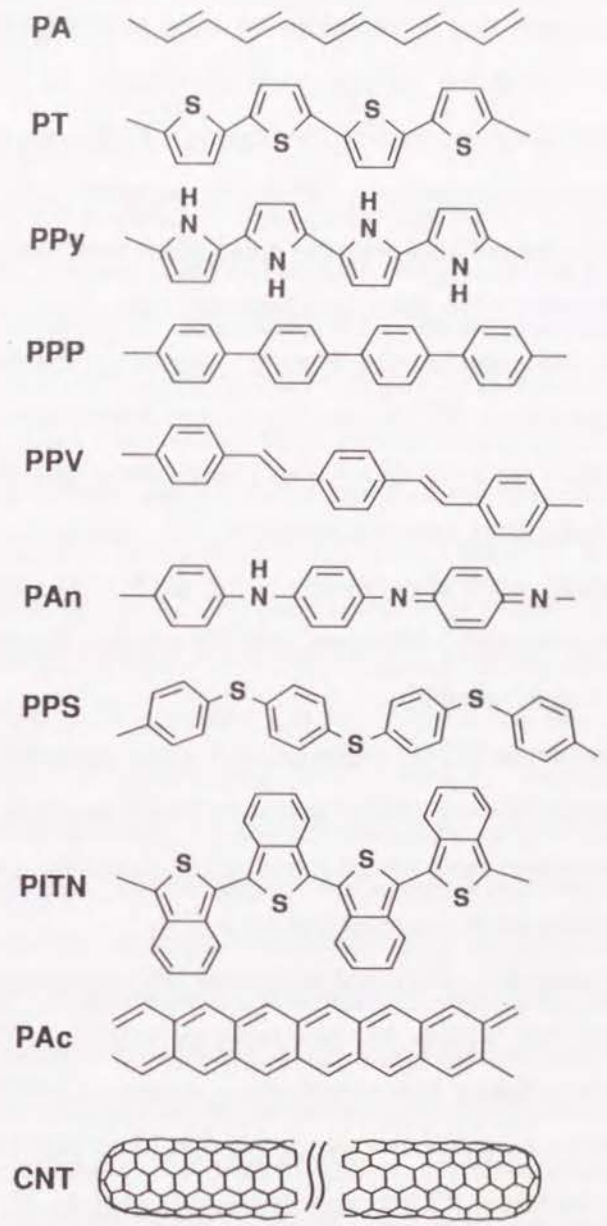

Figure 1. Chemical structures of one-dimensional (1D) and pseudo-1D polymers: polyacetylene (PA), polythiophene (PT), polypyrrole (PPy), poly(*p*-phenylene) (PPP), poly(*p*-phenylenevinylene) (PPV), polyaniline (PAn), poly(*p*-phenylenesulfide) (PPS), poly(isothianaphthene) (PITN), polyacene (PAc), and carbon nanotube (CNT).

There has been another interesting approach to establish a novel conducting polymer, that is, reduction of band gap to make a narrow-gap polymer. It is possible for this kind of polymer to become intrinsic conductor which does not require the dopant. Moreover, being free from dopants could enhance stability. With this purpose, mainly two types of polymers, that is, the polymer with the non-Kékule structure and the polymer with higher dimensionality (pseudo-1D polymer) have been studied from both the theoretical and experimental aspects. Based on the former direction, poly(isothianaphthene) (PITN, see Fig.1) was synthesized and showed a considerably small band gap (E_g~1.0 eV) being about half of that of PT (2.1 eV), but the conductivity was relatively low [22]. Along the latter direction, 1D graphite family, such as polyacene (PAc, see Fig. 1) and polyacenacene [23], has been proposed. However, the 1D graphite family has not been synthesized due to its instability.

Carbon nanotube (CNT) found in 1991 is also included to 1D polymer having an enhanced dimensionality and very long chain [24]. The nature of CNT is very exciting: both metallic and semiconducting properties can be expected depending on its diameter and pitch [25].

Poly(sulfur nitride) $(SN)_x$ and polysilane (PS) are also quite interesting, though they are not organic but inorganic polymers. $(SN)_x$ is only the polymer which exhibits superconducting nature (T_c=0.3 K) [26]. PS showed the electronic properties similar to that of an organic π-conjugated polymer. For instance, PS becomes semiconducting by the p-type doping (up to 10^{-7}~10^{-1} S/cm) [27], and its absorption spectrum shows the chain-length dependency, i.e., the absorption energy decreases with increasing the chain length. These facts provide the possibility of the new and quite different type of conducting polymers having a different conduction mechanism from standard π-conjugated polymers. Moreover, the

cooperative effect between the π-conjugated and inorganic systems is of great interest .

II. Magnetic property

Searching for organic ferromagnetic materials is one of the most challenging issues, because the most organic compounds are diamagnetic due to the closed shell structure, and even if the spins are generated they tend to align themselves to the opposite direction due to formation of a bonding orbital. In the initial stage of this field, theoretical design of ferromagnetic molecules and polymers was presented based on the nonbonding molecular orbitals (NBMOs) and the topology of the system [28,29]. In these studies, spin alternation is presumed and the favorable positions of the localized radical spins are suggested. For ferromagnetic molecular crystals, two guiding principles were provided [30,31]. First, the favorable stacking mode was discussed associated with the spin density. Second is shown for the CT complex concerning for the ferromagnetic alignment. In spite of these propositions, no genuine organic ferromagnet had been reported until quite recently, due to the experimental difficulty in preparation of stable organic radicals. Experimentally, four kinds of approaches have been tried to derive the ferromagnetic spin alignment in organic molecules or polymers.

The first one is based on the molecules possessing built-in-radicals. In 1986, using the oligomer of *m*-phenylcarbene, intramolecular parallel spin alignment with very high spin multiplicity (S=4) was confirmed [32], but this kind of molecule usually showed intermolecular antiferromagnetic interaction in bulk. In very recently, some organic ferromagnetic molecular crystals have been successfully prepared: β-phase *p*-nitrophenyl nitronyl nitroxide (*p*-NPNN, transition temperature is 0.6 K) [33], *N*,*N*'-dioxy-1,3,5,7-tetramethyl-2,6-diazaadamantane (TMAO, 1.5 K) [34], 4-benzylideneamino-

2,2,6,6,-tetramethylpiperidin-1-oxyl (TEMPO, 0.2 K) [35]. Because the intermolecular magnetic interaction in the crystal is very weak and strongly depends on the molecular orientation, it seems quite difficult to prepare ferromagnetic material with high transition temperature under this direction.

The second approach is utilization of CT. Only the complex of C_{60} and electron donor tetrakis(dimethylamino)ethylene (TDAE) has been presented to show the ferromagnetic transition at high temperature (16 K) [36]. Although several models for the origin of the ferromagnetic interaction have been proposed, it is still uncertain.

As the third candidate, several groups have investigated the magnetic properties of pyrolyzed polymers (amorphous carbon) and observed ferromagnetic state, even at room temperature. The materials investigated are the material pyrolyzed from 1,2-diaminopropane [37] and adamantane [38] and so on. Although the experiments lack the reproducibility, the mechanism of ferromagnetic spin alignment is expected to give a precious clue to the new type organic ferromagnet.

poly(*m*-phenylcarbene)

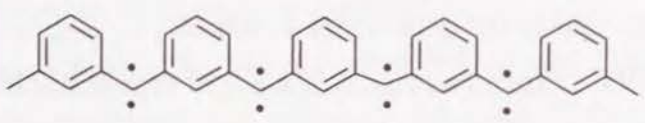

PMPOT-18

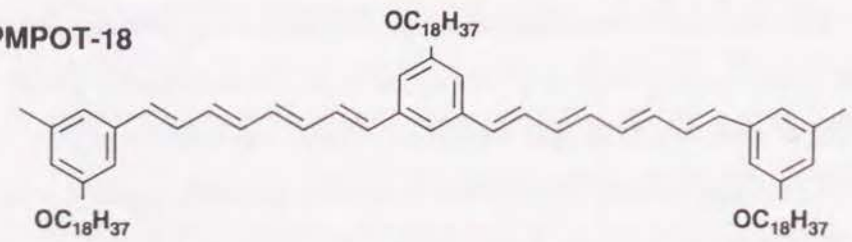

Figure 2. Chemical structures of poly(*m*-phenylcarbene) and poly(*m*-phenyleneoctatetraene) derivative, PMPOT-18.

The fourth is the polaronic ferromagnetic polymer proposed in 1987, in which the spin originates in polaron generated by doping [39]. In this polymer, the polaronic spins are expected to interact ferromagnetically through the π-conjugated coupling unit. Along this line, poly(m-phenyleneoctatetraene) derivative (PMPOT-18, see Fig. 2) was synthesized, in which polyene and *m*-phenylene units are designed as the spin supplier and coupling units, respectively. Actually, AsF_5-doped PMPOT-18 showed the intra-chain ferromagnetic spin alignment (S=5/2 in maximum) [40]. However, the inter-chain antiferromagnetic coupling occurs and hinders from appearance of the bulk ferromagnetism.

III. Optical property

Optical properties in synthetic metals, especially nonlinear optical properties, have been attracting a lot of interests not only from scientific but also from engineering points of view because they have great potential of applications to optoelectronics. For instance, the wavelength of incident light is reduced by half and a third (second and third harmonic generation, SHG, THG), and the index of reflection can be controlled by electric field (Pockels effect). The first report on the nonlinear optical property of organic molecules was presented for 1,2-benzanthracene with SHG efficiency of 5×10^{-6} esu in 1964 [41]. The microscopic polarization ($\boldsymbol{p}$) of a molecule induced by electric field $\boldsymbol{E}$ is expressed by,

$$\boldsymbol{p}=\boldsymbol{p}_0+\alpha\boldsymbol{E}+\beta\boldsymbol{E}^2+\gamma\boldsymbol{E}^3+\cdots \qquad (1)$$

where $\boldsymbol{p}_0$ is the permanent dipole momentum of the molecule and α, β, and γ are, respectively, the linear, second-order, and third-order polarizabilities.

The guiding principles for the molecule with high β have shown: low excitation energy, large transition dipole momentum, and large difference of the dipole momenta between the ground and the excited states. A number of π-conjugated molecules, such as *p*-nitroaniline have been examined because delocalized π-electrons are responsible for the rapid change of the polarization and, thus, suited to use in optoelectronics. However, due to the restriction of the inversion symmetry, the crystal structure of the molecule limits the performance.

As for the third-order polarizability, no definite guide has been suggested except for narrow-band gap state with developed π-conjugation. Only preliminary studies have been reported so far. Among the studies, π-conjugated polymers, such as poly(diacetylene) (PDA) [42] and PT [43] have shown to exhibit high THG efficiency ($\chi^{(3)}$ of PDA and PT are 4×10^{-10} and 3×10^{-11} esu, respectively).

IV. Applications to devices

For application to electronic devices, mainly π-conjugated polymers have been keenly studied owing to their high processibility and mass producibility. The applications to the electrode of rechargeable batteries and the light emitting diode (LED) have been intensively attempted.

Since the first demonstration of the reversible electrochemical doping-undoping cycles of PA in 1981 [44], a great number of efforts have been devoted to establishment of the polymer-based rechargeable batteries. As described in Part III, three types of the rechargeable batteries have been commercialized by taking advantages of the p- and/or n-type doping ability of π-conjugated polymers. High electrochemical performance has also been confirmed in pyrolyzed polymers. This is the most widely known successful

application of the conducting polymers. In 1990, it was reported PPV film shows green-yellow light emission with a high quantum efficiency (0.05 %) [45]. As a result of a number of studies, a very high efficiency diode (4%) [46] and the flexible one [47] have been manipulated. The double-layer organic thin film consisting of diamine derivatives and 8-hydroxyquinoline aluminum (Alq_3) has been shown to be an effective LED [48]. Preliminary reports on the polymer-based field-effect transistor (FET) [49] and the photovoltaic cell [50] were presented employing various conducting polymers but they still contain problems such as the interfacial contact and endurance.

As briefly looked back on the progress of synthetic metals, considerable research efforts have been paid on them. In spite of the efforts, there are only a few outstanding applications based on the peculiar characteristics of organic material such as π-electron conduction and marked low-dimensional structure. Therefore, in the present stage, the design based on the novel concepts like π-σ interaction, is strongly desired. In addition, as for the successful application to an electrode of rechargeable batteries, microscopic and deeper understanding will lead to further improvement. In this thesis, the author presents the study of the electronic and magnetic properties of several interesting functional polymers and related materials, concretely 1D π-σ mixing, narrow-gap polymer, and pyrolyzed carbon systems have been focused. The purpose of this thesis is to understand the electronic structures of these materials and design new functional materials.

In Part I, the interaction between π-conjugated oligothienylene and σ-conjugated silicon units of poly[disilanylene(thienylene)$_n$)] and its related polymers is studied in the both neutral and cationic states. Based on the result, a new type of polaronic ferromagnetic polymer is proposed, and the

nature of the spin is examined with respect to length of the oligothienylene unit.

In Part II, the electronic structures of the narrow-gap polymers are described. Because intrinsic conduction and nonlinear optical properties are expected from a narrow-gap polymer, it is valuable to study on the origin of such a narrow-gap nature. The effect of a magnetic field on such a delicate narrow-gap state is also presented.

In Part III, the electronic structures as well as Li-doping mechanism of the pyrolyzed polymer is presented. Polyacenic semiconductor (PAS) material prepared from phenol resin has been studied as the pyrolyzed polymer, because the PAS material shows excellent performance when used as the electrode of rechargeable batteries. The Li-doping mechanism has been studied with the aid of electron spin resonance, ^{7}Li and ^{129}Xe nuclear magnetic resonance measurements, and molecular orbital calculations.

References

[1] H. Akamatsu, H. Inokuchi, and Y. Matsunaga, *Nature*, **173**, 168 (1954).

[2] R. S. Mulliken, *J. Am. Chem. Soc.*, **72**, 600 (1950).

[3] J. Ferraris, D. O. Cowan, V. Walatka, Jr., J. H. Perlstein, *J. Am. Chem. Soc.*, **95**, 948 (1973).

[4] R. E. Peierls, *Qunatum Theory of Solids*, Oxford Univ. Press, London (1955).

[5] D. Jérome, A. Mazaud, M. Ribault, and K. Bechgaard, *J. Phys. Lett.*, **41**, L95 (1980).

[6] G. Saito, T. Enoki, T. Toriumi, and H. Inokuchi, *Solid State Commun.*, **42**, 557 (1982).

[7] K. Tanigaki, T. W. Ebbesen, S. Saito, J. Mizuki, J. S. Tsai, Y. Kubo, and S. Kuroshima, *Nature*, **352**, 222 (1991).

[8] H. Shirakawa and S. Ikeda, *Polymer J.*, **2**, 231 (1971).

[9] H. Shirakawa, E. J. Louis, A. G. MacDiarmid, C. K. Chiang, and A. J. Heeger, *J. Chem. Soc., Chem. Commun.*, 578 (1977).

[10] H. Naarmann and N. Theophilou, *Synth. Met.*, **22**, 1 (1987).

[11] W. P. Su, J. R. Schrieffer, and A. J. Heeger, *Phys. Rev.*, **42**, 1698 (1979).

[12] M. Nechtschein, F. Devreuz, R. L. Greene, T. C. Clarke, and G. B. Street, *Phys. Rev. Lett.*, **44**, 356 (1980).

[13] W. A. Little, *Phys. Rev.*, **A134**, 1416 (1964).

[14] J. W. -P. Lin and L. P. Dudek, *J. Polym. Sci., Poly. Chem. Ed.*, **18**, 2869 (1980).

[15] A. F. Diaz and J. I. Castillo, *J. Chem. Soc., Chem. Commun.*, 397 (1980).

[16] D. M. Ivory, G. G. Miller, J. M. Sowa, L. W. Shacklette, R. R. Chance, and R. H. Baughman, *J. Chem. Phys.*, **71**, 1506 (1979).

[17] G. E. Wnek, J. C. W. Chien, F. E. Karasza, and C. P. Lillya, *Polymer*, **20**, 1441 (1979).

[18] J. Langer, *Solid State Commun.*, **26**, 839 (1978).

[19] J. F. Rabolt, T. C. Clarke, K. K. Kanazawa, J. R. Reynolds, and G. B. Street, *J. Chem. Soc., Chem. Commun.*, 347 (1980).

[20] J. L. Brédas, R. R. Chance, and R. Silbey, *Phys. Rev.*, **B26**, 5843 (1982).
[21] J. C. Scott, P. Pfluger, M. T. Krounbi, and G. B. Street, *Phys. Rev.*, **B28**, 2140 (1983).
[22] M. Kobayashi, N. Colaneri, M. Boysel, F. Wudl, and A. J. Heeger, *J. Chem. Phys.*, **82**, 5717 (1985).
[23] For instance, T. Yamabe, K. Tanaka, K. Ohzeki, and S. Yata, *Solid State Commun.*, **44**, 823 (1982).
[24] S. Iijima, *Nature*, **354**, 56 (1991).
[25] K. Tanaka, K. Okahara, M. Okada, and T. Yamabe, *Chem. Phys. Lett.*, **191**, 469 (1992)
[26] R. L. Greene, G. B. Street, and L. J. Suter, *Phys. Rev. Lett.*, **34**, 577 (1975).
[27] R. West, L. D. David, P. I. Djurovich, K. L. Stearley, K. S. V. Srinivasan, and H. Yu, *J. Am. Chem. Soc.*, **103**, 7352 (1981).
[28] N. Mataga, *Theor. Chim. Acta.*, **10**, 372 (1968).
[29] A. A. Ovchinnikov, *Theor. Chim. Acta.*, **47**, 297 (1978).
[30] H. M. McConnell, *J. Chem. Phys.*, **39**, 1910 (1963).
[31] H. M. McConnell, *Proc. Robert A. Welch Found. Conf. Chem. Res.*, **11**, 144 (1967).
[32] Y. Teki, T. Takui, K. Itoh, H. Iwamura, and K. Kobayashi, *J. Am. Chem. Soc.*, **108**, 2147 (1986).
[33] M. Tamura, Y. Nakazawa, D. Shiomi, K. Nozawa, Y. Hosokoshi, M. Ishikawa, T. Takahashi, and M. Kinoshita, *Chem. Phys. Lett.*, **186**, 401 (1991).
[34] R. Chiarelli, M. A. Novak, A. Rassat, and J. L. Thoulence, *Nature*, **363**, 147 (1993).
[35] T. Nogami, K. Tomioka, T. Ishida, H. Yoshikawa, M. Yasui, F. Iwasaki, H. Iwamura, N. Takeda, and M. Ishikawa, *Chem. Lett.*, 29 (1994).
[36] P. -M. Allemand, K. C. Khemani, A. Koch, F. Wudl, K. Holczer, S. Donovan, G. Grüner, and J. D. Thompson, *Science*, **253**, 301 (1991).

[37] K. Murata, H. Ushijima, H. Ueda, and K. Kawaguchi, *J. Chem. Soc., Chem. Commun.*, 567 (1992).
[38] K. Tanaka, M. Kobashi, H. Sanekata, A. Takata, S. Mizogami, K. Kawabata, and J. Yamauchi, *J. Appl. Phys.*, **71**, 836 (1992).
[39] H. Fukutome, A. Takahashi, and M. Ozaki, *Chem. Phys. Lett.*, **133**, 34 (1987).
[40] D. A. Kaisaki, W. Chang, and D. A. Dougherty, *J. Am. Chem. Soc.*, **113**, 2764 (1991).
[41] P. M. Rentzepis and Y. -H. Pao, *Appl. Phys. Lett.*, **5**, 156 (1964).
[42] C. Sauteret, J. -P. Hermann, R. Frey, F. Pradére, J. Ducuing, R. H. Baughman, and R. R. Chance, *Phys. Rev. Lett.*, **36**, 956 (1976).
[43] T. Sugiyama, T. Wada, and H. Sasabe, *Synth. Met.*, **28**, C323 (1989).
[44] P. J. Nigrey, D. MacInnes, Jr., D. P. Nairns, A. G. MacDiarmid, and A. J. Heeger, *J. Electrochem. Soc.*, **218**, 1651 (1981).
[45] J. H. Burroughes, D. D. C. Bradley, A. R. Brown, R. N. Marks, K. Mackay, R. H. Friend, P. L. Burns, and A. B. Holms, *Nature*, **348**, 539 (1990).
[46] N. C. Green, S. C. Moratti, D. D. C. Bradley, R. H. Friend, and A. B. Holms, *Nature*, **365**, 628 (1993).
[47] G. Gustafsson, Y. Cao, G. M. Treacy, F. Klavetter, N. Colaneri, and A. J. Heeger, *Nature*, **357**, 477 (1993).
[48] C. W. Tang and S. A. VanSlyke, *Appl. Phys. Lett.*, **51**, 913 (1987).
[49] H. Koezuka, A. Tsumura, and T. Ando, *Synth. Met.*, **18**, 699 (1987).
[50] A. Usuki, M. Murase, and T. Kurauchi, *Synth. Met.*, **18**, 705 (1987).

PART I

Electronic Properties of Organosilicon Polymers Involving Thienylene Units

INTRODUCTION

Polythiophene (PT) and its derivatives have been attracting a great deal of interest, because they are fairly air-stable in the both doped and undoped states and can be modified in various ways by substitution at the β-position of the thiophene ring. PT shows an enhanced increase in the electrical conductivity from 10^{-12} S/cm to 10^{1} S/cm not only with electron acceptors but also with donors due to its high electron affinity [1]. This doping effect has now been widely understood with the concepts of polaron and bipolaron. In recent years, oligothiophenes have been intensively investigated as the model compound of PT, owing to their high crystallinity and well-controlled structure with no defect. The similarity between PT and the oligomer has been pointed out. For instance, the absorption spectra of the cationic and dicationic states of the oligomer resemble to those of polaronic and bipolaronic states of PT, respectively, though the former have finer structures than the latter [2].

On the other hand, there is an exotic polymer which shows σ-conjugation, polysilane (PS). This σ-conjugation has been confirmed by the chain length dependency of the absorption energy (bathochromic effect) [3]. Due to such a σ-conjugation, PS becomes semiconducting upon p-type doping and the conductivity increases from 10^{-11} to 10^{-1} S/cm [4]. Besides, PS has been found to be an excellent photoconductor with high hole mobility (10^{-4} cm^2/Vs), though the hole-generation efficiency is low [5].

As design of novel functional materials, mixing of π- and σ-conjugated units or, in other words, the interaction between mobile π- and σ-electrons is a very characteristic approach. There have been some interesting experiments and calculations of the π-σ mixing effect. The first is the effect of phenyl-substituent on the electronic structure of PS. The enhancement of

σ-conjugation was found and was interpreted as the σ-π interaction [6]. The second characteristics is the red-shift in the absorption spectrum of the disilane-substituted benzene molecule, which suggests the enhancement of delocalization of the π-electron through silicon atoms [7]. The third is the pronounced increase in the hole-generation efficiency observed in the C_{60}-doped PS system [8]. Since this effect is quite small in C_{60}-doped poly(*N*-vinylcarbazole) system, the increase in the efficiency has been understood in terms of the charge-transfer from the photoexcited PS to a C_{60} molecule. The fourth example is the magnetic interaction between π- and σ-electrons [9]. From the study on the magnetic property of bis(adizophenyl) tetramethyldisilanes, it has been shown that disilane can work as the ferromagnetic spin coupler between two π-radical spins via through-bond interaction, but the efficiency is smaller than vinylene by 1~2 orders of magnitude.

As shown above, the π-σ mixing effect in PS or its oligomer is of great interest, but their modification is very restricted on account of the simple chemical structure, i.e., only substituted group can be replaced by new groups. In this regard, the incorporation of π-conjugated unit into the backbone of PS has become a next target and, actually, several soluble polymers have been synthesized. In the present stage, it seems valuable to examine the electronic structure and properties of such an alternate π-σ one-dimensional (1D) system.

In this Part, the author has studied the electronic properties of one of the 1D π-σ alternating polymer, poly[disilanylene(thienylene)$_n$] (PDST-*n*) which has been synthesized by Ishikawa *et al.*, from the both theoretical and experimental aspects.

In Chapter 1 (*Organometallics*, **13**, 3496 (1994)), the author presents the result of the theoretical analysis of neutral PDST-*n* (*n*=1-5). It will be shown that the interaction between π- and σ-units is weak and that the observed absorption spectrum comes from the excitation of a π-electron confined in the oligothienylene unit. Based on these results, the electronic structure of the polymers has been represented by a 1D quantum well model as illustrated in Scheme 1. This kind of electronic structure has seldom been examined. The effects of dimensionality, depth of the well, and length of each unit upon the electronic and magnetic properties as well as tunneling effect are greatly attractive.

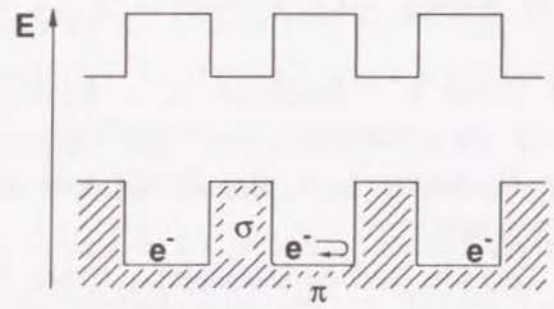

Scheme 1

In Chapter 2 (*Synth. Met.*, **72**, 225 (1995)), the electronic properties of the p-type doped PDST-*n* (*n*=1-3) and the related polymers have been studied by means of the unrestricted-Hartree Fock (UHF) method. When a π-electron is removed from each thienylene unit, it can be expected that the spins are located in 1D manner apart from each other by ~5 Å. Therefore, like molecular-based organic ferromagnetic crystal, through-space magnetic interaction between the spins are expectable. From the calculations, it has been clarified that the nature of a spin strongly depends on the length of oligothienylene unit and that the most hopeful polymer is PDST-3$^+$.

In Chapter 3 (*Chem. Mater.*, submitted), it has been investigated the electronic properties of $NOBF_4$-doped PDST-n^+ (n=1-5) with the aid of a variety of measurements. It will be shown that the polaronic spin can be generated in the polymers with n=3-5 but magnetic interaction among the spins is yet unobservable due to small number of the spins.

References

[1] K. Tanaka, T. Shichiri, and T. Yamabe, *Synth. Met.*, **16**, 207 (1986).

[2] D. Fichou, G. Horowitz, and F. Garnier, *Synth. Met.*, **39**, 125 (1990).

[3] C. G. Pitt, M. M. Bursey, and P. F. Rogrson, *J. Am. Chem. Soc.*, **92**, 519 (1970).

[4] R. West, L. D. David, P. I. Djurovich, K. L. Stearley, K. S. V. Srinivasan, and H. Yu, *J. Am. Chem. Soc.*, **103**, 7352 (1981).

[5] R. G. Kepler, J. M. Zeigler, L. A. Harrah, and S. R. Kurtz, *Phys. Rev.*, **B35**, 2818 (1987).

[6] K. Takeda, H. Teramae, and N. Matsumoto, *J. Am. Chem. Soc.*, **108**, 8186 (1986).

[7] H. Sakurai and M. Kuamada, *Bull. Chem. Soc. Jpn.*, **37**, 1894 (1964).

[8] Y. Wang, R. West, and C. -H. Yuan, *J. Am. Chem. Soc.*, **115**, 3844 (1993).

[9] T. Doi, A. S. Ichimura, N. Koga, and H. Iwamura, *J. Am. Chem. Soc.*, **115**, 8928 (1993).

Chapter 1

Electronic Structures of Organosilicon Polymers Including Thienylene Units

1. Introduction

In recent years polysilane (PS) and its derivatives have been studied from both theoretical and experimental points of view [1]. It is understood that there is a well developed σ-conjugation throughout the main chain [2,3]. This is quite different from the ordinary organic electrically conducting polymers with developed π-conjugation [4] and has stimulated a variety of studies with respect to PS including semiconducting behavior [5,6], enhancement of electrical conduction with doping [7], photoconduction [8-10], nonlinear optical properties [11], and thermochromism [12].

However, there is not much possibility of effective controlling the electronic properties of PS except by the modification of a substituent group attached to the silicon atoms. In this respect, organosilicon polymers containing π-conjugated unit in the main chain have received increasing attention, since these systems have the potential to be chemically modified in a more flexible manner than PS. Along this line, several numbers of organosilicon polymers, which consist of the combination of regular alternation of a disilanylene (-SiR_2-SiR_2-) unit and carbon π-conjugated unit such as ethenylene (-CH=CH-), ethynylene (-C≡C-), diethynylene (-C≡C-C≡C-), butenyne (-C=C-C≡C-), or phenylene in the main chain have been

synthesized [13-18]. These polymers show electrically conducting properties (σ=10^{-2}-10^{-4} S/cm in vacuum) at room temperature upon doping with SbF_5 [13-18]. The electronic structures of these polymers have also been studied to clarify the fundamental difference between the π-bonding behavior of such silicon-containing polymers and the ordinary organic π-conjugated polymers [19,20].

In the last several years, a similar class of polymers containing the combination of thienylene and silylene units in the main chain have been prepared [21-24]. More recently, a series of poly(disilanylene(thienylene)$_n$) (PDST-*n*; *n*=1-5) have been synthesized and their various optical properties have been examined [25,26]. This is of particular interest since polythiophene (PT) is one of the most stable conductive polymers in air and is applicable to various electronic devices such as field-effect transistor [27] and electrochromic element [28]. In this chapter we report the electronic structures of neutral PDST-*n*, some of the representative structures of which are illustrated in Fig. 1. For comparison, those of poly(ethylene-(thienylene)$_n$) (PET-*n*; *n*=1-3), poly(silylene(thienylene)$_n$) (PST-*n*; *n*=1), and PT have also been examined. Although the actual PDST-*n* series have been synthesized with different substituents in the disilanylene unit, here we employ hydrogen atoms for these side substituents for simplicity.

2. Method of Calculation

All of the calculations were performed on the basis of the one-dimensional tight-binding self-consistent field-crystal orbital (SCF-CO) method at the level of the CNDO/2 (complete neglect of differential overlap, version 2) approximation including all the valence electrons [29]. This program is able to handle the screw axis symmetry as well as the translational symmetry. The energy gradient method [30] was employed in order to

PDST-1

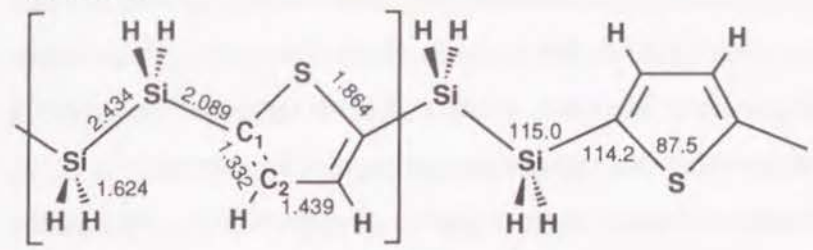

PDST-3

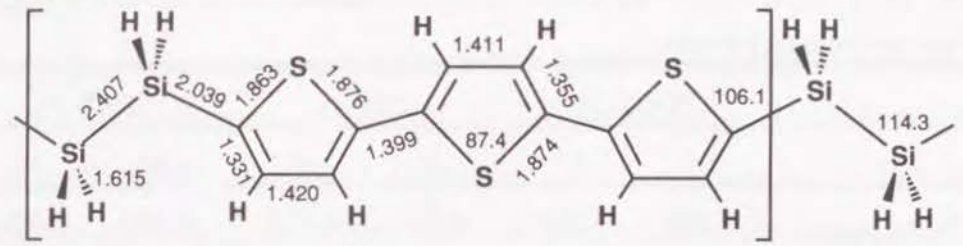

PET-1

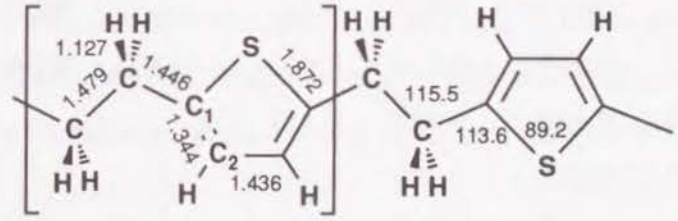

Figure 1. Skeletons of PDST-1, PDST-3, and PET-1 (see text). The bond lengths (Å) and angles (deg) indicated are those obtained by the energetical optimization.

optimize the polymer skeleton of PDST-*n* and PET-*n* (*n*=1-3). For PDST-4 and PDST-5, the polymer structures were constructed from the optimized one of PDST-3.

The number of the representative wave vectors was chosen as 21 with regular intervals ($\pi/10a$, where a is the unit vector of the translational symmetry or the screw axis symmetry, being parallel to the polymer chain axis) in the Brillouin zone. The overlap integrals and the electron repulsion

integrals were considered as far as the fourth nearest neighboring cell at a maximum (ca. 20-30 Å from the central cell on average). Polarization functions such as silicon 3d atomic orbitals (AOs) were suppressed, since it has been pointed out that these do not give an appreciable contribution to the electronic structure of silicon atoms in silane oligomers [31]. In fact, the

Table 1. Comparison of the π-bonding nature based on the semiempirical (S) and the *ab initio* (A) results.

	PDST-2[a]		PET-2[b]		PST-1[a]	
	S[c]	A[d]	S[c]	A[d]	S[c]	A[d]
$S\text{-}C_1$	0.258	0.026	0.260	0.025	0.253	0.024
$S\text{-}C_4$	0.245	0.022	0.241	0.022		
$C_1\text{=}C_2$	0.892	0.170	0.863	0.167	0.907	0.175
$C_2\text{-}C_3$	0.392	0.049	0.412	0.053	0.360	0.044
$C_3\text{=}C_4$	0.844	0.160	0.832	0.157		
$C_4\text{-}C_4'$	0.370	0.034	0.383	0.039		
C_1-Si (C_1-C for PET-2)	0.147	0.005	0.255	0.007	0.143	0.004
Si-Si (C-C for PET-2)	0.140	0.002	0.197	0.0001		

[a]For the atomic numberings, see the figures below. [b]For the atomic numberings, see also those of PDST-2 below. [c]π-bond order. [d]π-atomic orbital bond population determined by Mulliken population analysis; this value is smaller than the π-bond order due to the multiplication by the overlap integral.

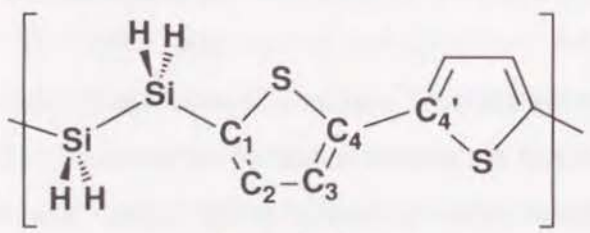

PDST-2

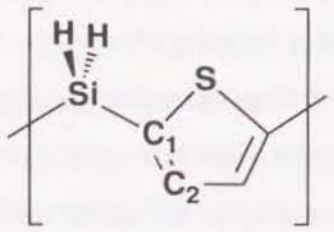

PST-1

calculation for PDST-1 including the silicon 3d AOs has resulted in a small draw back of positive charge on Si atoms (from 0.343 without 3d to 0.238 with 3d) and in a slight change in the σ-σ* type band gap (from 10.66 to 9.31eV). Although a remarkable change was only seen in the AO component in the lowest unoccupied crystal orbital (LUCO) upon the introduction of 3d AOs, this feature almost does not matter in the present work.

For some selected polymers (PDST-2, PET-2, and PST-1), *ab initio* SCF-CO calculations with the STO-3G basis set for the geometries obtained by the CNDO/2 optimization process were also carried out for the sake of comparison. No serious change was seen in the results of the semiempirical and the *ab initio* calculations. For instance, the π-bonding nature in PDST-2, PET-2, and PST-1 are listed in Table 1, where both of these calculation results clearly indicate the cut off of the π-conjugation of thienylene unit by sp^3-bonding at silylene and/or methylene units, as will be later discussed.

3. Results and Discussion

3.1. Optimized geometries. The planarity of the polymer skeleton of PDST-1 was first checked prior to the optimization process of all the polymers treated in the present work. Four kinds of the conformations of PDST-1 illustrated in Fig. 2, were energetically optimized to reveal that the planar-*trans* form is energetically most stable (see Table 2). Hence, all the other polymers were submitted to the optimization by starting from the planar-*trans* conformations.

Optimized geometrical parameters of planar-*trans* PDST-1 and PDST-3, for instance, along with PET-1 are also shown in Fig. 1. In these planar structures two Si or C atoms lie on almost the same plane within ±0.1 Å as

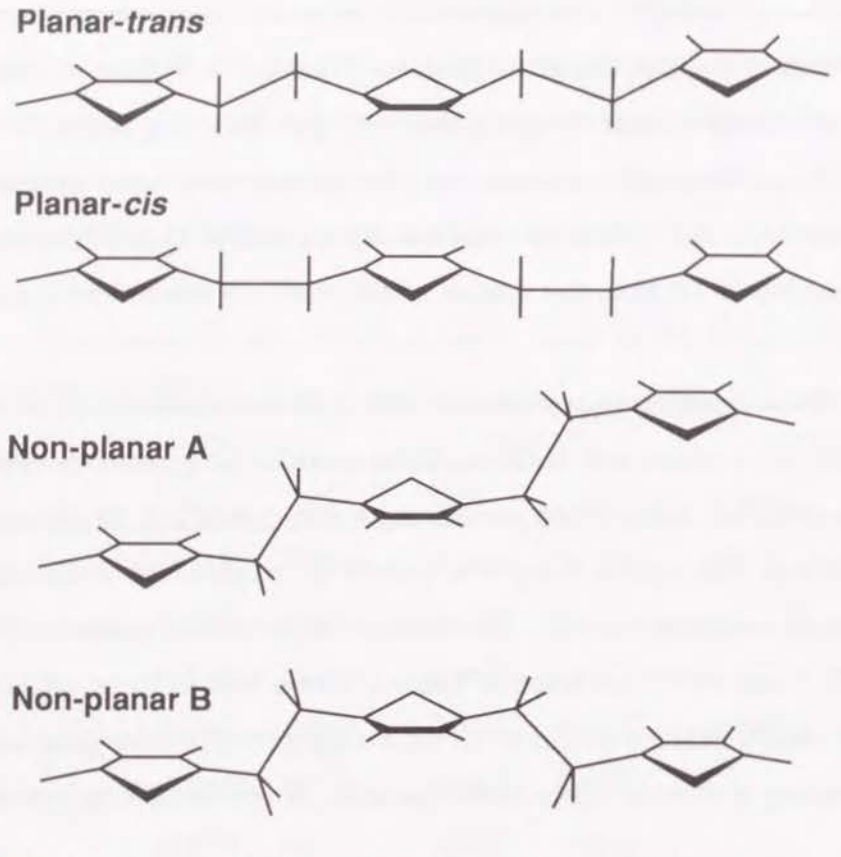

Figure 2. Four kinds of schematic conformations of PDST-1 examined, in which the unit cell contains a disilanylene and a thienylene units. Atomic notations are abbreviated

Table 2. Relative energies of four kinds of conformations of PDST-1.

Conformations[a]	Relative total energy[b] (in eV)
Planar-*trans*	0
Planar-*cis*	1.55
Non-planar A	0.06
Non-planar B	0.10

[a]See Fig. 2. [b]Positive values indicate instabilization of the total energy per unit cell compared with zero.

that of the thienylene unit. The Si-C and the Si-Si bond lengths of PDST-*n* decrease with an increase in the number of *n*. On the other hand, the geometry of thiophene rings does not show remarkable difference with a change in *n*.

3.2. Electronic structures. The band structures of PDST-1, PDST-3, and PET-1 are shown in Fig. 3. Since all of the present polymers possess the approximate C_s symmetry, the energy bands can be classified into the σ- and π-types. It is seen that the nature of both the highest occupied (HO) and the lowest unoccupied (LU) bands changes from σ-type to π-type with an increase in *n* in PDST-*n*, due to the development of the π-conjugation within the thienylene unit. The energy levels of the σ-type bands do not change much from PDST-1 to PDST-3, while π-type bands move considerably. The π-type bands of PET-1 are at the same level as those of PDST-1, and the σ-type bands lie at the lower level. The energy difference of the levels of the HO π-type and the next HO π-type bands varies according to the polymer types. In PDST-1, for instance, these two bands are almost degenerate due to the characteristics of the accompanied COs.

The electronic properties derived from the band structure are listed in Table 3. Since the Hartree-Fock theory, on which the present SCF-CO method is based, has a tendency toward overestimation of the band gap [33], the π-π* and σ-σ* gap energies have been proportionally scaled so as to reproduce the experimental values of PT and PS, respectively.

It is seen that the value of π-π* gap of PDST-*n* decreases as the number of thiophene rings increases, whereas that of σ-σ* gap does not change too much. The π-π* gap values of PET-*n* change in a similar

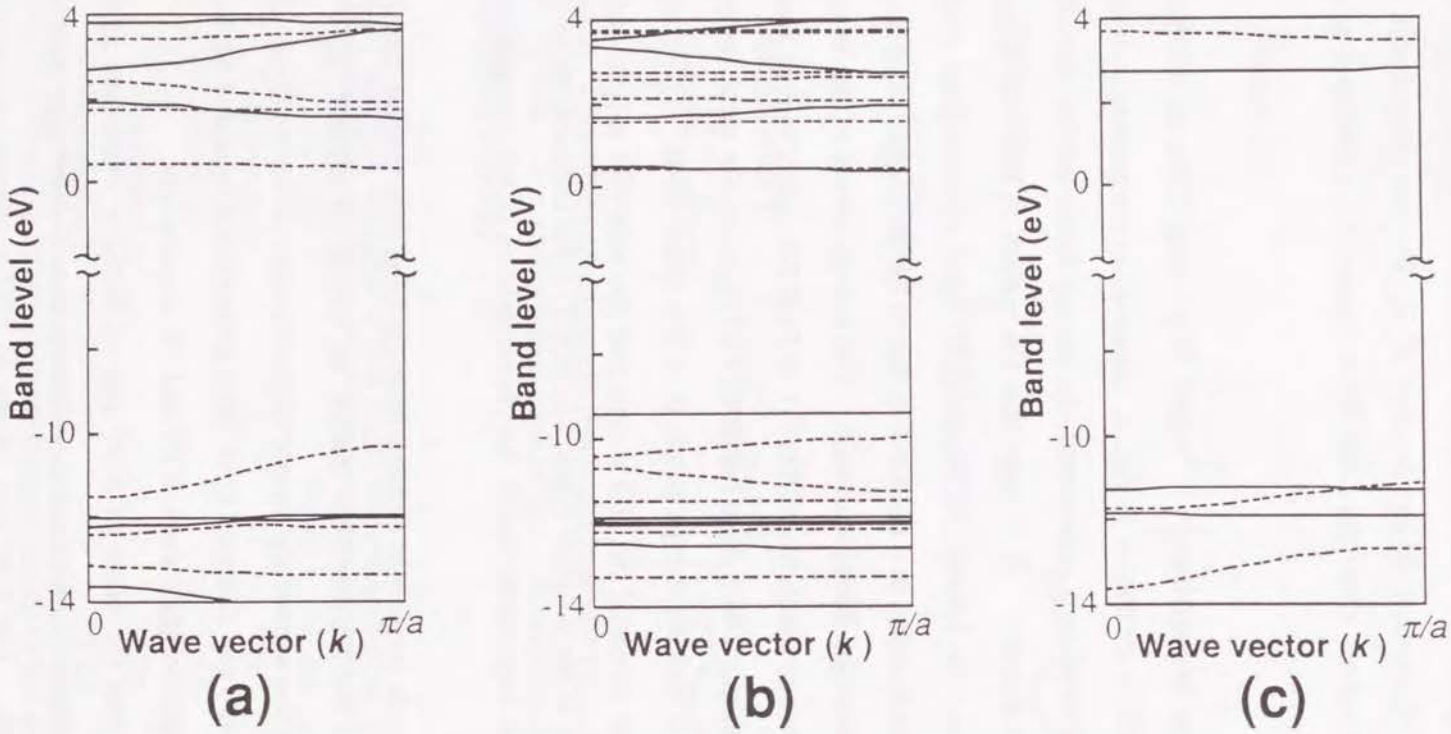

Figure 3. Band structures of (a)PDST-1, (b)PDST-3, and (c)PET-1. Solid and dashed lines indicate π- and σ-bands, respectively.

Table 3. Electronic properties of each polymer.[a]

	PDST-1	PDST-2	PDST-3	PDST-4	PDST-5	PET-1	PET-2	PET-3	PST-1	PT
HO bandwidth[b]										
π-type	0.01	0.01	≈ 0*	≈ 0*	≈ 0*	0.03	0.01*	0.06*	0.06	4.19
σ-type	1.20*	0.97*	0.41	0.13	0.06	0.61*	0.36	0.26	1.57*	0.74
LU bandwidth[b]										
π-type	0.39	0.29	0.07*	0.04*	0.02*	0.04*	0.08*	0.07*	0.94	6.72
σ-type	0.11*	0.02*	0.01	≈ 0	≈ 0	0.21	0.03	0.03	0.10*	0.52
Band gap										
π-π* type[c]	13.49 (4.79)	11.59 (4.11)	9.80 (3.48)	9.36 (3.32)	8.72 (3.09)	13.97 (4.96)	11.18 (3.97)	9.65 (3.42)	13.73 (4.87)	7.27 (2.58)
σ-σ* type[d]	10.66 (4.12)	10.20 (3.94)	10.42 (4.03)	10.55 (4.08)	10.66 (4.10)	14.59 (5.64)	13.32 (5.15)	13.02 (5.03)	10.63 (4.11)	13.02 (5.03)
Experimental[e]	4.60	3.62	3.19	2.99	2.90	-	-	-	-	2.58
Ionization pot.	10.34	9.84	9.43	9.17	8.84	11.15	9.93	9.25	9.98	8.15
Electron affinity	-0.31	-0.36	-0.36	-0.19	0.12	-2.70	-1.26	0.41	-0.65	0.88

[a]All the values are shown in eV. [b]The asterisk indicates the value with respect to the actual HO or LU band. [c]The values in parentheses are reestimated by a proportional scaling to the value obtained for PT (Ref. 32). [d]The values in parentheses are reestimated by a proportional scaling to the value obtained for PS (Refs.1,19). [e]Based on the measurements of λ_{max}.

manner to those of PDST, while the σ-σ* gap values remain larger than the π-π* gap ones. Note that the calculated σ-σ* gap of PS previously reported [19] is on the same level with that of PDST-1. Moreover, the HO bandwidths of PT (π) and PS (σ) are much wider than those of PDST-*n* and PET-*n*.

It is noteworthy that the π-π* gap values of $(\text{-SiH}_2\text{-(CH=CH)}_2\text{-})_n$ [20] and PST-1 are similar to that of PDST-1. This signifies that the π-π* gap of polymeric organosilicon-containing π-conjugated unit in the polymer main chain is rather independent of the number of silicon atoms in the silylene unit, in agreement with the previous work [19]. It is seen from the occupied bandwidth that PDST has more complete σ-conjugation and less complete π-conjugation than PET. This suggests that the π–conjugation of the thienylene unit is cut off by sp^3-bonding at silylene and/or methylene units but with a little bit different manner. A similar tendency was also seen in the results of the *ab initio* calculations for PDST-2, PET-2, and PST-1.

3.3. Orbital patterns. In Fig. 4 the orbital patterns examined for the both σ-and π-type COs are shown. In PDST-1, the σ-type HOCO and σ-type LUCO become the actual HOCO and LUCO, respectively. It is noted that the σ-type HOCO is mainly constructed from the combination of the pσ-orbitals extending along the polymer main chain, being similar to that in PS. Note that this pσ-orbital interaction passes through the C-S-C single-bond route in the thienylene unit not through the C=C double bonds. On the other hand, the σ-type LUCO localizes mainly on the 3s AO of the Si atom and the 1s AO of the H atom with an antibonding property, giving no inter-cell interactions.

The coefficients of the π-type HOCO are large on C atoms and small

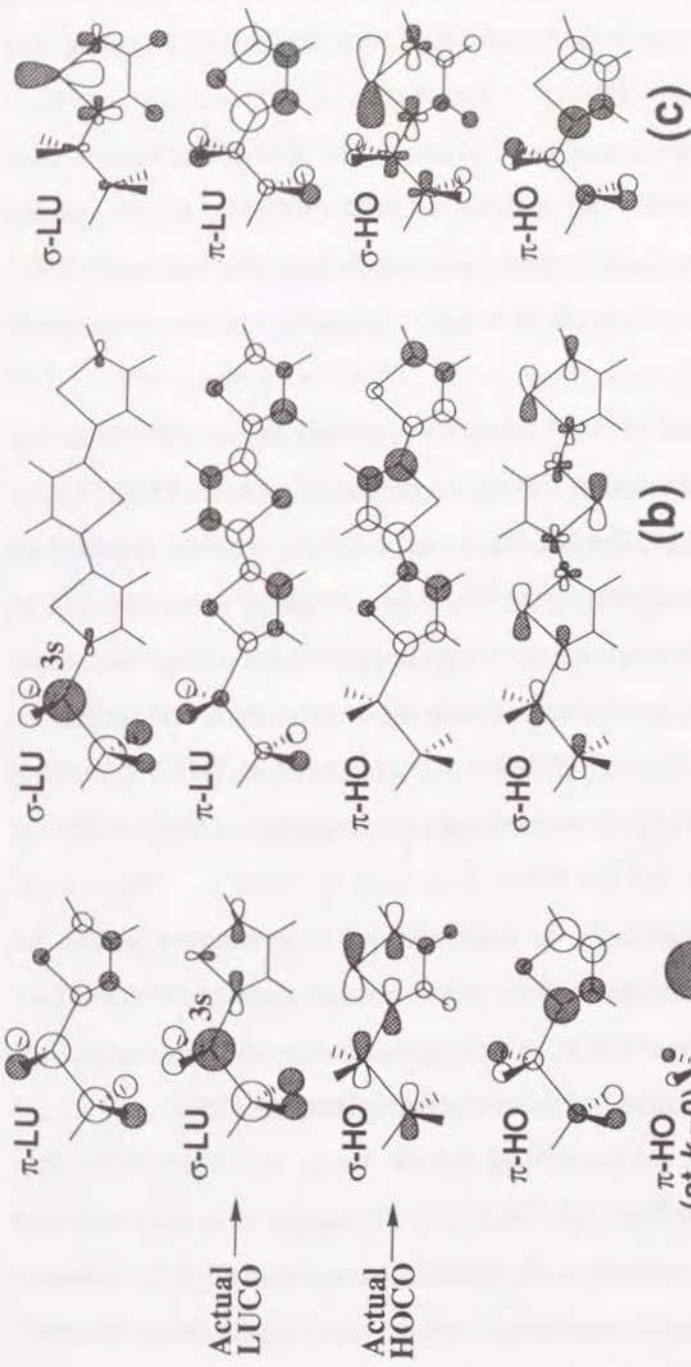

Figure 4. Patterns of the π-type and the σ-type HOCO and LUCO of (a)PDST-1, (b)PDST-3, and (c)PET-1. Note that there is the Fermi level between the second and third rows. The polymer skeletons are the same as those shown in Fig. 1.

on Si with antibonding characteristics at the Si-Si and C-Si bonds and pseudo π-bonding at the Si-H bond. On the contrary, the π-type LUCO pattern is mainly located on Si atoms, Si-Si and Si-H being bonding and antibonding natures, respectively. The π-type HOCO pattern at k=0 of PDST-1 is rather concentrated on S atom in the thienylene unit, which resembles the pattern of the HO molecular orbital (HOMO) of a thiophene molecule [34]. This strongly suggests that the disilanylene unit in PDST-1 works as a connector which hardly allows π-conjugation between separated thienylene units.

The CO patterns of PDST-3 basically resemble those of PDST-1 but show more characteristic aspects. Both the π-type HOCO and LUCO being the actual HOCO and LUCO of PDST-3, respectively, are concentrated on the thienylene unit but scarcely on the Si atoms. Thus the delocalization of π-electrons between thienylene units are suppressed even if each unit becomes larger. These phenomena explain the smaller width of the HO π-band compared with that of PDST-1. The σ-type HOCO is less satisfactorily conjugated at the inter-thiophene ring part yielding a HO σ-bandwidth smaller than that for PDST-1, as seen in Table 3. The σ-type LUCO is constructed from only the antibonding combination of 3s and 1s AOs of Si and H atom at disilanylene unit. Such feature of σ*-band has been observed in the previously reported organosilicon polymers containing ethenylene or phenylene units instead of the thienylene unit [19].

The patterns of the π-type HOCO and the π-type LUCO of PET-1 are essentially the same as those of PDST-1. Generally it is seen that σ-conjugation is more developed in the PDST-n series than PET-n. The σ-type HOCO of PET-1 has a remarkably large CO coefficient on the S atom, which makes the HO σ-bandwidth considerably narrow, being about half

that of PDST-1 (see Table 3). The σ-type LUCO is completely different from that of PDST-1, since the former is almost concentrated on the S atom and is slightly on C atoms in the thienylene unit.

3.4. Distribution of electrons. The π-bond orders, AO densities, and atomic net charges of PDST-1, PET-1, and PST-1 are listed in Table 4. The π-conjugation in PET-1 prevails over those in PDST-1 and PST-1. There is not much difference in the π-conjugation between PDST-1 and PST-1. With respect to PDST-3, the π-conjugation within a thienylene unit becomes stronger than in PDST-1.

From the atomic net charge it is seen that the Si atoms are positively charged (+0.343) in PDST-1, as usual, and the C atoms corresponding to the Si atom are almost neutral (+0.029) in PET-1. In PDST-1 Si atoms donate electron to H atoms bonding to Si and to the adjacent thienylene unit. In PST-1 the Si atom is more positive (+0.525), due to the loss of σ–electrons. From the balance of the atomic charge of H bonding to Si, the σ-electron of the Si atom is mainly transferred to the adjacent thienylene units.

3.5. Assignment of UV spectra. Strong UV absorption spectra have been observed in tetraethyl-substituted PDST-n (n=1-5) on the disilanylene unit, as shown in Fig. 5. It is clearly seen that the position of λ_{max} is red-shifted with an increase in n. This result is in good agreement with the calculated π-π* interband transition as shown in Fig. 6. Incidentally, this assignment can be confirmed in Br-terminated thiophene oligomers [25] as well as the ordinary thiophene oligomers [35], both of which show strong absorption with similar wavelength to that of PDST-n. Furthermore, no large shift of this absorption wavelength will be expected

Table 4. Calculated results of electronic structures of selected polymers.[a]

			PDST-1	PET-1	PST-1
π-bond order	Si-Si (C-C for PET-1)		0.137	0.189	-
	Si-C (C-C for PET-1)[b]		0.143	0.259	0.143
	thiophene ring:				
	S-C		0.247	0.258	0.253
	C=C		0.907	0.872	0.907
	C-C		0.359	0.391	0.360
AO density	Si (C)[c]	π	0.821	0.966	0.802
		σ	2.836	3.005	2.673
	S	π	1.899	1.893	1.894
		σ	4.199	4.273	4.224
	C_1	π	1.025	1.023	1.030
		σ	3.036	2.918	3.052
	C_2	π	1.017	1.052	1.016
		σ	2.969	2.961	2.963
Atomic net charge	Si (C)[c]		0.343	0.029	0.525
	S		-0.098	-0.166	-0.188
	C_1		-0.061	0.059	-0.082
	C_2		0.014	-0.013	0.021
	H[d]		-0.118	0.003	-0.137
	H[e]		-0.010	0.001	-0.008

[a]The numbering of carbon atoms are designated in Figure 1. [b]Between Si (or C) and the thiophene ring. [c]Carbon atom in parentheses signify those in the ethanylene unit of PET-1. [d]Attached to the disilanylene or ethanylene unit. [e]Attached to the thiophene ring.

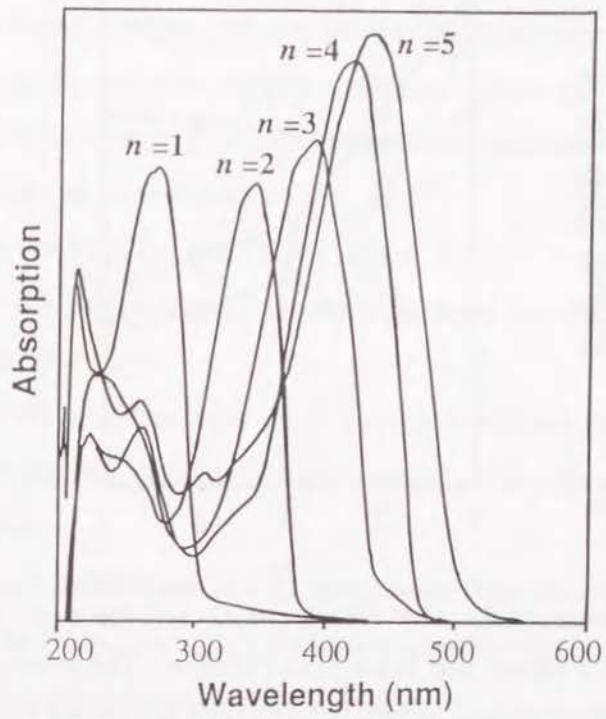

Figure 5. UV spectra of tetraethyl-substituted PDST-*n* (adapted from Ref. 25).

upon the change into the phenyl-substituent group attached to Si atoms of PDST-*n* in contrast with phenyl-substituted polysilane [36]. This prediction is based on the expectation of a small orbital interaction between a thienylene unit and a phenyl-substituent group as illustrated in Fig. 7. The orientation of a phenyl-substituent group is proposed in PS so as to make the interaction between σ-CO and π-MO of the phenyl-substituent group. As a matter of fact, there has been observed only 10 nm-shift of λ_{max} upon the introduction of two phenyl-substituent groups into PDST-1.

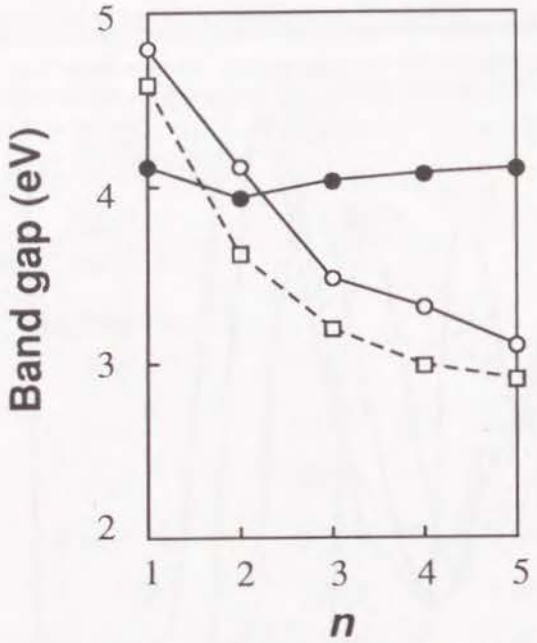

Figure 6. Changes of the σ-σ* (black circles) and the π-π* (white circles) band gaps (scaled values; see Table 3) of PDST-*n*. The squares indicate the experimental values of λ_{max} in Fig. 5. The lines are guides for the eye.

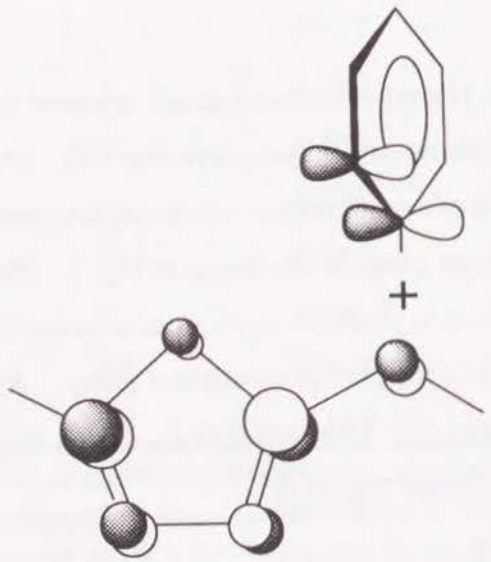

Figure 7. Orbital interaction between a phenyl substituent and a Si atom in PDST-1.

4. Conclusion

The electronic structures of simplified poly(disilanylene (thienylene)$_n$) (PDST-*n*; *n*=1-5) and the related polymers such as poly(ethylene (thienylene)$_n$) (PET-*n*; *n*=1-3) and so on have been studied. There are four major findings in the present chapter:

(1) In both the PDST-*n* and PET-*n* series, the π-π* band gap energies decrease upon the increase in *n*. On the other hand, the σ-σ* ones remain almost constant.

(2) The PDST-*n* series have more complete σ-conjugation and less complete π-conjugation throughout the whole polymer chain compared with the PET-*n* series.

(3) The actual HOCO and LUCO interchange from the σ-type to the π-type upon the increase in *n*. This obviously signifies that π-conjugation in PDST-*n* becomes strengthened at the thienylene unit.

(4) The experimentally observed λ_{max} of PDST-*n* is interpreted as the π-π* band gap.

References

[1] R. D. Miller and J. Michl, *Chem. Rev.*, **89**, 1359 (1989).

[2] H. Sakurai, *J. Organomet. Chem.*, **200**, 261 (1980).

[3] S. H. Yi, N. Maeda, T. Suzuki, and H. Sato, *Polym. J.*, **24**, 865 (1992).

[4] See for instance, *Handbook of Conducting Polymers*, T. A. Skotheim ed., Vols. 1 and 2, Marcel Dekker, NY (1986).

[5] D. J. Wolford, J. A. Reimer, and B.A. Scott, *Appl. Phys. Lett.*, **42**, 369 (1983).

[6] K. Furukawa and N. Matsumoto, *Solid State Commun.*, **48**, 539 (1983).

[7] R. West, L. D. David, P. I. Djurovich, K. L. Stearley, K. S. V. Srinivasan, and H. Yu, *J. Am. Chem. Soc.*, **103**, 7352 (1981).
[8] M. Fujino, *Chem. Phys. Lett.*, **136**, 451 (1987).
[9] M. Abkowitz, F. E. Knier, H. J. Yuh, R. J. Weagley, and M. Stolka, *Solid State Commun.*, **62**, 547 (1987).
[10] R. G. Kepler, J. M. Zeigler, L. A. Harrah, and S. R. Kurtz, *Phys. Rev.*, **B35**, 2818 (1987).
[11] F. Kajzar, J. Messier Jr., and C. Rosilio, *J. Appl. Phys.*, **60**, 3047 (1986).
[12] P. Trefonos III, J. R. Damewood Jr., R. West, and R. D. Miller, *Organometallics*, **4**, 1318 (1985).
[13] (a) J. Ohshita, D. Kanaya, M. Ishikawa, T. Koike, and T. Yamanaka, *Macromolecules*, **24**, 2106 (1991). (b) J. Ohshita, D. Kanaya, and M. Ishikawa, *Appl. Organomet. Chem.*, **7**, 269 (1993).
[14] M. Ishikawa, T. Hatano, Y. Hasegawa, T. Horio, A. Kunai, A. Miyai, T. Ishida, T. Tsukihara, T. Yamanaka, T. Koike, and J. Shioya, *Organometallics*, **11**, 1604 (1992).
[15] J. Ohshita, D. Kanaya, M. Ishikawa, and T. Yamanaka, *J. Organomet. Chem.*, **369**, C18 (1989).
[16] M. Ishikawa, H. Sakamoto, M. Ishii, and J. Ohshita, *J. Polym. Sci.: Part A, Polym. Chem.*, **31**, 3281 (1993).
[17] M. Ishikawa, Y. Hasegawa, A. Kunai, and T. Yamanaka, *J. Organomet. Chem.*, **381**, C57 (1990).
[18] J. Ohshita, A. Matsuguchi, K. Fukumori, R. F. Hong, M. Ishikawa, T. Yamanaka, T. Koike, and J. Shioya, *Macromolecules*, **25**, 2134 (1992).
[19] K. Tanaka, K. Nakajima, M. Okada, T. Yamabe, and M. Ishikawa, *Organometallics*, **10**, 2679 (1991).
[20] K. Tanaka, K. Nakajima, M. Okada, T. Yamabe, and M. Ishikawa, *Organometallics*, **11**, 3191 (1992).
[21] S. H. Yi, J. Nagase, and H. Sato, *Synth. Met.*, **58**, 353 (1993).
[22] P. Chicart, R. J. P. Corriu, and J. J. E. Moreau, *Chem. Mater.*, **3**, 8 (1991).
[23] S. S. Hu and W. P. Weber, *Polym. Bull.*, **21**, 133 (1989).

[24] S. K. Ritter and R. E. Noftle, *Chem. Mater.*, **4**, 872 (1992).
[25] A. Kunai, T. Ueda, K. Horata, E. Toyoda, I. Nagamoto, J. Ohshita, M. Ishikawa, and K. Tanaka, *Organometallics*, **15**, 2000 (1996).
[26] Also see, G. G. Malliaras, J. K. Herrema, J. Wildeman, R. H. Wieringa, R. E. Gill, S. S. Lampoura, and G. Hadziioannou, *Adv. Mater.*, **5**, 721 (1993).
[27] H. Koezuka, A. Tsumura, and T. Ando, *Synth. Met.*, **18**, 699 (1987).
[28] K. Yoshino, K. Kaneto, and Y. Inuishi, *Jpn. J. Appl. Phys.*, **22**, L157 (1983).
[29] A. Imamura and H. Fujita, *J. Chem. Phys.*, **61**, 115 (1974).
[30] K. Tanaka, T. Shichiri, M. Kobashi, and T. Yamabe, *Synth. Met.*, **24**, 167 (1988).
[31] J. T. Nelson and W. J. Pietro, *J. Phys. Chem.*, **92**, 1365 (1988).
[32] K. Tanaka, T. Shichiri, and T. Yamabe, *Synth. Met.*, **16**, 207 (1986).
[33] M. Kertész, *Adv. Quantum. Chem.*, **15**, 161 (1982).
[34] J. Kao and L. Radom, *J. Am. Chem. Soc.*, **101**, 311 (1979).
[35] D. D. Cunningham, L. L. Davidson, H. B. Mark Jr., C. V. Pham, and H. Zimmer, *J. Chem. Soc., Chem. Commun.*, 1021 (1987).
[36] K. Takeda, H. Teramae, and N. Matsumoto, *J. Am. Chem. Soc.*, **108**, 8186 (1986).

Chapter 2

Design of Ferromagnetic Polymers Consisting of Thienylene and Silicon Units

1. Introduction

Since Ovchinnikov [1] proposed organic ferromagnets with unpaired electrons accommodated in nonbonding molecular orbitals (NBMOs) based on the topological aspect, polymers and oligomers with high-spin multiplicity have been attracting much interest from both experimental [2-5] and theoretical [6-8] viewpoints. One of the recent topics is the proposition of a polaronic ferromagnetic polymer consisting of alternately aligned a spin supplier block (SSB) and a ferromagnetic coupling block (spacer) [9], one of the concepts of which is illustrated in Fig. 1. This concept has been experimentally examined based on the ferromagnetic couplings between paramagnetic centers introduced by the doping [10].

Meanwhile, polysilane (PS) is known to have a developed σ-conjugation along the main chain and to exhibit the ultraviolet (UV) absorption originating from the $\sigma-\sigma^*$ transition [11]. Copolymers alternately aligned a silicon unit (silylene or disilanylene) and a π-conjugated carbon unit in the main chain have been synthesized [12-15] and also studied theoretically [16,17]. In the previous chapter [18], the electronic structures of organosilicon polymers consisting of sequential disilanylene and

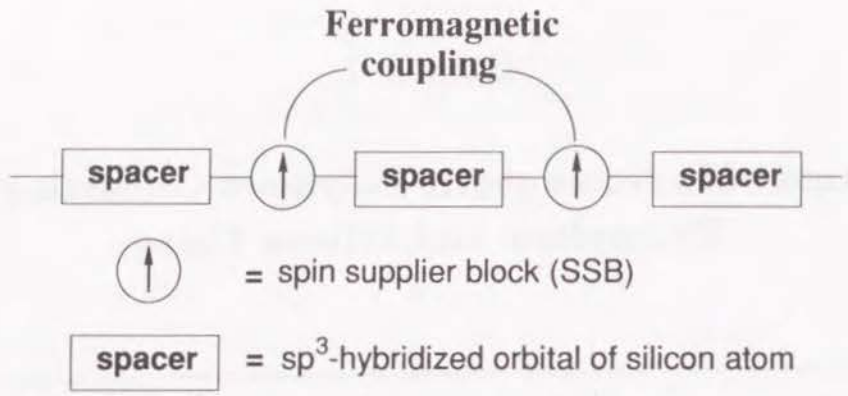

Figure 1. Concept of a polaronic ferromagnet in a one-dimensional array.

thienylene units, poly(disilanylene(thienylene)$_n$) (PDST-n; n=1-5), which have been actually synthesized [19,20], are described. It has been found that π-conjugation over the thienylene units is almost completely interrupted by sp^3-hybridized orbital of silicon atoms. Such a group of polymers may not be good as electrically conducting materials.

On the other hand, such a cut-off of the π-conjugation could be useful to the molecular design of polaronic ferromagnetic polymer illustrated in Fig. 1; polarons of π-nature generated in SSB (thienylene units) by an appropriate doping process [21,22] could be ferromagnetically coupled through the spacer consisting of sp^3-hybridized orbital of silicon. Moreover, the function of the spacer could be controlled by changing the number or kinds of atoms in the spacer.

In the present chapter, following this molecular design, we analyze the ferromagnetic properties of organosilicon polymer systems in their cationic states, changing the combination of SSB and spacer as shown in Fig. 2. We examine the electronic structures and magnetic properties of these polymers focusing on three points: (i) the relationship between the size of

SSB (thienylene unit) and the magnetic property, (ii) the influence of the size of the spacer (silylene or disilanylene units) bridging the SSB on the magnetic property of the whole polymer, (iii) the influence of the sp^3-hybridized orbital of silicon atoms on the spin distribution compared with those of carbon atoms in the spacer.

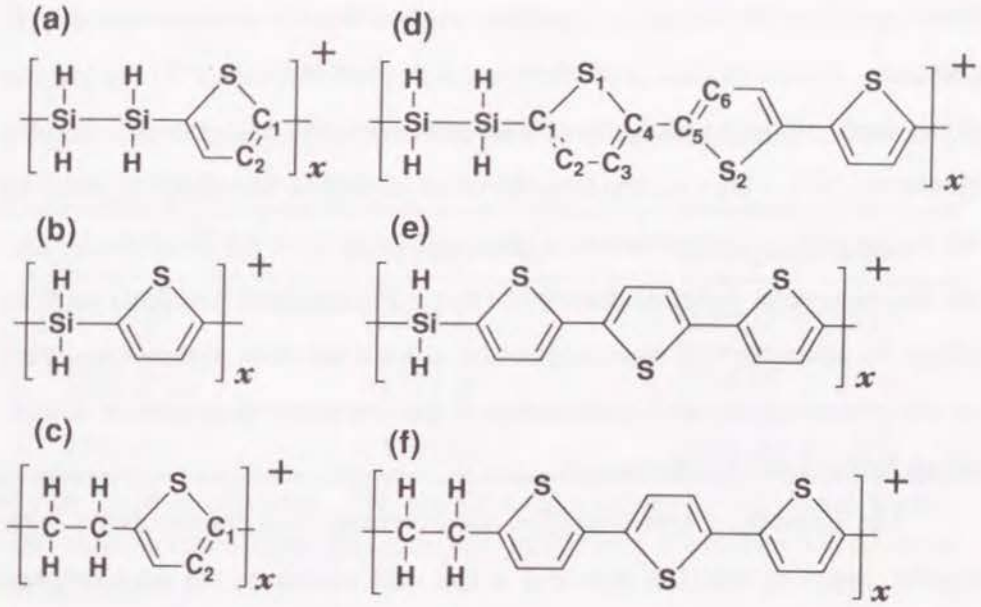

Figure 2. Schematic illustration of cationic polymer skeletons of poly(disilanylene(thienylene)$_n$) (PDST-n), poly(silylene(thienylene)$_n$) (PST-n), and poly(ethylene(thienylene)$_n$) (PET-n): (a) PDST-1$^+$, (b) PST-1$^+$, (c) PET-1$^+$, (d) PDST-3$^+$, (e) PST-3$^+$, and (f) PET-3$^+$.

2. Method of Calculation

The calculations were performed on the basis of the one-dimensional tight-binding self-consistent field crystal orbital (SCF-CO) method under the CNDO/2 approximation including all the valence electrons [23]. The program employed for the present calculation is able to handle the screw axis symmetry as well as the translational symmetry. The restricted Hartree-

Fock (RHF) and the unrestricted Hartree-Fock (UHF) methods were used for the calculation of the diamagnetic and the ferromagnetic states, respectively.

The geometries of the present model polymers in their cationic states possessing a hole in each unit cell shown in Fig. 2 were employed from those optimized by the energy gradient method for the neutral state of each polymer. Details of their geometries are described in Chapter 1 [18] and not given here. These optimized neutral polymers are coplanar with the C_s symmetry [18]. This assumption, however, seems to be plausible as far as for the purpose of determination of the stability between the diamagnetic and the ferromagnetic states as described later. Polarization functions such as silicon 3d atomic orbital were suppressed, since it has been reported that they do not give an appreciable contribution to the electronic structures of silicon atoms in this kind of polymer [18].

The number of representative wave vectors was chosen as 21 with regular intervals ($\pi/10a$, where a is the unit vector of the translational symmetry) in the Brillouin zone. The overlap and the electron repulsion integrals were considered as far as the second to fourth nearest neighboring cells (about 30Å), depending on the length of the unit cell of each polymer. The electronic structures of a thiophene molecule and its oligomers in their optimized geometries were also checked by the semiempirical PM3 molecular orbital calculations [24] for the sake of comparison

3. Results and Discussion

3.1. Total energies. Examination of the total energies of the selected cationic polymers is listed in Table 1. We have not shown here the antiferromagnetic state for these forms on account of technical difficulty in

performing the present mean-field-type calculation. Owing to the lack of exchange terms, it is difficult to compare the total energy of ferromagnetic and diamagnetic states in a simple manner. However one can see that PDST-1$^+$ and PST-1$^+$ favors the ferromagnetic state rather than PET-1$^+$. This feature of the silicon unit is more appropriate for the ferromagnetic spin alignment than the carbon unit.

Table 1. Total energies per unit cell (in eV) of the ferromagnetic and the diamagnetic states in the cationic polymers.

	Ferromagnetic state[a]	Diamagnetic state[b]
PDST-1$^+$	-1382.73	-1380.22 (+2.51)[c]
PST-1$^+$	-1229.00	-1226.05 (+2.95)
PET-1$^+$	-1561.93	-1560.70 (+1.23)

[a]By the UHF calculations. [b]By the RHF calculations for the closed-shells. [c]The value in parenthesis shows the energy difference between two kinds of energy values; see text.

3.2. Band structures. The band structures of the ferromagnetic state of PDST-1$^+$ and PDST-3$^+$ obtained by the UHF method are shown in Fig. 3 along with those of the neutral polymers [18]. It is seen that in cationic polymers electrons are removed from the π-type CO since the LU band of the spin-down part is of π-nature in both PDST-1$^+$ and PDST-3$^+$. Note that π-electrons are extracted in PDST-1$^+$ in spite of the HO band of σ-nature in PDST-1, the reason of which is discussed later. Although there is no appropriate way of estimating the exchange parameter J [25] applicable to the present crystal-orbital framework, feasibility of ferromagnetic spin correlation in the present system is considered to come from a sort of Hund's

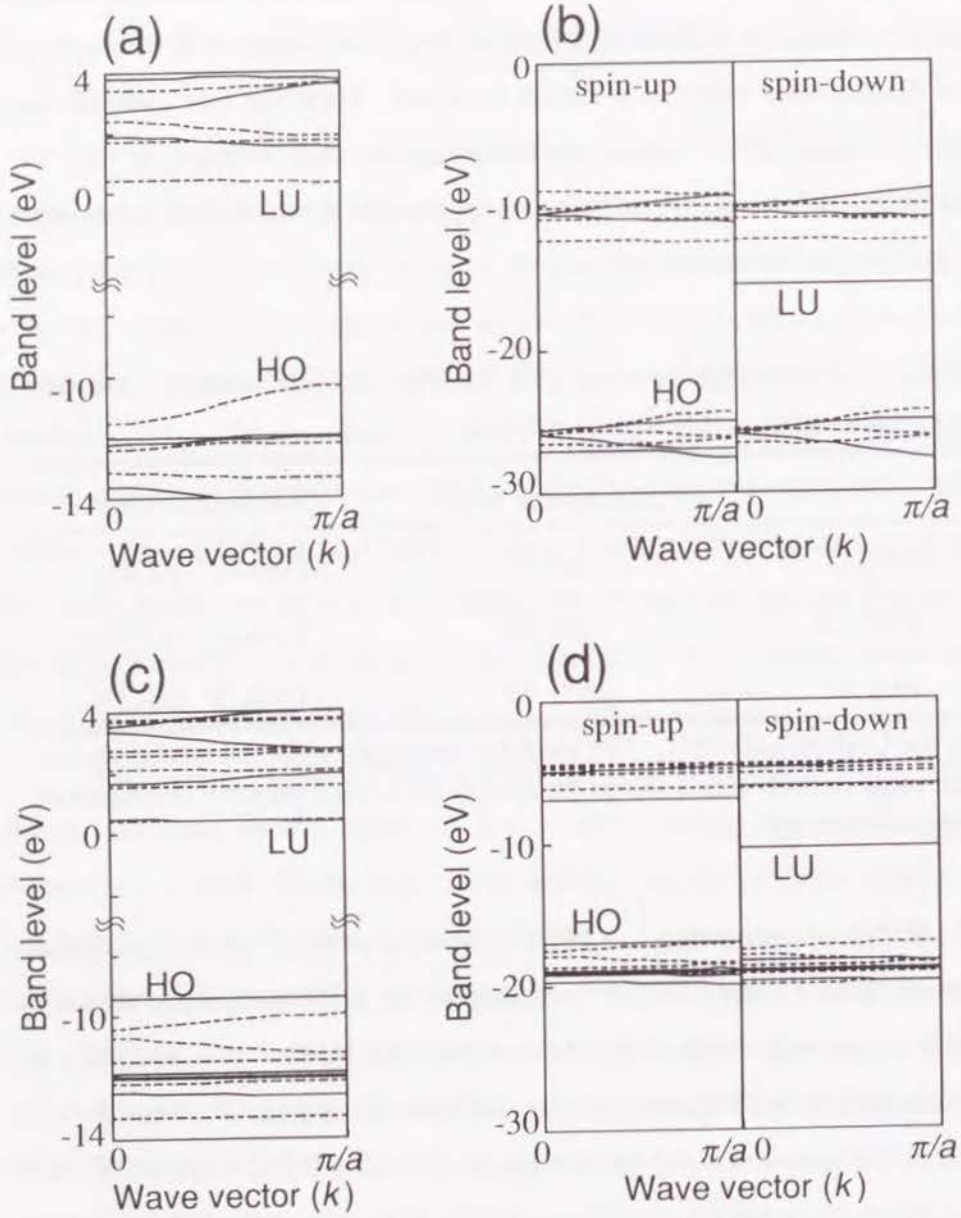

Figure 3. Band structures of (a) PDST-1, (b) PDST-1$^+$, (c) PDST-3, and (d) PDST-3$^+$, where solid and broken lines indicate π- and σ-bands, respectively.

rule favoring the highest spin multiplicity. Hence, the ferromagnetic correlation can operate on the radical π-spins in the degenerate COs in SSB separated by the spacer.

In Table 2 the electronic properties from the π-type COs for both the neutral and cationic states are listed. The π-π* band gaps of the spin-up part are almost the same with those of the neutral state, whereas those of the spin-down part are in general lower. It is seen that the HO π-bandwidths of the cationic polymers (ferromagnetic bandwidths) with three-thiophene rings in SSB (PDST-3$^+$ and PST-3$^+$) are smaller than those with one-thiophene ring (PDST-1$^+$ and PST-1$^+$). The ferromagnetic bandwidth of PDST-3$^+$ is thus 0.01 eV, being narrowest of all. This narrow bandwidth is appropriate to macroscopic spin alignment, the situation of which resembles poly(m-aniline) [8,26]. Longer thiophene oligomers such as pentamer or hexamer are not recommended for SSB, since a two-electron oxidation would occur yielding a bipolaron in a SSB, as is well known in polythiophene [27]. Moreover, a too long spacer would make the system paramagnetic by causing breakdown of ferromagnetic coupling between SSBs.

3.3. Orbital patterns. The patterns of the HO π-CO (spin-up part) and the LU π-CO (spin-down part) at the Brillouin zone boundary are illustrated in Fig. 4, since the energy levels of these COs at the boundary are the highest and the lowest, respectively. Except for this LUCO of PDST-1$^+$, the patterns of the HO π-CO and the LU π-CO resemble PDST-3$^+$ and PET-1$^+$ and are delocalized on the carbon skeletons in the thienylene unit. The reason for this peculiar feature of the LUCO of PDST-1$^+$ can be understood by the MO calculations (semiempirical PM3 [24]) for a thiophene and a bithiophene as shown in Fig. 5; that is, the HOMO of thiophene (b_1) has a

Table 2. Calculated band gap and the HO π-bandwidth (in eV).

	π–π* band gap			HO π-Bandwidth	
	Neutral	Ferromagnetic		Neutral	Ferromagnetic[a]
		spin-up part	spin-down part		
PDST-1	13.49	13.79	9.45	0.01	0.64
PDST-3	9.80	9.94	6.68	0.003	0.01
PST-1	13.73	15.37	9.51	0.06	1.41
PST-3	10.01	10.04	7.62	0.07	0.12
PET-1	13.97	13.76	6.84	0.03	0.22
PET-3	9.65	9.78	7.28	0.06	0.03

[a]For the spin-up part.

large coefficient on the sulfur atom and the next HOMO (NHO) (a_2), being lower by 0.34 eV, is delocalized on the carbon atoms. On the other hand, these two MO levels become reversed in bithiophene, where two essentially degenerated MOs (a_u and b_g) appear as the NHO. The situation of the MO levels of terthiophene is similar to that of bithiophene. Hence, the growth of π-conjugation through the carbon skeleton in a thienylene unit is found to rule the π-MO levels.

In Fig. 4(a) it is seen from the LU π-CO (spin-down part) of PDST-1$^+$ that an electron is extracted mainly from the sulfur atom as is deduced from the HOMO (b_1) of thiophene. The singly occupied CO accommodating the up-spin can be somewhat stabilized because of the decrease in the electron repulsion on the sulfur atom. Thus, the a_2-like orbital of thiophene in turn becomes the HO π-CO (spin-up part) of PDST-1$^+$. In other words, the b_1-like orbital mainly existing on the sulfur atom in the neutral state is split by the electron extraction, which explains the relatively wide band gap of the up-spin part of PDST-1$^+$ and PST-1$^+$. It is considered that the stabilization by splitting the b_1-like orbital is so large that π-electrons are expected in PDST-1$^+$. In contrast to PDST-1$^+$, both the LU π-CO (spin-down part) and the HO π-CO (spin-up part) of PET-1$^+$ is quite similar to the a_2-like orbital of thiophene, which can be explained by invoking the fact that hyperconjugation through pseudo π-orbitals in the ethylene moiety promotes the delocalization of π-electrons. From this result we can conclude that silicon atoms more strongly cut off the π-conjugation of thienylene unit compared with carbon atoms. This signifies that the disilanylene unit is more appropriate to the present design compared with the ethylene unit as the spacer.

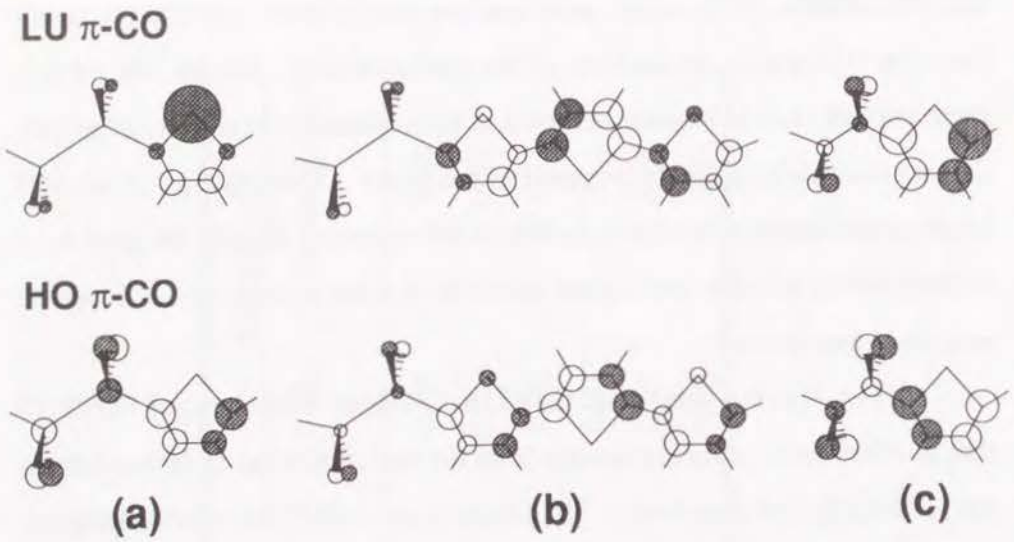

Figure 4. Orbital patterns of the LU π-CO (upper) and HO π-CO (lower) of (a) PDST-1$^+$, (b) PDST-3$^+$, and (c) PET-1$^+$.

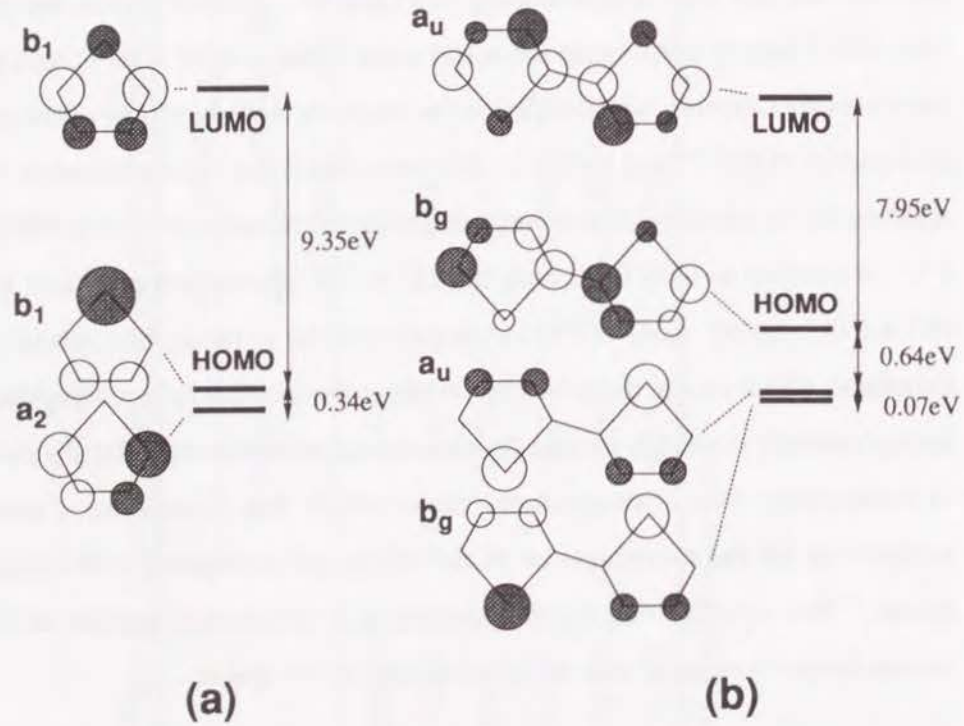

Figure 5. Frontier MO levels and orbital patterns of (a) thiophene and (b) bithiophene molecules.

3.4. Electron and spin densities. The calculated electron densities of the present polymers are listed in Table 3. It is seen that the silicon atoms of PDST-1 and PDST-3 are positively charged both in the neutral and cationic states. This is somewhat similar to the carbon atoms corresponding to silicon atoms in PET-1. On the other hand, the sulfur atom in PDST-1$^+$ loses one π-electron as seen from the π-AO density. In PDST-3$^+$ and PET-1$^+$, the electron is mainly extracted from the carbon atoms in the thienylene unit as a whole, agreeing with the CO patterns shown in Fig. 4. Also, the spin distribution in PDST-2$^+$ is similar to PDST-3$^+$.

In the present cationic polymers, almost all the spins are of π-spins as illustrated in Fig. 6. A large amount of up-spins (0.93) localizes on the sulfur atom in PDST-1$^+$ agreeing with the CO patterns in Fig. 4(a). On the other hand, PDST-3$^+$ and PET-1$^+$ show quite different spin distributions from PDST-1$^+$, in which the up-spins with π-nature are distributed through the carbon atoms in the thienylene unit and the magnitude of these spins duly correspond to the magnitude of the π-HOCO (spin-up part) in Fig. 4(b). In spite of the potentially spin-frustrated nature of five-membered rings, the present polymers show a certain definite ferromagnetic spin alignment in the cationic state. Note that the spin distribution of PST-1$^+$ is quite similar to that of PDST-1$^+$ and also in those of PST-3$^+$ and PDST-3$^+$, although the topological arrangements differ.

Table 3. Calculated results of the electronic structures.[a]

Polymer	Atom	Atomic net charge[b]		Atomic spin density
		Neutral	Ferromagnetic	(Ferromagnetic)
PDST-1	Si	0.34 (0.82)	0.39 (0.88)	-0.01
	S	-0.10 (1.90)	0.32 (1.00)	0.93
	C_1	-0.06 (1.03)	-0.07 (1.07)	-0.03
	C_2	0.01 (1.02)	0.06 (0.92)	0.06
	H(Si)	-0.12	0.06	0.00
	H(C_2)	-0.01	-0.05	0.00
PDST-3	Si	0.36 (0.82)	0.38 (0.85)	-0.02
	S_1	-0.13 (1.89)	-0.06 (1.90)	0.00
	S_2	-0.14 (1.88)	-0.08 (1.91)	-0.02
	C_1	-0.06 (1.04)	-0.02 (0.89)	0.15
	C_2	0.02 (1.01)	0.00 (1.04)	-0.04
	C_3	-0.02 (1.05)	0.09 (0.87)	0.19
	C_4	0.07 (1.01)	0.03 (1.04)	-0.04
	C_5	0.07 (1.03)	0.14 (0.87)	0.17
	C_6	-0.01 (1.03)	0.03 (0.95)	0.08
	H(Si)	-0.12	-0.08	0.01
PET	C_0	0.03 (0.97)	0.00 (1.00)	-0.01
	S	-0.17 (1.89)	0.04 (1.91)	-0.01
	C_1	0.06 (1.02)	0.18 (0.75)	0.31
	C_2	-0.01 (1.05)	0.05 (0.92)	0.11
	H(C_0)	0.00	0.09	0.06
	H(C_2)	0.00	0.08	0.00

[a]See Fig. 2 for the atomic numberings. [b]Parenthetic entries are the π-AO densities.

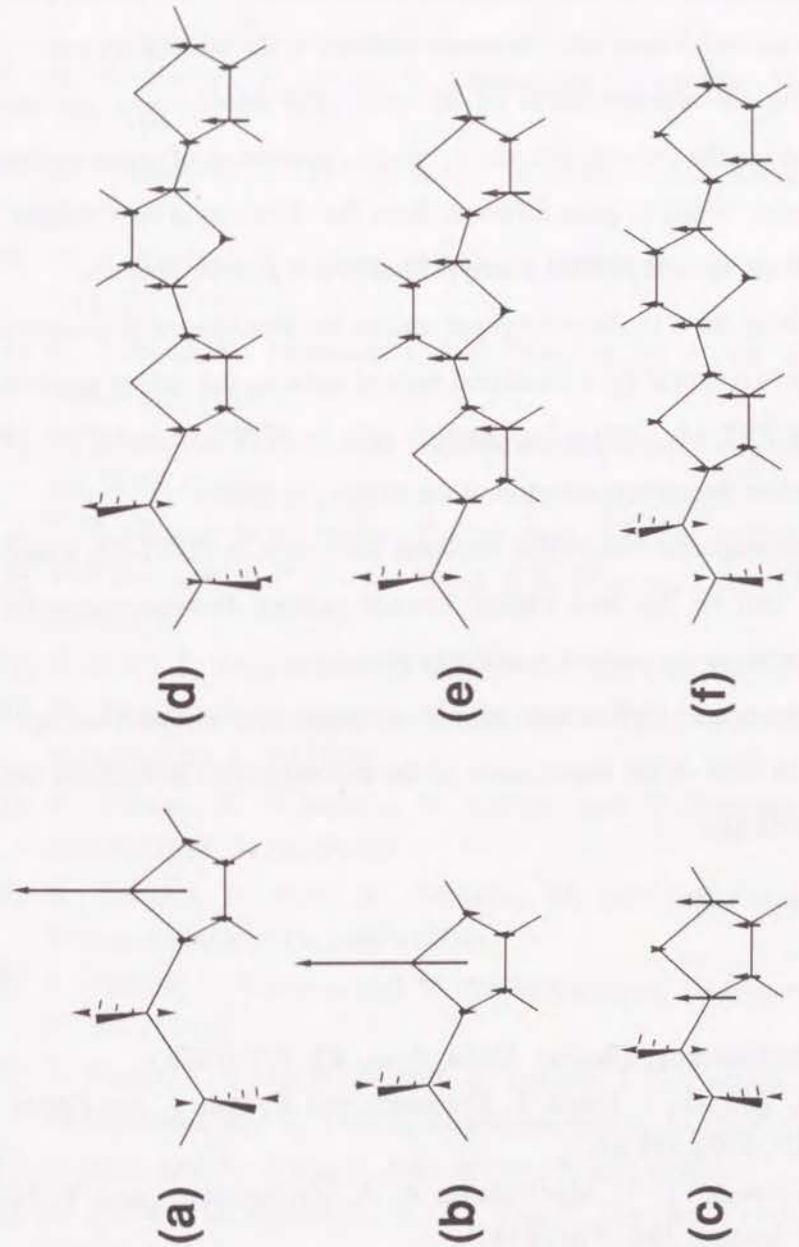

Figure 6. Spin distributions in (a) PDST-1^+, (b) PST-1^+, (c) PET-1^+, (d) PDST-3^+, (e) PST-3^+, and (f) PET-3^+.

4. Conclusion

We have performed a molecular design of new type of polaronic ferromagnetic polymer with an appropriate combination of the spin supplier block and the spacer. There are five major findings in the present chapter:

(1) Topological arrangements of up-spins and down-spins are not necessarily hold in the present polymeric systems consisting of spin supplier block and spacer, which is quite different from the situation in the "simple" polymer skeletons such as poly(*m*-phenylcarbene) and poly(*m*-aniline).

(2) The radical spins in the thienylene unit in the ferromagnetic state are classified into two types: (i) a localized radical spin on the sulfur atom in PDST-1$^+$ and PST-1$^+$. (ii) a "polaronic" spin in PDST-3$^+$ and PST-3$^+$ delocalized within the carbon skeleton of the thienylene units.

(3) The ferromagnetic bandwidth becomes narrowest in PDST-3$^+$, which we conclude will be the best choice toward getting ferromagnetically correlated polarons in the present candidates examined.

(4) As to the spacer, sp^3-silicon atoms are more appropriate than sp^3-carbon atoms in view of the suppression of the π-conjugation throughout the whole polymer chain.

References

[1] A. A. Ovchinnikov, *Theoret. Chim. Acta.*, **47**, 297 (1978).

[2] I. Fujita, Y. Teki, T. Takui, T. Kinoshita, and K. Itoh, *J. Am. Chem. Soc.*, **112**, 4074 (1990).

[3] Y. V. Korshak, T. V. Medvedeva, A. A. Ovchinnikov, and V. N. Spector, *Nature*, **326**, 370 (1987).

[4] J. B. Torrance, S. Oostra, and A. Nazzal, *Synth. Met.*, **19**, 709 (1987).

[5] K. Tanaka, T. Shichiri, and T. Yamabe, *J. Mol. Struct. (Theochem)*, **188**, 313 (1989).

[6] D. J. Klein, *J. Chem. Phys.*, **77**, 3098 (1982).

[7] N. Tyutyulkov, O. E. Polansky, P. Schuster, S. Karabunarliev, and C. I. Ivanov, *Theoret. Chim. Acta.*, **67**, 211 (1985).

[8] K. Yoshizawa, A. Takata, K. Tanaka, and T. Yamabe, *Polym. J.*, **24**, 857 (1992).

[9] H. Fukutome, A. Takahashi, and M. Ozaki, *Chem. Phys. Lett.*, **133**, 34 (1987).

[10] D. A. Kaisaki, W. Chang, and D. A. Dougherty, *J. Am. Chem. Soc.*, **113**, 2764 (1991).

[11] K. Takeda, H. Teramae, and N. Matsumoto, *J. Am. Chem. Soc.*, **108**, 8186 (1986).

[12] M. Ishikawa, T. Horio, T. Hatano, and A. Kunai, *Organometallics*, **12**, 2078 (1993).

[13] S. S. Hu and W. P. Weber, *Polym. Bull.*, **21**, 133 (1989).

[14] P. Chicart, R. J. P. Corriu, and J. J. E. Moreau, *Chem. Mater.*, **3**, 8 (1991).

[15] S. H. Yi, J. Nagase, and H. Sato, *Synth. Met.*, **58**, 353 (1993).

[16] K. Tanaka, K. Nakajima, M. Okada, and T. Yamabe, *Organometallics*, **10**, 2679 (1991).

[17] K. Tanaka, K. Nakajima, M. Okada, and T. Yamabe, *Organometallics*, **11**, 3191 (1992).

[18] K. Tanaka, H. Ago, T. Yamabe, M. Ishikawa, and T. Ueda, *Organometallics*, **13**, 3496 (1994).

[19] J. Ohshita, D. Kanaya, and M. Ishikawa, *Appl. Organomet. Chem.*, **7**, 269 (1993).

[20] A. Kunai, T. Ueda, K. Horata, E. Toyoda, I. Nagamoto, J. Ohshita, M. Ishikawa, and K. Tanaka, *Organometallics*, **15**, 2000 (1996).

[21] S. Hotta and K. Waragai, *Adv. Mater.*, **5**, 869 (1993).

[22] D. Fichou, G. Horowitz, B. Xu, and F. Garnier, *Synth. Met.*, **39**, 243 (1990).

[23] A. Imamura and H. Fujita, *J. Chem. Phys.*, **61**, 115 (1974).

[24] J. J. P. Stewart *et al.*, MOPAC ver 6.0 (PM3) program.

[25] See for instance, S. A. Alexander and D. J. Klein, *J. Am. Chem. Soc.*, **110**, 3401 (1988).
[26] K. Yoshizawa, K. Tanaka, and T. Yamabe, *J. Phys. Chem.*, **98**, 1851 (1994).
[27] See for instance, G. Tourillon, in *Handbook of Conducting Polymers*, T. A. Skotheim ed., Vol. 1, Chapter 9, Marcel Dekker, NY (1986).

Chapter 3

Electronic Properties of p-Type Doped Copolymers Containing Thienylene and Disilanylene Units

1. Introduction

In recent years, organic ferromagnets are one of the subjects of increased interest [1]. The organic ferromagnets, so far succeeded in preparation can be classified into two groups based on the different concepts for the magnetic interaction. The first group includes organic crystals consisting of the built-in-radicals such as nitroxide radical molecules [2-4]. This type of radical crystal utilizes the through-space magnetic interaction between the localized spins. The second is classified as charge-transfer complexes including e.g., tetrakis(dimethylamino)ethylene-C_{60} (TDAE-C_{60}) showing ferromagnetic transition at 17.5 K [5,6].

Apart from these, ferromagnetism occurring in organic polymers is of strong interest, since polymers have several advantages such as the ease of fabrication not requiring care for subtle crystal structure and the possibility of preparing the material with large area. The main strategy to endow organic polymers with ferromagnetic spin correlation is based on the idea of topological correlation of the localized spins via the through bond interaction [7,8]. Along this line, considerably high spin multiplicity (S=4) of *m*-phenylcarbene oligomers has been reported [9]. As the modification of the above second-class members, polaronic ferromagnetic polymer involving

delocalized polaronic spins which are generated by chemical doping has been proposed [10]. In this type of polymers spins generated in the spin supplier block (e. g., polyene) interact ferromagnetically through the coupling unit (e. g., *m*-phenylene). In fact, certain polymers with ferromagnetic spin alignment (S=5/2 at maximum) have been synthesized along this strategy [11].

Recently we have proposed, by extending this polaronic ferromagnet model, copolymers consisting of π-conjugated unit as the spin supplier and non-π-conjugated unit with several sp^3-hybridized atoms as the spacer toward a new candidate for polymeric organic ferromagnet [12]. The interaction between the polaronic spins generated in the spin supplier block by p-type doping is tunable by changing the length and atomic species of the spacer. Based on this prospect, polymeric organosilicon systems consisting of regularly aligned disilanylene and π-conjugated units have been examined (Fig. 1) [12], since it has been made clear that the electronic structures of these neutral polymers are rather well localized with a large band gap and small bandwidths indicative of weak interaction between the σ- and the π-units [13]. In fact, the electrical conductivity of the SbF_5-doped poly[disilanylene(thienylene)] [14,15] and poly[disilanylene(phenylene)] [16] are not remarkably large (10^{-3}~10^{-5} S/cm) comparing with those of the doped polythiophene (PT) [17] and poly(*p*-phenylene) (PPP) (10^{0}~10^{2} S/cm) [18]. Furthermore, pseudo π-conjugation in the disilanylene unit is less developed than in the ethylene one [13]. A one-dimensional unrestricted Hartree-Fock crystal orbital calculations [12] have found two types of spins in the cationic states of poly[disilanylene(thienylene)$_n$] (PDST-*n*; n=1-3): one is the spin localized on the sulfur atom in PDST-1 and another delocalized over the carbon skeletons in the oligothienylene unit in PDST-*n*

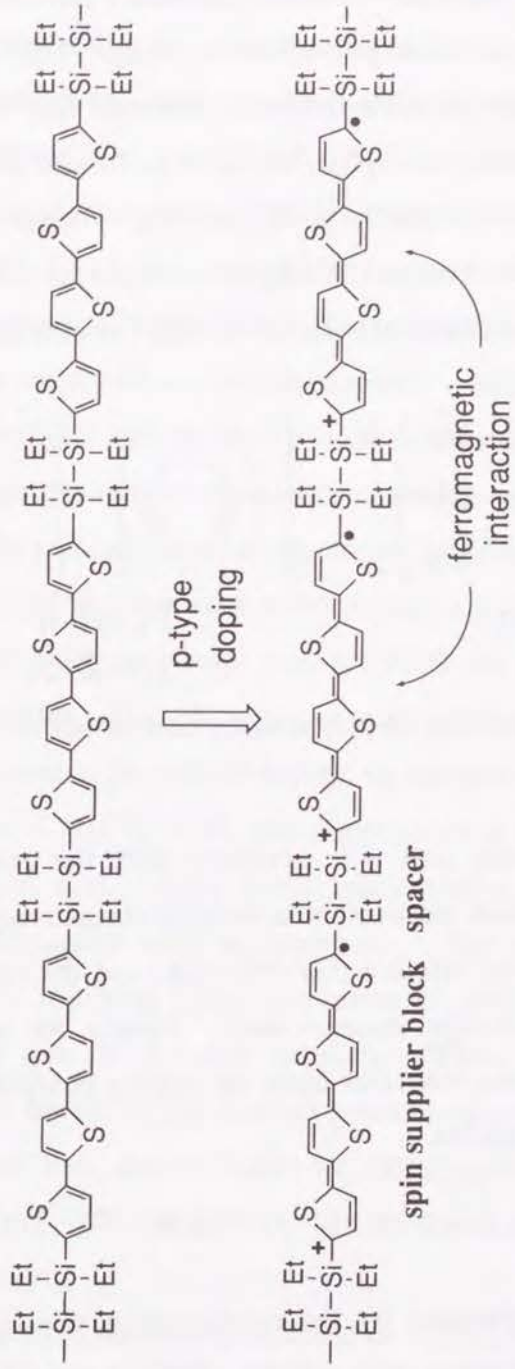

Figure 1. Illustrative description of the polaronic ferromagnet. In this model, the polarons are generated in each oligothienylene unit (spin supplier block) by chemical doping and these spins interact ferromagnetically through disilanylene unit (spacer).

for $n \geq 2$. The overall calculation in ref. 12 has suggested the cationic PDST-3 is the most promising candidate with ferromagnetically correlated polarons.

In the present chapter actual preparation of cationic PDST-n (n=1-5) is presented. To elucidate the nature of spins generated and the nature of interaction working among the spins, we have performed experimental investigation on the cationic PDST-n (n=1-5; see Fig. 2) doped by electron-accepting nitrosyl tetrafluoroborate ($NOBF_4$) so as to analyze their electronic properties. Their electrochemical behavior of PDST-n with respect to the

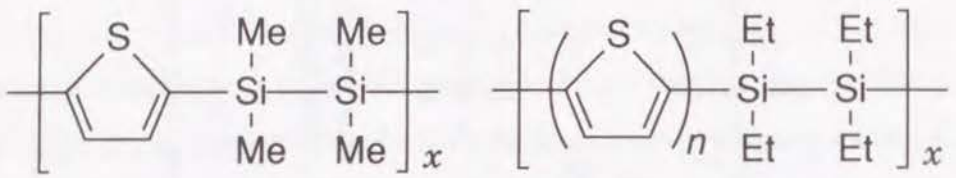

Figure 2. Chemical structures of poly[disilanylene(thienylene)$_n$)] (PDST-n).

length of oligothienylene unit n is examined with the use of cyclic voltammetry (CV), and their electronic structures are characterized based on the ultraviolet-visible-near infrared (UV-VIS-NIR) and the electron spin resonance (ESR) spectroscopic measurements. Finally, we mention the degradation of the disilanylene unit upon the doping confirmed by the infrared (IR) absorption spectra.

2. Experimental

PDST-1 was synthesized by the condensation reaction of 2,5-bis(chlorodiethylsilyl)thiophene with sodium. PDST-2 and PDST-4 were prepared by the reaction of 1,2-bis[2-(5-bromothienyl)]tetraethyldisilane (**1**)

and 1,2-bis[5-(5'-bromo-2,2'-bithienyl)]-tetraethyldisilane (**2**) with 1 equiv. of magnesium in THF, followed by treatment of the resulting solutions with a $NiCl_2$(dppe) catalyst in a sealed degassed tube. PDST-3 and PDST-5 were synthesized by cross coupling of the corresponding di-Grignard reagents obtained from **1** and **2** with 2,5-dibromothiophene in the presence of the nickel catalyst, as reported in the literature [19,20].

For the CV measurements a conventional combination of a potentiogalvanostat (Nikko NPGS-301) and a function generator (Nikko NFG-3) was employed and dry benzonitrile solution containing 1 M of oligothienylene unit and 0.1 M of n-tetrabutylammonium tetrafluoroborate (n-Bu_4NBF_4) as the electrolyte was examined with a potential scan rate of 50 mV/sec. The saturated caromel electrode (SCE) was used as a reference electrode and Pt wires were used as the counter and the working electrodes.

UV-VIS-NIR spectrum was recorded on a Shimadzu UV365 spectrophotometer. The spectroscopic grade of dichloromethane (CH_2Cl_2) solution was used as the solvent without further purification. Polymer was dissolved in CH_2Cl_2 with the concentration of 4×10^{-5} M of the oligothienylene unit. Such dilute concentration was adopted so that interchain interaction may be neglected. The chemical doping was performed by injecting CH_2Cl_2 solution of $NOBF_4$ (3×10^{-2} M) with microsyringe into the polymer solution. Three levels of the dopant concentration based on the prepared molar ratio of the dopant to the oligothienylene unit, that is, lightly ($NOBF_4$/oligothienylene unit=1-20), intermediately (20-40), and heavily (40-100) doped states are considered in the present study.

ESR spectrum was mainly recorded on a JEOL RE-2X spectrometer at the X band (9.1 GHz) in the temperature range 123-293 K. The sample was

doped by CH_2Cl_2 solution of $NOBF_4$ in an ESR quartz tube followed by the removal of the solvent under vacuum, and then sealed under vacuum. The doping degree is classified into three levels as described above. The $CuSO_4 \cdot 5H_2O$ crystal was used as the reference for the calculation of spin concentration and the Mn^{2+}-MgO solid solution was used for the determination of the peak-to-peak linewidth ($\Delta H_{p.p.}$) and the g-value. For several samples, the ESR spectra were measured down to 4.5 K by using a Varian E-112 with an Oxford cryogenic system.

The Fourier transform (FT)-IR spectra were measured on a BIO-RAD FTS-30 FT-IR spectrometer. The $NOBF_4$-doped samples were prepared in the CH_2Cl_2 solution. After evaporation and drying under vacuum, the sample was mixed with KBr to make a pellet, which was subjected to the IR measurement. The KBr used had been pre-treated at 300°C in vacuo to eliminate the moisture included.

3. Results and Discussion

3.1. CV measurements. The results of CV measurements for each polymer in 0.1M n-Bu_4NBF_4/benzonitrile solution with the scan rate of 50 mV/sec are listed in Table 1. Selected CV curves shown in Fig. 3. PDST-1 did not show any redox waves within the present scan range appropriate to the solvent and PDST-2, -3, and -4 showed relatively small and broad oxidizing waves without the reducing wave. In PDST-5 two clear oxidizing waves along with two reduction peaks were seen. Values of the first oxidation potential (E^{ox}_1) of PDST-2~5 are quite similar to those of the corresponding α,α'-bis(trimethylsilyl) substituted bithiophene (1.46 V vs. SCE), terthiophene (1.21 V), quaterthiophene (1.04 V), and quinquethiophene (0.98 V) molecules [21]. Note these values decrease as the

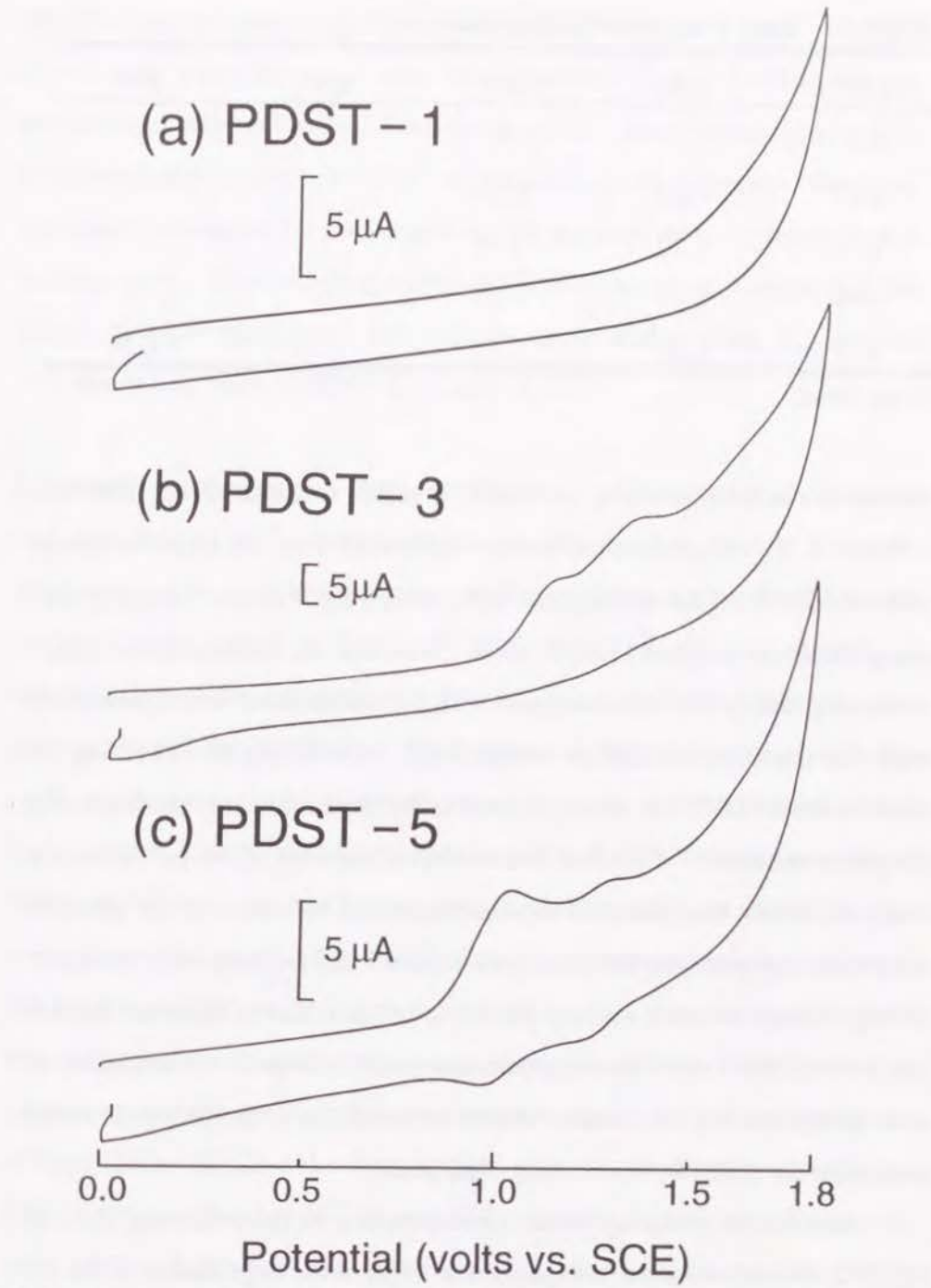

Figure 3. Selected CV diagrams of (a)PDST-1, (b)PDST-3, and (c)PDST-5 in 0.1 M n-Bu_4NBF_4/CH_2Cl_2 solution. Scanning rate was 50mV/sec.

Table 1. The CV data of PDST-*n* (in V vs. SCE).

PDST-*n*	E^{ox}_1	E^{ox}_2	E^{red}_1	E^{red}_2
n=1	–	–	–	–
n=2	1.32	1.54[a]	–	–
n=3	1.12	1.34	–	–
n=4	1.03	1.25	–	–
n=5	1.02	1.22	0.97	1.21

[a]Very weak.

number of the thiophene ring increases. It is thus understood that in PDST-*n* electrons are electrochemically removed mainly from the oligothienylene units and not from the disilanylene units, which signifies the π-conjugation along the whole polymer chain is weak. Note that the easiness of oxidation in the oligothienylene unit compared with the disilanylene unit is consistent with our previous calculation results [12]. Difficulty of extracting an electron from PDST-1 is closely related to the large ionization potential of a thiophene molecule. The fact that oxidation currents of the polymers are relatively lower than those of the corresponding solutions of the genuine thiophene oligomer with the same concentration [22] suggests conglomerates of oligothienylene units even in the dilute solution due to macromolecular structure of PDST-*n*. The conglomerates possibly impede the oxidation of each thienylene unit in a chain. Moreover, solubility of the polymers could also cause the difficulty in obtaining clear peaks.

Absence of reducing waves corresponding to the oxidizing ones in PDST-2, -3, and -4 would be explained in terms of the degradation of the Si-Si bond, since insoluble dark brown powder was observed after the cycle. Degradation of Si chain caused by the CV has been observed in several

organosilicon polymers [23]. Polymerization reaction eventually forming PT is also possible as it has been reported that PT film can be electrochemically synthesized from dimethyl-bis(2-thienyl)silane [24] or 2,5-bis(trimethylsilyl)thiophene [25]. In any case, as the polymers convert to insoluble components by such reactions, the apparent reducing wave should become weak. Two reducing waves of PDST-5, however, suggest that the doped quinquethienylene unit can be more stable than the shorter oligothienylene units of PDST-2, -3, and -4.

3.2. Optical absorption measurements. The electronic structures of p-type doped PDST-*n* have been examined in detail by the UV-VIS-NIR spectrum. The optical absorption peak positions of the heavily doped polymers are listed in Table 2 with those of the corresponding oligothiophenes for comparison. The λ_{max} values of the π-π^* transition peak in the neutral PDST-*n* are found to be red shifted compared with the corresponding neutral thiophene oligomers probably due to extension of the π-conjugation through the hyperconjugation in disilanylene unit as mentioned before and also due to the electron-donating nature of silicon atom [13]. In general, by oxidization, color of the oligothiophene solutions changed from yellow (or orange) to dark green (or dark blue). The changes in their electronic spectra caused by the p-type doping have been understood in a qualitative manner by change in the energy levels of the frontier molecular orbitals (MOs) [21,28-31]. For example, α,α'-dimethyl quinquethiophene (5T) shows two peaks at 747 nm and 1347 nm in its cationic state (polaronic state, $5T^{\bullet+}$) and one at 873nm in the dicationic state (bipolaronic state, $5T^{++}$) by continuous doping as shown in Table 2 [29].

Table 2. Peak positions of the pristine and the heavily doped PDST-*n* and the corresponding oligothiophenes (in nm).

PDST-*n*	pristine[a]	heavily doped[b]			oligothiophenes	pristine	lightly doped[c]	heavily doped[c]		
n=1	273 (transparent)	(transparent)			thiophene	215[e]				
n=2	343 (transparent)	442[d] (pale yellow)			bithiophene	302[f]	400[h]			
n=3	389 (pale yellow)	441 (dark orange)	617		terthiophene	350[g]	579[h]	886[h]		
n=4	412 (yellow)	441 (dark brown)	664	1137	quaterthiophene	388[g]	670[h]	1117[h]	667[h]	725[h]
n=5	427 (yellow)	478 (gree-blue)	780	1406	quinquethiophene	403[g]	747[h]	1347[h]	795[h]	873[h]

[a]In parentheses are shown the color of the solution of pristine PDST-*n*. [b]In parentheses are shown the color of the heavily doped PDST-*n* solution, respectively. [c]Definition of the doping degree does not necessarily agree with that for PDST-*n*. [d]Very weak. [e]Taken from ref. 26. [f]Taken from ref. 27. [g]Taken from ref. 28. [h]Taken from ref. 29.

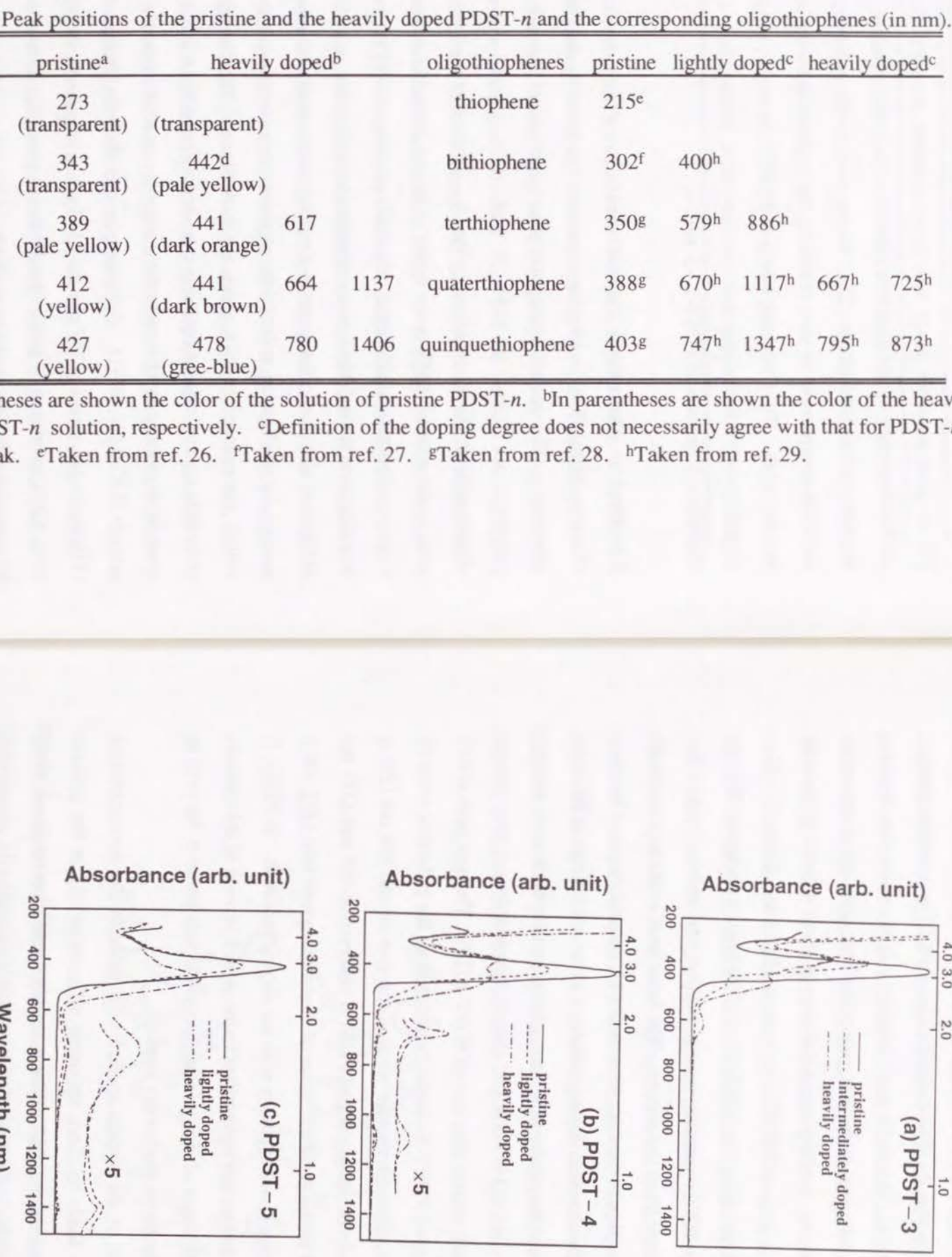

Figure 4. UV-VIS-NIR spectra of the pristine and the $NOBF_4$-doped (a)PDST-3, (b)PDST-4, and (c)PDST-5. Note there are three levels of the doping degrees (see Sec. 2).

The change in peak position upon the doping degree for PDST-3, -4, and -5 are shown in Fig. 4. The color change of PDST-*n* upon the doping is listed in Table 2. The main π-π^* transition splits upon the doping. Although the original transition peak causes the blue shift and decrease in intensity by the doping, a newly appearing peak at about 440 nm grows and is red-shifted by a little in PDST-5 as seen in Fig. 4 and Table 2. The former can be interpreted by the stabilization of the highest occupied (HO) π-type crystal orbital (CO) consisting mainly of thienylene units caused by the extraction of electron upon the doping. The latter peak could be associated with the π-π^* transition of the thienylene unit with quinoid structure because it is known that the chemical doping induces a structural change in PT from aromatic to less stable quinoid structure, giving smaller excitation energy. This peak is also observed in the doped oligothiophene solution, even though its intensity is much weaker than that of PDST-*n* [29]. The new peak at 617 nm of heavily doped PDST-3 can be considered as the polaronic state of terthienylene unit, although another weak absorption around 886 nm [29] is absent. New peaks of heavily doped PDST-4 observed at 664 and 1137 nm can be attributed to the polaronic state of quaterthienylene unit [29], since these peaks increase simultaneously with the doping proceeds. In PDST-5, the heavily doped state can be ascribed to the mixed version of the cationic and the dicationic states of the quinquethienylene unit because the peak at 1406 nm was reduced by the heavily doping.

Comparison of the optical spectra with those of the corresponding oligothiophenes leads to three apparent differences: (i) in the pristine polymers there occurs red shift of the main π-π^* transition by about 20-60 nm compared with the oligothiophene, (ii) a larger amount of the dopant than that in the oligothiophene is required to yield the new absorption peak at low

energy region corresponding to the cationic or the dicationic states of the oligothienylene units, and (iii) even after addition of the dopant to such larger amount, the new absorption peaks are much weaker and relatively broader than those of the oligothiophene. From the CV results, it is hard to remove electrons from each oligothienylene unit of PDST-*n*. We conjecture this is owing to the macromolecular structure of PDST-*n* shown, for instance, in Fig. 5. In the polymer solution, even though the solution is dilute, some oligothienylene units of one chain could surround the BF_4^- ion or, in other words, the oligothienylene units aggregate around the dopant. On the other hand, in a dilute solution of oligothiophene such aggregation would not occur due to the absence of closely located oligomers. Small charge-transfer (CT) between a BF_4^- ion and each oligothienylene unit results in several numbers of the partially charged units.

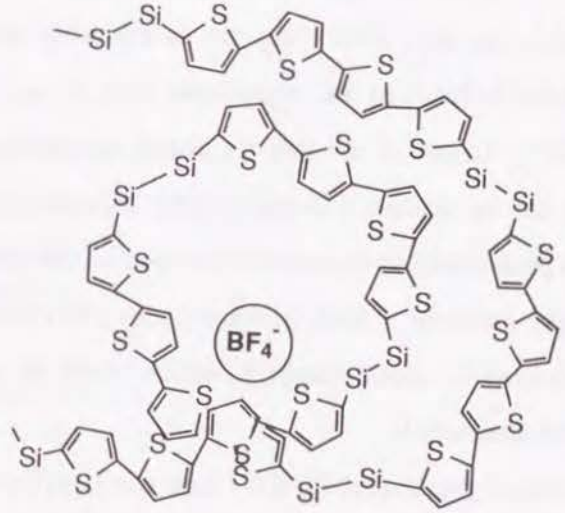

Figure 5. Schematic illustration of conformation of the doped PDST-4 in the solution. The oligothienylene units in a chain are considered to surround the dopant (BF4$^-$ ion) and to aggregate. This conformation may give partially charged states in the oligothienylene unit.

3.3. ESR measurements. The nature of spins generated in the doped PDST-*n* (powder sample) with $NOBF_4$ was examined by the ESR measurements. Note that there were detected no appreciable spin concentrations of each pristine PDST-*n*. The ESR spectra of the lightly $NOBF_4$-doped samples are shown in Fig. 6. It is clear that from the data in Table 3 the peak-to-peak linewidth ($\Delta H_{p.p.}$) decreases with increase in *n* for both the lightly and the heavily doped samples. The following relationship (Ohnishi's formula [32]) between $\Delta H_{p.p.}$ and the length of oligothienylene units *n* was satisfied in the lightly doped PDST-*n*,

$$\Delta H_{p.p.} \propto n^{-1/2} \qquad (1)$$

This *n* dependence of the linewidth strongly suggests that the spins generated are mostly confined in the oligothienylene unit but not in the disilanylene unit. The relationship (1) excludes the formation of PT. Moreover, there should be no silyl radicals, since they are so unstable that oxidation of disilanylene unit easily leads to the degradation [33], if any, as is discussed later. Larger $\Delta H_{p.p.}$ values of the heavily doped sample than those of the lightly doped one can be explained in terms of the spin-orbit interaction in the former, since the probability of location of the spin on the BF_4^- ion becomes larger as the doping proceeds. A slight discrepancy from the relationship (1) was found in the heavily doped samples, which could be attributed to the stronger spin-orbit interaction.

The *g*-values of the doped PDST-1 and the heavily doped PDST-2 were relatively large (~2.003) and that of the heavily doped one was slightly larger than that of the lightly doped one for all the samples. The large *g*-value of the doped PDST-1 is in agreement with the theoretical prediction in which the spin strongly localizes on the sulfur atom [12]. Thus it can be

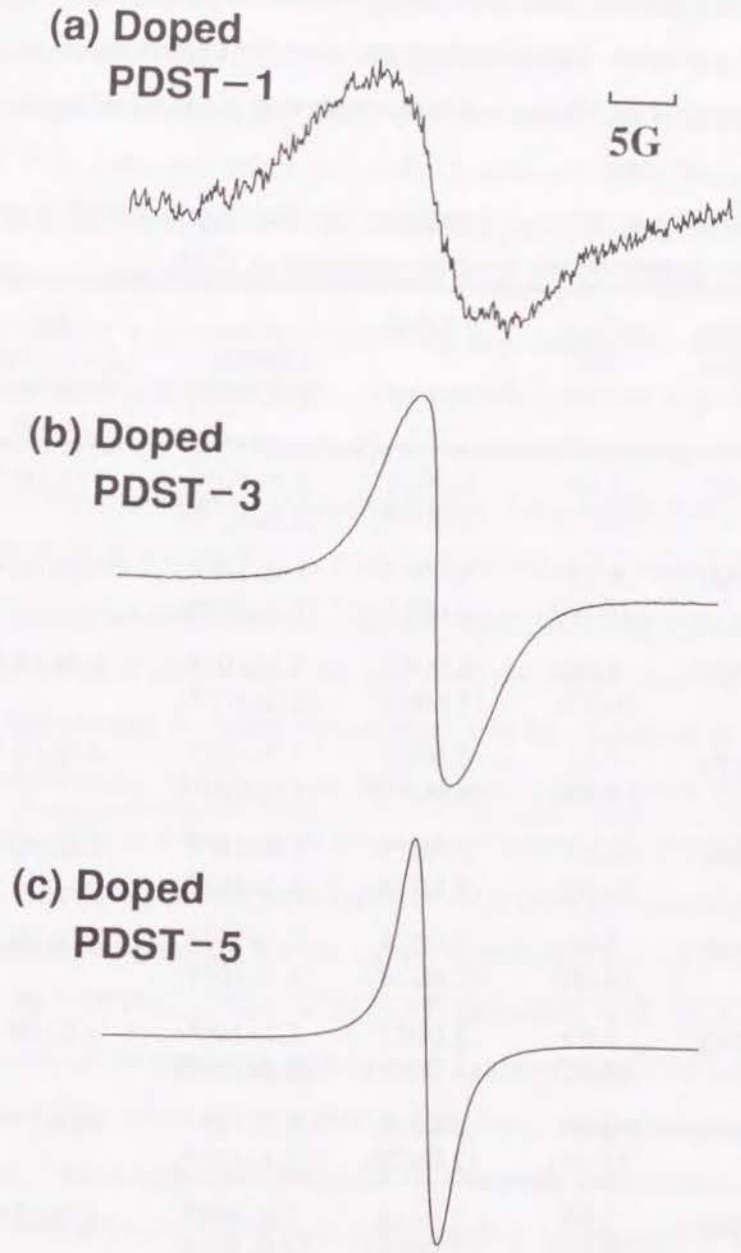

Figure 6. ESR spectra of the lightly $NOBF_4$-doped (a)PDST-1, (b)PDST-3, and (c)PDST-5 powders measured t room temperature.

concluded that a considerably large spin-orbit coupling constant of sulfur atom (ζ_S=382 cm^{-1}) [34,35] eventually gives the large g-value of the doped PDST-1. The calculations have also clarified that the spins of PDST-2 and PDST-3 have a polaronic nature delocalized over the carbon atoms in the oligothienylene unit [12]. Being consistent with this, g-values of the doped

Table 3. ESR data at room temperature of the doped PDST-n with $NOBF_4$. Values in parentheses are those measured at 123K.

PDST-n	doping degree	$\Delta H_{p.p.}$ (G)	g-value	N_S (spins/g-polymer)	N_S (spins/oligo-thienylene unit)[a]
n=1	lightly	8.58 (9.77)	2.0031 (2.0027)	9.8×10^{16} (2.4×10^{17})	3.0×10^{-5}
	heavily	8.72 (10.08)	2.0032 (2.0031)	1.0×10^{16} (5.3×10^{16})	3.0×10^{-6}
n=2	lightly	5.30 (6.27)	2.0022 (2.0022)	1.1×10^{18} (2.2×10^{18})	6.0×10^{-4}
	heavily	6.31 (5.25)	2.0029 (2.0030)	7.7×10^{16} (1.8×10^{17})	4.0×10^{-5}
n=3	lightly	3.97 (4.65)	2.0021 (2.0022)	1.4×10^{18} (3.0×10^{18})	1.0×10^{-3}
	heavily	5.66 (6.00)	2.0024 (2.0024)	2.8×10^{18} (6.3×10^{18})	2.0×10^{-3}
n=4	lightly	2.63 (3.12)	2.0022 (2.0022)	2.2×10^{18} (4.4×10^{18})	1.8×10^{-3}
	heavily	3.66 (4.39)	2.0026 (2.0028)	9.5×10^{17} (2.1×10^{18})	8.0×10^{-4}
n=5	lightly	2.03 (2.67)	2.0018 (2.0019)	2.0×10^{18} (4.9×10^{18})	1.9×10^{-3}
	heavily	2.59 (3.12)	2.0025 (2.0027)	2.6×10^{18} (5.9×10^{18})	2.5×10^{-3}

[a]Ratio of the number of spins to the oligothienylene unit at room temperature.

PDST-n approaches that of a free electron with acquiring mobility as n increases. Difference of g-values between the lightly and the heavily doped samples can also be explained by the spin-orbit coupling through, mainly, fluorine atoms (ζ_F=270 cm^{-1}) [34,35] in BF_4^- ion. The spin concentrations (N_S) were found to be considerably small, coinciding with the CV and UV-VIS-NIR data, and there was only 1 spin per 2000 thiophene rings in maximum (1 spin per 400-500 oligothienylene units), while the doped PT has been reported to have 1 spin per 670 rings [36]. Furthermore, N_s of the doped PDST-n is lower than that of the doped thiophene oligomer by about one order of magnitude [37]. The partially charged oligothienylene unit model shown in Fig. 5, therefore, may account for these small N_s values.

The linewidth of the doped PDST-3 and PDST-5 slightly increased under 60 K as seen in Fig. 7, where the results of the doped PDST-3 and -5 are representatively shown. On the other hand, the g-value was rather independent of temperature for almost all the doped samples (see Table 3). The broadening at lower temperature can be explained in terms of the suppression of the motional narrowing. Reciprocal ESR intensity, $(I_p\Delta H_{p.p.}{}^2)^{-1}$, as a function of temperature, where I_p is the full height of the ESR differential curves, were found to increase approximately linearly with increasing temperature for the lightly doped PDST-2, -3, and -4 (see Fig. 7(a) for PDST-3). This is in good agreement with the Curie law and indicative of no magnetic correlation. Lightly doped PDST-5 showed two types of Curie spins in the higher and the lower temperature regions as seen in Fig. 7(b), which again suggests no magnetic correlation. In addition, there was not seen any signal corresponding to Δm_S=±2 at about 1500 G characteristic of the triplet state even at 4.5 K. These facts suggests that there are no ferromagnetic interactions among the polaronic spins. This

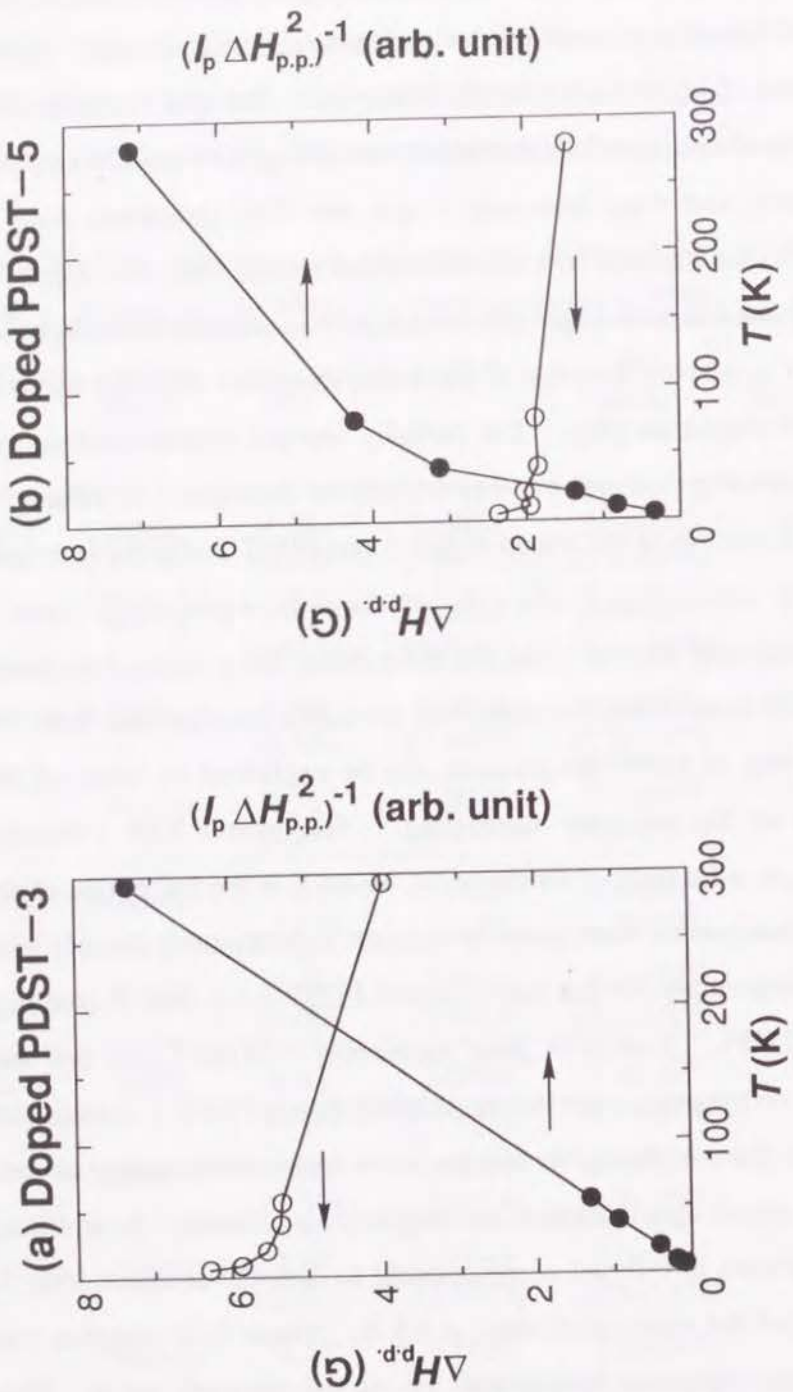

Figure 7. Temperature dependence of the peak-to-peak linewidth ($\Delta H_{p.p.}$) and the reciprocal of the peak intensity derived from $(I_p \Delta H_{p.p.}^2)^{-1}$ of the lightly doped (a)PDST-3 and (b)PDST-5. The lines are guides for the eye.

absence of ferromagnetism probably comes from the quite low spin concentrations (1 spin per 400 oligothienylene units in maximum) generated in the doped PDST-*n*.

3.4. IR measurements. Although formation of PT has been denied based on the ESR spectral measurement, there still remains possibility of degradation of the polymer due to cleavage of the Si-Si bond by the doping. For instance, it has been reported that a UV irradiation causes scission of the Si-Si bond in PDST-1 and poly(disilanylene(phenylenes)) to make silole (-Si-OH) and siloxane (-Si-O-Si-) fragments [20]. Note that the heavy doping brings about the scission of the Si-Si bond cleavage, by removing electrons from σ-type HOCO with the bonding nature between the $3p_\sigma$ orbitals of each silicon atom as well as the removal from π-type HOCO, whereas UV irradiation excites electrons in the σ-type HOCO to the σ-type LUCO with the antibonding nature between 3s orbitals of silicon atoms, resulting in the degradation of the Si-Si chain [12,13,20]. The IR spectra for both the pristine and the $NOBF_4$-doped PDST-5 are shown in Fig. 8. The pristine sample gave peaks at 664, 704, and 794 cm^{-1} and at 3062 cm^{-1} attributed to the out-of-plane vibration and the stretching, respectively, of C-H at the β-positions of 2,5-disubstituted thiophene. The bands appearing at 2871-2951cm^{-1} and 1410-1500cm^{-1} are assigned to the C-H stretching of ethyl group and the β-(C-H) in-plane vibration of thiophene rings, respectively. In the doped sample, strong CT bands were newly observed at 1000-1400 cm^{-1}, being characteristic of the doped PT [38,39] as well as the doped 5T [28,40] irrespective of the dopant species. Moreover, the sharp peak at 1083 and a broad band at 3210-3430 cm^{-1} seems to indicate the presence of

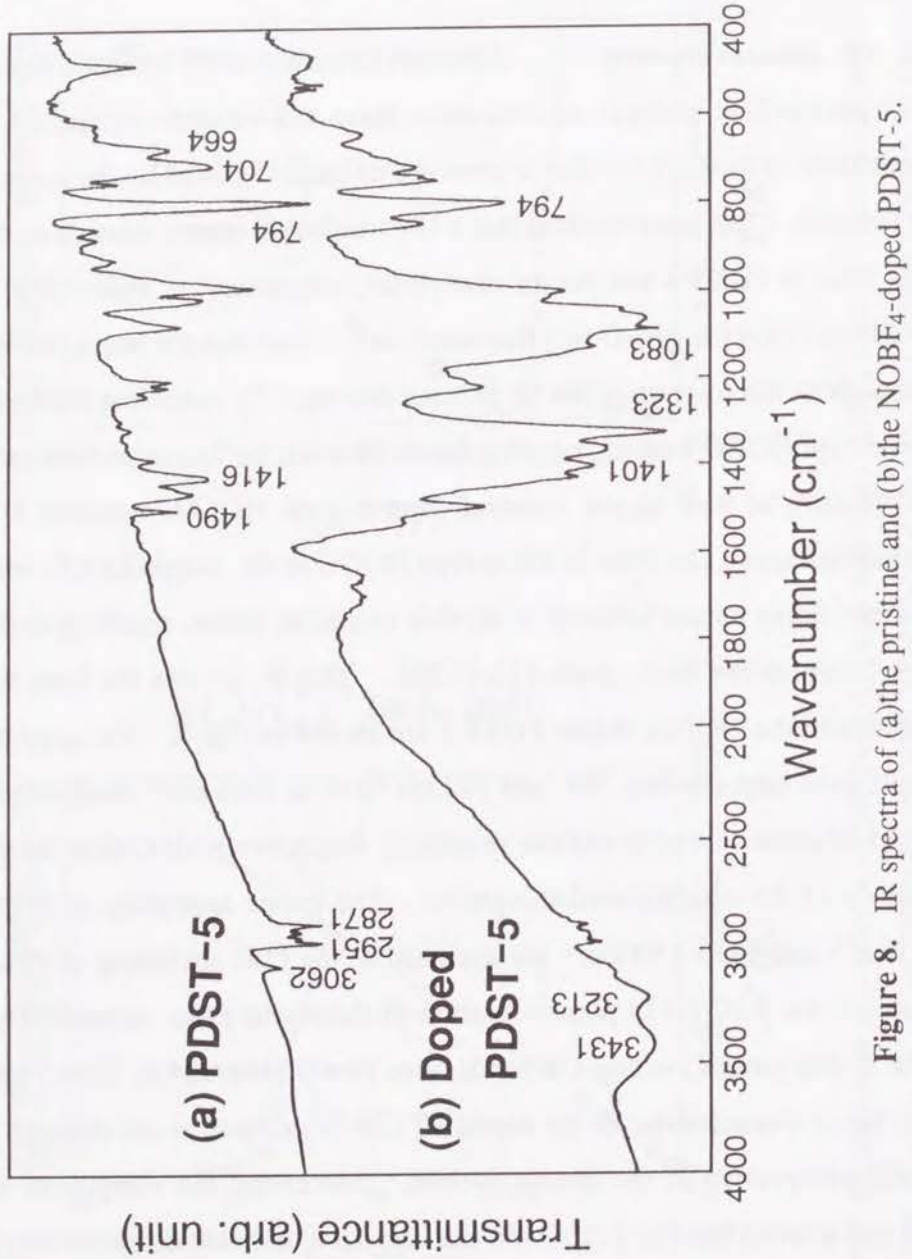

Figure 8. IR spectra of (a)the pristine and (b)the $NOBF_4$-doped PDST-5.

the Si-O-Si and Si-OH bonds, respectively [41], arising from the degradation mentioned above.

4. Conclusion

The electronic properties of p-type doped poly[disilanylene (thienylene)$_n$] (n=1-5) have been studied based on the CV, UV-VIS-NIR, ESR, and IR measurements. The oxidation is concluded to occur mainly at the oligothienylene units, generating π-type spins as has been predicted by the previous theoretical study. The spin generation, however, has been found to be rather difficult since oligothienylene units in a chain could aggregate and surround the dopant ion, resulting in a partially charged state as suggested by the UV-VIS-NIR spectra. Oxidation of disilanylene units could also occur followed by the Si-Si bond cleavage based on the IR spectral measurement. Being consistent with our previous theoretical prediction, polaronic spins delocalizing over the carbon skeleton of the oligothienylene units have been observed for n=2-5 and spins localized on the sulfur atom observed for n=1. Delocalization of the spin in the oligothienylene unit has also been confirmed from the n dependence of the ESR linewidth. The larger g-value and linewidth observed in the heavily doped sample compared with those of the lightly doped one suggests the spin-orbit interaction due to increasing possibility of the spins locating on the dopant ion. Since the spin concentrations are considerably small, ferromagnetic interaction among the polaronic spins has not yet been observed.

References

[1] (a) H. Iwamura, *Adv. Phys. Org. Chem.*, **26**, 179 (1990). (b) J. S. Miller and A. J. Epstein, *Angew. Chem. Int. Ed. Engl.*, **33**, 385 (1994). (c) C. Kollmar and O. Kahn, *Acc. Chem. Res.*, **26**, 259 (1993). (d) A. Rajca, *Chem. Rev.*, **94**, 871 (1994). (e) K. Yoshizawa and R. Hoffmann, *J. Am. Chem. Soc.*, **117**, 6921 (1995).

[2] M. Kinoshita, P. Trek, M. Tamura, K. Nozawa, D. Shiomi, Y. Nakazawa, M. Ishikawa, M. Takahashi, K. Awaga, T. Inabe, and Y. Maruyama, *Chem. Lett.*, 1225 (1991).

[3] T. Nogami, K. Tomioka, T. Ishida, H. Yoshikawa, M. Yasui, F. Iwasaki, H. Iwamura, N. Takeda, and M. Ishikawa, *Chem. Lett.*, 29 (1994).

[4] R. Chiarelli, M. A. Novak, A. Rassat, and J. L. Tholence, *Nature* **363**, 147 (1993).

[5] P. M. Allemand, K. C. Khemani, A. Koch, F. Wudl, K. Holczer, S. Donovan, G. Grüner, and J. D. Thompson, *Science*, **253**, 301 (1991).

[6] K. Tanaka, A. A. Zakhidov, K. Yoshizawa, K. Okahara, T. Yamabe, K. Yakushi, K. Kikuchi, S. Suzuki, I. Ikemoto, and Y. Achiba, *Phys. Lett. A*, **164**, 221 (1992).

[7] N. Mataga, *Theor. Chim. Acta*, **10**, 372 (1968).

[8] A. A. Ovchinnikov, *Theor. Chim. Acta* , **47**, 297 (1978).

[9] T. Sugawara, S. Bandow, K. Kimura, H. Iwamura, K. Itoh, *J. Am. Chem. Soc.*, **108**, 368 (1986).

[10] H. Fukutome, A. Takahashi, M. Ozaki, *Chem. Phys. Lett.*, **133**, 34 (1987).

[11] (a) D. A. Kaisaki, W. Chang, and D. A. Dougherty, *J. Am. Chem. Soc.*, **113**, 2763 (1991). (b) M. M. Murray, P. Kaszynski, and D. A. Kaisaki, W. Chang, and D. A. Dougherty, *J. Am. Chem. Soc.*, **116**, 8152 (1994). (c) D. A. Dougherty, S. J. Jacobs, S. K. Silverman, M. M. Murray, D. A. Shultz, A. P. West, and J. A. Clites, *Mol. Cryst. Liq. Cryst.*, **232**, 289 (1993).

[12] K. Tanaka, H. Ago, and T. Yamabe *Synth. Met.*, **72**, 225 (1995).

[13] K. Tanaka, H. Ago, T. Yamabe, M. Ishikawa, and T. Ueda, *Organometallics*, **13**, 3496 (1994).

[14] S. S. Hu and W. P. Weber, *Polym. Bull.*, **21**, 133 (1989).

[15] S. H. Yi, J. Nagase, and H. Sato, *Synth. Met.*, **58**, 353 (1993).

[16] T. Hayashi, T. Uchimaru, N. P. Reddy, and M. Tanaka, *Chem. Lett.*, 647 (1992).

[17] K. Tanaka, T. Shichiri, and T. Yamabe, *Synth. Met.*, **16**, 207 (1986).

[18] L. W. Shacklette, R. R. Chance, D. M. Ivory, G. G. Miller, and R. H. Baughman, *Synth. Met.*, **1**, 307 (1980).

[19] J. Ohshita, D. Kanaya, and M. Ishikawa, *Appl. Organometal. Chem.*, **7**, 269 (1993).

[20] A. Kunai, T. Ueda, K. Horata, E. Toyoda, I. Nagamoto, J. Ohshita, M. Ishikawa, and K. Tanaka, *Organometallics*, **15**, 2000 (1996).

[21] J. Guay, P. Kasai, A. Diaz, R. Wu, J. M. Tour, and L. H. Dao, *Chem. Mater.*, **4**, 1097 (1992).

[22] K. Tanaka, Y. Matsuura, Y. Oshima, T. Yamabe, and S. Hotta, unpublished results.

[23] M. C. Fang, A. Watanabe, and M. Matsuda, *Polymer*, **37**, 163 (1996).

[24] Y. Taniki, Y. Nakano, and K. Kaeriyama, *Synth. Met.*, **55-57**, 1596 (1993).

[25] (a) M. Lemaire, W. Büchner, R. Garreau, H. A. Hoa, A. Guy, and J. Roncali, *J. Electroanal. Chem.*, **281**, 293 (1990). (b) H. Masuda, Y. Taniki, and K. Kaeriyama, *J. Polym. Sci. A*, **30**, 1667 (1992).

[26] S. Gronowitz, *Ark. Kemi.*, **13**, 239 (1958).

[27] D. D. Cunningham, L. L. Davidson, H. B. Mark, C. V. Pham, and H. Zimmer, *J. Chem. Soc., Chem. Commun.*, 1021 (1987).

[28] (a) D. Fichou, G. Horowitz, and F. Garnier, *Synth. Met.*, **39**, 125 (1990). (b) D. Fichou, G. Horowitz, B. Xu, and F. Garnier, *Synth. Met.*, **39**, 243 (1990).

[29] S. Hotta and K. Waragai, *J. Mater. Chem.*, **1**, 835 (1991).

[30] M. G. Hill, J. F. Penneau, B. Zinger, K. R. Mann, and L. L. Miller, *Chem. Mater.*, **4**, 1106 (1992).

[31] G. Horowitz, A. Yassar, and H. J. Bardeleben, *Synth. Met.*, **62**, 245 (1994).
[32] S. Ohnishi, Y. Ikeda, S. Sugimoto, and I. Nitta, *J. Polym. Sci.*, **47**, 503 (1960).
[33] J. Ohshita, T. Watanabe, D. Kanaya, H. Ohsaki, M. Ishikawa, H. Ago, K. Tanaka, and T. Yamabe, *Organometallics*, **13**, 5002 (1994).
[34] B. A. Goodman and J. B. Raynor, *Electron spin resonance of transition metal complexes, advances in inorganic chemistry and radio chemistry*, H. J. Emeleus and A. G. Sharpe ed., Vol. 13, Academic Press (1970).
[35] J. A. McMilan and T. Halpern, *Hartree-Fock parameters for the atoms hellium to radon*, University of British Columbia (1966).
[36] S. Hayashi, K. Kaneto, K. Yoshino, R. Matsushita, and T. Matsuyama, *J. Phys. Soc. Jpn.*, **55**, 1971 (1986).
[37] K. Tanaka, Y. Matsuura, Y. Oshima, T. Yamabe, and S. Hotta, *Synth. Met.*, **66**, 295 (1994).
[38] S. Wang, K. Tanaka, and T. Yamabe, *Synth. Met.*, **32**, 141 (1989).
[39] S. Dong and W. Zhang, *Synth. Met.*, **30**, 359 (1989).
[40] Y. Cao, D. Guo, M. Pang, and R. Qian, *Synth. Met.*, **18**, 189 (1987).
[41] R. M. Silverstein, G. C. Bassler, and T. C. Morril, *Spectroscopic identification of organic compounds*, 4th ed., John Wiley & Sons (1981).

PART II

Electronic Properties of Narrow-Gap Polymers

INTRODUCTION

It is well known that in neutral *trans*-polyacetylene (PA) due to its peculiar one-dimensional (1D) characteristic Peierls transition takes place with leading to the change in the electronic structure from metallic to insulating state with a large band gap [1]. Therefore, the metallic conducting property is realized by doping with electron donor or acceptor to make the polaron band. Narrow-gap polymers have been eagerly sought from the both theoretical and experimental approaches, because they are expected to show not only good intrinsic conductivity but also good nonlinear optical properties. One can also expect from narrow-gap polymers a sensitive response to the applied electric or magnetic field, being applicable to devices.

One possible way to establish a narrow-gap polymer is the modification of a typical π-conducting polymer. Along this line, certain narrow-gap polymers have been synthesized so far [2-7]. A widely known polymer is poly(isothianaphthene) (PITN) which possesses the band gap of ~1 eV, being about half of polythiophene (2.1 eV) [2]. Elucidation of the relationship between the chemical structure of such a narrow-gap polymer and its band gap is invaluable in the designing of new narrow-gap polymers. Another possible way is to suppress the Peierls transition by increasing the dimensionality of a polymer. By following this direction, pseudo-1D polymers such as polyacene (PAc) and polyacenacene have been studied and shown to have extremely narrow band gaps [8], though they have not synthesized yet because they seems to be unstable. It is interesting to note that the carbon nanotube shows no gap state when a certain orientation of hexagons is satisfied [9] and that actually a metallic carbon nanotube has been experimentally confirmed [10].

In Chapter 1 (*J. Chem. Phys.*, **104**, 5528 (1996)), the quantum chemical analysis has been performed to the narrow-gap polymer: the periodic copolymer consisting of thienothiadiazole and thiophene with 1:2 ratio, whose band gap is very small (~0.9 eV) [5]. The origin of the narrow-gap nature has been investigated in detail by considering the evolution of electronic properties from the oligomer to the polymer.

In Chapter 2 (*Synth. Met.*, **79**, 145 (1996)), the effect of a magnetic field on the electronic properties of PAc, which also possesses an extremely small band gap, has been studied by introducing the vector potential ($\boldsymbol{A}$) into the Hückel Hamiltonian. It will be shown that the band gap as well as the total energy depends on the magnetic field and changes periodically with increasing the field.

References

[1] Y. Ooshika, *J. Phys. Soc. Jpn.*, **12**, 1238 (1957); **14**, 747 (1959).

[2] M. Kobayashi, N. Colaneri, M. Boysel, F. Wudl, and A. J. Heeger, *J. Chem. Phys.*, **82**, 5717 (1985).

[3] S. A. Jenekhe, *Nature*, **322**, 345 (1986).

[4] C. Taliani, G. Ruani, R. Zamboni, A. Bolognesi, M. Catellani, S. Destri, W. Porzio, and P. Ostoja, *Synth. Met.*, **28**, C507 (1989).

[5] S. Tanaka and Y. Yamashita, *Synth. Met.*, **55-57**, 1251 (1993).

[6] S. Tanaka and Y. Yamashita, *Synth. Met.*, **69**, 599 (1995).

[7] M. Karikomi, C. Kitamura, S. Tanaka, and Y. Yamashita, *J. Am. Chem. Soc.*, **117**, 6791 (1995).

[8] K. Tanaka, S. Yamashita, H. Yamabe, and T. Yamabe, *Synth. Met.*, **17**, 143 (1987).

[9] K. Tanaka, K. Okahara, M. Okada, and T. Yamabe, *Chem. Phys. Lett.*, **191**, 469 (1992).

[10] T. W. Ebbesen, H. J. Lezec, H. Hiura, J. W. Bennett, H. F. Ghaemi, and T. Thio, *Nature*, **382**, 54 (1996).

Chapter 1

Electronic Structures of Polymers Based on Thienothiadiazole and Thiophene

1. Introduction

Electrically conducting polymers have been the focus of enormous theoretical and experimental interest during the last more than a decade. These new materials, also called synthetic metals, combine the electrical properties of metals with the advantages of polymers such as lighter weight, greater workability, resistance to corrosion, and lower cost. Currently major efforts in the field of conducting polymers are on the molecular designing of novel conjugated polymers with narrow band gaps (E_g) [1-5]. Polymers with narrow band gaps are expected to show not only good intrinsic conductivity but also good nonlinear optical properties [6]. For successful molecular designing of conducting polymers, one needs to have a complete understanding of the relationship between the chemical structure of a polymer and its electronic and conduction properties. Once such an insight has been achieved, desired electronic properties could be obtained by specific synthesis after molecular design.

Various routes are presently followed for designing novel conducting polymers. One exciting possibility in this direction is provided by the quasi-one-dimensional copolymers which can have tailor-made conduction

properties depending on the choice of two semiconducting components, their relative amounts, and their arrangement in the polymer chain. It is already well known that copolymerization [7-10] can considerably influence the electronic properties of its constituent homopolymers. Recent theoretical and experimental investigations have shown that the narrow-band gap polymers can also be obtained from the copolymerization of alternating aromatic-quinoid units or donor-acceptor units [11-13]. Using this strategy, various novel polymers have been proposed.

In this chapter we investigate the electronic and geometric structures of the polymers based on thienothiadiazole and thiophene units (Scheme 1). The thienothiadiazole monomer (molecule 1a in Scheme 2) is known to have a very small separation between the HOMO (highest occupied molecular orbital) and the LUMO (lowest unoccupied MO), being lower than that of

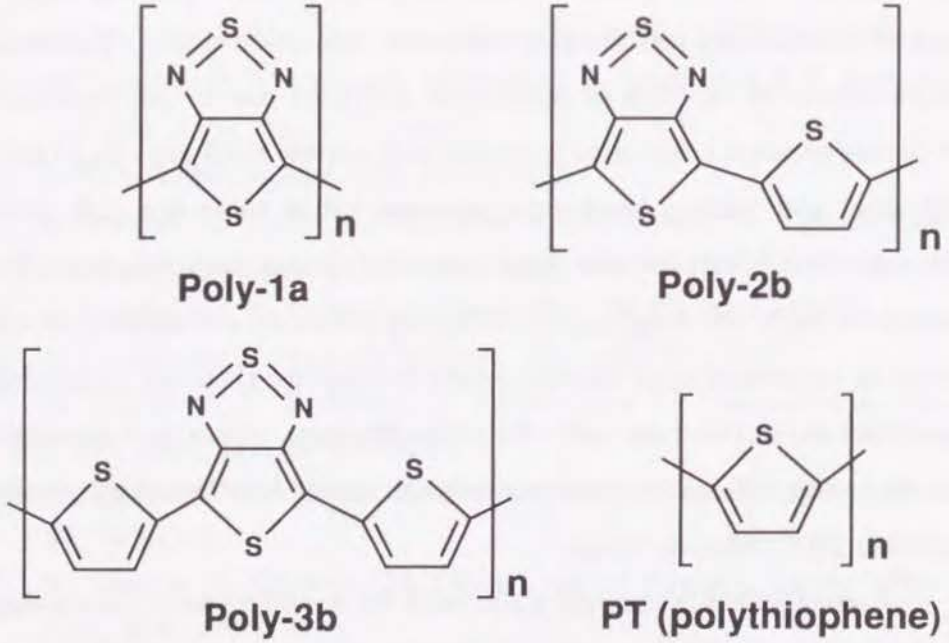

Scheme 1

isothianaphthene [14,15] whose polymer (PITN) is one of the lowest band gap conjugated polymers (E_g≈1.0 eV) [16]. If the low HOMO-LUMO separation of thienothiadiazole can be carried over to its polymer, one should expect a very narrow-band gap polymer. We report the results of our investigations of the electronic structures of poly(thienothiadiazole) (Poly-1a) and the periodic copolymers of thiophene and thienothiadiazole (Poly-2b and Poly-3b) shown in Scheme 1. Though poly(thienothiadiazole) has not yet been synthesized, there are reports on the synthesis of the copolymer (Poly-3b) by Tanaka and Yamashita [15], who have reported the band gap of 0.9 eV for this copolymer.

2. Method of Calculation

All the calculations of these polymers were performed on the basis of the *ab initio* one-dimensional self-consistent-field crystal orbital (SCF-CO) method. The minimal basis set (STO-3G) was used because of the size of the systems considered. The program employed for the present calculation is able to handle the screw axis symmetry as well as the translational symmetry. The energy gradient method was employed for optimizing the geometries of the polymers, assuming them to be planar. The geometry of Poly-3b was estimated by calculating ten structures, due to its size. The number of the representative wave vectors was chosen as 21 with regular intervals in the Brillouin zone. The overlap and electron-repulsion integrals were calculated as far as the fourth, third, and second nearest neighboring cell for Poly-1a, Poly-2b, and Poly-3b, respectively (ca. 20 Å from the central cell on an average).

To understand better the relationship between the nature of the polymers and their geometries, we also carried out *ab initio* molecular orbital

(MO) calculations using the same basis set (STO-3G). In order to compare the results obtained from the ultraviolet (UV) spectra, the excitation energies were calculated for the oligomers with various chain-lengths using the single excitation configuration interaction (SECI) method. The MO calculations were carried out using the GAUSSIAN 92 program [17].

3. Results and Discussion

3.1. Electronic properties of polymers. Let us first examine the electronic properties of Poly-1a, Poly-2b and Poly-3b. It may be noted that Poly-2b and Poly-3b are periodic copolymers of thiophene and 1a units in the ratio of 1:1 and 2:1, respectively. For the sake of comparison, polythiophene (PT) was also studied. Their geometries were optimized by the energy gradient method except for Poly-3b, as described in Sec. 2. From the band structures of all the four polymers shown in Fig. 1, it is found that the band gap decreases with an increase in the ratio of thiophene ring and that Poly-3b shows a considerably small direct gap of 5.97 eV (Table 1). Simple scaling with the experimental band gap of PT (2.0 eV) [18] gives a band gap of 1.3 eV for Poly-3b, though it is not so small as the

Table 1. Calculated electronic properties of polymers (in eV).

Polymer	E_g [a]		Bandwidth		IP	EA
			HO	LU		
Poly-1a	*ind*	9.13	3.54	0.24	5.48	-3.64
Poly-2b	*dir*	8.14	2.03	0.25	4.83	-3.31
Poly-3b	*dir*	5.97	1.03	0.50	3.82	-2.15
PT	*dir*	8.85	2.92 (5.42)	5.35	5.16	-3.70

[a]The signs, *ind* and *dir* , show an indirect and direct band gap, respectively.

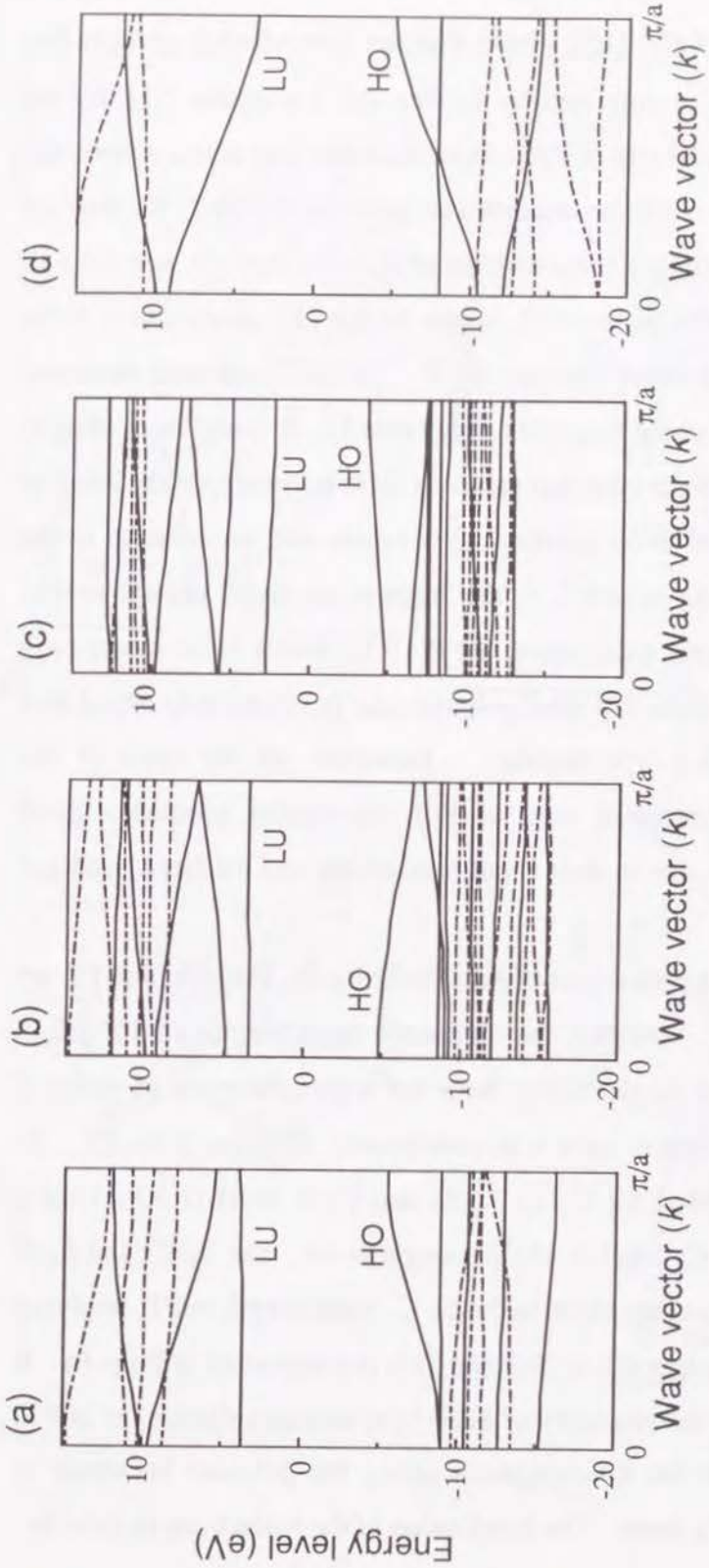

Figure 1. Band structures of (a)Poly-1a, (b)Poly-2b, (c)Poly-3b, and (d)PT. Solid and dashed lines indicate those from π- and σ-orbitals, respectively. HO and LU designate the highest occupied and the lowest unoccupied bands, respectively.

experimental one (0.9 eV) [15]. Note that the inter-chain π-conjugation through S-N contact, as supposed by Tanaka and Yamashita [15], for the explanation of the small gap of Poly-3b is not taken into account here, but such an effect seems not to be important as mentioned later. We also see that the HO and especially LU bandwidths of Poly-1a, Poly-2b, and Poly-3b are smaller compared to those of PT, except for the HO bandwidth of Poly-1a which is somewhat larger than that of PT. The HO bandwidth decreases as the ratio of the thiophene ring increases (Table 1). It is also interesting to note that the change of the band gap values in these polymers are the result of a decrease in the ionization potential (IP) values and an increase in the electron affinity (EA) values [i.e. the highest occupied crystal orbital (HOCO) and the lowest unoccupied CO (LUCO) levels move closer each other]. It therefore means that these polymers can be more easily doped than PT (through p- and n-type doping). However, on the basis of our calculations, copolymers as well as Poly-1a cannot become a good conducting materials, due to their small bandwidths and the large band gap for Poly-1a.

The optimized geometries of Poly-1a, Poly-2b, Poly-3b, and PT are depicted in Fig. 2. Note that the optimized bond lengths of PT are in agreement with those by the 6-31G basis set within the error of ±0.02 Å [19]. Poly-1a is found to have a geometry quite different from PT. In Poly-1a, inter-cell bond C_1-C_1' (1.33 Å) and C_2-N bond (1.30 Å) are a double bond and C_1-C_2 bond (1.48 Å) a single bond. The S_1-C_1 and S_2-N bond lengths in Poly-1a are close to the S_1-C_1 bond length in PT, implying hereby that the resonance effect (Scheme 2) is not important in Poly-1a. It should be noted that the geometry of Poly-1a is neither aromatic (as in PT) nor quinoid because the π-conjugation along the polymer backbone is disrupted at the C_2-C_2' bond. The localization of the π-electrons in Poly-1a

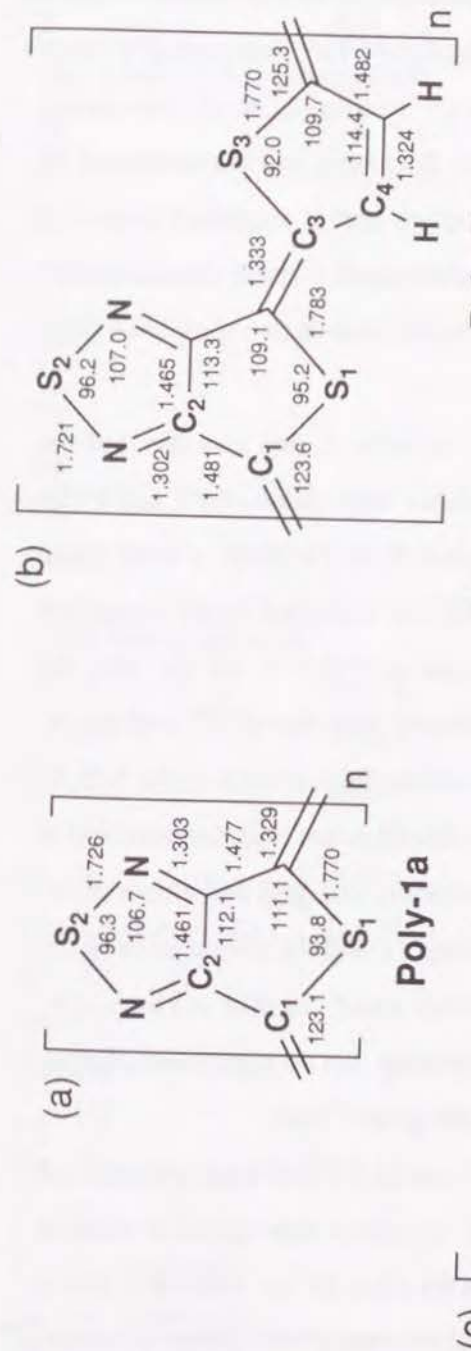

Figure 2. Optimized geometries of each polymer shown in Scheme 1. Bond lengths and angles are in Å and degrees, respectively.

therefore leads to the flat bands. In case of Poly-2b, the 1a unit geometry is almost identical to that of Poly-1a and the thiophene unit is found to take a quinoid structure as a result of strong influence of 1a. Interestingly, clear difference is observed in the geometry of Poly-3b from those of Poly-1a and Poly-2b. In Poly-3b, aromatic nature of the thiophene unit is maintained by the C_1-C_3 single bond, and the geometry of 1a unit is supposed to have a resonance structure without distinct bond alternation. These characteristics are derived from the stabilization through the successive two thiophene rings in a Poly-3b chain.

From π-AO bond population given in Table 2, one can see that the bonding features of Poly-1a and Poly-2b differ from those of PT and Poly-3b. The inter-cell bonds in Poly-1a and Poly-2b have a very large population of 0.17 as compared to PT (0.03), as indicated in the optimized geometries. From the population analysis of Poly-3b we see that the thiophene unit has almost the same π-character with that of PT and that π-conjugation of 1a spreads homogeneously within the unit even in the S-C, S-N bonds. Atomic charges and π-electron densities are also summarized in Table 2. The atoms S_1, S_2 and S_3 are positively charged and atoms N are negatively charged. Charge transfer between 1a and thiophene units in the two copolymers Poly-2b and Poly-3b is very small: 1a unit is charged by -0.10 in Poly-2b and -0.03 in Poly-3b, suggesting that no significant charge-transfer occurs between these two units in the ground state.

The frontier crystal orbitals (HOCO and LUCO) of each polymer are shown in Fig. 3. These patterns of all the polymers correspond to those at the Brillouin zone boundary (k=π/a) except for Poly-2b, for which the data at the zone center (k=0) is used because the direct band gap shows minimum value at these k points. One can see a clear difference between the patterns

Table 2. Calculated net charge, π-AO population, and π-AO bond population of each polymer.[a]

	Poly-1a	Poly-2b	Poly-3b	PT
Net charge (π-AO population)[b]				
S_1	0.28 (1.87)	0.21 (1.89)	0.34 (1.61)	0.26 (1.78)
C_1	-0.10 (1.05)	-0.11 (1.08)	-0.13 (1.14)	-0.11 (1.06)
C_2	0.06 (1.02)	0.06 (1.02)	0.01 (1.08)	-0.11 (1.05)
N	-0.30 (1.10)	-0.31 (1.10)	-0.34 (1.23)	
S_2	0.43 (1.80)	0.42 (1.81)	0.54 (1.52)	
S_3		0.27 (1.87)	0.28 (1.77)	
C_3		-0.09 (1.02)	-0.10 (1.06)	
C_4		-0.07 (1.00)	-0.09 (1.07)	
C_5			-0.09 (1.06)	
C_6			-0.11 (1.06)	
π-AO bond population				
S_1 - C_1	0.015	0.012	0.053	0.035
C_1 - C_2	0.027	0.028	0.098	0.153
C_2 - C_2'	0.045	0.045	0.073	0.061
C_2 - N	0.151	0.151	0.081	
N - S_2	0.027	0.026	0.058	
C_1 - C_1' (inter-cell)	0.170			0.029
C_1 - C_3		0.167	0.040	
S_3 - C_3		0.018	0.035	
S_3 - C_6			0.035	
C_3 - C_4		0.031	0.149	
C_6 - C_5			0.153	
C_4 - C_5			0.062	
C_1 - C_3' (inter-cell)		0.167		
C_6 - C_6' (inter-cell)			0.030	

[a]See Fig. 2 for the atomic notations. [b]π-AO population is shown in the parentheses.

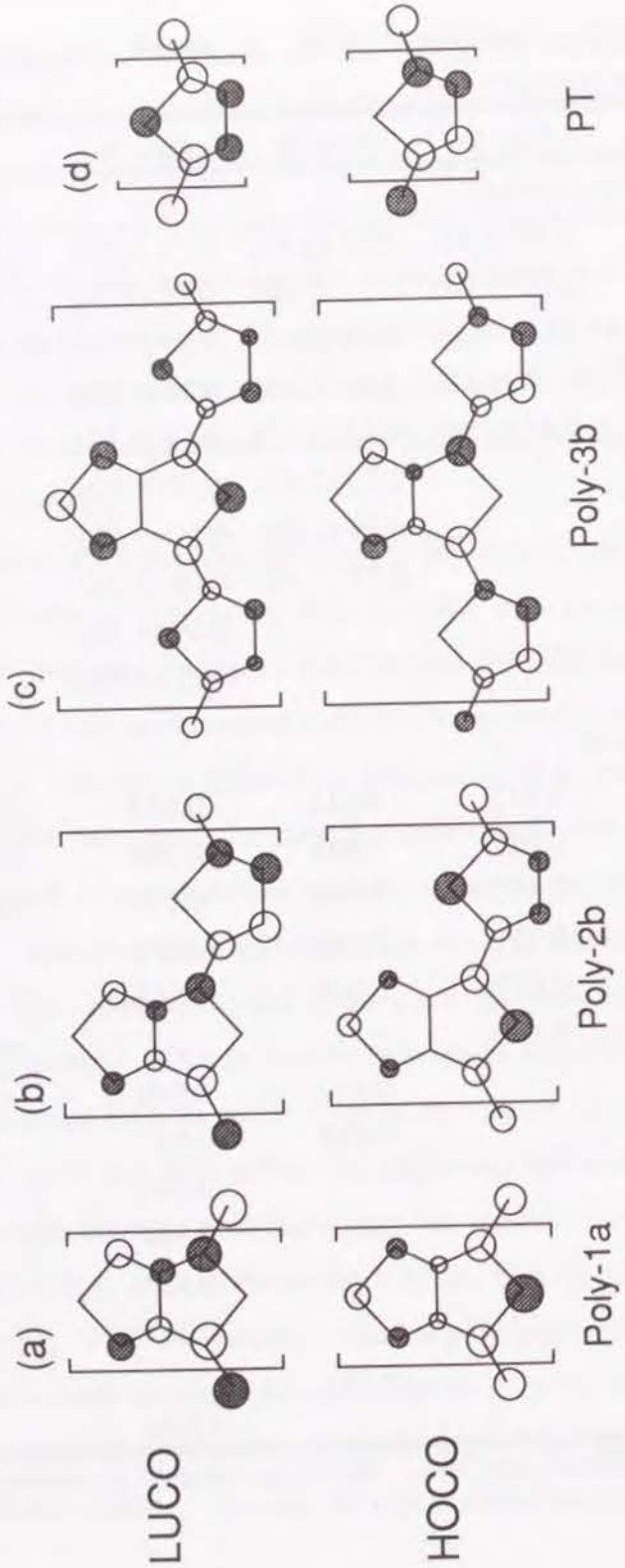

Figure 3. Orbital patterns of (a)Poly-1a, (b) Poly-2b, (c)Poly-3b, and (d)PT. All these patterns correspond to those at the Brillouin zone boundary ($k=\pi/a$) except for those of Poly-2b which correspond to zone center ($k=0$).

of Poly-1a and PT. The signs of the orbital coefficients of the HOCO (LUCO) in Poly-1a resemble those of the LUCO (HOCO) in PT. It is worth noting that the atoms C_2 make a relatively smaller contribution to the HOCO and LUCO of Poly-1a, in contrast to their contributions to the frontier orbitals of PT. The degree of π-conjugation, therefore, along the main chain of Poly-1a is expected to be smaller than that in PT. The orbital patterns of Poly-2b as well as those of thiophene unit are similar to those of Poly-1a, suggesting hereby that 1a units exert a great influence on their electronic structures. Note that the characters of the inter-cell bonds of Poly-1a, Poly-2b are bonding and antibonding in the HOCO and the LUCO, respectively, while those of PT show the opposite natures. Being different from Poly-1a and Poly-2b, the orbital patterns of both 1a and thiophene units of Poly-3b are similar to the patterns of the corresponding orbitals of PT with antibonding and bonding natures in the inter-cell bonds of the HOCO and the LUCO, respectively. The contributions of the atoms C_2 to the frontier orbitals are also quite small in Poly-3b, provided less π-conjugation along the polymer backbone resulting in narrow bandwidths. Because the π-conjugation along a polymer backbone is very weak in Poly-3b, the delocalization through the inter-chain S-N contact, suggested in ref. 15, probably does not play an important role in such a small band gap of Poly-3b. Despite the above common features in the orbital patterns of the polymers, it still remains unclear (i) why the increase in the portion of thiophene units reduce the band gap, giving such a small band gap in Poly-3b and (ii) why the orbital patterns of the HOCO and the LUCO of PT get reversed in Poly-1a and Poly-2b.

In order to check the influence of geometry on the electronic properties, we have also calculated the electronic properties of Poly-1a with the

Table 3. Calculated electronic properties of Poly-1a using different geometries.

Polymer	Geometry	C_1-C_1' bond length (Å)[a]	Relative energy (eV)[b]	E_g[c] (eV)	Bandwidth (eV) HO	Bandwidth (eV) LU	IP (eV)	EA (eV)
Poly-1a	optimized[d]	1.33	0.0	*ind* 9.13	3.54	0.24	5.48	-3.64
	X-ray result (1)[e]	1.33	+1.26	*dir* 7.28	3.88	1.07	4.44	-2.84
	X-ray result (2)[e]	1.40	+1.35	*dir* 6.38	4.07	1.48	4.02	-2.36
	X-ray result (3)[e]	1.45	+1.59	*dir* 5.71	4.20	1.78	3.71	-2.00
PT	optimized[d]	1.48		*dir* 8.85	2.92	5.35	5.16	-3.70

[a]See Fig. 2 for the position of C_1 atom. [b]Positive values indicate instability as compared with the optimized Poly-1a. [c]*ind* and *dir* mean indirect and direct gap, respectively. [d]The geometry obtained by the energy gradient method was used. [e]The geometry of the unit cell is derived from the X-ray result in ref. 15 (S_1-C_1=1.71 Å, C_1-C_2=1.39 Å, C_2-N=1.35 Å, N-S_2=1.61 Å, and C_2-C_2=1.44 Å; as for the atomic notations shown in Fig. 2).

geometries taken form the X-ray result [15], as shown in Table 3. Three types of bond lengths were employed for the C_1-C_1' bond. In all the cases, the band gap of Poly-1a gets reduced strongly as C_1-C_1' bond distance becomes longer. The stability of Poly-1a is also found to decrease with an increase in the C_1-C_1' bond length. Furthermore, the bandwidths of HOCO and LUCO increase with an increase in the inter-cell C_1-C_1' bond length. In all the geometries, no significant change in the orbital pattern is observed (Fig. 3(a)). The reasons for such observed behavior of Poly-1a with the change in the C_1-C_1' bond length shall be discussed later.

3.2. Electronic properties of molecules. *Ab initio* MO calculations were further performed for deeper understanding of the electronic structure of poly(thienothiadiazole) and the copolymers with the minimal (STO-3G) basis set. One-particle picture (SCF approximation) deteriorates for estimating an energy gap, so that excitation energies were calculated on the basis of the single excitation configuration interaction (SECI) method for the molecules displayed in Scheme 2. The geometry optimization was performed prior to the SECI calculation for the molecules shown in Fig. 4.

Comparison of the geometries of 1a and 2a with that of the unit cells of Poly-1a and Poly-2b (Fig. 2) shows that S_1-C_1 and S_2-N bonds in the molecules are shorter than the corresponding bonds in the polymers. However, the lengths of the bonds in these molecules are not so short as to regard them as double bonds. In the case of 2a and 3a, the geometry of 1a unit is essentially preserved and the inter-cell C_1-C_1' bond is quite long (~1.43 Å). One can thus notice a significant change in the geometries as one moves from oligomers (molecules) with several rings to infinite polymers in Poly-1a and Poly-2b. The geometry of 1c resembles that of Poly-1a

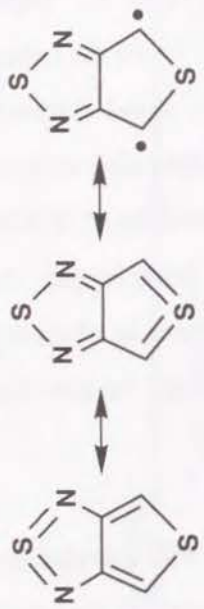

resonance structure of 1a

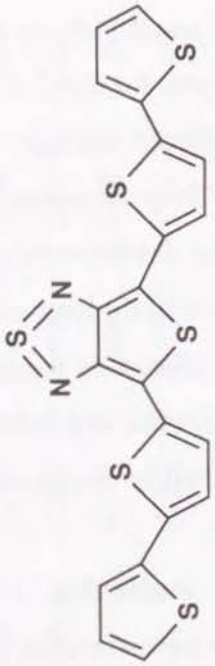

5b

Scheme 2

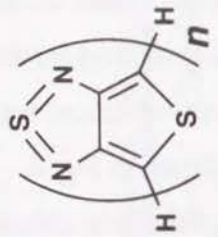

na

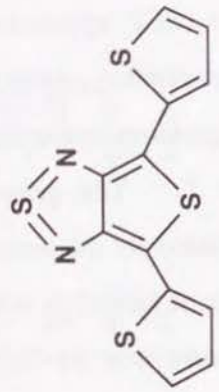

3b

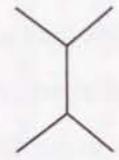

TME (tetramethyleneethane)

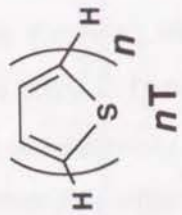

nT

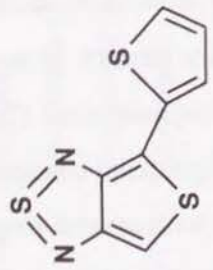

2b

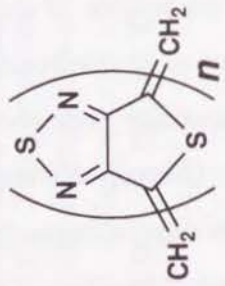

nc

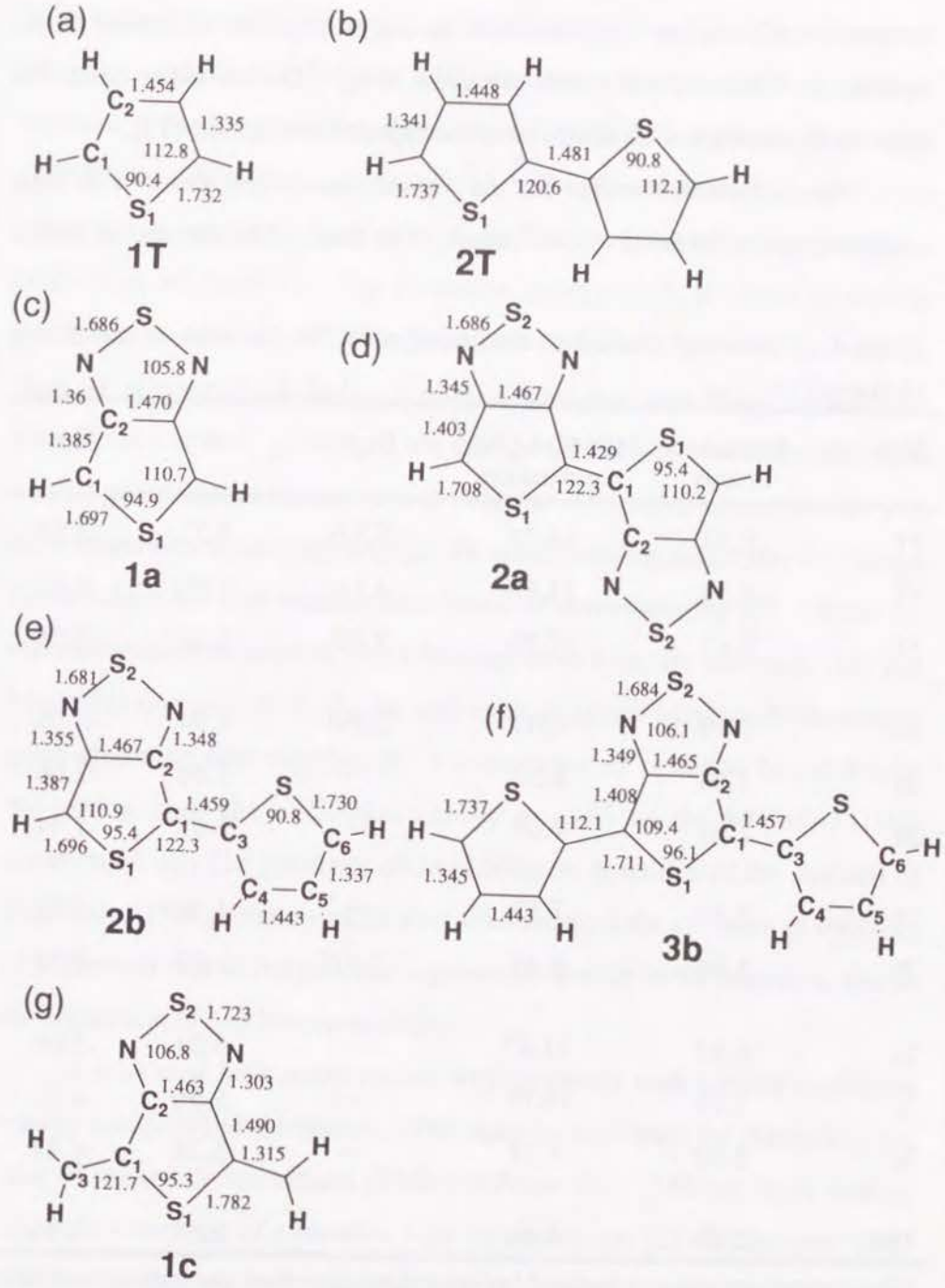

Figure 4. Optimized geometries of (a)1T, (b)2T, (c)1a, (d)2a, (e)2b, (f)3b, and (g)1c. Bond lengths and angles are shown in Å and degrees, respectively.

because the C_1-C_3 and C_2-N bonds of 1c can be regarded as double bonds and the S_1-C_1 and S_2-N bonds are quite long. On the other hand, the optimized geometry of 3b is similar to the experimental results [15].

The excitation energies for the various molecules along with their experimental results are given in Table 4. The trend of the theoretical results

Table 4 Calculated excitation energies (in eV) of the various molecules (Scheme 2).[a]

Molecule	Excitation energy	HOMO-LUMO separation	Expl.[b]	IP	EA
1T	8.33	14.75	5.77[c]	7.22	-7.53
2T	6.59	11.90	4.11[d]	6.00	-5.90
3T	5.81	10.70	3.49[d]	5.56	-5.24
1a	3.79	8.03	2.99[e]	4.94	-3.09
2a	2.64	5.52	–	3.46	-2.06
3a	1.97	4.09	–	2.65	-1.44
2b	3.37	7.17	–	4.36	-2.81
3b	2.94	6.46	2.01[f]	3.92	-2.54
1c	6.93	11.47	–	6.31	-5.06
2c	5.79	10.07	–	5.56	-4.51
3c	5.50	9.71	–	5.24	-4.47
TME	2.69	4.60	–	2.67	-1.93

[a]The geometries were optimized before calculating their excitation energies, except 3c whose geometry is built from 2c. [b]The experimental excitation energy is determined from λmax of UV spectrum. [c]From ref. 20. [d]From ref.21. [e]From refs. 14, 15. [f]From ref. 15.

is in agreement with the experimental results. In both the *n*T and *n*a oligomers indicated in Scheme 2, the excitation energies decrease with an increase in the length of the oligomer, due to the out-of-phase coupling of HOMO and the in-phase coupling of LUMO. The excitation energies of *n*a show much smaller values than those of the corresponding thiophene oligomers, *n*T (*n*=1-3). The excitation energy of 3a becomes extremely small with a value of 1.97 eV. Molecule 3b has a larger transition energy than 3a, whereas Poly-3b has a smaller band gap than Poly-1a (Table 1). The SECI was also performed for the molecules *n*c (*n*=1-3), which have similar geometries as the unit cell of Poly-1a. Molecules *n*c are calculated to have larger excitation energies than the corresponding molecules *n*a, though these values are still smaller than those of corresponding *n*T. From the aforementioned discussion, the following three facts are obtained. (i) The excitation energies of 1a, 2a, 3a, and even of 3b are very small, showing a good agreement with experiment. The extension of 1a unit to 2a and then to 3a lowers both the excitation energy as well as the HOMO-LUMO separation. (ii) The geometry of 1a is different from that of the unit cell of Poly-1a, and the geometry of 2b also different from the structure of Poly-2b. (iii) The unit cell of Poly-3b has a geometry similar to 3b molecule, due to the separation of two thiophene rings.

Let us now look at the reason why 1a shows such a small excitation energy compared to thiophene. This may be explained by discussing the case of tetramethyleneethane (TME) (Scheme 2). TME has been studied from the viewpoint of a possible high-spin molecule [22-24] because TME has non-Kekulé geometry and has two degenerate nonbonding molecular orbitals (NBMOs) at the Hückel level. As shown in Fig. 5, TME is in a triplet state at the Hückel level but the electron correlation brings a more

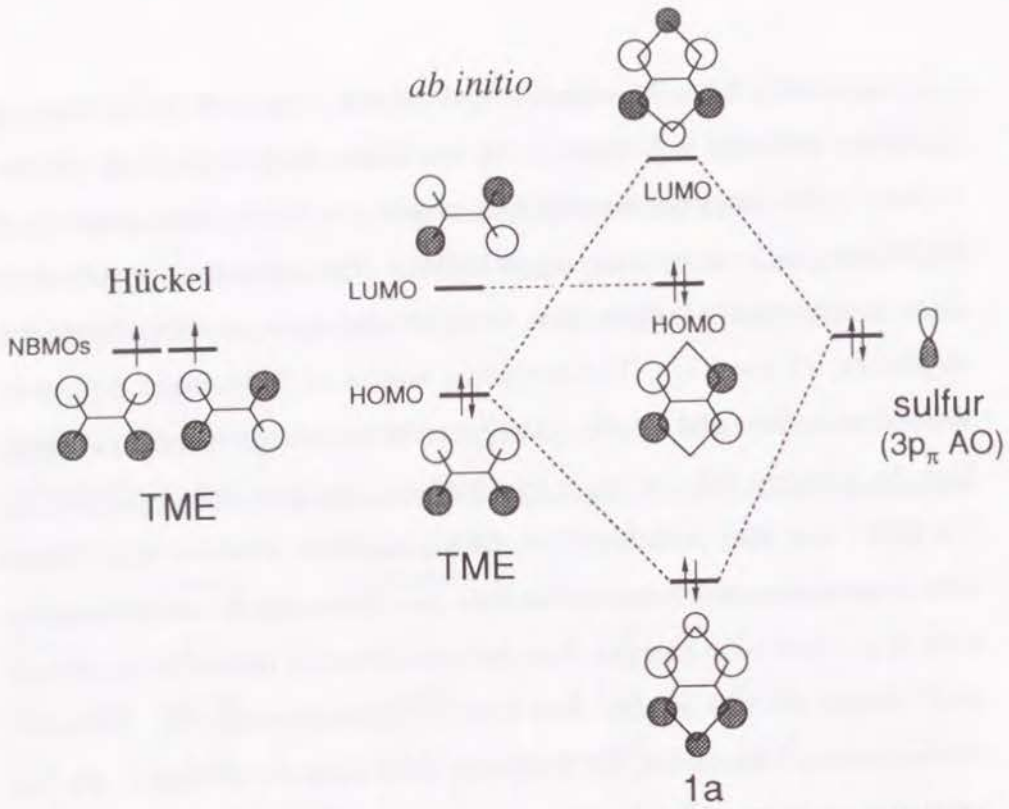

Figure 5. Models of orbital interaction between TME and $3p_\pi$ orbital of a S atom.

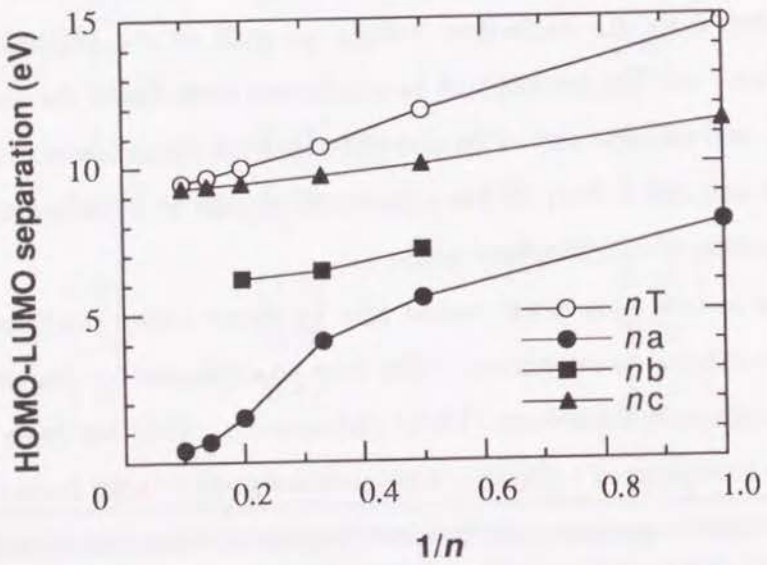

Figure 6. Plot of the HOMO-LUMO separation as a function of oligomer length. Open circles, closed circles, squares, and triangles indicate *n*T, *n*a, *n*b, and *n*c, respectively. Lines are the guides for the eye.

stable singlet state with a very small HOMO-LUMO separation due to through-space interaction. The introduction of p_π orbital of sulfur atom causes an interaction between the HOMO of TME and p_π of S atom. No orbital interaction occurs between the LUMO and Sp_π, due to the symmetry restriction. Because the HOMO-LUMO separation is considerably small in TME, that of 1a shows a small value, too. Note that substitution by nitrogen does not significantly affect the separation as the substitution just lowers the energies of the MOs.

3.3. Extension from molecule to polymer. The reasons for the different behavior between oligomers *n*a and Poly-1a are still not completely clear. It needs to be noted that substantial changes in electronic states may occur as a result of the transition from molecules (oligomers, *n*a) to Poly-1a. To examine such an interesting transition of electronic and geometric structures, effect of the chain length was investigated for longer oligomers with up to 10 units, as shown in Fig. 6. Owing to the dimensional restriction, the HOMO-LUMO separation is used instead of the excitation energy since it is confirmed from Table 4 that the HOMO-LUMO separation has good correlation with the excitation energy. For longer oligomers ($n \geq 4$ for *n*T, *n*a, *n*b and $n \geq 3$ for *n*c), fixed geometries built up from the optimized geometries of the dimer and trimer were utilized for the calculation. The HOMO-LUMO separation decreases with increasing n in every oligomer because of the out-of-phase coupling in the HOMO and the in-phase coupling in the LUMO. There is a marked decrease in the separation of *n*a at $n \geq 4$ and very low separation is observed at n=10 (0.43 eV). The crossing of *n*T and *n*c lines is observed at about 10 units.

From the results mentioned above, we show the changes in the energy levels of the frontier orbitals with an increase in the number of 1a units in Fig. 7. The corresponding changes in the energy levels of the frontier orbitals of PT with an increase in the number of thiophene units are, for the sake of comparison, illustrated in Fig. 8. It is interesting to note that the patterns of the frontier orbitals in both the oligomers of thiophene (nT) and PT ($k=\pi/a$ for both the HOCO and the LUCO) are same (Fig. 8), whereas the patterns of the frontier orbitals of the na get reversed in Poly-1a ($k=\pi/a$ for the HOCO and $k=0$ for the LUCO) (Fig. 7). Because the low-gap state seen in 7a-10a is unstable, rearrangement of the geometry as well as the electronic state are expected to occur, being similar in the charge-density-wave (CDW) state of polyacetylene (PA) [25]. This drastic change of na at $n\sim10$ in the geometry and the electronic state will lead to the characteristics of nc. Therefore the larger band gap of Poly-1a than that of PT can be understood from the extrapolation of the nc and nT lines in Fig. 6. Although the orbital patterns of the HOMO and LUMO of 10a is actually not similar to those of 1a nor to Poly-1a, due to the orbital mixing between the two MOs closely situated. Further extension of a na chain will give the patterns of nc or Poly-1a.

As far as the π-conjugation is concerned, it is weaker in both the na oligomers and Poly-1a than in the corresponding thiophene systems. But in the case of Poly-1a, the bonding and antibonding nature of the inter-cell bond (C_1-C_1') becomes significant, due to the relatively small intra-cell interaction (orbital coefficient of atom C_2 in both the frontier orbitals is quite small). From the frontier orbital patterns, Poly-1a can be regarded as a derivative of the linearly aligned isolated ethylene molecules. Therefore in Poly-1a, although the contribution of the intra-cell interactions to its both HOCO and

LUCO is quite small, the inter-cell interaction through C_1-C_1' bond is quite large, leading to a large band gap and small bandwidths. In other words, the orbital patterns of inter-cell C_1-C_1' bonds can determine the energy levels or orbitals in the case of polymers. On the basis of this, one can explain the observed dependence of the band gap and the stability of Poly-1a on the C_1-C_1' bond length (Table 3). Longer inter-cell bond weakens the inter-cell interaction, resulting in the smaller band gap and less stability. In the case of Poly-2b the transition is supposed to occur too, judging from the geometry and orbital patterns, accompanying with the change to the quinoid structure of thiophene unit. The reason for the lower band gap of Poly-2b than Poly-1a is the weakening of the localization upon the inter-cell C_1-C_1' bond, as can be seen in the bond distance (see Fig. 2).

The CO patterns of Poly-3b are directly correlated with orbital interactions in the oligomers without transition like PT. Stability of aromatic structure of the thiophene unit compared with quinoid structure may overcome the instability of the 1a geometry, signifying the retention of the nature of the oligomer. Extremely narrow gap of Poly-3b can be also expected from the extrapolation of nb in Fig. 6. This narrow-gap mainly arises from the narrow-gap nature of 1a unit.

It is also probable that both Poly-1a and Poly-2b, if succeeded in synthesis, may show a very small transition energy because the synthesized polymer is usually an oligomer with a finite length. One may, however, say that Poly-1a and the copolymers Poly-2b and Poly-3b are not expected to be better candidates than PT for intrinsic conductivity in view of their smaller bandwidths. Note that the conductivity of a system somewhat similar to Poly-3b has been reported to be rather low in the I_2-doped state (6×10^{-3} S/cm) [26].

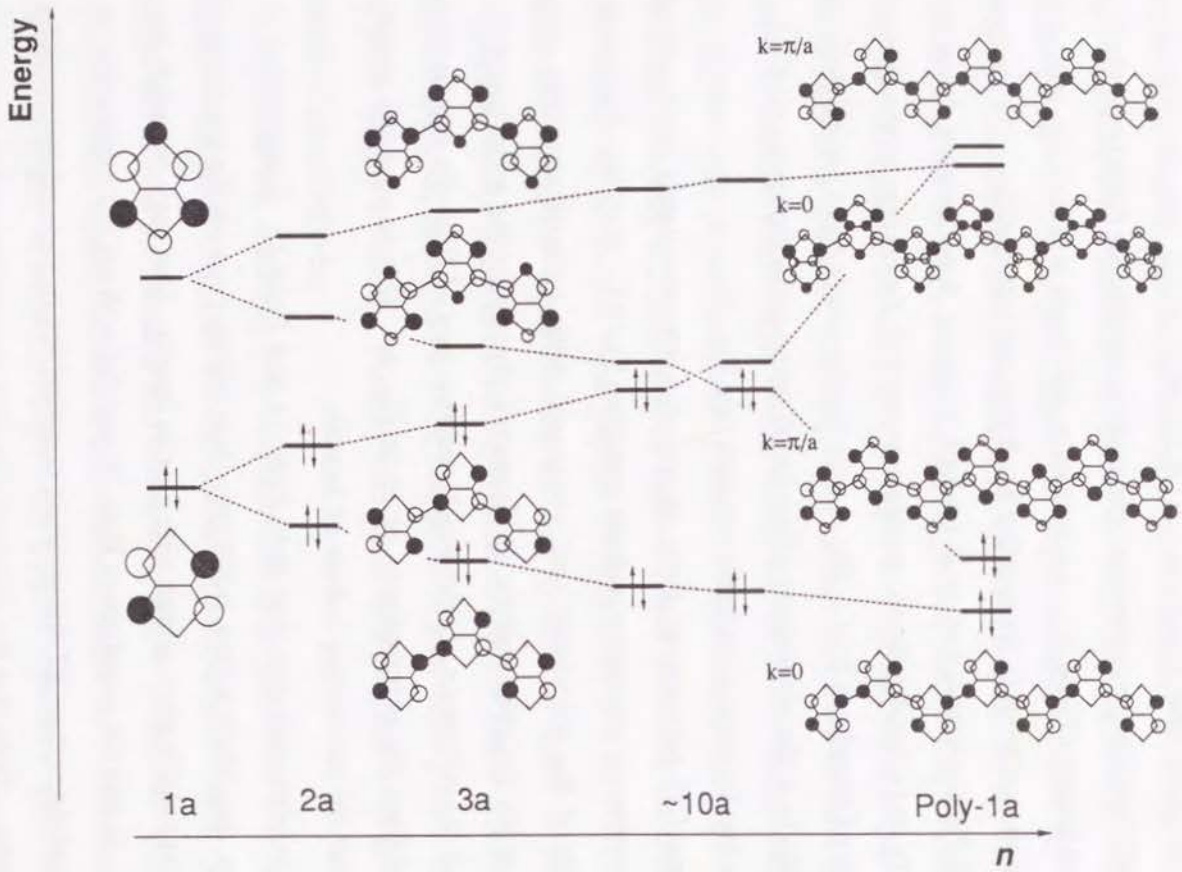

Figure 7. Illustration of the evolution of the orbital levels of Poly-1a from its oligomers. In the case of oligomers, only the orbitals in which all the inter-ring C_1-C_1' bonds are either bonding or antibonding have been shown.

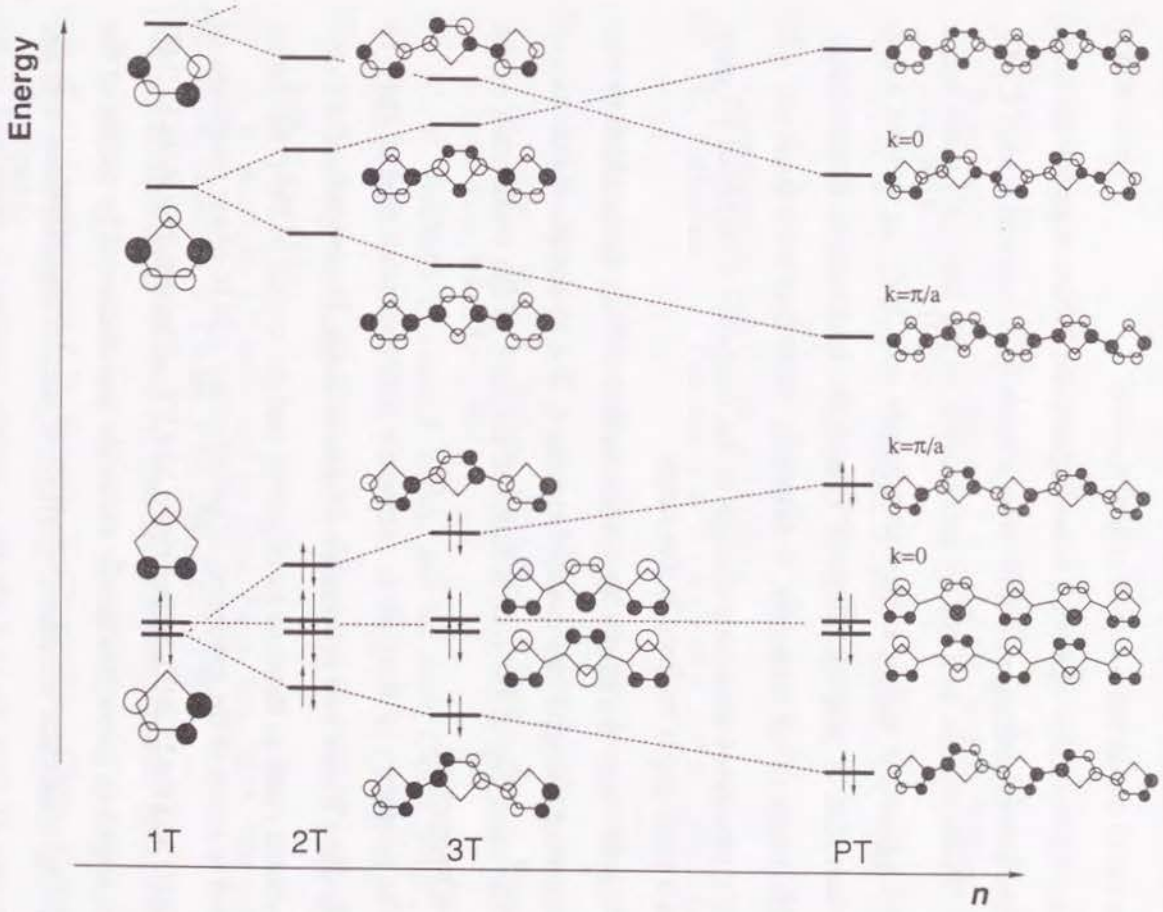

Figure 8. Illustration of the evolution of the orbital levels of polythiophene (PT) from its oligomers. In the case of oligomers, only the orbitals in which all the inter-ring C_1-C_1' bonds are either bonding or antibonding have been shown.

4. Conclusion

The geometric and the electronic properties of poly(thienothiadiazole) (Poly-1a) and the periodic copolymers of thienothiadiazole and thiophene units with the ratio of 1:1 (poly-2b) and 1:2 (poly-3b) have been investigated with the aid of the *ab initio* crystal orbital method.

The optimization of Poly-1a showed a quite different geometry from that of the corresponding molecule with a short inter-cell and a long C_1-C_2 bonds. Probably due to a strong localization in the inter-cell bond and a weak delocalization within a thienothiadiazole unit, Poly-1a showed a gap larger than that of polythiophene (PT) and the bandwidths not so large. From the study of its oligomer, it becomes clear that the electronic and geometric structures obviously change in the oligomer with about 10 units and that a small gap is realized in this range.

Poly-2b showed a geometry similar to that of Poly-1a in which even a thiophene ring changed to a quinoid structure, due to the thienothiadiazole unit. The band gap of Poly-2b is reduced because of the weakening of the inter-cell interaction.

The geometry of Poly-3b is extremely different from that of Poly-1a and Poly-2b. By the two successive thiophene rings, the properties of Poly-3b are almost same as those of its oligomer and the orbital of Poly-3b can be explained in terms of the extension of out-of-phase and in-phase couplings of the HOMO and the LUMO, respectively, like PT. The small HOMO-LUMO separation seen in thienothiadiazole molecule was discussed by means of the nonbonding molecular orbitals (NBMOs) of tetramethyleneethane and the narrow gap of Poly-3b (1.3 eV by a simple scaling) is supposed to be originated in this. Though Poly-3b is expected to possess narrow-band gap

nature, it is not expected to be a better candidate than PT for the conducting polymer, due to the relatively small π-conjugation along polymer backbone.

References

[1] (a) J. L. Brédas, A. J. Heeger, and F. Wudl, *J. Chem. Phys.*, **85**, 4673 (1986). (b) D. S. Boudreaux, R. R. Chance, R. L. Elsenbaumer, J. E. Frommer, J. L. Brédas, and R. Silbey, *Phys. Rev.*,**B31**, 652 (1985).

[2] (a) A. Karpfen and M. Kertesz, *J. Phys. Chem.*, **95**, 7680 (1991). (b) M. Kertesz, *Macromolecules*, **28**, 1475 (1995).

[3] A. K. Bakhshi, *Annual Reports of the Royal Society (Physical Chemistry)* Section C, **89**, 147 (1992).

[4] K. Nakajima, K. Tanaka, and T. Yamabe, *Synth. Met.*, **62**, 91 (1994).

[5] K. Yoshizawa and R. Hoffmann, *Chem. Eur. J.*, **1**, 403 (1995).

[6] (a) G. P. Aggarusal, C. Cojan, and C. Flytzanis, *Phys. Rev.*, **B17**, 776 (1978). (b) J. L. Brédas, C. Adant, P. Tackx, and A. Persoons, *Chem. Rev.*, **94**, 243 (1994).

[7] A. K. Bakhshi, P. Otto, J. Ladik, and M. Seel, *Chem. Phys.*, **108**, 215 (1986).

[8] A. K. Bakhshi, J. Ladik, and M. Seel, and P. Otto, *Chem. Phys.*, **108**, 233 (1986).

[9] A. K. Bakhshi, J. Ladik, and M. Seel, *Phys. Rev.*, **B35**, 704 (1987).

[10] A. K. Bakhshi, *J. Chem. Phys.*, **96**, 2339 (1992).

[11] E. E. Häwinga, W. Hoeve, and H. Wynberg, *Synth. Met.*, **55**, 299 (1993).

[12] T. L. Lambert and J. P. Ferraris, *J. Chem. Soc., Chem. Commun.*, 752 (1991).

[13] M. Hanack, K. M. Mangold, U. Röhrig, and C. M. Mössmer, *Synth. Met.*, **60**, 199 (1993).

[14] (a) M. P. Cava and M. V. Lakshmikantham, *Acc. Chem. Res.*, **8**, 139 (1975). (b) R. Meyer, H. Kleinert, S. Richter, and K. Gewald, *J. Prakt. Chem.*, **20**, 244 (1963).
[15] S. Tanaka and Y. Yamashita, *Synth. Met.*, **55-57**, 1251 (1993).
[16] M. Kobayashi, N. Colaneri, M. Boysel, F. Wudl, and A. J. Heeger, *J. Chem. Phys.*, **82**, 5717 (1985).
[17] M. J. Frisch, J. J. P. Stewart, and J. A. Pople, *et al.*, Gaussian 92, Gaussian Inc., Pittsburgh, PA (1992).
[18] K. Tanaka, T. Shichiri, and T. Yamabe, *Synth. Met.*, **16,** 207 (1986).
[19] H. O. Villar, P. Otto, M. Dupuis, and J. Ladik, *Synth. Met.*, **59**, 97 (1993).
[20] E. Jones and I. M. Moodie, *Tetrahedron*, **21**, 2413 (1965).
[21] D. D. Cunningham, L. L. Davidson, H. B. Mark Jr, C. V. Pham, and H. Zimmer, *J. Chem. Soc., Chem. Commun.*, 1021 (1987).
[22] H. C. Longuet-Higgins, *J. Chem. Phys.*, **18**, 265 (1950).
[23] D. J. Klein, C. J . Nelin, S. Alxander, and F. A. Matsen, *J. Chem. Phys.*, **77**, 3101 (1982).
[24] W. T. Borden, H. Iwamura, and J. A. Berson, *Acc. Chem. Res.*, **27**, 109 (1994).
[25] K. Tanaka, H. Kobayashi, S. Yamanaka, K. Yoshizawa, and T. Yamabe, *J. Chem. Phys.*, **91**, 3724 (1989).
[26] M. Karikomi, C. Kitamura, S. Tanaka, and Y. Yamashita, *J. Am. Chem. Soc.*, **117**, 6791 (1995).

Chapter 2

Effect of a Magnetic Field on the Electronic Property of Polyacene

1. Introduction

The electronic properties of one-dimensional (1D) materials such as regular polymers under a magnetic field are important, as well as those without such a field, when one discusses the magnetic susceptibility or magnetoresistance of these materials. Moreover, if the electronic property of the material can be changed considerably by applying a magnetic field, the material could be applied to the future device. However, the electronic properties under a magnetic field have not been widely hitherto examined theoretically, except for carbon nanotubes having similarity to a two-dimensional (2D) graphitic sheet [1,2]. Therefore, it seems meaningful to examine the electronic properties of a "pure" 1D polymer having a 2D surface in their skeletons.

In the present chapter, the theoretical analysis of the electronic properties with respect to the constant magnetic field applied perpendicularly to the condensed hexagons of polyacene employed as a typical 1D polymer (see Fig. 1) was presented. For ease of calculation, the tight-binding crystal orbital method in the framework of the Hückel approximation is adopted.

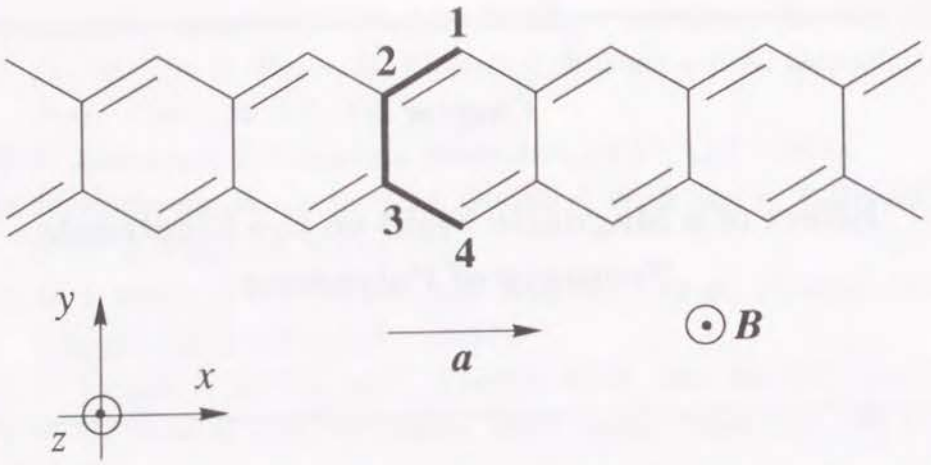

Figure 1. Skeleton of polyacene and the employed coordinate, where the magnetic field $\boldsymbol{B}$ is applied parallel with the z-axis. Bold line denotes the unit cell.

2. Method of Calculation

The Hamiltonian H of an electron in a 1D crystal under a magnetic field $\boldsymbol{B}$ (=(0, 0, B_z)) applied to the z-axis, when the interaction between the electron spin and the magnetic field is neglected, can be expressed by

$$H = \frac{(\boldsymbol{p} + \frac{e\boldsymbol{A}(\boldsymbol{r})}{c})^2}{2m} + V(\boldsymbol{r}) \qquad (1)$$

with the usual variables, e and $V(\boldsymbol{r})$ being the absolute value of an electron charge and periodic potential, respectively.

The Bloch function derived from this Hamiltonian can be expressed by

$$\Psi_k(\boldsymbol{r}) = \frac{1}{\sqrt{N}} \sum_j^N \sum_m \exp(\mathrm{i}kja) \exp(-\mathrm{i}\frac{e}{\hbar c} G_{j,m})\, C_{k,m}\, \phi(\boldsymbol{r} - ja - \boldsymbol{R}_m) \qquad (2)$$

in the tight-binding approximation at the Hückel level, when the 2D vector potential $\boldsymbol{A}(\boldsymbol{r})$ (= $(-B_z y, 0)$) can be chosen so that the Hamiltonian may retain the translation symmetry for the 1D crystal. Here each atomic site assigned by $\boldsymbol{R}_m$ in the j-th cell accompanies only one atomic orbital $\phi(\boldsymbol{r} - ja - \boldsymbol{R}_m)$ and $\boldsymbol{a}$ and a designate the primitive translation vector and its absolute value, respectively. In the case of polyacene, $\phi(\boldsymbol{r} - ja - \boldsymbol{R}_m)$ denotes the π-atomic orbital of a carbon atom. The phase factor $G_{j,m}$ is expressed by [3]

$$G_{j,m} = \int_{ja+\boldsymbol{R}_m}^{\boldsymbol{r}} \mathrm{d}\boldsymbol{s} \cdot \boldsymbol{A}(\boldsymbol{s})$$
$$= \int_0^1 \mathrm{d}\lambda\, (\boldsymbol{r} - ja - \boldsymbol{R}_m) \cdot \boldsymbol{A}(ja + \boldsymbol{R}_m + \lambda(\boldsymbol{r} - ja - \boldsymbol{R}_m)) \qquad (3)$$

where the integration is taken on the line from $ja + \boldsymbol{R}_m$ to $\boldsymbol{r}$. Note that we only deal with the case that the magnetic field is not so large that it may not cause change in the atomic orbitals.

From eqs. (1)-(3), the transfer integral under the magnetic field, $\beta_{jm,j'm'}$, between the π atomic orbitals $\phi(\boldsymbol{r} - ja - \boldsymbol{R}_m)$ and $\phi(\boldsymbol{r} - j'a - \boldsymbol{R}_{m'})$ can be expressed by

$$\beta_{jm,j'm'} = \beta^{(0)}_{jm,j'm'} \exp(\mathrm{i}\theta_{jm,j'm'}) \qquad (4)$$

in the approximation that atomic orbital localizes at its center and that the magnetic field varies much more slowly than the atomic orbital [2,3], where

$$\theta_{j,m,j'm'} = -\frac{e}{\hbar c} \int_0^1 \mathrm{d}\lambda (ja + \boldsymbol{R}_m - j'a - \boldsymbol{R}_{m'})$$
$$\cdot A(j'a + \boldsymbol{R}_{m'} + \lambda(ja + \boldsymbol{R}_m - j'a - \boldsymbol{R}_{m'})) \qquad (5)$$

Here the superscript (0) of β in eq. (4) implies the absence of the magnetic field. On the other hand, in this approximation, the Coulomb integral under the magnetic field is equal to that without the field.

We are now ready to examine the electronic structure of polyacene shown in Fig. 1 in a constant magnetic field $\boldsymbol{B}$ perpendicular to the x-y plane. The π-energy band of polyacene is derived from the following secular equation:

$$\begin{vmatrix} f & h_1 & 0 & 0 \\ h_1^* & f & \beta_2 & 0 \\ 0 & \beta_2 & f & h_2 \\ 0 & 0 & h_2^* & f \end{vmatrix} = 0 \qquad (6)$$

where

$$f = \alpha - E(k) \qquad (7)$$

$$h_1 = \beta_1 \exp(\mathrm{i}\theta_1) + \beta_2 \exp[\mathrm{i}(ka - \theta_2)] \qquad (8)$$

and

$$h_2 = \beta_2 \exp(\mathrm{i}\theta_2) + \beta_1 \exp[-\mathrm{i}(ka + \theta_1)] \qquad (9)$$

Here, the notation α indicates the Coulomb integral, and the notations β_1 and β_2 the transfer integrals associated with the double and singe bonds, respectively, in the absence of a magnetic field. The phase factors θ_1 and θ_2, the subscripts of which correspond to those of β_1 and β_2, respectively, as in eq. (4) are obtained from eq. (5) by executing the line integrals from the carbon atom 1 to 2 and from carbon 4 to 3, respectively (see Fig. 1).

The analytical solution of eq. (6) gives the π-energy band expressed

by

$$E(k) = \alpha \pm \beta_2 \left[\frac{1 + x + y \pm [(1 + x + y)^2 - 4xy]^{1/2}}{2} \right]^{1/2} \qquad (10)$$

where

$$x = 1 + (\beta_1 / \beta_2)^2 + 2(\beta_1 / \beta_2)\cos(ka + \theta) \qquad (11)$$

$$y = 1 + (\beta_1 / \beta_2)^2 + 2(\beta_1 / \beta_2)\cos(ka - \theta) \qquad (12)$$

$$\theta = \theta_1 + \theta_2 = \pi \frac{\phi_{\mathrm{hex}}}{\phi_0} \qquad (13)$$

The notations ϕ_{hex} and ϕ_0 indicate magnetic flux which penetrates through a hexagon of the polyacene and magnetic flux quantum (hc/e), respectively. Note that eq. (10) can also be applied to the case that the magnetic field is not perpendicular to hexagons of polyacene. In such a case, ϕ_{hex} is taken as the magnetic flux passing through the hexagon.

For numerical calculation, the double bond length d_1 and the single bond length d_2 were fixed to 1.350 Å and 1.435 Å, respectively, taken from the values employed for polyacene in our previous work [4], in which the transfer integrals β_1 and β_2 were evaluated as -2.72 and -2.32 eV, respectively, from

$$\beta_i = -34.56 \exp(-d_i / 0.531) \ (i = 1, 2) \ (\text{in eV}) \qquad (14)$$

d_i being the bond length in Å. The value of the Coulomb integral α was fixed to be -7.06 eV proposed for an sp^2 carbon in aromatic compounds [4].

3. Results and Discussion

The π-energy band structure and the density of states (DOS) obtained for several values of ϕ_{hex}/ϕ_0 are shown in Fig. 2. It is seen that the π-energy band structure and the DOS drastically change, depending on the value of ϕ_{hex}/ϕ_0 and, hence, electronic properties periodically change with ϕ_0. A similar tendency has also been found in the 2D cosine band system [5].

The band gap versus ϕ_{hex}/ϕ_0 is plotted in Fig. 3. The band gap becomes largest at $\phi_{hex}/\phi_0 = n + 1/2$ and smallest at $\phi_{hex}/\phi_0 = n$, n being an integer. It is interesting that the band gap slowly changes around the points of $\phi_{hex}/\phi_0 = n + 1/2$, while it rapidly increases or decreases at the points near $\phi_{hex}/\phi_0 = n$. For example, the band gap changes from 0.73 to 0.72 eV as the value of ϕ_{hex}/ϕ_0 goes from 0.5 to 0.6, whereas it changes from 0.14 to 0.45 eV as the value of ϕ_{hex}/ϕ_0 changes from 0 to 0.1. Although the band gap does not become zero in the present polyacene system under a constant magnetic field, the electronic properties associated with the band gap can be controlled to a certain extent by applying the magnetic field.

In Fig. 4, the total electronic energy per unit cell, E_{tot}, is plotted as a function of ϕ_{hex}/ϕ_0. The system becomes the most unstable at $\phi_{hex}/\phi_0 = n + 1/2$, while it becomes the most stable at $\phi_{hex}/\phi_0 = n$. Such behavior is determined by the summation of the energy change in the two filled bands of polyacene shown in Fig. 2. It is noted that the decrease in the band gap does not necessarily cause the destabilization of the total electronic energy.

The magnetic susceptibility of polyacene per gram at 0 K coming from the π-energy band structure can be calculated as

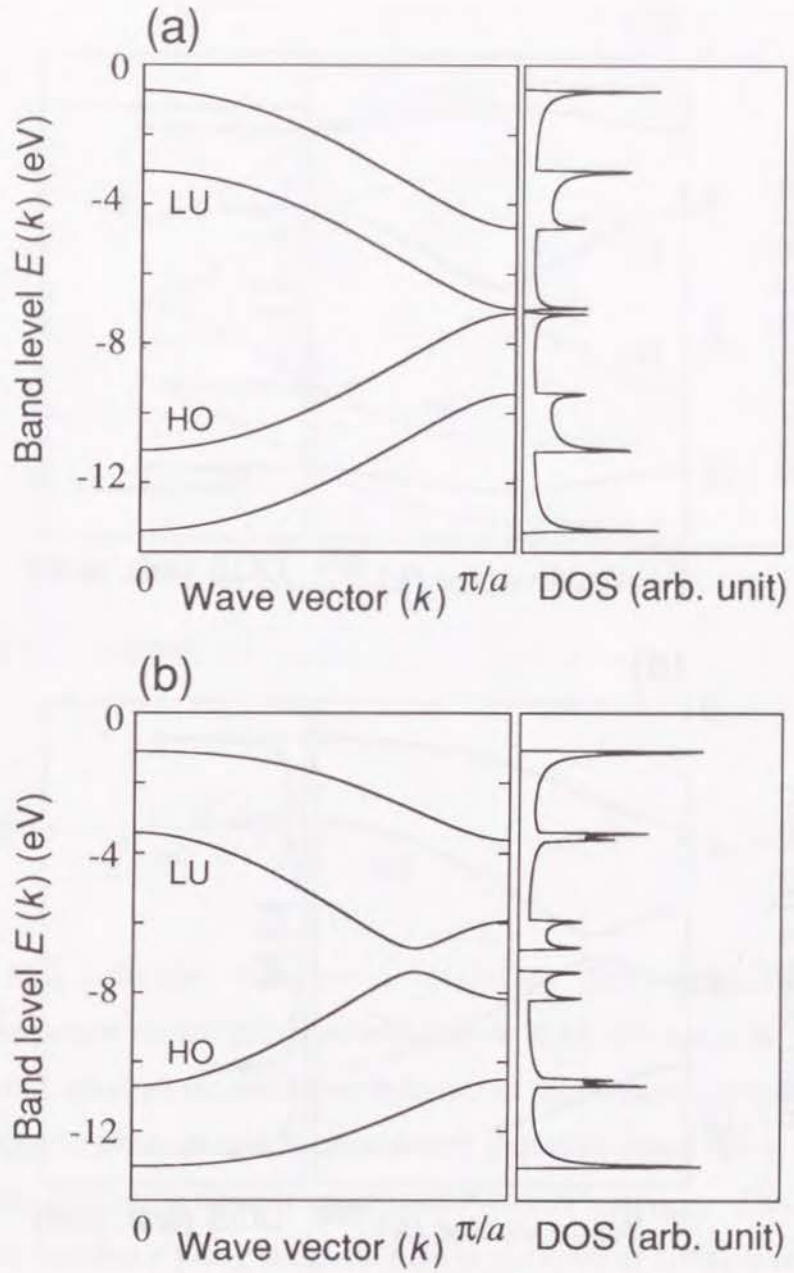

Figure 2. The π-energy band structure and the density of states (DOS) of polyacene for several values of a constant magnetic field: (a)ϕ_{hex}/ϕ_0=0; (b)ϕ_{hex}/ϕ_0=1/4; (c)ϕ_{hex}/ϕ_0=1/2; (d)ϕ_{hex}/ϕ_0=3/4; (e)ϕ_{hex}/ϕ_0=1. HO and LU denote the highest occupied and the lowest unoccupied π-bands, respectively.

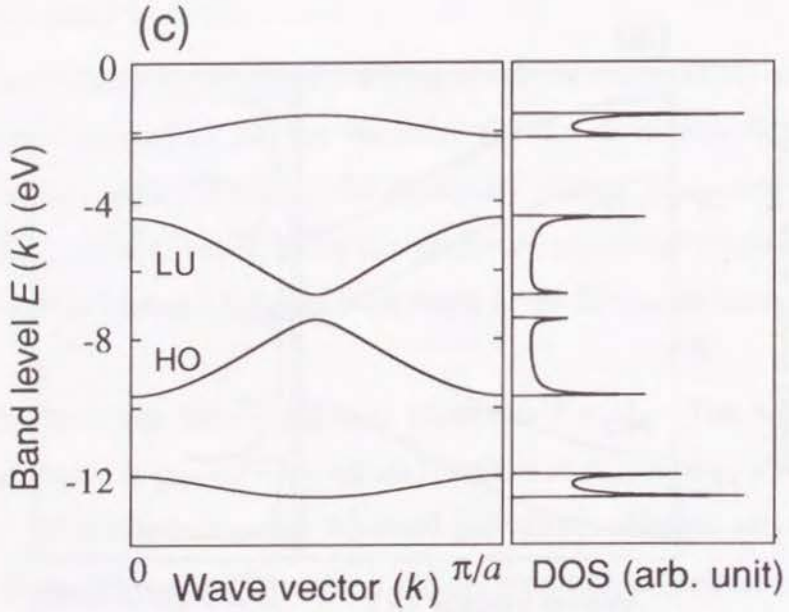

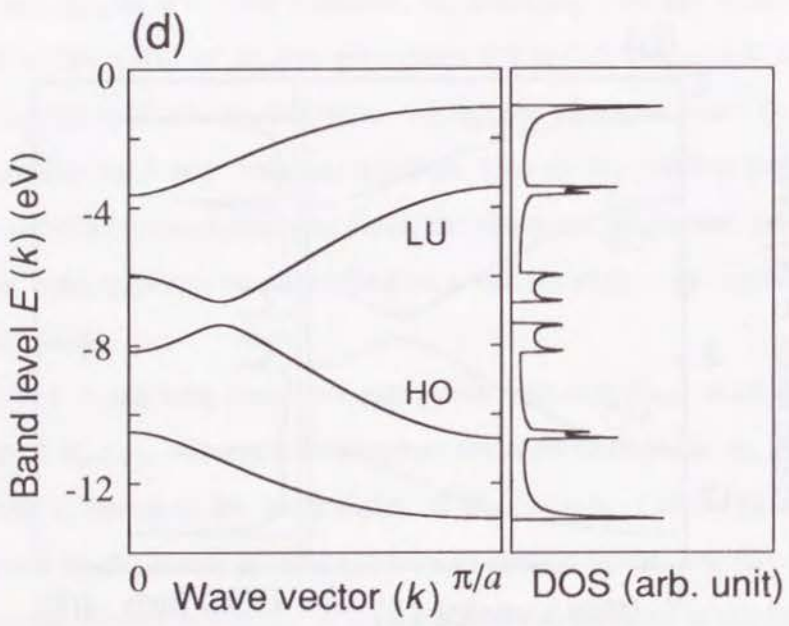

Figure 2. continued.

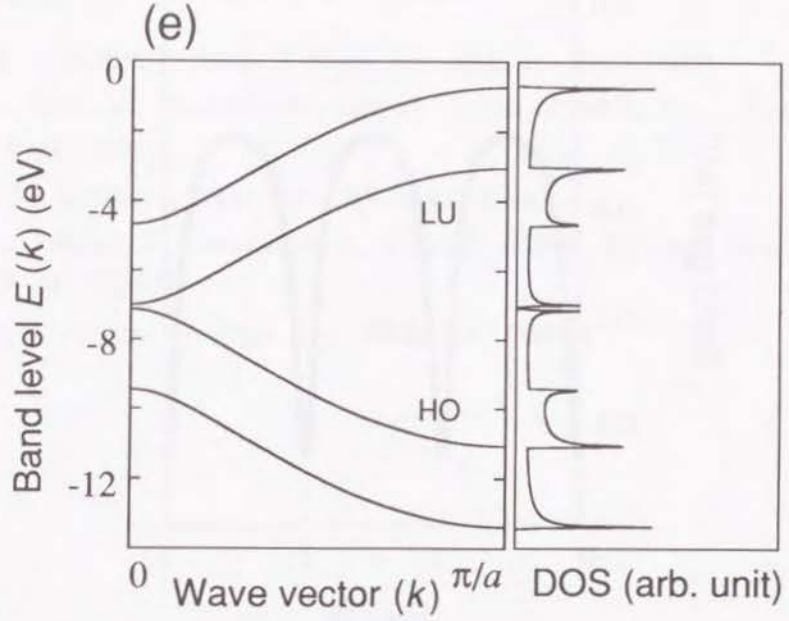

Figure 2. continued.

$$\chi(0) = -\frac{1}{M_{\text{unit}}}\left[\frac{\partial^2 E_{\text{tot}}}{\partial H^2}\right]_{H=0} \tag{15}$$

where M_{unit} is the mass of the unit cell (4C+2H). Employing $a = 2.412$ Å as in the present model, $\chi(0)$ is estimated to be -0.48×10^{-6} e.m.u./g.

Finally, although the periodical behavior of the electronic properties on the magnetic field strength is attractive, it should be noted that it will be generally difficult to observe experimentally such behavior. This comes from the fact that a strong magnetic field in the order of 10^9 G is required, due to the angstrom size of the bond lengths. It is also noted that under such a strong magnetic field the interaction between the electron spin and the magnetic field also becomes important.

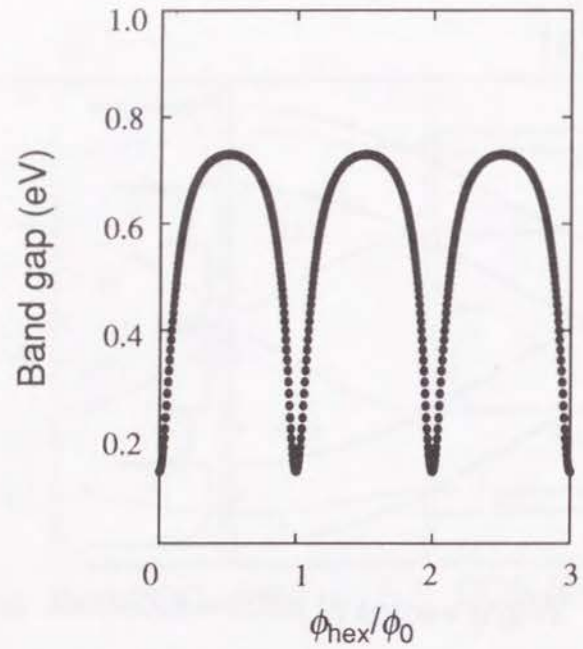

Figure 3. Change of the band gap with respect to the magnetic field represented by ϕ_{hex}/ϕ_0.

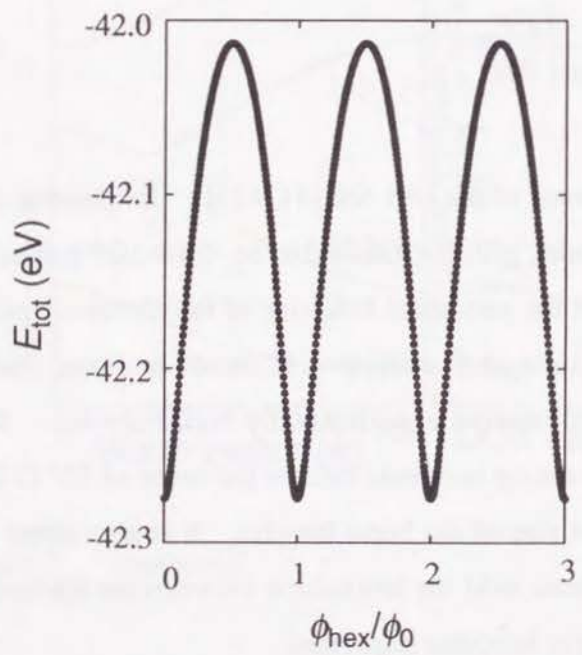

Figure 4. Total electronic energy per cell vs. ϕ_{hex}/ϕ_0.

References

[1] H. Ajiki and T. Ando, *J. Phys. Soc. Jpn.*, **64** , 260 (1995).

[2] R. Saito, G. Dresselhaus, and M. S. Dresselhaus, *Phys. Rev.*, **B50**, 14698 (1994).

[3] J. M. Luttinger, *Phys. Rev.*, **84**, 814 (1951).

[4] K. Tanaka, S. Yamashita, H. Yamabe, and T. Yamabe, *Synth. Met.*, **17**, 143 (1987).

[5] D. R. Hofstadter, *Phys. Rev.*, **B14**, 2239 (1976).

PART III

Electronic Structure and Li-Storage Mechanism of Polyacenic Semiconductor (PAS) Material

---

INTRODUCTION

In order to restrain the Peierls transition, the attempt to increase dimensionality of a π-conjugated polymer from one-dimensional (1D) to pseudo-1D structure has been carried out. Although theoretical calculations suggest that the pseudo-1D polymers represented by 1D graphite family including polyacene (PAc) and polyphenanthrene (PPh) become excellent electrical conductors [1], their synthesis is currently rather difficult.

Pyrolyzed polymers, therefore, have been examined as an alternative candidate for the prototype of 1D graphite family. Pyrolyzed polymers are

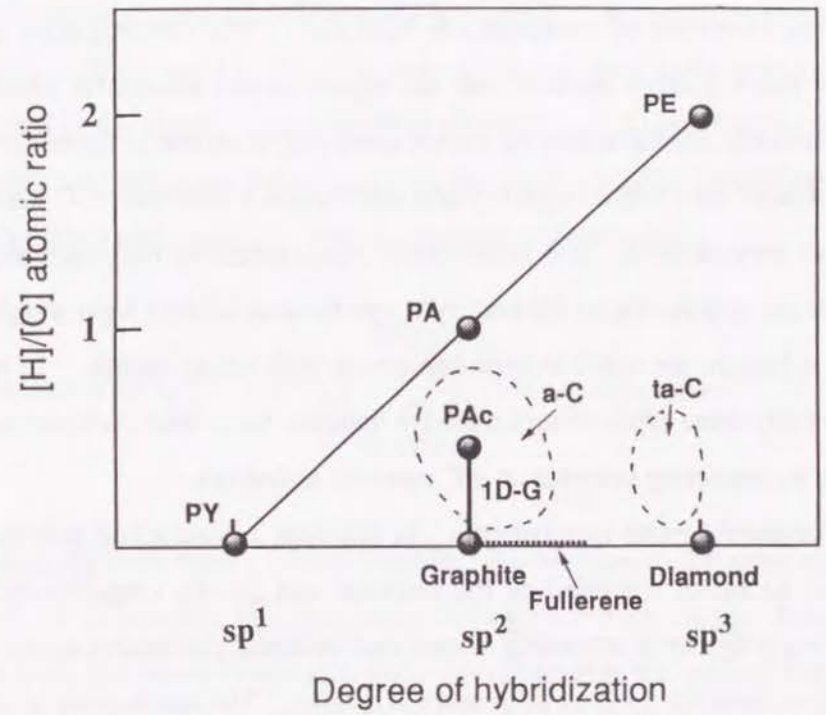

Figure 1. A "phase" diagram including carbon materials and organic polymers. PY, PA, PE, PAc, 1D-G, a-C and ta-C represent polyyne, polyacetylene, polyethylene, polyacene, one-dimensional graphite family, the amorphous carbon having sp^2-hybridized carbon atoms, and the tetrahedrally bonded amorphous carbon with sp^3-hybridization, respectively.

quite appropriate to the application because they are highly stable and their electronic as well as structural properties can be controlled by choosing the starting material and reaction conditions. From the simplified diagram of carbon allotropes shown in Fig. 1, one can see that pyrolyzed polymers can be included into the ambiguous region named amorphous carbon (a-C) near the 1D graphite polymers. It is well known that coal, coke, charcoal pitch, and so on also belong to a-C, but have seldom been considered as the electronic materials.

One of the most successful applications of conducting polymers is the use as the electrode of rechargeable batteries. The investigation into a polymer-based battery started from the report on the successful reversible electrochemical doping-undoping cycles using polyacetylene (PA) in 1981 [2]. On account of their higher stability and microporous structure, a-C materials have also been studied. It is noteworthy that conducting polymers and a-C materials are appropriate to the battery usage because of their light weight and smaller effect on the environment compared with heavy metals. In recent years, mainly three types of rechargeable batteries have been commercialized by using a conducting polymer or a-C material as follows.

(1) Polymer/Li metal-type battery: In this type a conducting polymer (or a-C) and Li metal are used as the cathode and anode, respectively. A conducting polymer is reversibly doped and undoped electrochemically with an electron acceptor such as BF_4^- and ClO_4^- ions. The mechanism is shown by

$$\text{polymer} + a\,\text{LiClO}_4 \underset{\text{discharge}}{\overset{\text{charge}}{\rightleftarrows}} \left[\text{polymer}^{a+}(\text{ClO}_4^-)_a\right] + \text{Li (metal)}$$

(2) Polymer/Polymer-type battery: In this type, a conducting polymer (or a-C) is used as the both electrodes. The polymer, therefore, must be doped with not only by an electron acceptor but also by a donor (mainly Li ion). The mechanism of the battery using $LiClO_4$ electrolyte becomes

$$2\,\text{polymer} + a\,\text{LiClO}_4 \underset{\text{discharge}}{\overset{\text{charge}}{\rightleftarrows}} \left[\text{polymer}^{a+}(\text{ClO}_4^-)_a\right] + \left[\text{polymer}^{\delta a-}(\text{Li}^{\delta+})_a\right]$$

(3) Transition metal oxide/Polymer-type battery: A transition metal oxide such as $Li_{1-x}NiO_2$ and $Li_{1-x}CoO_2$ is used as the cathode, and a polymer (or a-C) is used as the anode. Since the both electrodes are doped with Li ions in a reversible way as shown below, this type battery is called a "Li-ion battery" or "rocking-chair type battery". The mechanism is expressed by

$$\text{polymer} + \left[(\text{NiO}_2)_n^{\Delta a-}(\text{Li}^{\Delta+})_a\right] \underset{\text{discharge}}{\overset{\text{charge}}{\rightleftarrows}} n\,\text{NiO}_2 + \left[\text{polymer}^{\delta a-}(\text{Li}^{\delta+})_a\right]$$

Among these three types of batteries, the third one is the most attractive because of its specifically high output voltage and high energy density [3]. In this type, the anode material is known to determine the greater part of the performance of a battery. Therefore, research for a material which can store a considerable number of Li and, at the same time, highly endurable one has been intensively carried out. It has been clarified a-C material is the most suitable one, but the Li-doping as well as storage mechanism is still unclear on account of disordered structure and, hence, a clear guide has not been

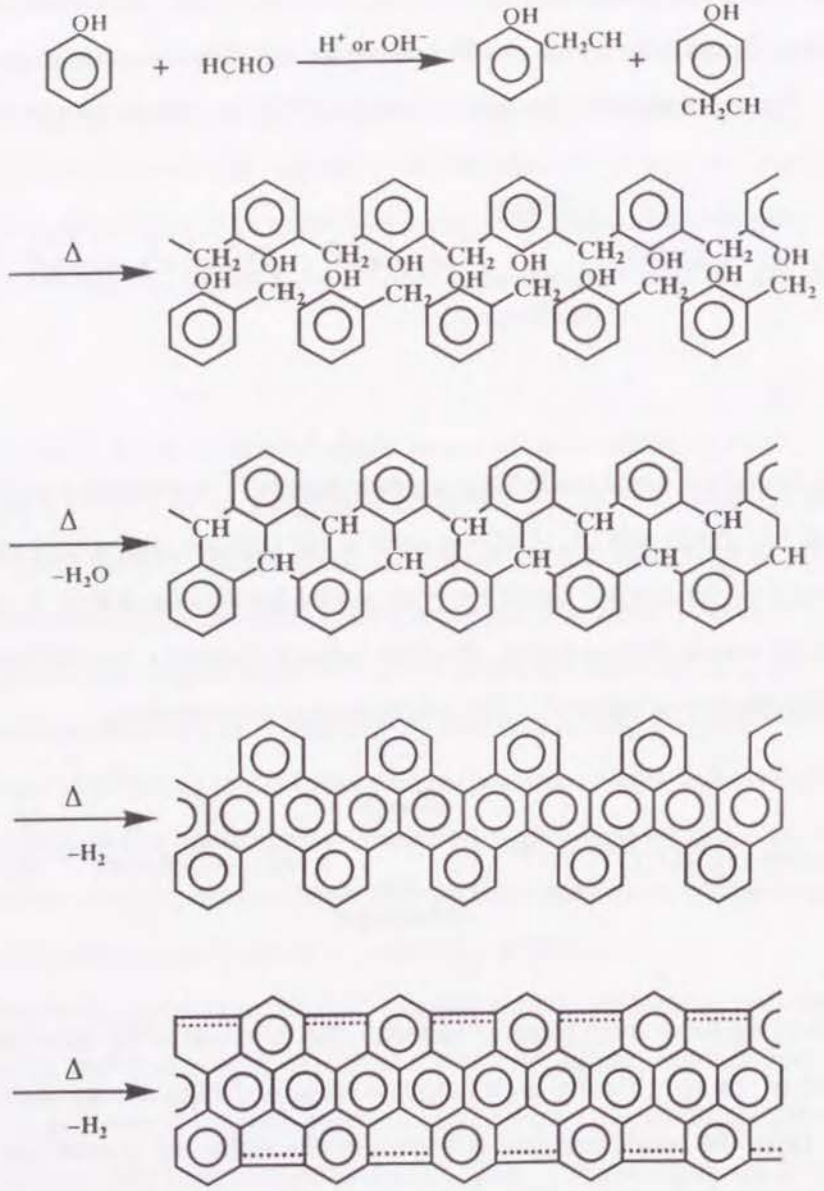

Figure 2. Reaction diagram of the preparation of the PAS materials. Note that the polymers are exaggerated forms.

obtained. It is noted that graphite has also been employed as the anode due to its clear structure and constant output voltage. Recently, a review on the electrochemical characteristics of carbon materials is presented [4].

Polyacenic semiconductor (PAS) materials which are prepared by the pyrolytic treatment of phenol-formaldehyde resin at relatively low temperatures (500-1000 °C) also belong to the a-C or, in more restrict sense, hydrogen-containing carbon. Fig. 2 shows a presumed reaction diagram of PAS. Their electronic and structural properties have been intensively studied to find out that these properties strongly depends on the treatment temperature [5]. It has been shown that PAS materials are air-stable and can be doped with electron donor as well as acceptor resulting in an increase of the electrical conductivity about 11 orders of magnitude in maximum. Another important feature of PAS materials is loose structure as illustrated in Fig. 3: the interlayer distance of PAS (d_c=3.7-4.2 Å) is longer than that of graphite (3.35 Å). Owing to these characteristic properties, the PAS material, especially prepared at 600-700 °C, exhibits excellent electrochemical performance when used as

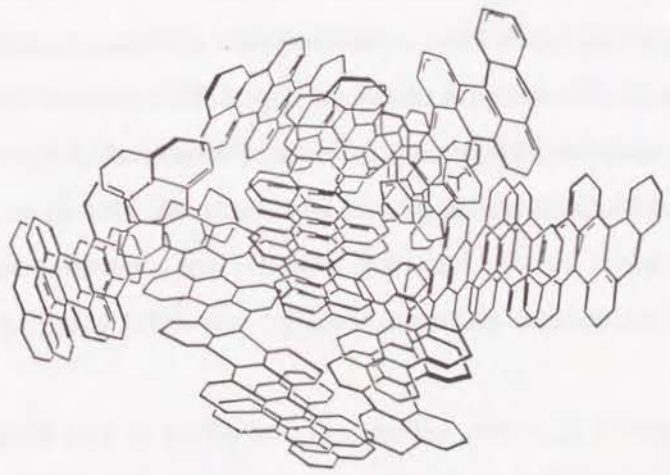

Figure 3. A model structure of PAS material.

the anode. For instance, the PAS ([H]/[C]=0.22) electrode shows the extraordinary highly Li-doped state with the capacity of 1100 mAh/g corresponding to the C_2Li stage which is obviously much more highly doped state than that of graphite (C_6Li in maximum), along with good reversibility and long cycle life [6]. Nowadays, two types of PAS batteries have been manufactured and are used in a variety of electronic appliances. However, a-C including the PAS material have two disadvantages, one is the incomplete undoping in the first cycle which results in a certain amount of useless Li, and another is inconstant output voltage, i.e., the voltage decreases with proceeding the undoping. It is very interesting to investigate the Li-doping mechanism which probably relates to the above disadvantages of a-C material closely. Furthermore, the clarification of the mechanisms is quite important for further development of Li rechargeable battery.

In this Part, the author presents electronic and structural properties of the Li-doped PAS material using some characteristic approaches because there have been only the reports on X-ray diffraction (XRD) and X-ray photoelectron spectroscopy (XPS) analyses [7].

In Chapter 1 (*Synth. Met.*, submitted), the result of a detailed electron spin resonance (ESR) analysis of the Li-doped PAS material is presented. Change in the electronic structure upon the electrochemical Li-doping has been monitored through the behavior of unpaired electrons. It will be shown that the Li-doping causes metallic transition from the semiconducting state and that the generated conduction electrons undergo spin-orbit coupling by the Li dopants.

In Chapter 2 (*Carbon*, submitted), the effect of four kinds of alkali metals (Li, Na, K, and Rb) on the electronic structure of the PAS material has been examined based on the ESR measurement. The decomposition reaction

of a series of alkali azides has been employed for the alkali-doping method, which is applied to a-C material for the first time. It becomes clear that the ESR linewidth depends on the atomic number of the dopant, manifesting the spin-orbit interaction suggested in Chapter 1.

In Chapter 3 (*Phys. Rev. B*, submitted), the electronic state of Li dopants has been directly investigated by means of ^{7}Li nuclear magnetic resonance (^{7}Li NMR). From appearance of the Knight shift, it is inferred that there occurs the Fermi contact interaction along with the spin-orbit interaction. Information about the mobility of Li dopants will also be presented.

In Chapter 4 (*Carbon*, submitted), the author presents the result of structural analysis of the PAS material through adsorption of Xe atoms using ^{129}Xe NMR measurement. It will be shown that the pure PAS sample possesses a number of micropores with the diameter of 7.7±1.6 Å. Effects of the binder, solvent, and Li-doping which could afford crucial standpoint for the Li-doping mechanism, have been also examined.

In Chapter 5 (*Carbon*, submitted), the Li-doping and storage mechanisms in a-C material are theoretically examined with the aid of semiempirical molecular orbital method. It will be shown that there exists a clear difference between the Li dopant intercalated in the carbon layers and that adsorbed on the carbon surface. In the latter, the possibility of small Li cation clusters concomitant with fully ionized Li atoms is suggested. In addition, it is found the edge-structure of a-C affords a significant effect on the stability of Li dopants.

References

[1] K. Tanaka, S. Yamashita, H. Yamabe, and T. Yamabe, *Synth. Met.*, **17**, 143 (1987).

[2] P. J. Nigrey, D. MacInnes, Jr., D. P. Nairns, A. G. MacDiarmid, and A. J. Heeger, *J. Electrochem. Soc.*, **128**, 1651 (1981).

[3] K. Brandt, *Solid State Ionics*, **69**, 173 (1994).

[4] J. R. Dahn, T. Zheng, Y. Liu, and J. S. Xue, *Science*, **270**, 590 (1995).

[5] For instance, K. Tanaka, S. Yata, and T. Yamabe, *Synth. Met.*, **71**, 2147 (1995).

[6] S. Yata, Y. Hato, H. Kinoshita, N. Ando, A. Anekawa, T. Hashimoto, M. Yamaguchi, K. Tanaka, and T. Yamabe, *Synth. Met.*, **73**, 273 (1995).

[7] S. Yata, H. Kinoshita, M. Komori, N. Ando, K. Tanaka, and T. Yamabe, *Synth. Met.*, **62**, 153 (1994).

Chapter 1

ESR Study of Li-Doped PAS Material

1. Introduction

In recent years, growing interests have been paid to amorphous carbon (a-C) materials as a new type of anode material of the Li rechargeable battery [1]. Utilization of adequate a-C materials can be free from the generation of the lithium dendrite during the charging-discharging cycle, being one of the most serious problems in the batteries using metallic Li. Furthermore, a-C materials exhibit useful properties such as good reversibility, light weight, and long cycle life. Among those materials the carbons treated at relatively low temperature have been proved especially suitable to this purpose, since they exhibit higher capacity compared with graphite owing to their loose structures. Although several studies have been presented to explain such characteristics of a-C materials [2,3], microscopic aspects of Li storage has never been elucidated yet.

We have been studying the polyacenic semiconductor (PAS) materials prepared by the pyrolysis of phenol-formaldehyde (PF) resin at relatively low temperatures (400-800°C) [4] as one of the most promising a-C materials. In order to understand fundamental aspects of the PAS material, a variety of studies have been carried out based on the observed data, for instance, the electron spin resonance (ESR) [5], X-ray diffraction (XRD)

[6], ^{13}C nuclear magnetic resonance (NMR) [7], magnetic susceptibility [8], thermoelectric power [9], and electrical transport measurements [9]. The PAS materials are air-stable and can be doped with both p- and n-type dopants, resulting in a maximum increase of the electrical conductivity about 11 orders of magnitude [4]. It has also been found that the PAS materials have loose structure and a relatively longer interlayer distance (d_c = 3.7-4.0 Å) [6] than that of graphite (d_c = 3.35 Å) [10]. The PAS materials, therefore, have been intensively examined toward the application to the electrodes of Li rechargeable batteries [11-13]. Owing to the loose structure, the PAS material can accommodate larger amount of dopants compared with graphite. For instance, we have confirmed that the PAS ([H]/[C] = 0.22) electrode with the capacity of 850 mAh/g (0.005-1.0 V vs. Li/Li^+) shows good stability and reversibility [13]. Moreover, the most deeply Li-doped state of 1100 mAh/g corresponding to the molar ratio [Li]/[C] = 1/2 has been achieved without liberation of Li clusters from the voltage profile of the cell. The C_2Li stage is obviously a much more highly doped (charged) one than that of graphite (C_6Li). This C_2Li state has been pointed out to have an energy density per volume almost equal to Li metal [11]. These facts are promising in fabrication of a new type of safe and high energy density Li rechargeable batteries. Nowadays, two types of PAS batteries have been commercialized and are used in a variety of electronic devices [12].

Search for the electronic states of Li-doped PAS from a microscopic view point is obviously desirable for fundamental characterization of the doped Li and the PAS material as well as the better understanding of Li-storage mechanism toward further development in Li rechargeable batteries. Since there has been an only preliminary report on the ESR analysis of Li-

doped a-C [14], in the present chapter, detailed ESR observation data and their analyses of the electronic states of the pristine and the Li-doped PAS materials are presented for further clarification of the electronic states of the Li-doped PAS materials. We will demonstrate that the electronic state is greatly influenced by doped Li atoms mainly through a spin-orbit coupling.

2. Experimental

PAS material was prepared by the pyrolytic treatment of PF resin in a non-oxidative atmosphere as described in the previous paper [4]. The PAS sample employed in the present chapter was prepared at the pyrolysis temperature (T_p) of 680°C showing the molar ratio [H]/[C] = 0.22 and the d.c. electrical conductivity $\sigma = 2.7\times10^{-3}$ S/cm which has been measured separately [11]. The Li-doping process of the PAS material was performed electrochemically with a constant current (0.1-0.25 mA/cm^2) using a charge-discharge unit (Hokuto HJ-201B). The PAS sample was finished into the sheet shape by adding 10 wt.% of polyfluorocarbon as a binder and was used as the electrode. A rectangular polypropylene cell was set up with this PAS electrode and Li metal for the counter and working electrodes. A Cu foil was pressed onto the back side of the PAS electrode as the electric collector. Solution of 1M $LiPF_6$ in propylene carbonate-diethyl carbonate was used as the electrolyte after careful purification.

The Li-doping amount, x (%), was controlled by the coulometry according to the following equation,

$$x\,(\%) \equiv \frac{[\mathrm{Li}]}{[\mathrm{C}]} \times 100 = \frac{3.6Q(12+r)}{96500} \times 100 \qquad (1)$$

where Q (in mAh/g) is the amount of transferred charge during the doping process and r the [H]/[C] molar ratio of the PAS material employed (=0.22 in the present study). For instance, the designations C_6Li and C_2Li correspond to 17 and 50 %-doped stages, respectively. The 60 %-doped sample was also intentionally prepared for the ESR examination of the heavily doped PAS sample with liberated metallic Li clusters based on the electrochemical report [11,13]. After the doping process the sample was washed out by dimethoxyethane and thoroughly evacuated. The handling procedures were carefully carried out in dry argon atmosphere. The PAS samples were sliced off from the Cu foil and then sealed in a quartz tube (o.d. 5 mm) *in vacuo* and subjected to the ESR measurement.

The ESR spectra were recorded on a JEOL JES RE-2X spectrometer at the X band (9.1 GHz) in the temperature range 123-293 K and on a Varian E-112 with Oxford cryogenic system down to liquid He temperature (4.5 K). The modulation width was changed from 0.05 to 1.0 G according to the peak-to-peak linewidth ($\Delta H_{p.p.}$) values of the spectrum. The g-values and $\Delta H_{p.p.}$ were determined using a Mn^{2+}-MgO solid solution. For the spin concentration, $CuSO_4 \cdot 5H_2O$ was used as a reference. In order to check the ESR lineshape the ratio $\Delta H_{1/2}/\Delta H_{p.p.}$, where $\Delta H_{1/2}$ stands for the outside half-height linewidth) of each peak was also calculated. Rigorous Gaussian and Lorentzian lineshapes give the values 1.92 and 2.40, respectively, for this ratio.

3. Results

The observed ESR results of the pristine and the Li-doped PAS materials are listed in Table 1. Relative errors of the observed g-values, $\Delta H_{p.p.}$, and spin concentrations are less than 5×10^{-4} %, 20 %, and 60 %,

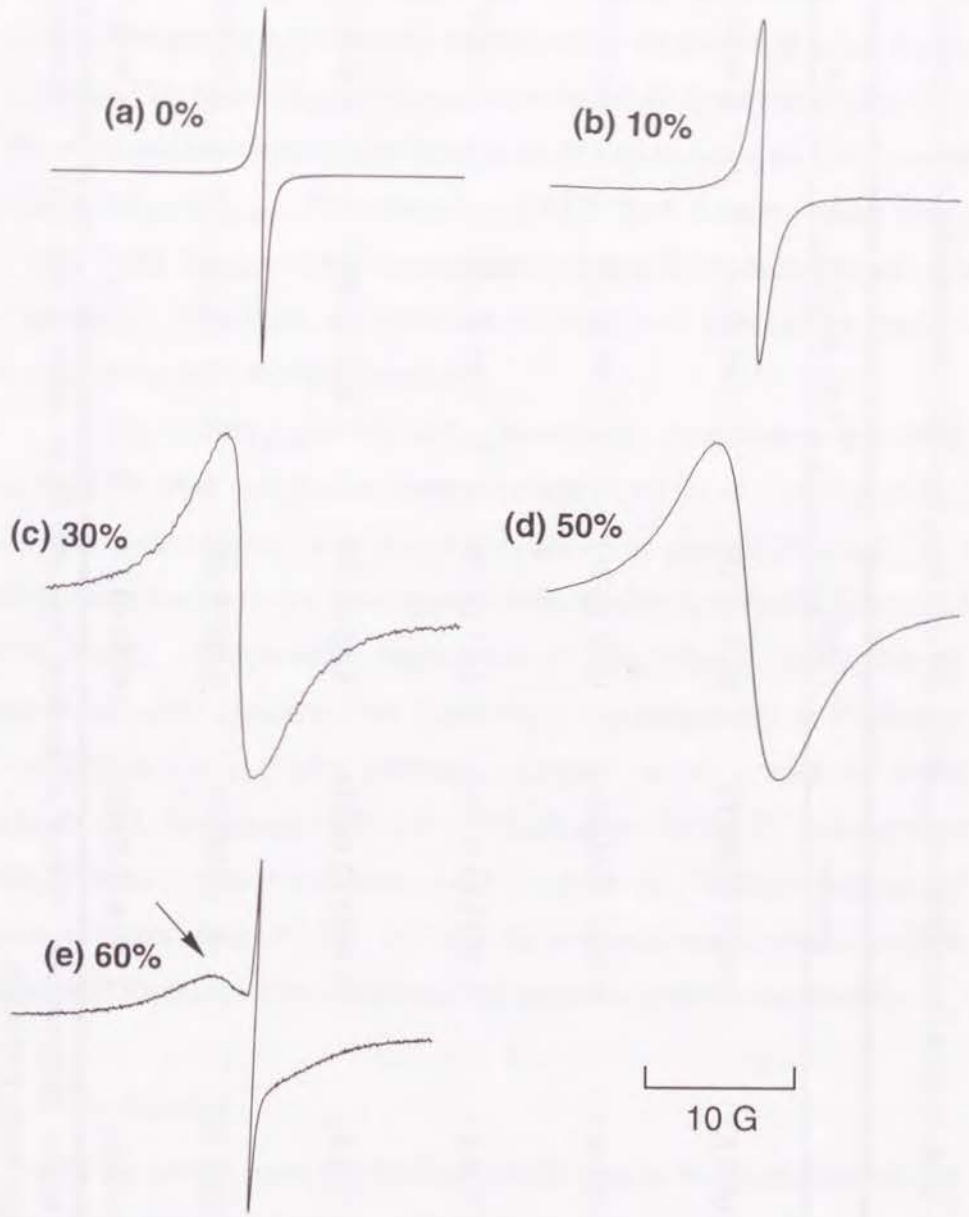

Figure 1. ESR lineshapes of (a)pristine and the Li-doped ((b)10 %, (c)30 %, (d)50 %, and (e)60 %) PAS materials at room temperature. The broad component observed in the 60 %-doped PAS is shown by an arrow.

Table 1. g-value, peak-to-peak linewidth ($\Delta H_{p.p.}$ in G), $\Delta H_{1/2}/\Delta H_{p.p.}$, and spin concentration (N_s in spins/g) of the PAS samples.

Samples	g-value	$\Delta H_{1/2}/\Delta H_{p.p.}$	$\Delta H_{p.p.}$	N_s [a]
pristine				
measured at 280 K (6.4 K)	2.0021 (2.0022)	2.24 (2.14)	0.42 (0.35)	2.4×10^{19}
10 % Li-doped				
measured at 283 K (5.3 K)	2.0023 (2.0022)	2.98 (2.12)	0.52 (0.21)	2.1×10^{19}
30 % Li-doped				
measured at 277 K (7.8 K)	2.0023 (2.0023)	2.73 (2.21)	2.63 (0.23)	8.4×10^{19}
50 % Li-doped				
measured at 280 K (5.6 K)	2.0023 (2.0023)	2.50 (2.40)	3.68 (0.37)	4.9×10^{19}
60 % Li-doped				
measured at 280 K (5.4 K)[b]	–[c] (2.0024)	–[c] (2.83)	3.80 (0.45)	6.3×10^{19}
spike				
measured at 280 K (69 K)	2.0018 (2.0018)	–[c] (–[c])	0.30 (0.22)	6.5×10^{17}[d]

[a]Data are for the higher temperatures. [b]Broad component indicated by an arrow in Fig. 1(e). [c]Immeasurable. [d]Determined by a simulation procedure.

respectively. The ESR spectra in Figs. 1(a)-(d) (pristine-50 %-doped) have single lineshapes without hyperfine splitting and show that the electrochemical doping makes the spectrum broader according to the doping amount. This broadening was observed up to the 50 %-doping (C_2Li) level. These spectra are mostly considered to be of Lorentzian type based on the ratio of $\Delta H_{1/2}/\Delta H_{p.p.}$. When doped over 50 % level, a narrow spike with g = 2.0018 and $\Delta H_{p.p.}$ = 0.24 G newly appeared in addition to the broad peak (Fig. 1(e)). This spike is considered to come from liberated Li clusters. We will come back to this point later.

In Fig. 2, $\Delta H_{p.p.}$ and $1/(I_{p.}\Delta H_{p.p.}{}^2)$, where $I_{p.}$ designates a full height of the ESR peak, are plotted versus temperature. It is seen that $\Delta H_{p.p.}$ changes almost linearly with the temperature. The quantity $1/(I_{p.}\Delta H_{p.p.}{}^2)$ is proportional to the reciprocal magnetic susceptibility (χ^{-1}) for the Lorentzian ESR shape. Temperature dependence of $1/(I_{p.}\Delta H_{p.p.}{}^2)$ shows that the nature of spins changes from Curie-type (paramagnetic) to Pauli-type (metallic) as the Li doping proceeds. Change in $\Delta H_{p.p.}$ upon the doped amount of Li measured at 293 and 123 K are given in Fig. 3. It is seen that $\Delta H_{p.p.}$ remains almost constant ($\approx$ 0.3 G) up to ca. 7%-doped regime and then increases continuously. In Fig. 4 the measurement results of the ESR peak saturation depending on the applied microwave power are shown.

4. Discussion

In the present study the ESR spectra of spins in the pristine and the Li-doped PAS materials are systematically discussed using the total Hamiltonian specific to spins in the magnetic field,

$$H = H_{Zeeman} + H_{exch} + H_{dipole} + H_{spin-orbit} + H_{hfs} \qquad (2)$$

where H_{Zeeman} causes the ordinary Zeeman splitting, H_{exch} an exchange interaction between two electron spins, H_{dipole} a dipole interaction between two electron spins, $H_{\text{spin-orbit}}$ a spin-orbit interaction, and H_{hfs} a hyperfine term by dipole interactions between a electron spin and a nuclear, all of which are explicitly shown below with the usual notations:

$$H_{\text{Zeeman}} = g_{\text{e}} \mu_{\text{B}} \sum_i \boldsymbol{H} \cdot \boldsymbol{s}_i \tag{3}$$

$$H_{\text{exch}} = 2 \sum_{i>j} J_{ij} \boldsymbol{s}_i \cdot \boldsymbol{s}_j \tag{4}$$

$$H_{\text{dipole}} = g_{\text{e}}^2 \mu_{\text{B}}^2 \sum_{i>j} \frac{\boldsymbol{s}_i \cdot \boldsymbol{s}_j}{r_{ij}^3} - \frac{3(\boldsymbol{r}_{ij} \cdot \boldsymbol{s}_i)(\boldsymbol{r}_{ij} \cdot \boldsymbol{s}_j)}{r_{ij}^5} \tag{5}$$

$$H_{\text{spin-orbit}} = \xi \sum_i \boldsymbol{l}_i \cdot \boldsymbol{s}_i \tag{6}$$

$$H_{\text{hfs}} = g_{\text{e}} g_{\text{I}} \mu_{\text{B}} \mu_{\text{I}} \sum_{i,k} \frac{8\pi}{3} \delta(r_{ik})\, \boldsymbol{s}_i \cdot \boldsymbol{I}_k - \frac{\boldsymbol{s}_i \cdot \boldsymbol{I}_k}{r_{ik}^3} - \frac{3(\boldsymbol{r}_{ik} \cdot \boldsymbol{s}_i)(\boldsymbol{r}_{ik} \cdot \boldsymbol{I}_k)}{r_{ik}^5} \tag{7}$$

Lineshape of the ESR spectrum can be affected by three types of interactions, that is, dipolar spin-spin (H_{dipole}), spin-lattice ($H_{\text{spin-orbit}}$ and H_{hfs}), and exchange (H_{exch}) interactions. The first two are associated with the relaxation process and the last one with the inter-spin interactions. In the following, behavior of the ESR spectra is to be interpreted with the use of the above Hamiltonian terms.

4.1. Pristine PAS. The electronic and structural properties of the PAS materials have been investigated as a function of T_p applied in the series of papers [5-9]. At T_p lower than 700°C, the degree of the carbonization is yet small and, hence, there are a number of unpaired electrons [5] ascribed to dangling bonds or radical spins occurring in the graphitized fractions [15]. It has been demonstrated that the three-dimensional variable-range hopping (3D-VRH) mechanism is dominant for the electrical transport [9] since these fractions are so small and/or incomplete that they cannot yet be defined as metallic islands at least in the pristine stage.

The pyrolysis of PF resin above 700°C enhances graphitization through nucleation or condensation resulting in formation of larger graphitized fragments functioning as metallic islands [9], in which the delocalized conduction electrons contributing as Pauli spins are newly generated [8]. In the present pristine PAS sample, $\Delta H_{\text{p.p.}}$ is quite small, being almost the same value reported earlier [5], due to a spin-spin exchange interaction (H_{exch}) arising from the high spin concentration such as 2.4×10^{19} spins/g (see Table 1). It is noted that from the g-value (2.0021-2.0023) the signal is confirmed to come from carbon π-radicals. Since the PAS material examined in the present study was prepared at 680°C, nature of radical spins is marginal between those from localized and delocalized ones. In fact, electrical conductivity of the pristine PAS separately measured was not so high (2.7×10^{-3} S/cm at room temperature [11]).

4.2. Metallic transition in the Li-doped PAS. A separate electrical conductivity measurement has shown the conductivity steeply increases right after the Li doping [11]. From Fig. 2, metallic nature already appears in 10 % Li-doped PAS at room temperature in terms of Pauli paramagnetic

contribution. Although at 30 %- (50 %-) doped level, the apparent Pauli nature remains down to 100 K (50 K), Curie paramagnetic contribution is still dominant in the lower temperature region. The steep rise in $1/(I_{p.}\Delta H_{p.p.}^2)$ of the 60%-doped sample observed at 40 K (Fig. 2 (e)) is currently not interpretable, but its origin could be attributed to the Curie spin with a very large $\Delta H_{1/2}/\Delta H_{p.p.}$ value (4.36). Curie paramagnetism originates from the paramagnetic spins obeying Curie-law ($\chi = C/T$), while Pauli paramagnetism from the conduction electrons with its intensity being proportional to the density of states at Fermi energy ($\chi = CN(E_F)$) and, hence, independent of temperature.

An unpaired π-electron (that is, π-spin) is known to show the g-value close to that of a free electron (2.0023) since the π-electron can be mobile due to delocalization through the π-conjugation. On the other hand, a σ-spin shows smaller g-value (2.0014-19) [16,17] and is relatively localized with a larger $\Delta H_{p.p.}$ value. Since a σ-spin localizes on a single atom, it is expected to be highly reactive [15] and not to generally remain in the present PAS materials by compensation to make up C-H bonds. Note that in the present PAS materials electrons responsible for both the Pauli and the Curie paramagnetic behavior are of π-type from their g-values.

All the Li-doped PAS samples can evade the skin effect as well as Li clusters in the 60 %-doped sample (see Sec. 4.4) because they are essentially fine particles due to porous and amorphous structures [6]. From the microscopic viewpoint, Li atoms are considered to be doped in the different ways, such as intercalation and location upon the surface and at the edge of graphitized fragments [18]. These Li atoms could simultaneously augment the conduction paths among graphitized fragments acting as metallic islands,

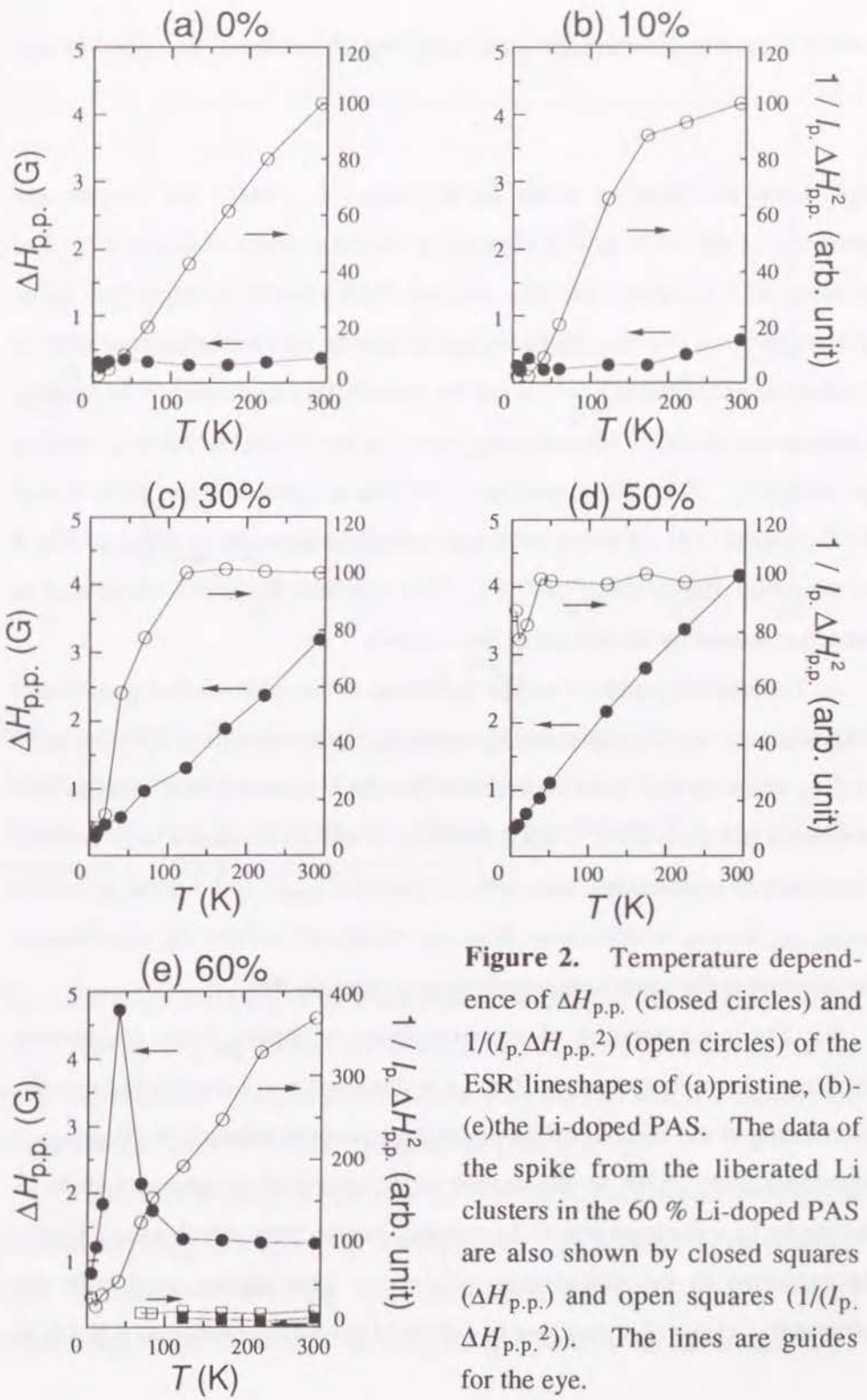

Figure 2. Temperature dependence of $\Delta H_{p.p.}$ (closed circles) and $1/(I_{p.}\Delta H_{p.p.}^2)$ (open circles) of the ESR lineshapes of (a)pristine, (b)-(e)the Li-doped PAS. The data of the spike from the liberated Li clusters in the 60 % Li-doped PAS are also shown by closed squares ($\Delta H_{p.p.}$) and open squares ($1/(I_{p.}\Delta H_{p.p.}^2)$). The lines are guides for the eye.

which is evident from the spin-orbit coupling phenomenon described in Sec. 4.3.

4.3. Line broadening upon Li doping. Here we discuss the behavior of the ESR spectra depending on the amount of doped Li. The process of Li-doping into the present PAS sample is supposed to be inhomogeneous due to possible irregular doping into miscellaneous sites in contrast to graphite [18], which can be seen in the monotonically increasing (decreasing) charging (discharging) curve in the electrochemical Li-doping process [11]. The voltage profile of graphite is quite different from that of PAS material [19]. There is seen a reluctance in increase of $\Delta H_{\mathrm{p.p.}}$ in Fig. 3 at the initial doping range (0-7 %). This apparent flatness is considered to be accompanied by the following two factors:

(i) The impurity spins of π-type occurring in the undeveloped graphitized fragments are rapidly scavenged by injection of electrons from Li at the early doping stage as has been reported in the ESR measurement with *in situ* doping of halogens [20]. Such a decrease in the spin concentration reduces two kinds of interactions, spin-spin exchange (H_{exch}) and dipolar spin-spin (H_{dipole}) terms, which cause both the exchange narrowing and dipolar broadening at the same time, resulting in a constant $\Delta H_{\mathrm{p.p.}}$.

(ii) The concentration of electron spins occurring from conduction electrons successively injected from Li at this stage is not enough to cause the broadening of the ESR signal based on the spin-orbit interaction ($H_{\mathrm{spin\text{-}orbit}}$) discussed later. Also, in this doping range, attack of the impurity spins of π-type by Li will create new C-Li covalent bonds, from which Li can hardly be extracted in the discharging process. This agrees well with the observation of the charging loss of 190 mAh/g (corresponding to 8 % Li) at

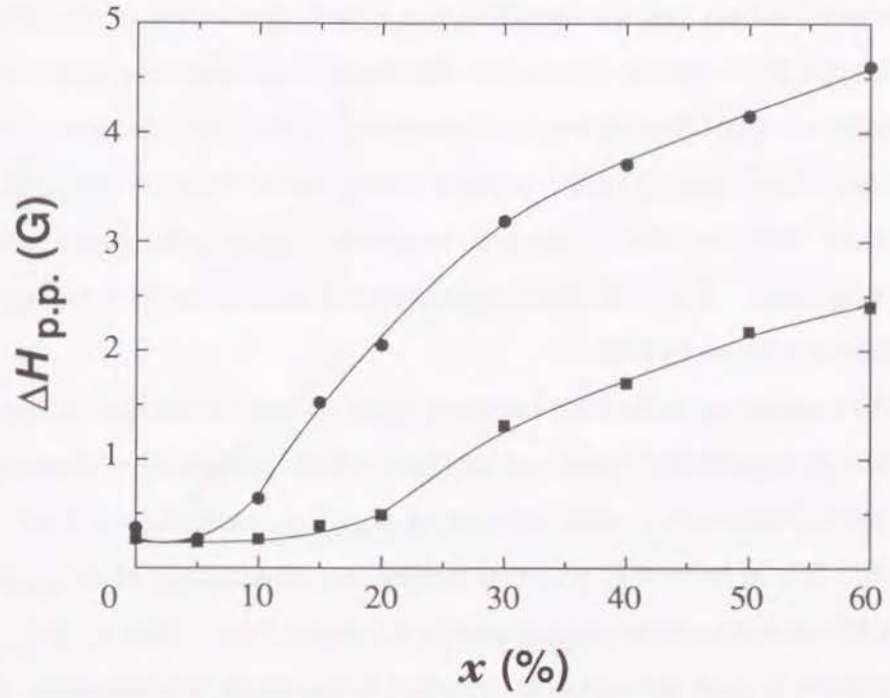

Figure 3. Change in the peak-to-peak linewidth ($\Delta H_{\mathrm{p.p.}}$) of the ESR lineshape of carbon π radical spins depending on Li-doping amount. The circles and squares indicate the values measured at 273 and 123 K, respectively. The lines are guides for the eye.

the initial stage of doping in the electrochemical charging-discharging process [11]. Moreover, the electrochemical a.c. impedance measurement for the PAS electrode has confirmed this tendency by the fact that the dopants are trapped more firmly in the early stage of the doping [21].

Further Li-doping up to the range 7-50 % has caused a monotonical increase in $\Delta H_{\mathrm{p.p.}}$ as seen in Fig. 3 without any sign of liberated metallic Li. This is consistent with the X-ray photoelectron spectroscopy (XPS) observation of the Li-doped PAS samples specified by the molar ratio C_3Li

and C_2Li stages [11], where the electronic state of Li has been proved to be in-between the ionic and the metallic ones. Such broadening of the ESR spectra upon the Li doping is considered to come from a perturbation to the conduction electrons through a spin-lattice relaxation based on the spin-orbit interaction ($H_{\text{spin-orbit}}$) [22,23]. A slight change in the slopes of $\Delta H_{\text{p.p.}}$ vs. x plot at $x = 30$ % suggests the spin-orbit interaction begins to decrease above that doping range. This may signify that Li atoms doped over 30 % become more loosely trapped by PAS.

The broadening of the ESR lineshape signifies that conduction carriers generated on the carbon π-atomic orbitals have a finite probability of locating on Li atoms, on which a small amount of $H_{\text{spin-orbit}}$ works ($\zeta = 0.2$ cm^{-1} [24,25]). It is of interest to note that temperature dependence of $\Delta H_{\text{p.p.}}$ is quite different between the pristine and the Li-doped PAS. That is, $\Delta H_{\text{p.p.}}$ of the pristine is small and almost temperature independent, whereas those of the doped PAS are large and decrease almost linearly with decrease in temperature. Although this independence in the pristine is somewhat similar to that in the porous PAS sample with $T_p = 800$ °C ($\Delta H_{\text{p.p.}} = 1.2$-$1.6$ G) [26], there occurs, in the present pristine PAS sample, almost no suppression of motional narrowing nor broadening due to H_{dipole} even at liquid He temperature. This signifies that spins are quite mobile in the graphitized fragments and that no spatial long-range correlation of spins is expected at low temperatures.

On the other hand, the remarkable reduction of $\Delta H_{\text{p.p.}}$ with decreasing temperature observed in the Li-doped PAS is considered to be associated with the following three factors:

(i) Appearance of large $\Delta H_{\text{p.p.}}$ values comes from the effect of $H_{\text{spin-orbit}}$ between the conduction electron injected and the Li atom when the former is

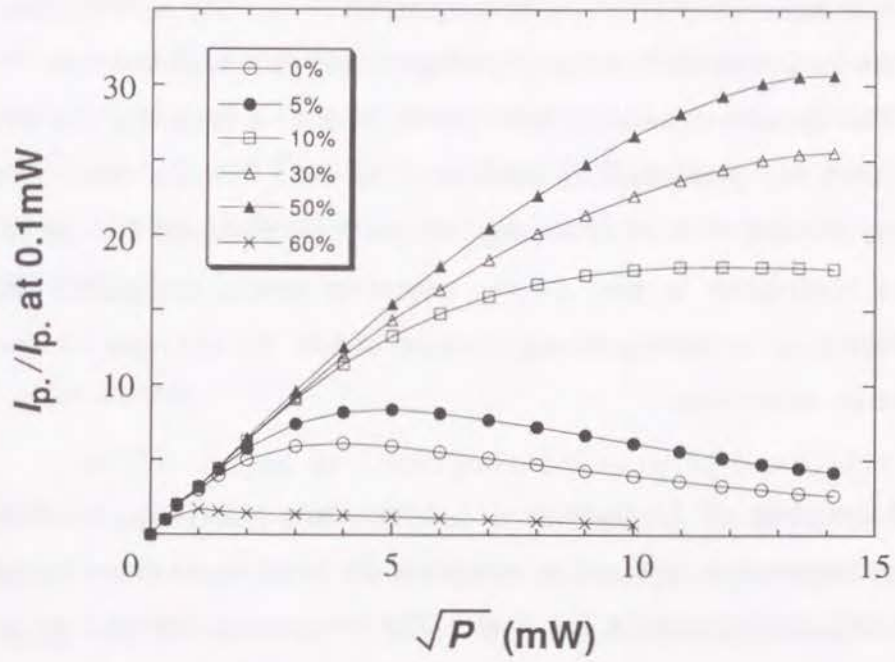

Figure 4. Saturation curves of the ESR peak heights of pristine and the Li-doped PAS materials. For the 60 %-doped sample, only that for the narrow peak is shown.

located on the latter. This situation is caused by a kind of hopping accompanied with a certain activation process. Hence this hopping could be influenced by decrease in temperature.

(ii) Exchange narrowing mechanism caused by H_{exch} is enhanced at low temperatures due to a suppression of phonon vibration.

(iii) Li-doped PAS is accompanied with a Korringa-type mechanism [27] for the spin-lattice relaxation time T_1 and temperature T as is expressed by,

$$T_1 T = \text{const.} \qquad (8)$$

The combination of Eq.(8) and relationship $T_1 \approx T_2 = 2/(\sqrt{3}\,\pi\Delta H_{\text{p.p.}})$ yields the linear dependency of $\Delta H_{\text{p.p.}}$ on temperature. Here the latter equality holds for the Lorentzian lineshape, T_2 being the spin-spin relaxation time.

The saturation measurement shown in Fig. 4 suggests that the microwave energy-dissipation process in the PAS systems drastically changes at about 10 % of Li doping. Hence it is concluded that the Li-doping contributes to raise of the saturation power, suggesting the contribution of the doping to augmentation of both the spin-spin and the spin-lattice interactions.

4.4. Liberation of Li clusters. A new sharp peak ($\Delta H_{\text{p.p.}}$=0.30 G at room temperature) appeared in addition to the broad signal above the 50 %-doped level as shown in Fig. 1(e). The broader one indicated by an arrow is considered to come from the carbon π-spins as is evident from Fig. 3. The narrow spike, on the other hand, is considered to be due to metallic Li clusters since it saturates very fast, indicating highly adiabatic separation between spins and the lattice system, as the case in alkali metals. In addition, the intensity of the spike is found to be independent on temperature down to 120 K as shown in Fig. 2(e). Furthermore, 70% Li-doped PAS exhibited a lustrous silver color, reflecting the deposition of metallic Li. Relatively small g-value ($g = 2.0018$) agrees well with that of Li cluster dispersed in the methylamine solution ($g = 2.0014$-18) [28]. From $\Delta H_{\text{p.p.}}$ of this spike, the size of liberated Li cluster in the 60 % Li-doped PAS can be estimated to be about 0.1-10 μm based on the ESR results of ultrafine particles of Li [29]. The skin depth δ is expressed as follows [30]

$$\delta = (\pi\sigma\nu)^{-1/2} \qquad (9)$$

where σ and ν represent conductivity and microwave frequency, respectively. Since δ becomes 100-1000 μm, the skin effect is negligible and, hence, no Dysonian peak was observed. A typical Dysonian shape of a thick plate of Li, for instance, has been shown in ref. 31. The present observation of liberated Li clusters at 60 and 70 % Li-doped PAS completely agrees with the electrochemical data, in which the potential change was saturated [13].

5. Conclusion

The ESR analyses have been performed on the Li-doped polyacenic semiconductor (PAS) materials used as the anode in the Li rechargeable batteries in order to clarify the change in the electronic states upon the Li-doping. The present results obtained can be summarized as follows:

(1) The pristine and the Li-doped PAS have shown the ESR spectra with almost the same g-values (2.0021-2.0024) in the temperature range 5-280 K probably coming from carbon π-radical spins.

(2) In the 10 % Li-doped PAS, for instance, there has appeared Pauli-type contribution in the magnetic susceptibility in addition to Curie-type one. This signifies there occurs metallic transition from semiconducting state in the Li-doped PAS.

(3) The Li-doping above 7 molar % has caused a remarkable increase in the peak-to-peak linewidth ($\Delta H_{\text{p.p.}}$). This line broadening can be interpreted as coming from the spin-lattice relaxation based on $H_{\text{spin-orbit}}$ felt by conduction electrons when they migrate onto Li atoms.

(4) No change in $\Delta H_{\text{p.p.}}$ of the Li-doped PAS at $x < 7$ % can be considered to come from (i)competition of the exchange narrowing due to

H_{exch} and dipolar broadening due to H_{dipole} and/or (ii)insufficient spin-orbit coupling $H_{spin\text{-}orbit}$.

(5) Decrease in $\Delta H_{p.p.}$ according to temperature decrease can be due to (i)suppression for conduction electrons to migrate onto Li atoms and, in a more strict sense, (ii)restriction by Korringa rule for the conduction electrons.

(6) In the Li-doped PAS with $x > 50$ % a narrow spike has shown up in the ESR spectrum. This spike is due to liberated Li clusters, which proves that C_2Li is the highest doped stage for the PAS from the ESR viewpoint.

References

[1] For instance, *Recent Advances in Rechargeable Li Batteries*, in *Solid State Ionics*, **69** (1994).

[2] K. Sato, M. Noguchi, A. Demachi, N. Oki, and M. Endo, *Science*, **264**, 556 (1994).

[3] Y. Matsumura, S. Wang, and T. Mondori, *Carbon*, **33**, 1457 (1995).

[4] K. Tanaka, K. Ohzeki, T. Yamabe, and S. Yata, *Synth. Met.*, **9**, 41 (1984).

[5] K. Tanaka, T. Koike, T. Yamabe, J. Yamauchi, Y. Deguchi, and S. Yata, *Phys. Rev.*, **B35**, 8368 (1987).

[6] K. Tanaka, M. Ueda, T. Koike, T. Yamabe, and S. Yata, *Synth. Met.*, **25**, 265 (1988).

[7] T. Yamabe, S. Yamanaka, K. Tanaka, T. Terao, S. Maeda, and S. Yata, *Phys. Rev.*, **B37**, 5808 (1988).

[8] K. Tanaka, M. Kobashi, H. Sanekata, T. Yamabe, J. Yamauchi, and S. Yata, *Phys. Rev.*, **B43**, 8277 (1991).

[9] K. Tanaka, S. Yamanaka, T. Koike, T. Yamabe, K. Yoshino, G. Ishii, and S. Yata, *Phys. Rev.*, **B32**, 6675 (1985).

[10] See, e.g., A. Hérold, *Physics of Intercalation Compounds*, L. Pietronero and E. Tosati ed., Springer, Berlin, p.7 (1981).

[11] (a) S. Yata, H. Kinoshita, M. Komori, N. Ando, T. Kashiwamura, T. Harada, K. Tanaka, and T. Yamabe, *Proc. Symp. New Sealed Rechargeable Batteries and Supercapacitors*, Honolulu, HI, USA, Vol. **93-23**, p.502 (1993). (b) S. Yata, H. Kinoshita, M. Komori, N. Ando, T. Kashiwamura, T. Harada, K. Tanaka, and T. Yamabe, *Synth. Met.*, **62**, 153 (1994).

[12] (a) S. Yata, Y. Hato, K. Sakurai, T. Osaki, K. Tanaka, and T. Yamabe, *Synth. Met.*, **18**, 645 (1987). (b) S. Yata, K. Sakurai, T. Osaki, Y. Inoue, K. Yamguchi, K. Tanaka, and T. Yamabe, *Synth. Met.*, **38**, 185 (1990).

[13] S. Yata, Y. Hato, H. Kinoshita, N. Ando, A. Anekawa, T. Hashimoto, M.Yamaguchi, K. Tanaka, and T. Yamabe, *Synth. Met.*, **73**, 273 (1995).

[14] K. Tanaka, M. Ata, H. Kimura, and H. Imoto, *Bull. Chem. Soc. Jpn.*, **67**, 2430 (1994).

[15] See, for instance, K. Yoshizawa, K. Okahara, T. Sato, K. Tanaka, and T. Yamabe, *Carbon*, **32**, 1517 (1994).

[16] P. J. Krusic and T. A. Rettig, *J. Am. Chem. Soc.*, **92**, 722 (1970).

[17] R. W. Fessenden and R. H. Schuler, *J. Chem. Phys.*, **39**, 2147 (1963).

[18] H. Ago, K. Nagata, K. Yoshizawa, K. Tanaka, and T. Yamabe, *Carbon*, submitted.

[19] J. R. Dahn, *Phys. Rev.*, **B44**, 9170 (1991).

[20] K. Tanaka, T. Koike, H. Nishino, T. Yamabe, J. Yamauchi, Y. Deguchi, and S. Yata, *Synth. Met.*, **18**, 521(1987): In this case, the scavenging of the impurity spins has been caused by halogen molecules.

[21] K. Tanaka, S. Nishio, S. Yamanaka, T. Yamabe, and S. Yata, *Synth. Met.*, **60**, 39 (1993).

[22] R. J. Elliot, *Phys. Rev.*, **96**, 266 (1954).

[23] Y. Yafet, *Solid State Phys.*, **14**, 1 (1963).

[24] B. A. Goodman and J. B. Raynor, *Adv. Inorg. Chem. and Radio Chem.*, H. J. Emeleus and A. G. Sharpe, ed., Academic Press, NY, Vol. **13**, p.135 (1970).
[25] J. A. McMillan and T. Halpern, Based upon the wavefunctions of Charlotte Froese, *Hartree-Fock Parameters for the Atoms Helium to Radon*, Dept. Math., Univ. British Columbia (1966).
[26] K. Tanaka, M. Kobashi, H. Sanekata, T. Yamabe, J. Yamauchi, and S. Yata, *Phys. Rev.*, **B44**, 1101(1991).
[27] J. Korringa, *Physica (The Hague)*, **16**, 601 (1950).
[28] P. P. Edwards, A. R. Lusis, and M. J. Sienko, *J. Chem. Phys.*, **72**, 3103 (1980).
[29] S. Sako, J. *Phys. Soc. Jpn.*, **59**, 1366 (1990).
[30] F. J. Dyson, *Phys. Rev.*, **98**, 349 (1955).
[31] G. Feher and A. F. Kip, *Phys. Rev.*, **98**, 337 (1955).

Chapter 2

ESR Study of Alkali-Doped PAS Material Prepared by Thermal Decomposition of Azide

1. Introduction

The electronic as well as the structural properties of amorphous carbon materials prepared by pyrolytic treatment have been well known to depend strongly on the starting material and the treatment condition such as heat treatment temperature (T_p) and reaction atmosphere [1,2]. It has been investigated the air-stable polyacenic semiconductor (PAS) materials prepared from phenol-formaldehyde (PF) resin at relatively low temperatures (500-900°C) [3] with a variety of experiments such as the electrical transport [4], thermoelectric power [4], electron spin resonance (ESR) [5], x-ray diffraction [6], ^{13}C nuclear magnetic resonance (NMR) [7], and magnetic susceptibility [8] measurements.

It was clarified that PAS materials can be doped with both p- and n-type dopants (I_2 and Na), resulting in an increase in the electrical conductivity [3]. This effect is more obvious in the lower T_p samples and a maximum increase in the electrical conductivity by 11 orders of magnitude was obtained [4]. Another important feature of PAS materials lies in an amorphous and incomplete structure compared with that of graphite. The interlayer spacing of PAS material becomes 3.7-4.4 Å [6], being larger than that of graphite (3.35 Å) [9].

Making use of these characteristics of the PAS material, application to the electrode of the lithium rechargeable battery has been extensively examined. Owing to the loose structure and n-type doping ability, an extraordinary high capacity of 1100 mAh/g corresponding to C_2Li ([Li]/[C]=0.5) has been achieved without liberation of lithium metals [10,11]. Note that the maximum composition achieved by graphite (Li-GIC) has been known as C_6Li ([Li]/[C]=0.17) corresponding to the capacity of 372 mAh/g under ambient condition [12]. Nowadays, two types of PAS batteries are commercialized and used in a variety of electronic devices [13]. One is the battery using PAS for the both cathode and anode and another consists of PAS cathode and Li-predoped PAS anode. The latter-type battery is more useful because it shows higher voltage (3.3 V) than the former. Since the predoping procedure indispensable in the latter type has been carried out by the laborious electrochemical method, an alternative simple doping method is strongly desired.

In this study we have employed the PAS material prepared at 680 °C with [H]/[C] molar ratio of 0.22, because it has been confirmed that this PAS is preferable to the anode of the Li rechargeable battery [10,11]. It has been shown that the PAS treated at this temperature possesses two kinds of spins [4,5]: (i) the unpaired spins in small graphitized fractions due to incomplete carbonization process and (ii) the delocalized conduction electrons arising from the p-type or n-type doping. In this connection, systematic study of the change in the natures of these spins introduced by the doping with different n-type dopants would be of great interest.

In the present chapter we attempt to dope the PAS material with four kinds of alkali metals (Li, Na, K, and Rb) based on the decomposition of a series of alkali azides (AN_3) and investigate the change in the electronic structure with respect to the alkali metal species based on detailed ESR study.

This kind of doping method has been applied to amorphous carbon materials for the first time. Based on the same method, the alkali metal doped C_{60} has been successfully prepared [14,15] and substantial improvement in the superconducting volume fraction compared with the sample conventionally doped in the gas-phase metal has been reported [14]. This method is very simple and possibly applied to Li-predoping of the PAS anode. We will demonstrate that PAS material can be doped with alkali metal and that the ESR linewidth is significantly influenced by the dopant metal species as well as by temperature.

2. Experimental

PAS material was essentially prepared by the pyrolytic treatment of phenol-formaldehyde (PF) resin at 680 °C in a non-oxidative atmosphere as described in our previous paper [3]. The PAS sample in the present study has the molar ratio [H]/[C]=0.22 with the electrical conductivity $\sigma=2.7\times10^{-3}$ S/cm [10]. Lithium and sodium azides (LiN_3, NaN_3) were purchased from Eastman Kodak and Nacalai Tesque, respectively, and used without further purification. Potassium and rubidium azides (KN_3, RbN_3) were prepared from the alkali hydroxide (AOH), hydrazine hydrate, and butyl nitrate, according to ref. 16 and were purified by the precipitation. Their thermal properties except for LiN_3 have been discussed in ref. 17.

The mixture of AN_3 and the PAS sample was placed in a quartz tube and heated slowly up to the decomposition temperature of AN_3 (see Table 1) *in vacuo*. The initial amount of AN_3 did not necessarily determine the final [A]/[C] ratio of the doped PAS. This is a quite different feature from the electrochemically doped PAS materials, in which the doping amount is well controllable [10]. Hence several numbers of the doped PAS samples

starting from different amounts of AN_3 (0.05-0.50 for the nominal [A]/[C] ratios) for each A were prepared, and the ESR data with the largest $\Delta H_{p.p.}$ could be adopted because the largest $\Delta H_{p.p.}$ is presumed to reflect the maximum doping degree [18].

Decomposition of AN_3 was monitored by generation of nitrogen gas which deteriorates the vacuum. After the decomposition was completed, the sample was cooled down to room temperature and subjected to the ESR measurement (X-band). The main ESR spectra were recorded on a JEOL TE200 spectrometer with Oxford cryogenic system down to 1.8 K. The g-values and $\Delta H_{p.p.}$ were determined using a Mn^{2+}-MgO solid solution. The spin concentration (N_s) at room temperature was determined using JEOL RE-2X spectrometer equipped with JEOL ESPRIT 330 data processing system using $CuSO_4 \cdot 5H_2O$ as a reference. Temperature dependence of the spin intensity was estimated based on $I_p \Delta H_{p.p.}^2$, where I_p stands for the peak height. The error of this quantity was estimated to be ±12 % by the comparison with the N_s determined by ESPRIT 330 in the range of 120-300 K.

3. Results and Discussion

3.1. Decomposition of alkali azide. An alkali azide molecule AN_3 decomposes into alkali metal and nitrogen at a certain decomposition temperature (T_d) as described [17],

$$2AN_3 \rightarrow 2A \text{ (melting)} + 3\ N_2 \uparrow \qquad (1)$$

Hence pure alkali metal can be obtained with successive doping if the mixture of AN_3 and PAS is heated under vacuum. For instance, one can see clear

decomposition reactions from the pressure profiles of LiN_3 and NaN_3 used doping shown in Fig. 1. The nature of the two main peaks observed only in the Li-doping procedure is not clear although it was found that the Li-doping was completed after both peaks appeared. The data of T_d and the melting temperature (T_m) as well as the ESR results are listed in Table 1. Since T_d of each azide is much higher than the corresponding T_m except for LiN_3, the generated metal is expected to instantaneously disperse into the PAS

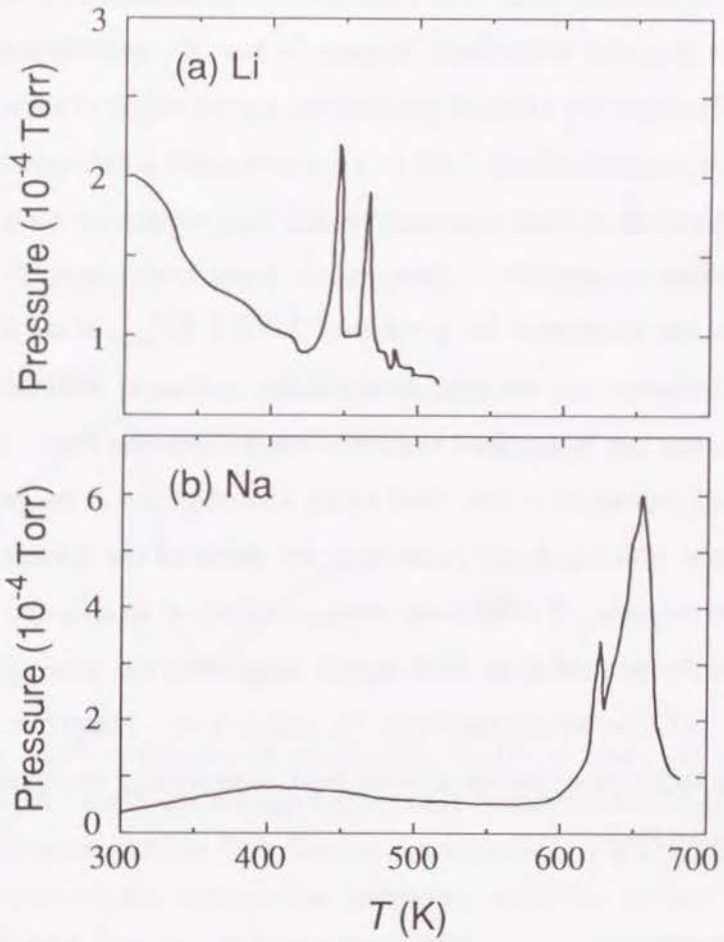

Figure 1. The pressure profiles of (a) LiN_3- and (b) NaN_3-used doping processes. Decomposition reactions deteriorate the vacuum.

micropores. In the case Li-doped sample, a reddish brown deposition was observed due to the following side reaction,

$$3\,LiN_3 \rightarrow Li_3N + 4\,N_2\uparrow \qquad (2)$$

because lithium metal is very reactive with nitrogen especially at high temperature [20].

The ESR shapes of the alkali-doped PAS are displayed in Fig. 2 along with that of the pristine PAS. Quite narrow signals indicated by the arrows appear as the shoulder to the broad signals for Na-, K-, and Rb-doped PAS samples. There are two kinds of possibilities for the origin of these narrow peaks: (i) non-reacted pristine PAS or (ii) non-reacted alkali metal cluster. The latter should show Pauli-type temperature dependence, i.e. temperature-independent spin susceptibility. Temperature dependence check [21] for the narrow peak has confirmed the g-value of 2.0022, $\Delta H_{p.p.}$ of ca. 0.3G and Curie-type behavior, i.e. the spin susceptibility increases with decreasing temperature, that can be ascribed to the non-reacted pristine PAS. Lustrous silver-colored deposition of the alkali metal was observed at the portion of the quartz tube which is much colder than the inside of the furnace and far from the sample area. Furthermore, decomposition of alkali azide without the PAS sample resulted in no ESR signal, suggesting the generated alkali metal in the hot area would react with the quartz tube. Hereafter, we will focus on the behavior of the broad ESR peak representing the spin state of the alkali-doped PAS.

3.2. Z dependence. ESR spectrum of the pristine PAS is almost identical to that of the Li-doped PAS as shown in Table 1 and Fig. 1. The g-value of the pristine suggests that the spins are of π-nature derived from

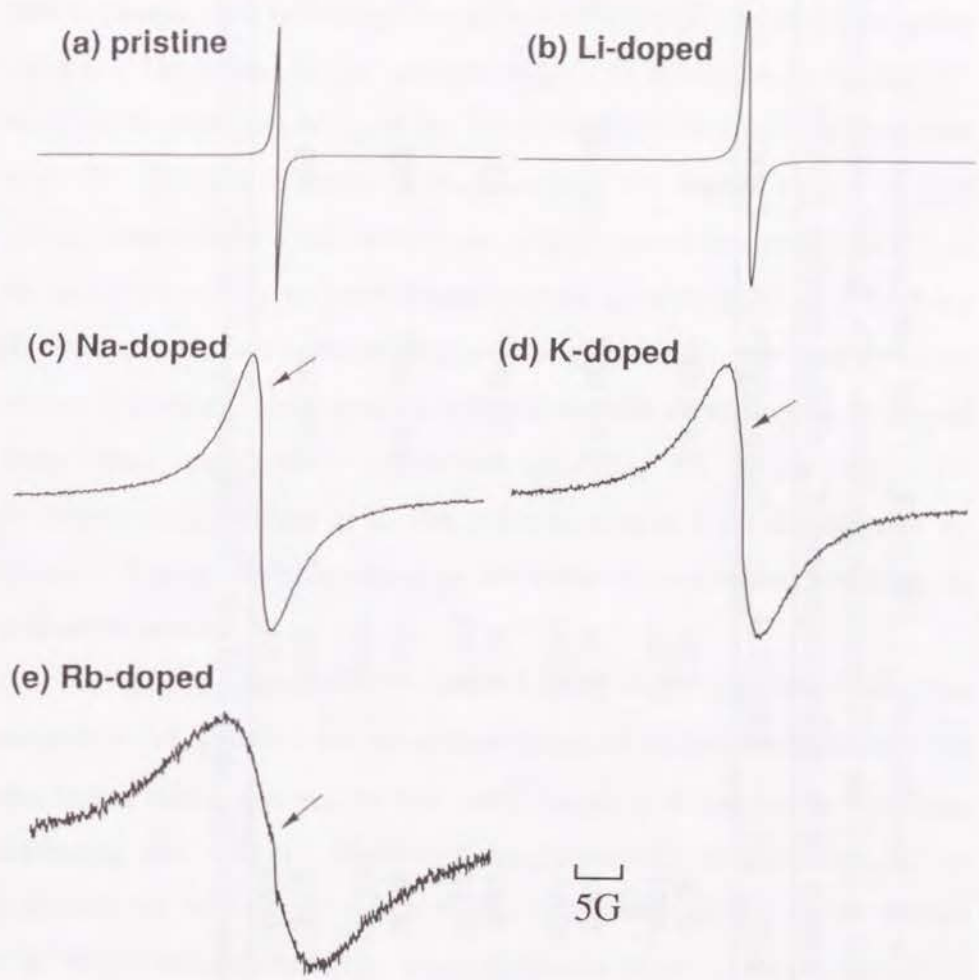

Figure 2. ESR lineshapes of (a) pristine, (b) Li-, (c) Na-, (d) K-, and (e) Rb-doped PAS materials at room temperature measured at X-band. Arrows indicate the peaks coming from the non-reacted pristine PAS (see text). The field modulation and microwave frequency were 0.1 G and 9.1 GHz, respectively.

Table 1. The g-value, peak-to-peak linewidth ($\Delta H_{p.p.}$), $\Delta H_{1/2}/\Delta H_{p.p.}$,[a] and spin concentration (N_s) of alkali-doped PAS samples. The data measured at 1.8 K are indicated in the parentheses. The decomposition temperature (T_d) of mixture of alkali azide and PAS material and the melting temperature (T_m) of alkali metal are also shown.

	g-value	$\Delta H_{p.p.}$ (G)	$\Delta H_{1/2}/\Delta H_{p.p.}$[a]	N_s (spins/g-PAS)	T_d (K)	T_m (K) [b]
pristine	2.0022	0.26	2.53	2.4×10^{19}	-	-
	(2.0022)	(0.27)	(2.20)			
Li	2.0022	0.44	3.31	2.5×10^{19}	446, 467	454
	(2.0023)	(0.36)	(3.15)			
Na	2.0022	2.47	3.50	1.3×10^{19}	651	371
	(2.0022)	(0.32)	(2.57)			
K	2.0022	4.38	3.07	1.9×10^{19}	732	336
	(2.0023)	(0.33)	(3.42)			
Rb	2.0023	8.74	2.80	1.9×10^{19}	739	312
	(2.0025)	(0.96)	(2.94)			

[a] Lorentzian and Gaussian lineshapes give the values 2.40 and 1.92, respectively, where $\Delta H_{1/2}$ is the half-height linewidth.
[b] From Ref. 17.

carbon atoms as usual [5]. Alkali-doped PAS materials showed almost similar g-values to that of the pristine, which suggests the alkali-doped PAS also have π-type spins. Moreover, in the doped state, $\Delta H_{p.p.}$ of the broad peak increases with increasing the atomic number (Z) of the dopant metal species. The actual doping amount [A]/[C] is estimated to be 0.05-0.1 based on the observed $\Delta H_{p.p.}$ of the Na-doped PAS material in the previous work [5]. The rest of the metal from azide, if any, should react with ESR tube or deposit as the alkali metal at the cold portion of the quartz tube except for the Li-doping. It has been recognized that in the range [A]/[C]=0.05-0.1 all the localized spins in the pristine are scavenged and conduction electrons are newly generated in the graphitized fractions with occupying the density of states corresponding to the conduction band [5]. On the contrary to the electrochemical method [11], the achievement of high doped state by chemical doping methods including the azide decomposition seems to be difficult at present.

In Fig. 3 is plotted $\Delta H_{p.p.}$ versus Z value of the dopant metal. The increase in $\Delta H_{p.p.}$ with Z reveals enhancement of the relaxation through the spin-lattice interaction via the spin-orbit coupling of conduction electrons depending on Z. That is, these new conduction electrons are supposed to delocalize not only on the π-AOs of the carbon skeleton but on the dopant atom with a finite probability. Little difference in $\Delta H_{p.p.}$ between the ESR lineshapes of the pristine and the Li-doped PAS could be ascribed to a small spin-orbit coupling constant of Li (ζ_{Li}=0.2 cm^{-1}, while ζ_{Na} and ζ_K are 11 and 38 cm^{-1}, respectively) [22]. The $\Delta H_{p.p.}$ is almost proportional to $Z^{1.2}$, being different from the Z-dependency observed in the alkali-doped polyacetylene ($Z^{2.3\text{-}4.0}$) [18,23] and the alkali-doped C_{60} (Z^4) and graphite (Z^4) [24,25]. This relationship was considered to come from the fact that spin-orbit coupling constant ζ is almost proportional to Z^4 [26].

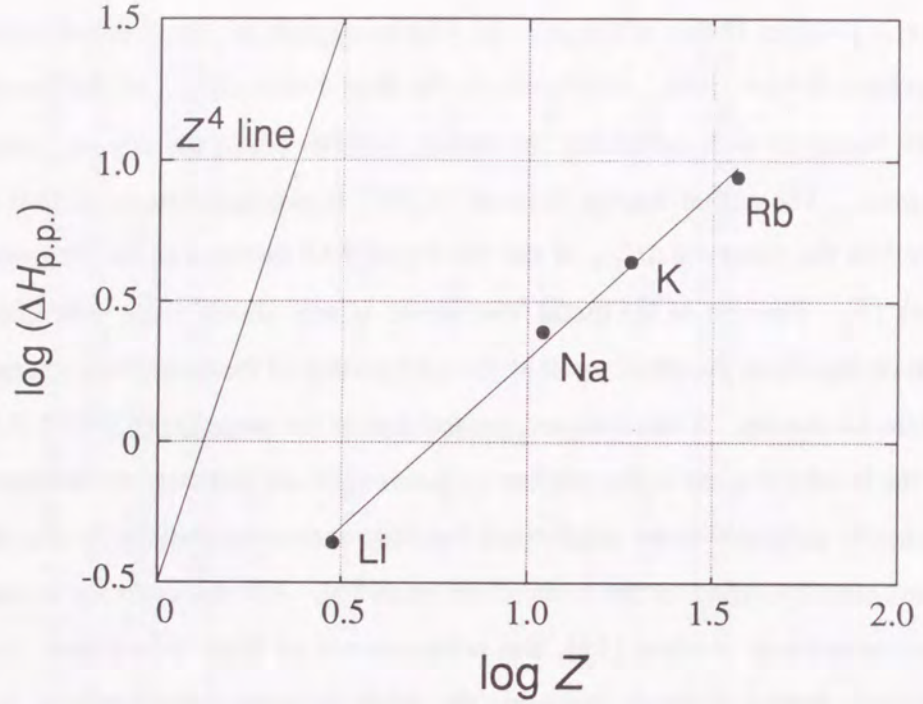

Figure 3. Plot of peak-to-peak linewidth ($\Delta H_{\mathrm{p.p.}}$) vs. the atomic number (Z) of the dopant metal measured at room temperature. Fitted line is drawn for the understanding of the deviation from Z^4 line.

Several reasons accounting for the smaller exponential factor observed in the present study are considered: (i) The doping is insufficient due to the side-reactions or deposition of the alkali metal. It has been reported that the unsaturated doped state gives a smaller exponential factor than 4 [18]. (ii) Steric hindrance for atoms with larger Z to be effectively doped on account of the microporous structure of the PAS material [27] can be presumed. Note that ionic radius of Rb^+ (1.49 Å) is about three times larger than that of Li^+ (0.59 Å) [28]. (iii) Difference in ionization potentials of the alkali metals could also be a cause. For instance, the ionization potentials of Li and Rb are 5.39 and 4.18 eV, respectively [29]. The probability for electrons to

locate on the dopant or, in other words, the spin-orbit coupling could be larger in the atoms with smaller Z. (iv) The exact expression of ζ is written for alkali atom with the principle quantum number n as [30],

$$\zeta(n,l) = \frac{e^2\hbar^2}{m^2c^2a_0^2}\,\frac{Z^4}{n^3\,l\,(2l+1)\,(l+1)} \qquad (3)$$

where a_0 and l are the Bohr radius and the orbital angular momentum quantum number, respectively. Therefore, n reduces the apparent exponential factor approximately down to $\zeta \propto Z^{2.3}$.

3.3. Temperature dependence. Temperature dependence of $\Delta H_{\mathrm{p.p.}}$ of each alkali-doped sample is plotted in Fig. 4. A linear decrease of $\Delta H_{\mathrm{p.p.}}$ with decrease in temperature is observed in Na-, K-, and Rb-doped samples and $\Delta H_{\mathrm{p.p.}}$ values of all the samples converge at 1.8 K. The temperature dependence obtained here suggests the following two factors. Firstly, there is a certain activation process for the electron hopping between graphitized fragments and alkali metals on which the spin-orbit coupling works to cause the linewidth broadening. Secondly a Korringa-type mechanism [31] involving the magnetic interaction between a conduction spin and the fluctuation of its surrounding magnetic momentum can work in the present system. This mechanism is represented by,

$$T_1T = \text{const.} \qquad (4)$$

where T_1 and T are spin-lattice relaxation time and temperature, respectively. When the sample has an ESR lineshape accompanied by a strong exchange

narrowing, T_1 becomes almost equal to spin-spin relaxation time (T_2). The expression of T_2 is given for the sample with a Lorentzian lineshape,

$$T_2 = \frac{2}{\sqrt{3}\,\pi \Delta H_{\text{p.p.}}} \tag{5}$$

Thus a linear dependency of $\Delta H_{\text{p.p.}}$ on T can be derived based on Eqs.(4) and (5). Note that the above two discussions are irrespective of Z.

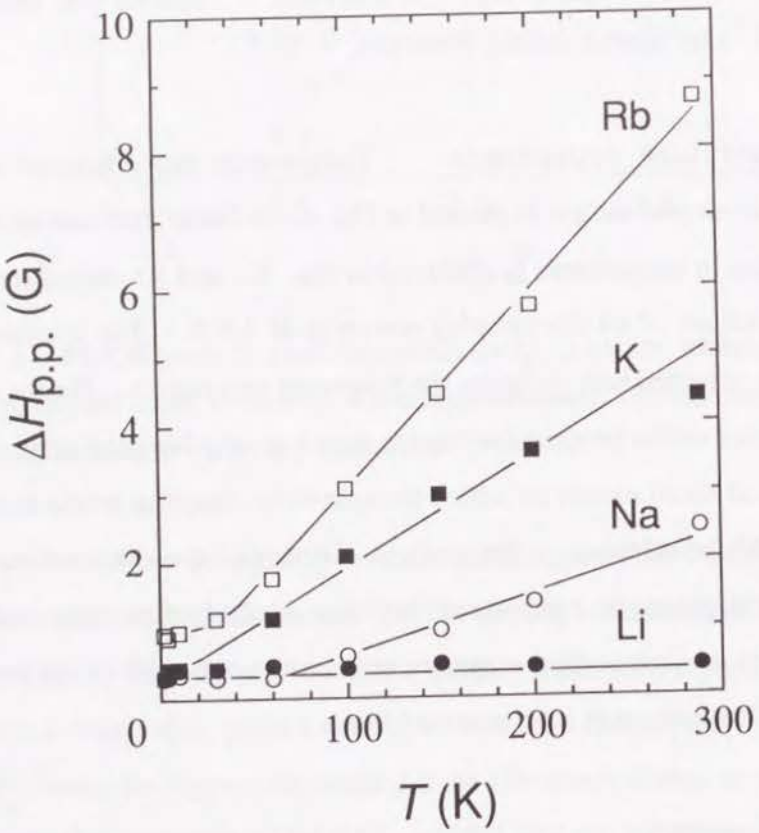

Figure 4. Temperature dependence of $\Delta H_{\text{p.p.}}$ of Li- (closed circles), Na- (open circles), K- (closed squares), and Rb- (open squares) doped PAS samples. The lines are guides for the eye.

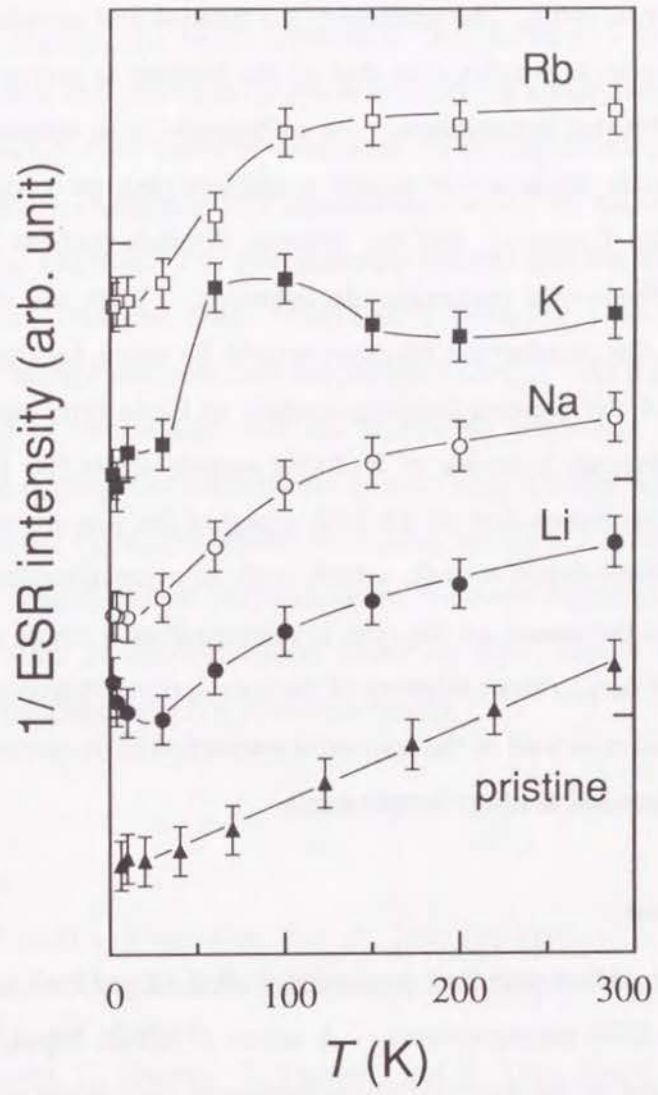

Figure 5. Temperature dependence of the reciprocal ESR intensity $1/(I_{\text{p}}\Delta H_{\text{p.p.}}{}^2)$, where I_{p} stands for the peak height. Triangles indicate the data of the pristine PAS sample and for other symbols see Fig. 4. The lines are guides for the eye.

Temperature dependence of the reciprocal ESR intensity ($1/(I_p \Delta H_{p.p.}{}^2)$) is plotted in Fig. 5 together with the data of the pristine for comparison. Data of the pristine shows linear correlation arising from the simple Curie-type spins. The gradient of the alkali-doped sample, except for the K-doped one, is smaller than that of the pristine at above 100 K but increases under that temperature. At sufficiently high temperature, e.g. room temperature, the newly generated conduction electron delocalizes over the graphitized fragments and the dopants through thermal excitation, resulting in Pauli-type paramagnetic behavior. With the decrease in temperature, the conduction electron would be more localized due to suppression of the thermal hopping leading to Curie-type paramagnetic behavior. Unusual behavior of K-doped sample at 50-100 K could be ascribed to superimposition of the ESR signal of the non-reacted pristine PAS on the alkali-doped π-peak, which leads to overestimation of the I_p. The change in the nature of the spin is consistent as a whole with the T dependence of $\Delta H_{p.p.}$, since hopping of the conduction electron responsible for metallic nature as well as the spin-orbit interaction in the present samples should be suppressed at lower temperatures.

4. Conclusion

We have studied electronic properties of alkali-doped PAS materials by means of the ESR measurements. A series of alkali doping has been performed based on the thermal decomposition of each alkali azide for the present analysis. Although the side reactions or deposition of alkali metals took place, a clear increase of the ESR linewidth depending on the atomic number of alkali metal has been observed ($\Delta H_{p.p.} \propto Z^{1.2}$). This relationship suggests the spin-orbit interaction felt by the conduction electron migrating

on alkali metal plays a crucial role in determining $\Delta H_{p.p.}$. Such migration ought to be assisted by a kind of hopping from graphitized fragments. The above small exponential factor (1.2) would be explained in terms of (i) insufficient doping, (ii) steric hindrance, (iii) difference of ionization potential, and/or (iv) principle quantum number, of alkali metals. Linear decrease in $\Delta H_{p.p.}$ on T could be elucidated by the suppression of hopping of the conduction electron at low temperatures and/or by Korringa rule for the conduction electron. The ESR intensity showed that the dominant spin characteristics changes from Pauli- to Curie-type with decreasing temperature, being consistent with the change in $\Delta H_{p.p.}$. As for the attempt of Li-doping in connection with the predoping procedure of the PAS electrode, the doping was not sufficiently achieved probably due to the side reaction forming Li_3N. However, the Li_8C_{60} complex has been obtained based on the present method [15] and, hence, we could expect that additional techniques, such as decomposition under Ar flow, would bring about successful Li-doping, which is now under study.

References

[1] R. E. Franklin, *Proc. Roy. Soc. A.*, **209**, 196 (1951).

[2] D. E. G. Austen, D. J. E. Ingram, and J. G. Tapley, *Trans. Faraday Soc.*, **54**, 400 (1958).

[3] K. Tanaka, K. Ohzeki, T. Yamabe, and S. Yata, *Synth. Met.*, **9**, 41 (1984).

[4] K. Tanaka, S. Yamanaka, T. Koike, T. Yamabe, K. Yoshino, G. Ishii, and S. Yata, *Phys. Rev.*, **B32**, 6675 (1985).

[5] K. Tanaka, T. Koike, T. Yamabe, J. Yamauchi, Y. Deguchi, and S. Yata, *Phys. Rev.*, **B35**, 8368 (1987).

[6] K. Tanaka, M. Ueda, T. Koike, T. Yamabe, and S. Yata, *Synth. Met.*, **25**, 265 (1988).
[7] T. Yamabe, S. Yamanaka, K. Tanaka, T. Terao, S. Maeda, and S. Yata, *Phys. Rev.*, **B37**, 5808 (1988).
[8] K. Tanaka, M. Kobashi, H. Sanekata, T. Yamabe, J. Yamauchi, and S. Yata, *Phys. Rev.*, **B43**, 8277 (1991).
[9] See, e.g., A. Hérold, *Physics of Intercalation Compounds*, L. Pietronero and E. Tosatti ed., Springer. Berlin, p. 7 (1981).
[10] S. Yata, H. Kinoshita, M. Komori, N. Ando, T. Kashiwamura, T. Harada, K. Tanaka, and T. Yamabe, *Synth. Met.*, **62**, 153 (1994).
[11] S. Yata, Y. Hato, H. Kinoshita, N. Ando, A. Anekawa, T. Hashimoto, M. Yamaguchi, K. Tanaka, and T. Yamabe, *Synth. Met.*, **73**, 273 (1995).
[12] J. R. Dahn, T. Zheng, Y. Liu, and J. S. Xue, *Science*, **270**, 590 (1995).
[13] (a) S. Yata, Y. Hato, K. Sakurai, T. Osaki, K. Tanaka, and T. Yamabe, *Synth. Met.*, **18**, 645 (1987). (b) S. Yata, K. Sakurai, T. Osaki, Y. Inoue, K. Yamguchi, K. Tanaka, and T. Yamabe, *Synth. Met.*, **38**, 185 (1990).
[14] M. Tokumoto, Y. Tanaka, N. Kinoshita, T. Kinoshita, S. Ishibashi, and H. Ihara, *J. Phys. Chem. Solids*, **54**, 1667 (1993).
[15] K. Imaeda, K. Yakushi, and H. Inokuchi, *Fullerene Sci. and Tech.*, **3**, 545 (1995).
[16] M. W. Miller and L. F. Audrieth, *Inorganic Syntheses*, **3**, 139 (1950).
[17] A. W. Browne, *Inorganic Syntheses*, **1**, 79 (1939).
[18] P. Bernier, F. Rachdi, A. E. Khodary, and C. Fite, *Synth. Met.*, **24**, 31 (1988).
[19] *Lange's Handbook of Chemistry*, 11th ed., J. A. Dean ed., McGraw Hill, NY (1973).
[20] For instance, W. Mellor, *Mellor's Comprehensive Treatise on Inorganic and Theoretical Chemistry*, Vol II. supplement II. Longmans, London, p. 77 (1961).
[21] A. M. Alquié, C. Taupin, and A. P. Legrand, *Comptes Rendus, Serie B, Acad. Sci.*, **272**, 973 (1971).

[22] (a) B. A. Goodman and J. B. Raynor, *Adv. Inorg. Chem. and Radio Chem.*, Vol. 13, H. J. Emeleus and A. G. Sharpe ed., Academic Press, NY, p. 135 (1970). (b) J. A. McMillan and T. Halpern, *Hartree-Fock Parameters for the Atoms Helium to Radon*, Dept. Math., Univ. British Columbia (1966).
[23] F. Rachdi and P. Bernier, *Phys. Rev.*, **B33**, 7817 (1986).
[24] J. Conard, A. Messaoudi, F. Beguin, and V. Nalimova, *J. Phys. Chem. Solids*, **55**, 787 (1994).
[25] P. Lauginie, A. Messaoudi, and J. Conard, *Synth. Met.*, **55-57**, 3002 (1993).
[26] Y. Yafet, *Solid State Phys.*, **14**, 1 (1963).
[27] S. Yata, Y. Hato, S. Nagura, K. Tanaka, and T. Yamabe, *Proceedings of 44th Meeting of the Society of Polymer Science, Jpn.*, IIE10, March, Yokohama (1995).
[28] R. D. Shannon and C. T. Prewitt, *Acta Crystallogr.*, **B25**, 925 (1969).
[29] C. E. Moore, *Atomic Energy Levels*, Natl. Bur. Stand. (U.S.) Circ., 467, Vol. I-III (1949-1958).
[30] See, for instance, S. Takagi, *Quantum Mechanics II*, Iwanamj-Koza (in Japanese), H. Yukawa, K. Inoue, and T. Toyoda ed., Iwanami, Tokyo, p. 72 (1972).
[31] J. Korringa, *Physica (The Hague)*, **16**, 601 (1950).

Chapter 3

^{7}Li NMR Study of Li-Doped PAS Material

1. Introduction

In recent years, studies on carbon materials not only from the physical (such as, mechanical, structural, and adsorptive) properties but also from the electronic properties have been energetically performed, accompanying by discovery of striking electronic properties of fullerenes [1]. Pyrolyzed carbon materials have now been attracting a great deal of interests in the application to anode material of the lithium rechargeable battery, because some carbon materials can incorporate a large number of Li ions and this opens up a new type of the high capacity anode material [2-6]. Although Li metal itself is a good anode material, Li dendrites, which possibly leads to short circuit with taking fire, often grows on the surface of Li metal. Carbon material prevents Li dendrites and, at the same time, show good reversibility and long cycle life together with high capacity. In spite of a number of researches, the Li doping and storage mechanisms are still subjects of controversy on account of their disordered structures [5-8].

It has been intensively studied structural and electronic properties of polyacenic semiconductor (PAS) materials prepared by the thermal pyrolysis of phenol-formaldehyde resin at relatively low temperature range (500-1000

°C) in an inert gas [9-14]. The PAS materials have longer interlayer distance (3.7-4.2 Å) compared with that of graphite (3.35 Å) and can be doped by both the p- and n-type dopants [9,10,13]. Owing to such specific features, the PAS material prepared at 680 °C exhibits highly Li-doped C_2Li state (corresponding to capacity of 1100 mAh/g), without liberation of Li clusters [3,15]. This C_2Li state contains much larger amount of Li atoms than that of graphite (C_6Li state, 372 mAh/g) [3]. Such a high Li-doping ability of the PAS material is of great interest not only from engineering but also from fundamental view points. However, all the Li dopants in the PAS material are not available in the charging-discharging cycle of the battery, and a considerable amount of Li atoms remain in the PAS material even after full undoping [3], which we call residual Li atoms hereafter. This irreversible capacity of the PAS material originating in residual Li atoms reaches 250 mAh/g corresponding to 23 % of the full capacity [15]. It is, therefore, important to know whether this irreversible capacity can be reduced or not, in addition to substantial understanding of Li doping and storage mechanisms.

For these reasons, X-ray diffraction (XRD) [3], X-ray photoelectron spectroscopy (XPS) [3], and electron spin resonance (ESR) [16] analyses have been carried out for the Li-doped PAS samples and have obtained several interesting features: (i) In contrast with Li-graphite intercalation compound (Li-GIC), the interlayer distance is reduced by Li-doping from 4.2 Å to 4.0 Å [3]. (ii) Nature of the Li dopant changes from fully ionized state (Li^{1+}) to partially ionized state ($Li^{\delta+}$: $0<\delta<1$) with proceeding of the doping [3]. (iii) Conduction electrons undergo the spin-orbit interaction by Li dopants [16].

It is quite valuable to investigate ^7Li nuclear magnetic resonance (NMR), because NMR shift provides direct and precise information on the effective local field at the nucleus under study. Moreover, the spin-lattice

relaxation time T_1 can signify dynamic behavior of the nucleus. Several groups have reported on the ^7Li NMR spectra of Li-doped carbon anode materials and shown that the NMR signal strongly depends on the starting material as well as the heat-treatment temperature of the carbon material [5,17-19].

In the present paper we have studied ^7Li NMR of the Li-doped PAS material. The NMR shift and T_1 value are investigated with respect to the Li-doping amount. It is presented that the NMR signal consists of only one component based on the relaxation measurement and that the shift comes from the Fermi contact interaction between a Li nucleus and conduction electrons. Results of the over-doped and the undoped samples are also discussed.

2. Experimental

2.1. Sample preparation. The PAS material employed in the present study was prepared by the pyrolytic treatment of phenol-formaldehyde resin at 680 °C in a non-oxidative atmosphere. The [H]/[C] atomic ratio and the electrical conductivity of the PAS material are 0.22 and 2.7×10^{-3} S/cm, respectively.

For electrochemical Li-doping, black powdered PAS material was fabricated into the sheet-shaped electrode by adding 10 % of polyvinylidene fluoride. The doping was carried out by using a rectangular cell consisting of PAS electrode, Li metal as the counter electrode, and solution of 1M $LiPF_6$ in propylene carbonate as the electrolyte. The Li-doping amount, x (%), was controlled by coulometry according to the following equation,

$$x\,(\%) \equiv \frac{[\mathrm{Li}]}{[\mathrm{C}]} \times 100 = \frac{3.6Q(12+r)}{96500} \times 100 \qquad (1)$$

where Q (in mAh/g) is the amount of transferred charge and r the [H]/[C] atomic ratio of the PAS material (0.22 in the present study). After a doping process, the sample was washed by dimethoxyethane and thoroughly evacuated. The doping and sample transfer into an NMR tube were carefully conducted in dry argon atmosphere. About 300 mg of Li-doped PAS sample was sealed in a pyrex tube *in vacuo* for the NMR measurements.

2.2. NMR measurements. NMR experiments were carried out on a modified JEOL GSX-200 spectrometer operating at a resonance frequency of 77.64 MHz for ^{7}Li nucleus. The radio-frequency field strength was about 113 kHz. T_1 measurement was made by the inversion recovery method. The ^{7}Li chemical shifts were calibrated in ppm relative to 1M LiCl solution as an external reference standard.

3. Results and Discussion

3.1. Knight shift. The ^{7}Li NMR spectra and their data at room temperature for several doping degrees are shown in Fig. 1 and Table 1, respectively. Undoped (30→10 %: doped to 30 % and then undoped to 10 %) sample was also surrendered to the NMR measurement. All the samples showed a broad signal at -2~9 ppm with respect to that of LiCl reference. Moreover, in the over-doped (60 %) sample, a very small signal was observed at 265 ppm in addition to the main peak. While other carbon materials indicate multi-peaks with two or three components which are assigned to the Li nuclei located at the different positions [5,17], PAS samples showed the single broad peak except for the 60 %-doped sample.

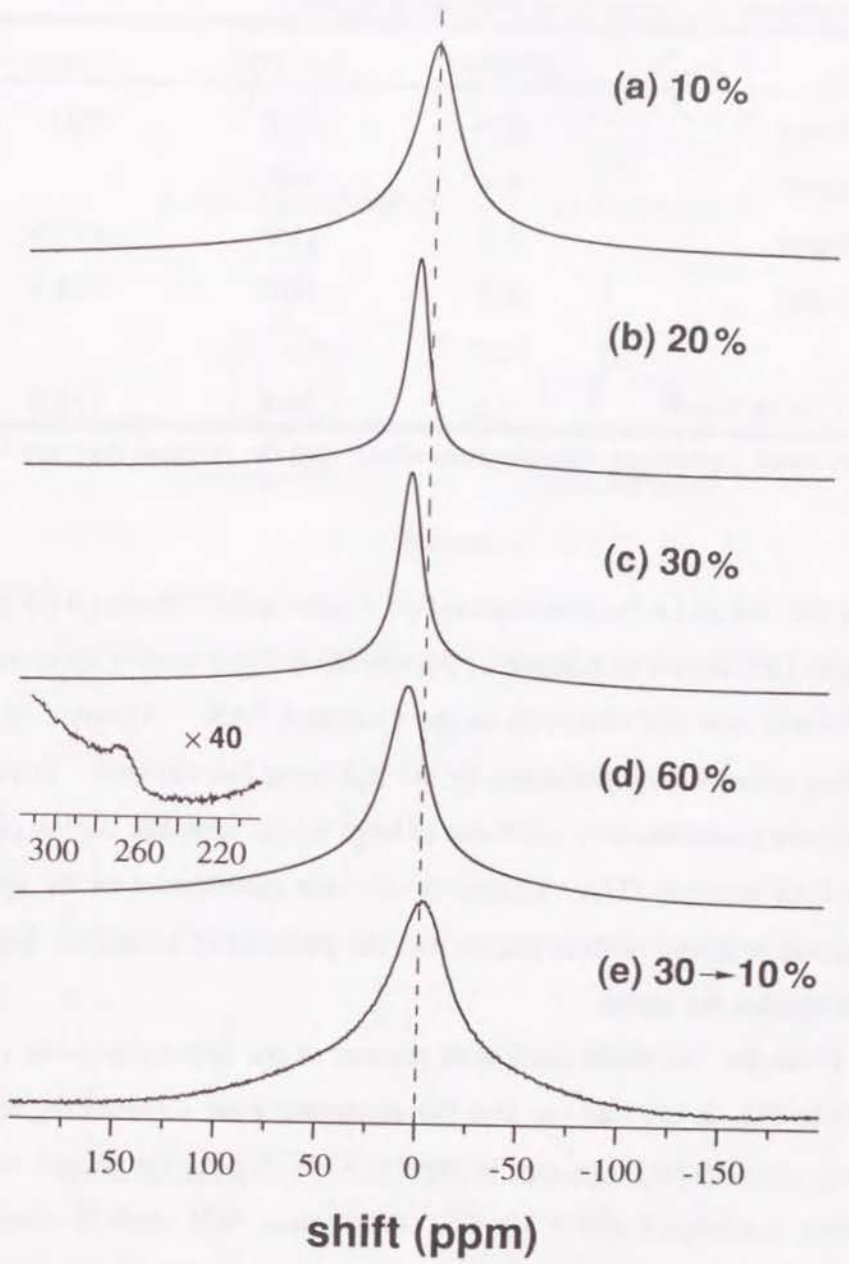

Figure 1. ^{7}Li NMR spectra of (a)10 %-, (b)20 %-, (c)30 %-, (d)60 %-doped, and (e)30→10 %-undoped samples measured at room temperature. The 1 M LiCl solution was employed as an external standard.

Table 1. ^{7}Li NMR shift (δ), half-height linewidth ($\Delta\nu$), and spin-lattice relaxation time (T_1) of the Li-doped PAS samples.

Samples	δ (ppm)	$\Delta\nu$ (Hz)	T_1 (msec)
10%-doped	-0.4	2200	99.0
20%-doped	6.4	900	
30%-doped	8.3	1100	197.9
60%-doped	8.7	2400	249.1
	260[a]	-	
30 → 10%-undoped	-1.5	3000	158.6

[a]A very small signal was also observed along with the original one (see Fig. 1 (d)).

Unlike the case of Li-cyclopentadienyl (-8.4 ppm) and Li-fluorenyl (-7 ppm) solutions [20] shown in Scheme 1, the shielding effect caused by aromatic ring current was not observed in the Li-doped PAS. Absence of this shielding effect can be explained by the following two reasons. First, the ring current is considerably small due to large size of aromatic carbon planes in the PAS material [21]. Second is the wide distribution of the size of condensed aromatic carbon planes and the position of Li atoms, both of which broaden the signal.

From the ^{7}Li NMR shift with respect to the doping amount x (%) shown in Fig. 2, one can see that the electronic state surrounding the Li nucleus considerably changes in the 10-30 % doping range and that it becomes unchanged above 30 %. This lower field shift is plausibly explained in terms of the Fermi contact interaction between a Li nucleus and conduction electrons, that is, the Knight shift (K_s) of the Li nucleus described as [22],

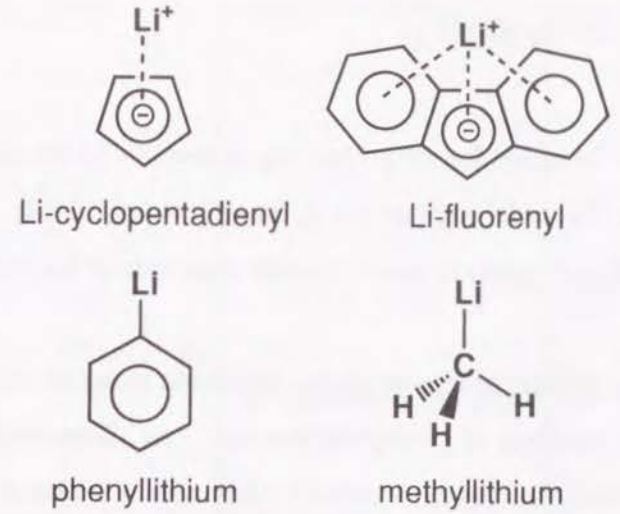

Scheme 1

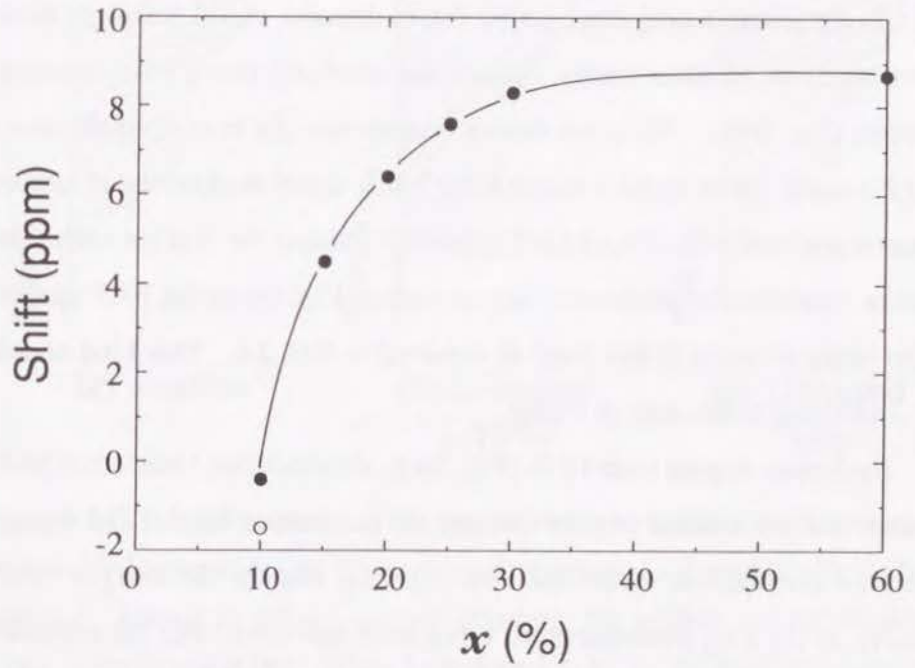

Figure 2. Line shift plotted vs. the Li concentration, x(%). Doped and undoped samples are shown in the closed and open circles, respectively. The line is a guide for eye.

$$K_s = \frac{8\pi}{3}\left\langle |\psi(0)|^2 \right\rangle \chi_s \qquad (2)$$

where $<|\psi(0)|^2>$ stands for the probability of location of the electron near the Fermi energy (E_F) at Li nucleus and χ_s the spin susceptibility. Note that the observed shift (~9 ppm) is much smaller than that of Li metal (260 ppm) [23].

Let us consider the change in the electronic structure of Li-doped PAS material as a function of Li-doping amount. As illustrated in Fig. 3, the pristine PAS material has the localized states within the band gap due to the amorphous structure. These localized states are supposed to consist of the unpaired electrons with π-nature in the condensed aromatic carbon planes [12]. In the initial doping stage ($x \leq 10$ %), Li dopants would scavenge these defect levels or, in other words, occupy the localized states with donating electrons (Fig. 3(b)). Since the carrier density near E_F is reasonably small and Li is supposed to be fully ionized, the NMR signal is observed at almost the same position with that of LiCl reference without the Knight shift. In addition, formation of passivation layers such as Li_2CO_3 on the PAS surface is also likely to occur in this stage as reported in Ref. 24. This kind of salt also contributes to the peak at 0 ppm.

By further doping over 10 % (Fig. 3(c)), the electrons transferred from Li atoms to PAS material begin to occupy the conduction band. The doping generates conduction electrons near E_F and causes the Knight shift. Actually, in the ESR measurements, it has been confirmed that the unpaired electrons begin to be influenced by Li dopants in the doping range over 10% and that metallic nature arises in terms of Pauli paramagnetic contribution to the ESR spectrum from this range [16]. Thus from the NMR results it

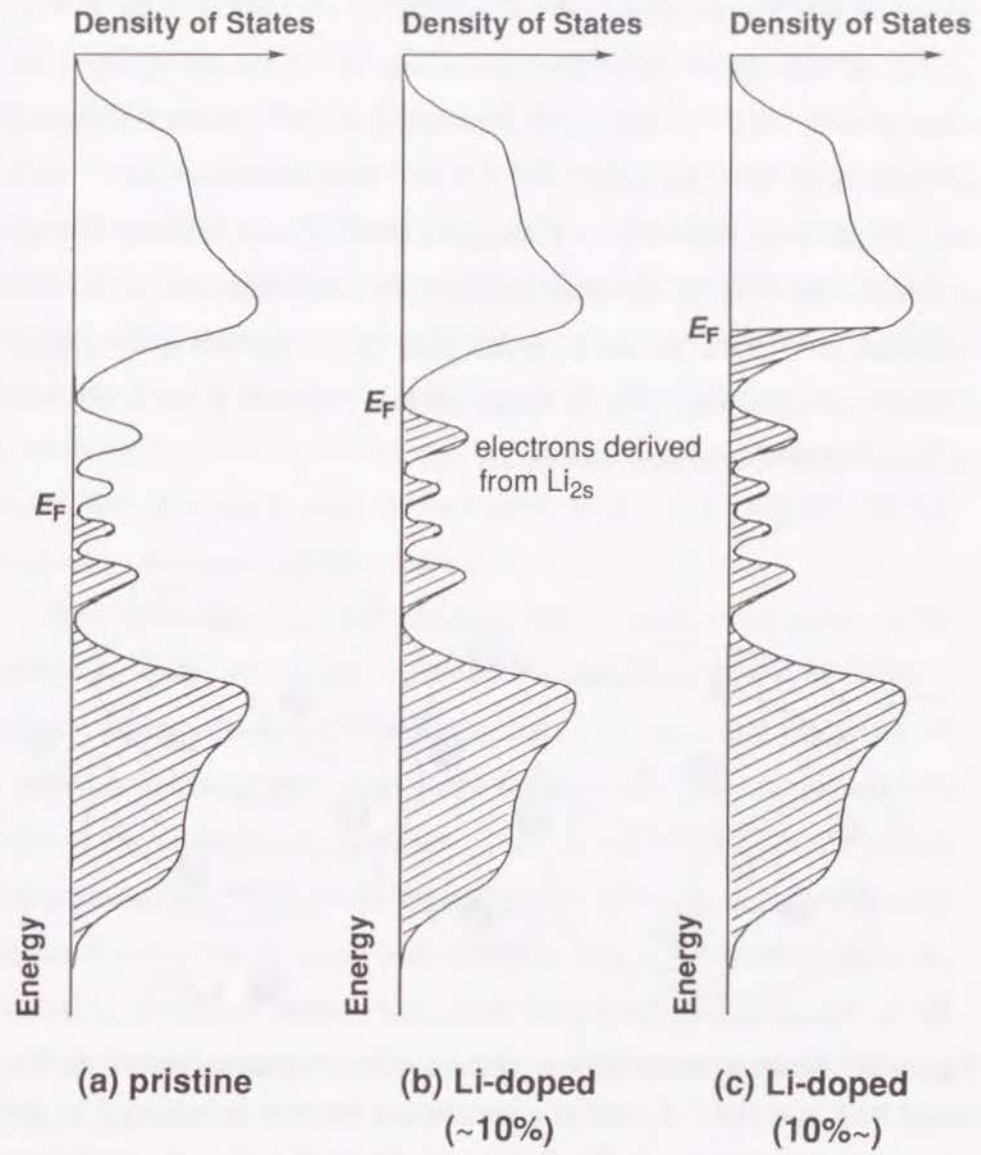

Figure 3. Simple models of the density of states (DOS) of (a)pristine, (b)initially Li-doped ($x \leq 10$ %), and (c)successively Li-doped (x>10 %) PAS material. Owing to the amorphous structure, the pristine has the localized states in the bandgap (a). When Li is doped to 10 %, the localized states are filled by electrons transferred from Li atoms (b). Further doping generates the conduction electrons with energy near E_F, by occupying the conduction band (c).

becomes clear that the Fermi contact interaction also works in the present system as well as the spin-orbit interaction as convinced by the ESR measurements [16]. Therefore, the broadening of ESR spectra is supposed to come from both the spin-orbit and the contact interactions. In a microscopic sense, one can have an image in which Li nuclei interact with the conduction electrons as illustrated in Fig. 4; thermally activated conduction electrons pass by the Li nuclei on the way to a neighboring condensed aromatic carbon plane. The Li nuclei are also expected to be mobile and exchange each other as described in Sec. 3.2.

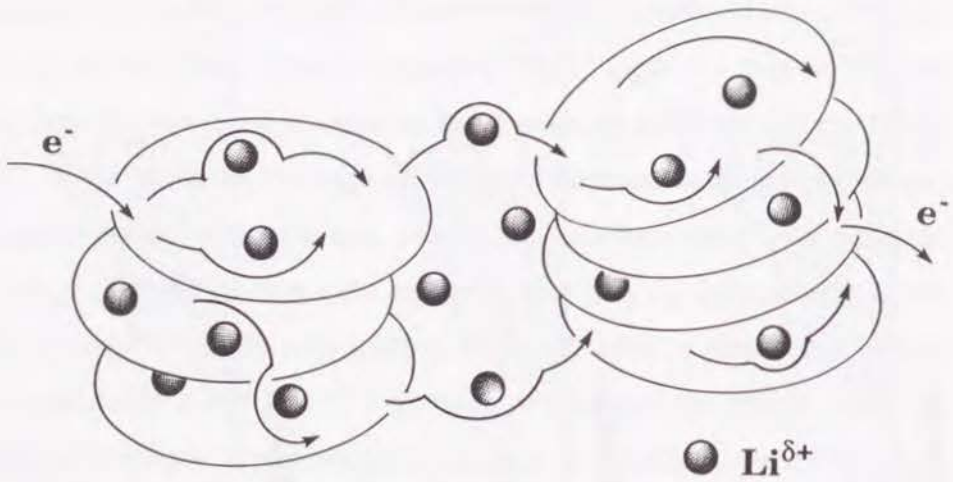

Figure 4. Illustrative description of the conduction mechanism of the Li-doped PAS material. A path of a conduction electron is indicated by the arrow, and a Li dopant ($Li^{\delta+}$: $0<\delta\leq1$) by the dark ball. A conduction electron is supposed to interact with Li nuclei through the thermal hopping. Though it is expected that Li dopants migrate and exchange each other, this effect is omitted for simplicity.

Saturation of the Knight shift observed at 30-60 % doping region (see Fig. 2) could indicate that the electronic state at a Li nucleus remains

unchanged in this region. The ESR linewidth increases continuously up to 60 % [16], while the Knight shift shows almost constant value. This discrepancy is understood by difference in numbers of conduction electrons and Li nuclei. While the latter increases with x, the former does not significantly change according to the decrease in the Li charge from Li^{1+} to $Li^{\delta+}$ ($0<\delta<1$) [3]. Therefore, the perturbation to the conduction electron by Li nuclei would increase with x, resulting in continuous increase in the ESR linewidth. On the other hand, since the number of conduction electrons per Li nuclei are expected not to increase, the Knight shift is not enhanced. We should note that the K_s and the ionization degree of Li dopants are not necessarily correlated in a linear manner.

The undoped sample was also examined to identify the nature of the residual Li atoms which cause irreversible capacity. In the 30→10 %-undoped sample, the shift goes to higher field (-1.5 ppm) than that of the 10 %-doped sample (-0.4 ppm) without the Knight shift. This higher field shift might be explained by the formation of Li-C bonds referring to the shift of phenyllithium (-1.3 ppm) and methyllithium (-1.0 ppm) [25] shown in Scheme 1 and to the T_1 value as described in Sec. 3.2. In this picture, the residual Li atoms are responsible for the Li-C bond species as well as the passivation layer. Moreover, it becomes that Li-C bonds are formed during the undoping process.

The Knight shift to 10 ppm has been reported in the concentrated Li-ammonia [26] and Li-methylamine [27] solutions. The shift of the Li-methylamine solution increases from 12 to 19 ppm with increasing the Li concentration at 204 K, in association with the transition from simple Curie-like behavior to Pauli-like one [27]. In the Li-methylamine solution (K_s=16 ppm), 2s character of the conduction electron was calculated to be 0.5 % [27]. Although spin susceptibility of the Li-doped PAS is different from

that of the methylamine solution, one can say that a conduction electron locates on the Li nucleus *with a small probability* in the Li-doped PAS material even in the highly doped regime.

Recently, pyrolyzed carbon materials have been reviewed and classified into three groups (highly graphitic carbons, hydrogen-containing carbons, and hard carbons) from an electrochemical aspect [6]. Among these three types of carbon materials the hydrogen-containing carbons have shown the extraordinary high Li-doping state [6]. In fact, the PAS material belongs to this hydrogen-containing carbon group. Several papers have pointed out that the Li-doped hydrogen-containing carbons show relatively small Knight shift. For instance, poly(*p*-phenylene)-based carbon (K_s~10 ppm) [5], furfuryl alcohol-based carbon (5~20 ppm) [4], and coke-based carbon (5~20 ppm) [17] have been reported. One can, therefore, confirm that the electronic state at a Li nucleus is substantially the same in these hydrogen-containing carbons, apart form their structural difference. While the Knight shift of Li metal is temperature independent, that of the coke-based carbon material decreases by cooling [17]. This can be understood by suppression of thermal hopping of the conduction electrons to Li nuclei (see Fig. 4). It is noteworthy that the suppression of the thermal hopping has also been confirmed by narrowing of the ESR spectrum at low temperatures [16]. The Knight shift of C_6Li state of graphite has been reported as 37 ppm ($//c_0$; c_0 signifies the axis perpendicular to a graphite sheet) and 21 ppm ($\perp c_0$) [28], but this origin is not simple due to the nuclear quadrupolar interaction.

As already established by the ESR measurements, over-doping (x> 50 %) results in liberation of the Li cluster [16]. In the NMR spectrum of 60%-doped sample, we can also confirm existence of Li cluster showing a very weak signal at 265 ppm. The Knight shift to 100-200 ppm observed in the

Li-doped hard carbons [18] is absent in the present system. We consider that the Knight shift at 100-200 ppm probably comes from Li clusters with relatively large size stored in the void space (100-1000 Å) of hard carbons, since the Knight shift moved to the lower magnetic field by cooling [17]. This is opposite to the situation of hydrogen-containing carbons. In the hard carbon, the conduction electron originally belongs to the Li cluster and, at sufficiently high temperature, the conduction electron is perturbed by carbon atoms. Thus the Knight shift at 265 ppm in the 60 %-doped PAS sample would indicate isolated Li clusters free from carbon planes.

For rationalization of the high capacity and the large hysteresis of hydrogen-containing carbons observed in the voltage-capacity profile, direct interaction between a Li atom and the peripheral C-H bond has been proposed based on the linear relationship between reversible capacity and [H]/[C] atomic ratio [6]. The ^1H decoupling measurement, however, has shown no significant change in the NMR signal. This can be understood as follows: (i)There is no H nucleus near Li, and/or, (ii)dipole interaction between H and Li atoms is averaged and diminished due to fast Li motion. Both these mechanisms provide no specific interaction between Li and H nuclei.

3.2. Relaxation time. Dynamic behavior of the Li nucleus has been evaluated based on the spin-lattice relaxation time (T_1). The inversion recovery of the 30 %-doped PAS sample shown in Fig. 5 suggests that the peak consists of only one component since the signal relaxed with keeping the shape almost symmetric. The situations in other samples (10 %, 60 %-doped, and 30→10 %-undoped) were also the same. One may, however, say that a slight distortion in the lineshape exists in Fig. 5, that is, one more component might be seen at ca. 0 ppm (0 Hz) during 110-140 msec.

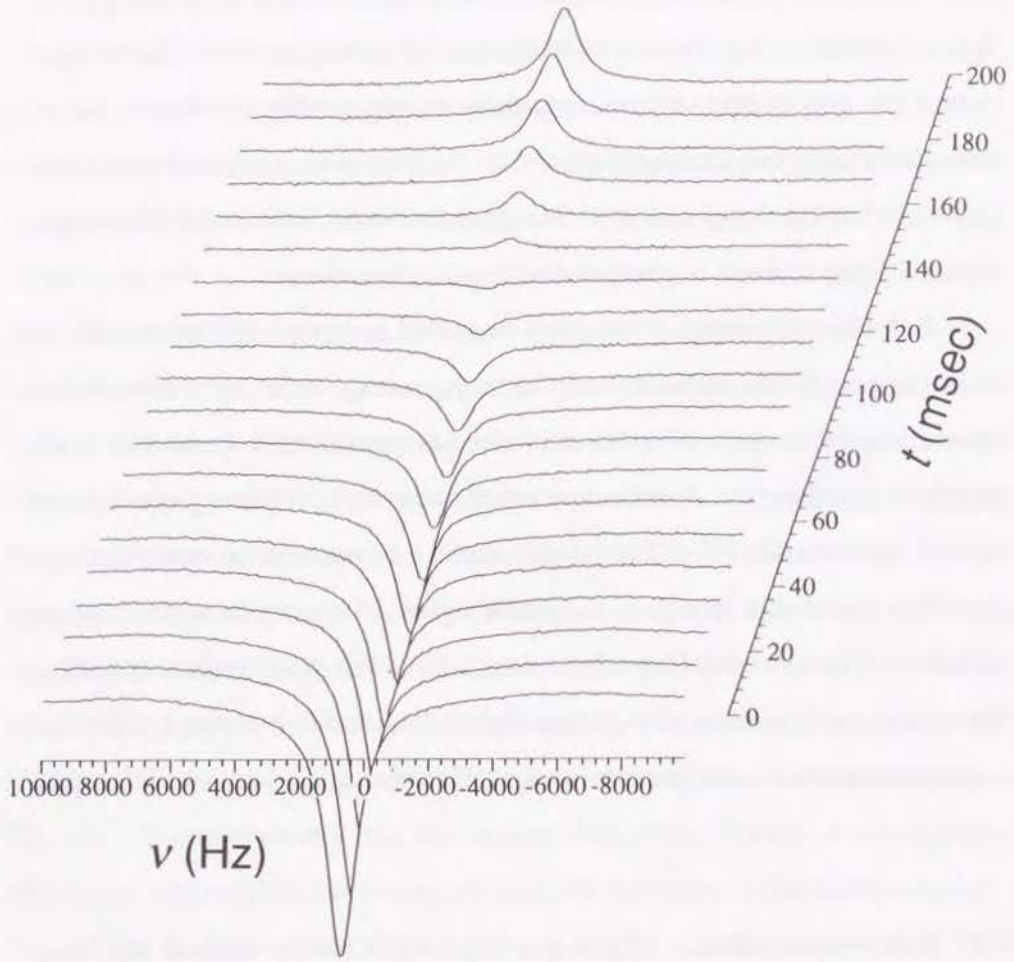

Figure 5. The inversion recovery profile of the 30 %-doped PAS material. After the first 180° pulse, the relaxation of the NMR signal was recorded by applying the second 90° pulse at 10 msec intervals.

However, it is very difficult to distinguish the NMR spectrum into two components because the relaxation rate of the peak at 0 ppm (0 Hz), if any, is very close to the original peak at 9 ppm (350 Hz).

Fig. 6 shows the normalized inversion recovery behavior of magnetization of the 30 %-doped sample at 9 ppm. The recovery is expressed by a single exponential function (the solid line). Other samples, 10 %-, 60 %-doped and 30→10 %-undoped samples, also showed similar single exponential behavior. On the basis of the recovery of the NMR shape (Fig. 5) and the single exponential behavior (Fig. 6), we can say that the ^{7}Li lineshape is homogeneous. To confirm this, we have performed the spin-

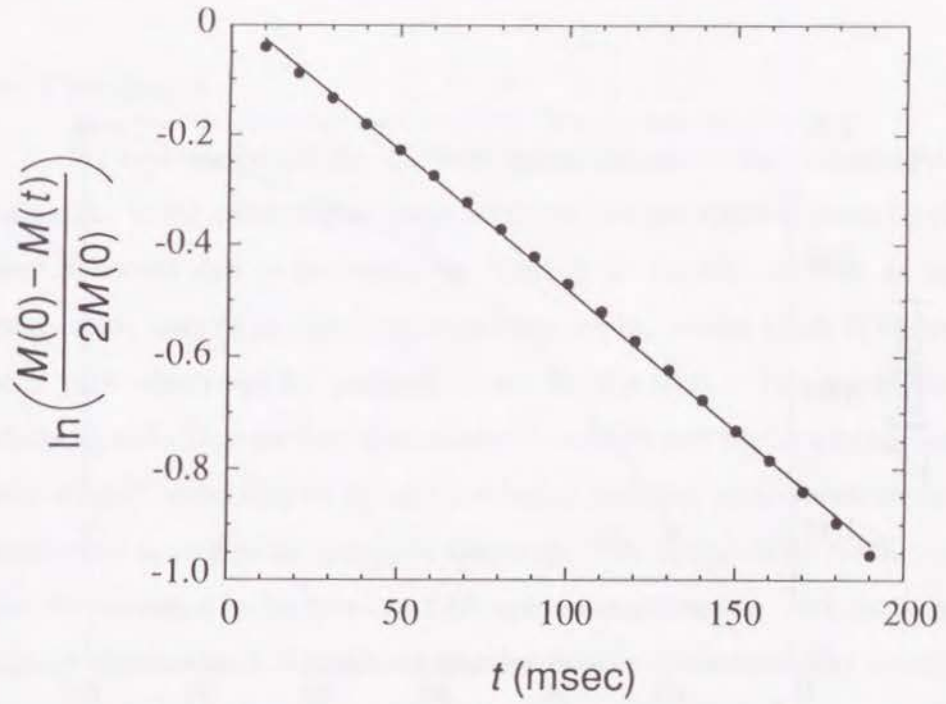

Figure 6. Normalized inversion recovery of ^{7}Li magnetization measured for 30 %-doped sample (open circles). $M(t)$ represents the magnetization measured at time t after the first 180° pulse. Data can be fitted by a linear line almost completely, implying that the recovery is single exponential.

echo experiments for the 30 %-doped sample. Neither the Hahn echo nor the quadrupole echo [29] was formed even with a very short pulse interval of 10 μs. This result clearly shows that the ^{7}Li lineshape is homogeneous and that the linewidth is attributed to a lifetime broadening [29]. The homogeneous lineshape indicates facile exchange of Li nuclei at various positions of PAS at room temperature. This mobility would explain the observed shorter T_1 values (100-250 msec) compared with that of Li-GIC (2000 msec) at room temperature [30]. The Li nucleus in the PAS material is more loosely trapped and, in other words, it can move more freely compared with that in Li-GIC. Similar fast exchange has been reported for the Li-corannulene system; the Li atoms located in and on the carbon plane(s)

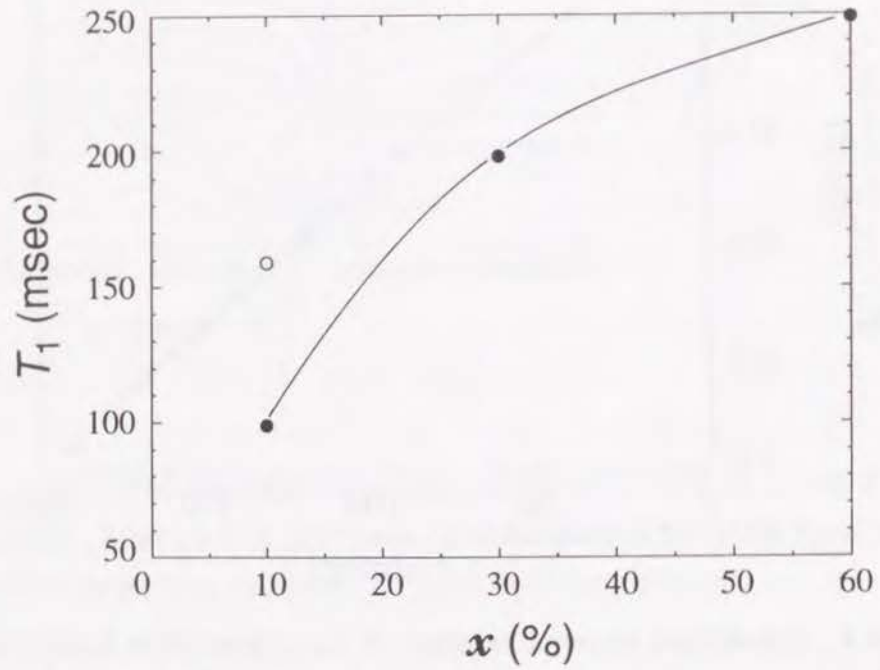

Figure 7. Spin lattice relaxation time T_1 plotted with x. Doped and undoped samples are shown in the closed and open circles, respectively. The line is a guide for eye.

can exchange and show a sole NMR peak at 265 K [31]. It is also noted that the T_1 value of ^{7}Li electrochemically doped into polyacetylene is 200±50 msec [32], being close to that of the present system.

In Fig. 7, T_1 is plotted versus x. The T_1 value increases with increasing x. This indicates that the Li nucleus becomes less mobile with proceeding the doping, probably due to the occupation of neighboring positions which holds the Li nucleus more tightly through an electrostatic interaction, mainly through the coulomb repulsion of $Li^{\delta+}$. Longer T_1 value of the 30→10 % undoped sample than that of the 10 %-doped one signifies that the residual Li atoms are less mobile than the initially doped Li atoms, being suggestive of formation of the Li-C bond, as mentioned above.

4. Conclusion

We have performed the ^{7}Li NMR measurements for the Li-doped PAS material. In the initial doping stage (x≤10 %), a broad signal at about 0 ppm was observed and is explained by ionized Li dopants as well as the passivation layer of Li salt. The successive doping caused lower field shift to 9 ppm which can be assigned to the Knight shift. The conduction electrons delocalize on the carbon π-atomic orbitals and hop to a Li nucleus with a small probability by thermal activation, resulting in the Fermi contact interaction as well as the spin-orbit coupling. The change in the NMR shift can be correlated to the previous ESR spectra qualitatively. All the broad signals obtained at -2~9 ppm were found to consist of almost one Li species, providing the Li nuclei can easily exchange with each other. Moreover, a Li nucleus is found to lose its mobility by the surrounding Li nuclei with proceeding the doping, but can move more frequently than that in C_6Li state of graphite even at the fully doped state. It is suggested the residual Li atom

is more rigidly confined than the initially doped Li atoms, probably due to formation of the Li-C bonds. Detailed mechanism of this formation is now under investigation and will be reported elsewhere.

References

[1] M. S. Dresselhaus, G. Dresselhaus, and P. C. Eklund, *Science of Fullerenes and Carbon Nanotubes*, Academic Press, San Diego (1996).

[2] S. Yata, H. Kinoshita, M. Komori, N. Ando, T. Kashiwamura, M. Harada, K. Tanaka, and T. Yamabe, *Proc. Symp. New Sealed Rechargeable Batteries and Supercapacitors*, Vol. **93-23**, p. 502, May, Hawaii (1993)

[3] S. Yata, H. Kinoshita, M. Komori, N. Ando, T. Kashiwamura, T. Harada, K. Tanaka, and T. Yamabe, *Synth. Met.*, **62**, 153 (1994).

[4] K. Tanaka, M. Ata, H. Kimura, and H. Imoto, *Bull. Chem. Soc. Jpn.*, **67**, 2430 (1994).

[5] K. Sato, M. Noguchi, A. Demachi, N. Oki, and M. Endo, *Science*, **264**, 556 (1994).

[6] J. R. Dahn, T. Zheng, Y. Liu, and J. S. Xue, *Science*, **270**, 590 (1995).

[7] H. Ago, K. Nagata, K. Yoshizawa, K. Tanaka, and T. Yamabe, *Carbon*, submitted.

[8] Y. Matsumura, S. Wang, and J. Mondori, *Carbon*, **33**, 1457 (1995).

[9] K. Tanaka, K. Ohzeki, T. Yamabe, and S. Yata, *Synth. Met.*, **9**, 41 (1984).

[10] S. Yata, U.S. Patent No. 4601849 (July 1986).

[11] K. Tanaka, S. Yamanaka, T. Koike, T. Yamabe, K. Yoshino, G. Ishii, and S. Yata, *Phys. Rev.*, **B32**, 6675 (1985).

[12] K. Tanaka, T. Koike, T. Yamabe, J. Yamauchi, Y. Deguchi, and S. Yata, *Phys. Rev.*, **B35**, 8368 (1987).

[13] K. Tanaka, M. Ueda, T. Koike, T. Yamabe, and S. Yata, *Synth. Met.*, **25**, 265 (1988).

[14] T. Yamabe, S. Yamanaka, K. Tanaka, T. Terao, S. Maeda, and S. Yata, *Phys. Rev.*, **B37**, 5808 (1988).

[15] S. Yata, Y. Hato, H. Kinoshita, N. Ando, A. Anekawa, T. Hashimoto, M. Yamaguchi, K. Tanaka, and T. Yamabe, *Synth. Met.*, **73**, 273 (1995).

[16] K. Tanaka, H. Ago, T. Kuga, Y. Matuura, T. Yamabe, S. Yata, Y. Hato, and N. Ando, *Synth. Met.*, submitted.

[17] (a) Y. Mori, T. Iriyama, T. Hashimoto, S. Yamazaki, F. Kawakami, H. Shiroki, and T. Yamabe, *J. Power Sources*, **56**, 205 (1995). (b) T. Hashimoto, T. Iriyama, S. Yamazaki, Y. Mori, and H. Shiroki, *Proc. 36th Battery Symp. Jpn.*, 1B06, September, Kyoto (1995).

[18] M. Ishikawa, N. Sonobe, H. Chuman, and T. Iwasaki, *Proc. 35th Battery Symp. Jpn.*, 2B10, June, Nagoya (1994).

[19] K. Tatsumi, T. Akai, T. Imamura, K. Zaghib, N. Iwashita, S. Higuchi, and Y. Sawada, *J. Electrochem. Soc.*, **143**, 1923 (1996).

[20] J. Ficini and J. Pouliquen, *J. Am. Chem. Soc.*, **93**, 3297 (1971).

[21] K. Tanaka, M. Kobashi, and T. Yamabe, *Intern. J. Quantum. Chem.: Quantum Chem. Symp.*, **23**, 641 (1989).

[22] W. D. Knight, *Solid State Phys.*, **2**, 93 (1956).

[23] *Progress in Material Science*, G. C. Carter ed., Pergamon, England, vol. **20**, p. 239 (1977).

[24] Y. Matsumura, S. Wang, and J. Mondori, *J. Electrochem. Soc.*, **142**, 2914 (1995).

[25] P. A. Scherr, R. J. Hoga, and J. P. Oliver, *J. Am. Chem. Soc.*, **96**, 6055 (1974).

[26] D. E. O'Reilly, *J. Chem. Phys.*, **41**, 3729 (1964).

[27] D. M. Holton, P. P. Edwards, W. McFarlane, and B. Wood, *J. Am. Chem. Soc.*, **105**, 2104 (1983).

[28] G. Roth, K. Lüders, P. Pfluger, and H.-J. Güntherodt, *Solid State Commun.*, **39**, 423 (1981).

[29] (a) M. Mehring, *High Resolution NMR in Solids*, 2nd ed., Springer Verlag, Berlin (1983). (b) C. P. Slichter, *Principles of Magnetic Resonance*, Harper & Row, NY (1963).

[30] H. Estrade, J. Conard, P. Lauginie, P. Heitjans, F. Fujara, W. Buttler, G. Kiese, H. Ackermann, and D. Guérard, *Physica*, **99B**, 531 (1980).

[31] A. Ayalon, A. Sygula, P. C. Chemg, M. Rabinovitz, P. W. Rabideau, and L. T. Scott, *Science*, **265**, 1065 (1994).

[32] A. K. Whittaler, C. Fite, K. Zniber, and P. Bernier, in *Electronic Properties of Conjugated Polymers*, Kuzmany ed., Springer Verlag, NY p. 170 (1987).

Chapter 4

Structural Analysis of PAS Material with ^{129}Xe NMR Measurement

1. Introduction

Polyacenic semiconductor (PAS) materials prepared by thermal treatment of phenol-formaldehyde resin at relatively low temperatures (500-1000°C) are air-stable and have loose structures with longer interlayer distances (d_c= 3.7-4.2 Å) compared with graphite (3.35 Å) [1,2]. PAS materials can be doped not only by the electron donor but also by acceptor, resulting in an increase in the electrical conductivity by 11 orders of magnitude in maximum [1,3]. Owing to its loose structure, the PAS material can incorporate a much larger number of Li ions (C_2Li state in maximum) than graphite (C_6Li state), which promises a new type of high capacity anode material utilized in the lithium rechargeable battery [4-6]. Moreover, the PAS material also shows good reversibility and long cycle life in the electrochemical doping-undoping cycles. Nowadays, the batteries employing the PAS material are commercialized and widely used in the portable electronic appliances [6-8]. In order to clarify the Li-doping and storage mechanism in the PAS material, X-ray photoelectron spectroscopy (XPS) [5], X-ray diffraction (XRD) [5], electron spin resonance (ESR) [9], and ^{7}Li nuclear magnetic resonance (^{7}Li NMR) [10] measurements have been performed so far.

From the first experiment of Xe-adsorbed zeolite [11], ^{129}Xe NMR has been recognized as a powerful method for structural analysis, especially for the analysis of microporous structure with diameters less than 20 Å. A Xe chemical shift provides the characteristic information on the adsorbate such as surface structure, porosity, and adsorbed species, because perturbation to the large and polarizable electron cloud of Xe atom directly influences on the nucleus environment [12]. For instance, such applications of the ^{129}Xe NMR to liquid solutions, amorphous polymers, and liquid crystals have been successfully carried out [12]. It would be, therefore, interesting to apply this method to PAS material because the pyrolyzed carbon materials possess a lot of micropores (~20 Å) along with mesopores (20~500 Å) and macropores (500 Å~), and those micropores are considered to be essential in determining the amount of dopable Li. Actually, ^{129}Xe NMR has been applied to bituminous coal (e.g., Illinois No. 6) [13,14] and activated carbons [15], and valuable information on their microporous structures has been obtained based on their chemical shifts. Furthermore, this method is appropriate to the system involving Li atoms, owing to inertness of a Xe atom (a Xe atom can only react with fluorine compounds) [16]. For example the nitrogen adsorption measurement is inappropriate to analysis of the Li-doped sample due to reactivity of Li with N_2 [17].

In the present chapter, the examination results of microporous structure of the pure PAS material based on the ^{129}Xe NMR measurements are presented. The microporous structure has been characterized based on the chemical shift, Xe-pressure dependence, and two-dimensional (2D) exchange NMR spectrum. Moreover, in association with the high electrochemical performance of the PAS electrode mentioned above, it is also presented the results for the PAS electrode dipped into the electrolyte solution as well as that doped with Li electrochemically.

2. Experimental

2.1. Sample preparation. The PAS material employed in the present study was prepared from phenol-formaldehyde resin at 680 °C under non-oxidative atmosphere as described in Ref. 1. This PAS material has been characterized by the molar ratio [H]/[C]=0.22, the electrical conductivity σ=2.7×10^{-3} S/cm [5], the crystallite size L_c=7.6 Å, L_a=26.9 Å [2], and the macroscopic grain size 6-7 μm [18].

Specifically, the following four kinds of samples were examined: (1) Pure PAS with no treatment after the pyrolysis. (2) PAS electrode made by mixing and kneading of the pure sample with 3 wt.% of polytetrafluoroethylene (PTFE) as a binder so as to finish in sheet form appropriate to the electrode (250 μm thickness). (3) Dipped PAS electrode made by dipping the PAS electrode into the electrolyte solution of the battery. The 1M $LiPF_6$ dissolved in propylene carbonate (PC) was employed as the electrolyte solution. (4) Li-doped PAS electrode for which the electrochemical doping was carried out up to the 5%-Li-doped level ([Li]/[C]=0.05) by using a three-electrodes cell. Details of the Li-doping process has been described elsewhere [5]. Dipped electrode sample as well as the Li-doped one was thoroughly washed by dimetoxyethane and evacuated under vacuum at 60 °C for 1 hour prior to transferring into a high-pressure-endurable NMR tube equipped with a greaseless stopcock. All the processes of dipping, Li-doping, and sample transfer were conducted in a dry box filled with highly purified argon gas.

2.2. NMR measurements. The NMR tube containing each sample was connected to the vacuum line attached with a xenon balloon and then thoroughly evacuated in order to remove the adherent impurities on the

sample. After evacuation, desired amount of Xe gas was introduced into this vacuum line, followed by cooling the NMR tube with liquid N_2. For complete Xe adsorption, the sample was made to stand for 12 hours in Xe atmosphere at room temperature. ^{129}Xe NMR measurements were performed on a JEOL-GSX200 spectrometer with a ^{129}Xe resonance frequency of 55.26 MHz at room temperature. The chemical shift was calibrated using a non-adsorbed (free) Xe gas extrapolated to zero pressure as the reference. The 2D exchange NMR spectrum was measured employing the conventional three-pulse sequence [19].

3. Results and Discussion

3.1 Pure PAS sample. The ^{129}Xe NMR spectrum and the detailed data of the pure PAS sample measured after introduction of 5 atm Xe gas are shown in Fig. 1(a) and Table 1, respectively. Pure sample shows a chemical shift at 152 ppm with a wide linewidth of 1405 Hz. It is obvious that this broadness represents a wide distribution of pore sizes because PAS material has amorphous structure [2]. Note that the Xe NMR spectrum of zeolite has shown a narrower peak than that of this pure PAS sample because the former substance possesses a well defined cage structure [20]. The present NMR signal consists of one peak, while those of bituminous coal [14] and activated carbon [15] two or three peaks with different chemical shifts. Therefore, the pure PAS material is supposed to have micropores with a wide but relatively unified distribution.

In Fig. 2, the 2D exchange NMR spectrum of the pure PAS sample measured with the mixing time of 100 msec at room temperature is indicated. Since the spectrum showed almost circular form, we can infer that Xe atoms in different micropores diffuse and interchange almost completely within the

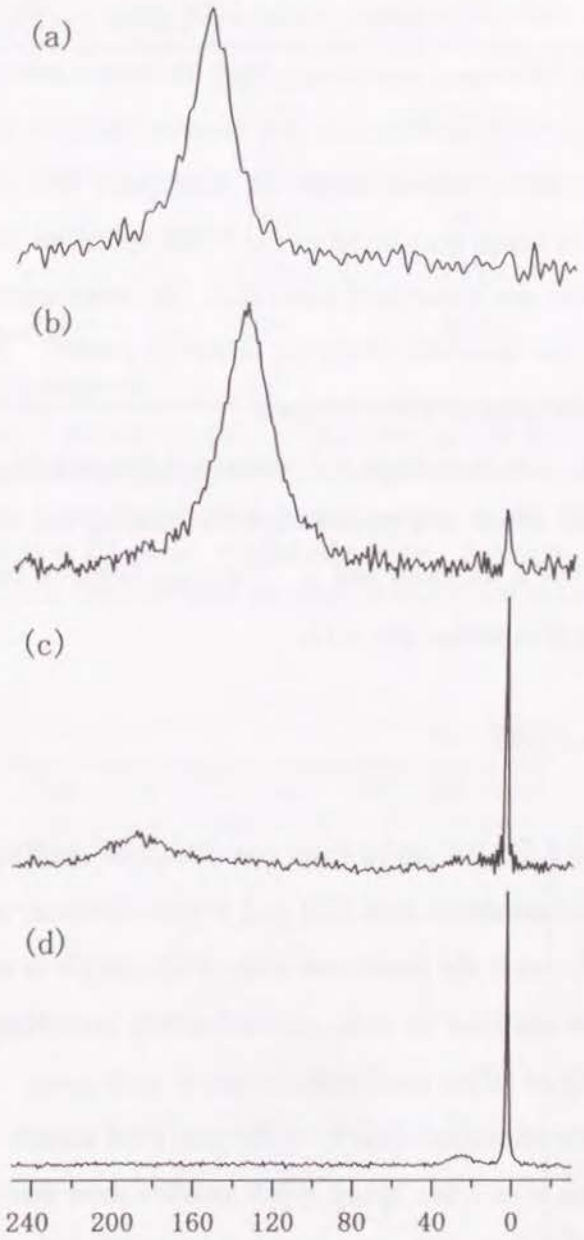

Figure 1. ^{129}Xe NMR spectra under 5 atm of Xe gas of (a)the pure PAS, (b)the PAS electrode kneaded with PTFE binder, (c)the dipped PAS electrode impregnated into the 1 M $LiPF_6$ dissolved PC electrolyte solution, and (d)the 5%-Li-doped PAS electrode.

characteristic correlation time (τ) of ~100 msec. Therefore, at room temperature, the Xe atom is expected to have the kinetic energy larger than the activation energy for migration from one adsorbed position to the other. It is true that the Xe atoms diffuse within the micropores in a time scale of 100 msec, but the exchange narrowing of the NMR spectrum originating in this Xe diffusion was not apparently observed. In other words, the diffusion cannot average the linewidth (1405 Hz under Xe 5 atm). Thus, τ of the Xe diffusion is in the order of a few 10 msec.

We would like to estimate the maximum distance (d_{max}) between the pores which Xe atoms can interchange by making use of the diffusion coefficient (D) of a Xe atom and τ. The d_{max} is given by the simple 2D diffusion model of a perfect gas [21],

$$d_{max} = \sqrt{2 D \tau} \qquad (1)$$

Employing D =8.3×10^{-6} cm^2/s from the diffusion coefficient of CH_4-N_2 mixed gas in a bituminous coal [22] and τ =10~30 msec, we obtain d_{max}= 4.1~7.1 μm. Because the grain size of the PAS sample is 6-7 μm [18], it is expected that an adsorbed Xe atom can sufficiently interchange with, at least, the that adsorbed on all the pores existing in the same grain.

Spin-lattice relaxation time T_1 of the pure PAS sample measured under 5 atm of Xe gas was 1 sec being much smaller than that of the Xe atom dissolved in polystyrene (15 sec) and poly(vinylmethylether) (6 sec) [23,24]. This fact signifies that the relaxation of a Xe nucleus adsorbed on the pure PAS sample is faster than these polymers. Possible reasons for this faster relaxation rate considered are: (i) Xe-Xe two body collision occurs more frequently in the pure PAS sample than in the polymers, because the pore size of the former is larger than the voids of the latter (the latter chemical shifts are

Table 1. ^{129}Xe NMR results of the PAS samples.

	Chemical shift[a] (ppm)	Half linewidth[a] (Hz)	Pore size[b] (Å)
Pure PAS	152	1405	7.7±1.6
PAS electrode	134[c]	1673	8.1±1.8
Dipped PAS electrode	193[c]	2617	5.1[d]
5%-Li-doped PAS electrode	27[e]	-	-

[a]Measured under 5 atm of Xe gas. [b]Diameter of the micropore with the maximum population, estimated from the extrapolation of the chemical shift to 0 atm of Xe. [c]A very narrow peak corresponding to the non-adsorbed Xe atom was observed at 2.5 ppm. [d]Indefinite value. See text. [e]A quite small signal was observed, together with the peak from the non-adsorbed Xe atom.

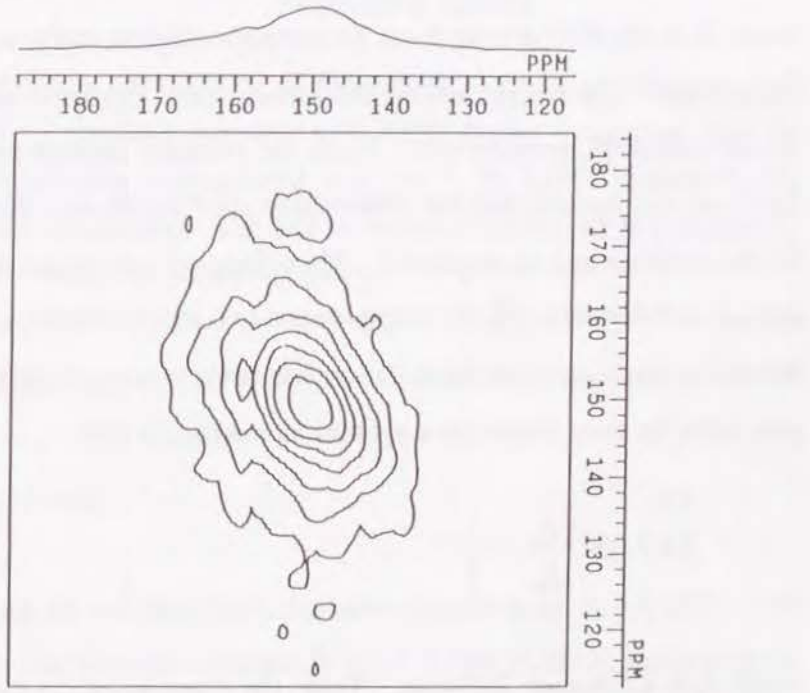

Figure 2. The 2D exchange NMR spectrum of the pure PAS sample measured under 5 atm of Xe gas with the mixing time of 100 msec.

200-225 ppm under Xe 10 atm). (ii) The relaxation of a Xe nucleus is enhanced by the magnetic interaction with a number of the radical spins and the delocalized π-type spins. We infer the second possibility is predominant due to high spin concentration of the PAS material (ca. 10^{20} spins/g [25]).

Pressure dependence of the chemical shift was examined to distinguish the interaction between a Xe atom and internal surface of the micropores, which we call Xe-surface collision hereafter. In Fig. 3 the chemical shift (δ) is plotted versus the Xe pressure (P). The chemical shifts at ρ, which is the density of adsorbed Xe atoms in the unit of atom per gram-PAS sample, can be expressed as [11],

$$\delta(\rho) = \delta_0 + \delta_1\rho + \delta_2\rho^2 \qquad (2)$$

where δ_0 is the shift arising from Xe-surface collision and is independent of Xe pressure. The second and the third terms come from two- and three-body Xe-Xe collisions, respectively. From the pressure dependency of the δ on the P, we can assume that the relationship $\rho \propto P$ holds and, thus, three-body Xe-Xe collision can be neglected. Therefore, we can obtain the simple Xe-surface collision term (δ_0) by extrapolation to 0 atm (ρ=0 atom/g-PAS). The following semiempirical formulation has been proposed for the mean-free path l of a Xe atom located in a cylindrical micropore [26],

$$l = 2.054\left(\frac{\delta_a}{\delta_0} - 1\right) \qquad (3)$$

where δ_a is a constant, 243 ppm. Then, the diameter of the cylindrical pore

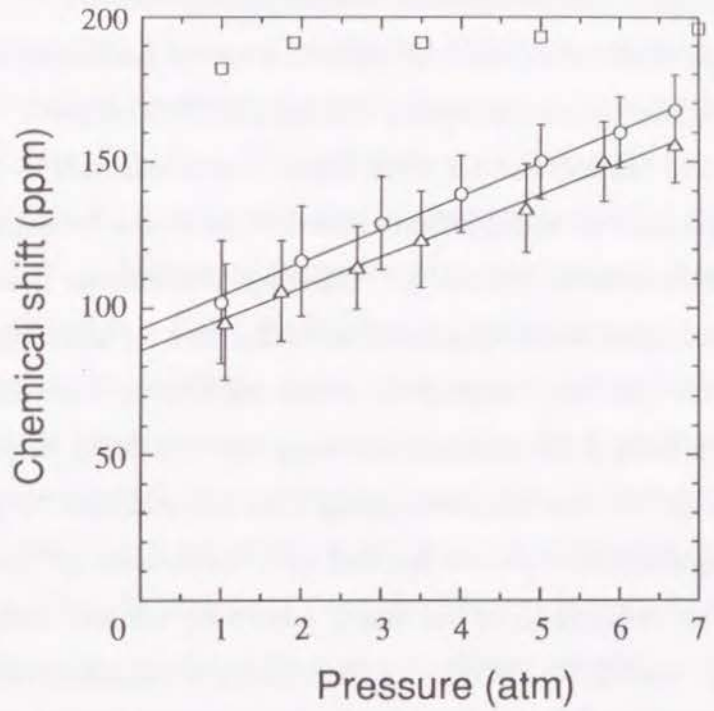

Figure 3. Pressure dependence of the chemical shifts of the pure PAS (circles), the PAS electrode kneaded with PTFE binder (triangles), and the dipped PAS electrode impregnated into the 1 M $LiPF_6$ dissolved PC electrolyte solution (squares). The half linewidth of each peak is indicated by the vertical bar. Lines are guides for the eye.

(d_{pore}) is expressed as,

$$d_{pore} = l + d_{Xe} \qquad (4)$$

where d_{Xe} stands for van der Waals diameter of a Xe atom, 4.4 Å [27]. The calculated pore size from the obtained δ_0 is 7.7 Å (see Table 1) and is in good agreement with the result based on the N_2 adsorption (8 Å) [28]. Note that the Xe NMR chemical shifts of bituminous coal and activated carbon do not show a linear dependency of the chemical shift on the Xe pressure, i.e., the

shift becomes saturated at a certain pressure (0.3-0.7 atm) [14,15]. This fact may suggest these carbon materials possess a smaller number of micropores in which Xe atoms adsorb compared with the pure PAS sample.

The half linewidth of the NMR signal is also indicated by the bars in Fig. 3. Also from the extrapolation to 0 atm of these bars, we determined the pore distribution to be 7.7±1.6 Å. However, it should be noted that the obtained micropore distribution could be smaller than the actual one, because it is plausible that interchange of Xe atoms reduced the linewidth to some extent on the basis of the observed narrowing with increasing Xe pressure.

From the fact that the peak coming from non-adsorbed Xe gas, which will be mentioned later, was not detected up to Xe pressure of 7 atm, one can infer that all the introduced Xe atoms adsorb on internal surface of the micropores. Hence, we can estimate the number of micropores (N_{pore}) from P and the volume of the NMR tube, under an assumption that one micropore is filled with one Xe atom since the micropore is small (7.7±1.6 Å). The calculation, $N_{pore} \geq 1\times10^{21}$ pores/g-PAS, indicates the existence of a great many micropores in the pure PAS sample.

3.2. Structural changes in the PAS electrode. Investigation into the structural change induced by the Li-doping is a very important and attractive subject for understanding the doping mechanism as well as further developing the carbon-based Li rechargeable battery. However, to the authors' knowledge, there has been no report on the structural change of micropores, except that in the interlayer distance measured by the X-ray diffraction [5,29]. Therefore, we have examined the ^{129}Xe NMR spectra of the PAS electrode as well as those of the dipped and Li-doped samples.

As shown in Fig. 1, mixing of 3 wt.% of PTFE binder caused higher field shift (152→134 ppm) when compared with the pure sample. When the

P exceeds 5 atm, a small peak was also observed at 2.5 ppm which originates in the non-adsorbed Xe gas. The pressure dependence of the peak arising from the adsorbed Xe atoms gives the diameter of the micropores to be 8.1±1.8 Å (see Fig. 3). The obtained pore size with the maximum population (8.1 Å) is larger than that of the pure sample by about 0.4 Å. Considering the appearance of the peak arising from non-adsorbed Xe gas, it can be presumed that PTFE binder fills the micropores with a relatively smaller diameter and repels Xe atoms, resulting in the non-adsorbed Xe peak and somewhat larger pore size. Actually, from the P at which the non-adsorbed gap appeared, the number of micropores is calculated to be $N_{pore} \sim 8\times10^{18}$ pores/g-PAS, being much smaller than that of the pure PAS sample. However it should be noted that this value (8×10^{18} pores/g-PAS) is rather rough because the introduced Xe atoms are almost adsorbed even at 7 atm considering a small increase in the peak intensity of the non-adsorbed gas peak. It is also interesting to note that the electrode sample kneaded with 10 wt.% of polyvinylidene fluoride (PVDF) instead of PTFE gave only the peak originating from the non-adsorbed Xe gas (the spectrum is not shown here). Thus, PVDF binder completely prevents Xe atoms from entering into the micropores by 'filling' the micropores or 'wrapping' the whole PAS sample. In spite of the exclusion of Xe atom by PVDF, no hindrance for the Li-doping has been observed [30]. This will be discussed later.

Dipping of the PAS electrode into the electrolyte solution led to a sharp peak at 2.5 ppm and a broad one at around 193 ppm (Fig. 1(c)) coming from the non-adsorbed and the adsorbed Xe atoms, respectively. The low field shift of the peak of the adsorbed Xe atom reveals drastic reductions of the average micropore size, and its small intensity shows that the absolute number of micropores for Xe adsorption is reduced. As shown in Fig. 3, the chemical shift saturates even at 1 atm, indicating that only a small portion

of the introduced Xe atoms can adsorb on internal surface of the micropores and that the relationship $\rho \propto P$ does not hold in the pressure range studied. The pore size estimated to be 5.1 Å with a certain indefiniteness (see Table 1), being 2.6 Å smaller than that of the pure PAS sample. The number of micropores is estimated to be $N_{pore} << 1 \times 10^{18}$ pores/g-PAS. Since a separate observation for the dipped sample impregnated only to PC solution without $LiPF_6$ electrolyte gave essentially the same spectrum with that shown in Fig. 1(c), one can conclude that it is the solvent molecules (PC in this study) which repel Xe atoms. It is plausible that PC molecules themselves are adsorbed on internal surface of the micropores or, at least, occupy room for Xe atoms because a full length of electron cloud of a PC molecule (6.2 Å) [31] is comparable to the van der Waals diameter of a Xe atom (4.4 Å) [27]. In this sense, even drying at 60 °C under vacuum is insufficient to remove the adsorbed solvent, suggesting rather strong physisorption of a PC molecule onto the internal surface. The broadening of the signal observed in the dipped sample (Table 1) may be explained in terms of suppression of the diffusion or interchange of adsorbed Xe atoms because the pores become so small that each of them is almost filled up with one Xe atom and this Xe atom becomes less mobile. The fact that T_1 value of the dipped sample (0.1 sec) was much shorter than that of the pure sample (1 sec) would stand for the enhancement of the collision between an adsorbed Xe atom and a PC molecule and/or the Xe-surface collision.

Finally, we have examined the effect of the Li-doping (Fig. 1(d)). The 5%-Li-doped sample showed an intense peak at 2.5 ppm arising from non-adsorbed Xe gas together with a very small peak at 27 ppm. Appearance of the latter peak could be interpreted by trapping Xe atoms into the mesopores as a result of complete filling of micropores caused by the Li-doping. A close inspection reveals the existence of this signal also in the PAS electrode

and the dipped samples (Fig. 1(b), (c)). Even heating of this sample at 100 °C under vacuum gave no change. These results are rather surprising because it has been well known that more numbers of Li ions can enter into the 5%-doped sample by usual electrochemical doping [5]. Three reasons can be considered for such complete exclusion of Xe atoms. First, the solvent molecules are solvated to Li ions to some extent and have completely occupied the room for Xe atoms in micropores. If this is the case, relationship between the battery capacity and the solvent size could become of much importance. For instance, less bulky solvent molecule is expected to make more space leading to a larger amount of Li ions into the PAS electrode. Second, the passivation layer like Li_2CO_3 has covered the sample surface [32]. In both of these cases, the main reason accounting for absence of hindrance for Li-doping is assumed to be the difference in the diameter of a Xe atom and a Li ion: the ionic diameter of a Li ion is 1.20 Å [33] being about 1/4 of the van der Waals diameter of a Xe atom. Therefore, more numbers of Li ions can be expected to diffuse into and adsorbed on the small space between PC molecules due to smaller size of a Li ion than a Xe atom. The same situation could occur in the PVDF-used electrode. The third possibility comes from that negatively charged carbon skeleton of the Li-doped PAS declines adsorbing electron-rich Xe atoms. In this case, there occurs no hindrance for the Li-doping since the doped Li is positively charged. By taking the drastic change brought by the impregnation into account, the first possibility is supposed to be the most dominant.

4. Conclusion

Microporous structures of the PAS samples have been examined based on the ^{129}Xe NMR measurement. There are three major findings in the present study:

(i) The pure PAS sample showed a broad NMR peak and almost circular 2D exchange spectrum. We infer from these results that the pure PAS sample possesses micropores with a wide distribution and that the adsorbed Xe atoms diffuse and interchange rapidly. Based on the Xe-pressure dependence of the chemical shift, the average pore size of the pure sample was determined to be 7.7±1.6 Å in reasonable agreement with the measurement based on the N_2 adsorption. It was also shown that there exist a number of the micropores for Xe atoms to adsorb ($N_{pore} \geq 1 \times 10^{21}$ pores/g-PAS).

(ii) The PAS electrode involving PTFE as a binder showed two peaks coming from the adsorbed Xe atom and non-adsorbed Xe gas. The former shifted to a higher field compared with the pure PAS sample. These results are explained by the assumption that PTFE binder fills the relatively smaller micropores and repel Xe atoms. Furthermore, this hindrance was found to depend on the binder species, e.g., adsorbed Xe atoms were not observed at all when PVDF was used as a binder.

(iii) Once the PAS electrode is dipped into the electrolyte, marked reductions in both the pore size (down to ca. 5.1 Å) and the number of pores ($N_{pore} << 1 \times 10^{18}$ pores/g-PAS) for Xe atoms to enter were observed. The occupation of micropores by the solvent molecule (PC in this study) can be the cause. Moreover, after the PAS electrode was doped with Li electrochemically up to only 5 mol%, Xe atoms could not be adsorbed onto internal surface of the micropores at all.

The observations (ii) and (iii) could afford crucial standpoint for understanding of the electrochemical Li-doping mechanism into the PAS electrode. Detailed study from another aspect such as, for instance, the X-ray photoelectron spectroscopy is now undertaken and will be reported in the near future.

References

[1] K. Tanaka, K. Ohzeki, T. Yamabe, and S. Yata, *Synth. Met.*, **9**, 41 (1984).

[2] K. Tanaka, M. Ueda, T. Koike, T. Yamabe, and S. Yata, *Synth. Met.*, **25**, 265 (1988).

[3] K. Tanaka, S. Yamanaka, T. Koike, T. Yamabe, K. Yoshino, G. Ishii, and S. Yata, *Phys. Rev.*, **B32**, 6675 (1985).

[4] S. Yata, H. Kinoshita, M. Komori, N. Ando, T. Kashiwamura, M. Harada, K. Tanaka, and T. Yamabe, *Proc. Symp. New Sealed Rechargeable Batteries and Supercapacitors*, Vol. 93-23, p. 502, Hawaii, May (1993).

[5] S. Yata, H. Kinoshita, M. Komori, N. Ando, T. Kashiwamura, T. Harada, K. Tanaka, and T. Yamabe, *Synth. Met.*, **62**, 153 (1994).

[6] S. Yata, Y. Hato, H. Kinoshita, N. Ando, A. Anekawa, T. Hashimoto, M. Yamaguchi, K. Tanaka, and T. Yamabe, *Synth. Met.*, **73**, 273 (1995).

[7] S. Yata, Y. Hato, K. Sakurai, T. Osaki, K. Tanaka, and T. Yamabe, *Synth. Met.*, **18**, 645 (1987).

[8] S. Yata, K. Sakurai, T. Osaki, Y. Inoue, K. Yamguchi, K. Tanaka, and T. Yamabe, *Synth. Met.*, **38**, 185 (1990).

[9] K. Tanaka, H. Ago, T. Kuga, Y. Matuura, T. Yamabe, S. Yata, Y. Hato, and N. Ando, *Synth. Met.*, submitted.

[10] H. Ago, K. Tanaka, T. Yamabe, K. Takegoshi, T. Terao, S. Yata, Y. Hato, and N. Ando, *Phys. Rev. B*, submitted.

[11] T. Ito and J. Fraissard, *J. Chem. Phys.*, **6**, 5225 (1982).

[12] For instance, D. Raftery and F. Chmelka, in *Xenon NMR spectroscopy*, in Solid State NMR I, B. Blümich ed., Vol. 30, p. 111, Springer Verlag, Heidelberg (1994).
[13] P. C. Wernett, J. W. Larsen, Y. Osamu, and H. J. Yue, *Energy and Fuels*, **4**, 412 (1990).
[14] C. Tsiao and R. E. Botto, *Energy and Fuels*, **5**, 87 (1991).
[15] D. J. Suh, T. Park, S. Ihm, and R. Ryoo, *J. Phys. Chem.*, **95**, 3767 (1991).
[16] F. A. Cotton and G. Wilkinson, *Advanced Inorganic Chemistry*, 4th ed., John Wiley & Sons, NY (1980).
[17] H. Ago, T. Kuga, T. Yamabe, K. Tanaka, S. Yata, Y. Hato, and N. Ando, *Carbon*, submitted.
[18] unpublished result.
[19] J. Jeener, H. B. Meier, P. Bachmann, and R. R. Ernst, *J. Chem. Phys.*, **71**, 4546 (1979).
[20] L. C. de Menorval, D. Raftery, S. -B. Liu, K. Takegoshi, R. Ryoo, and A. Pines, *J. Phys. Chem.*, **94**, 27 (1990).
[21] P. W. Atkins, *Physical Chemistry*, 4th ed., Oxford (1990).
[22] R. T. Yang, R. -T. Liu, and M. Steinberg, *Ind. Eng. Chem., Fundam.*, **16**, 486 (1977).
[23] M. Tomaselli, B. H. Meier, P. Roybr, U. Suter, and R. R. Ernst, *Chem. Phys. Lett.*, **205**, 145 (1993).
[24] T. Miyoshi, K. Takegoshi, and T. Terao, *Polymer*, submitted.
[25] K. Tanaka, T. Koike, T. Yamabe, J. Yamauchi, Y. Deguchi, and S. Yata, *Phys. Rev.*, **B35**, 8368 (1987).
[26] J. Demarquay and J. Fraissard, *Chem. Phys. Lett.*, **136**, 314 (1987).
[27] Chem. Soc. Jpn. ed., *Kagaku Binran (Kisohen)*, (in Japanese) 3rd ed., Maruzen, Tokyo (1984).
[28] Partly reported in: S. Yata, Y. Hato, S. Nagura, K. Tanaka, and T. Yamabe, *Polym. Prep. Jpn.*, **44(3)**, 381 (1995). In the measurable range of nitrogen adsorption (8-20 Å), the micropores with diameter of 8 Å has given the maximum population (about 8 % of all the measurable micropores).

[29] For instance, Y. Mori, T. Iriyama, T. Hashimoto, W. Yamazaki, F. Kawakami, H. Shiroki, and T. Yamabe, *J. Power Sources*, **56**, 205 (1995).
[30] unpublished result.
[31] The molecular structure of PC has been obtained by the semiempirical molecular orbital calculation (MNDO version) based on the optimization of the molecular geometry.
[32] Y. Matsumura, S. Wang, and J. Mondori, *J. Electrochem. Soc.*, **142**, 2914 (1995).
[33] See, e.g., A. Hérold, in *Physics of Intercalation Compounds*, L. Pietronero and E. Tosatti ed., Springer, Berlin (1981).

Chapter 5

Theoretical Study of Li-Doped Amorphous Carbon Materials

1. Introduction

In recent years carbon materials have been extensively studied for its application to anode materials of lithium rechargeable battery [1-5]. Carbon materials do not lead to the formation of lithium dendrite which is one of the most serious problems in applying Li-based materials to an electrode of battery. A high capacity, high output voltage, good reversibility, and long cycle life, which are essential properties for high-performance rechargeable batteries, can be realized by using carbon materials prepared from appropriate starting materials and heat treatment [3,5].

There are two main approaches for the formation of carbon anode materials with high electrochemical performance. One approach is to use highly graphitic carbon materials, in which Li atoms can intercalate the carbon layers up to the so-called C_6Li state indicated in **1**. In this state, Li atoms are located over every three benzene rings [6]. The theoretical capacity of the fully intercalated graphite is 372 mAh/g [3]. Highly graphitic carbons exhibit several advantages such as a constant output voltage and good reversibility. The preparation of highly graphitic carbon materials is

technologically not so difficult; it is prepared by heat treatment at high temperature (2000-3000°C) to achieve a high crystalinity.

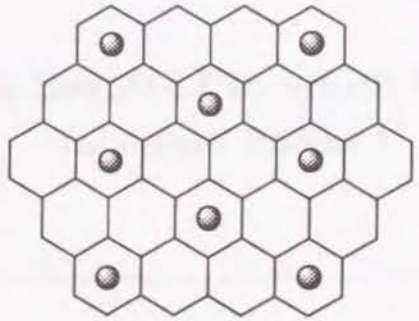

1

Another approach is to utilize amorphous carbon (a-C) materials which have been investigated extensively because of their capacity higher than that of graphite. a-C materials can be classified into two main categories, *i.e.*, soft (graphitizable) and hard (non-graphitizable) carbon materials. The electrochemical properties of such a-C materials as well as highly graphitic carbons were recently reviewed [3].

A remarkably high capacity of 1100 mAh/g which corresponds to the C_2Li state has been reported in polyacenic semiconductor (PAS) materials prepared from heat treatment of phenol-formaldehyde resin at relatively low temperature (600-800°C) [7,8]. The study of the Li storage mechanism and the electronic structure of such highly doped a-C materials is very interesting not only from engineering but also from scientific viewpoints. However, when using a-C materials for Li rechargeable batteries, it has been suggested that there are disadvantages such as Li loss in the first charging-discharging cycle and a large hysteresis in electrode potential vs. capacity profile [3].

The Li storage mechanism of a-C materials have been studied extensively, but still a subject of controversy, due to their disordered

structures which are still not clear at present. A lot of experiments have been performed to explain the unique characteristics of Li-doped a-C materials. For instance, an interesting model that Li atoms are located over every benzene ring (C_2Li) has been proposed on the basis of ^7Li NMR measurements [9]. On the other hand, the high capacity of a-C materials was explained by the presence of three kinds of Li species, *i.e.*, intercalation between the layers, deposition on the surface, and deposition in the edge of the carbon layer(s) [10]. On the basis of a linear relationship between capacity and [H]/[C] molar ratio, a direct correlation between Li and C—H bonds has been also suggested [3,11].

In spite of a large amount of work, there is no satisfactory answer for the Li storage mechanism in a-C materials. Thus, it is important to investigate the electronic and geometric structures of Li-doped a-C materials from a theoretical viewpoint. To the best of our knowledge, there have been a few theoretical studies on the Li-doping mechanism [4,12-14]. These studies have treated mainly the interaction between carbon materials and just one Li atom. We study the electronic and geometrical structures of Li-doped polycondensed aromatic hydrocarbons (PAH) as a function of the number of Li atoms, using a molecular orbital (MO) method. We believe that such analyses can help in deep understanding of the Li-doping mechanism and in the design of high performance a-C materials. In this chapter MO calculational results of Li-doped PAHs with respect to favorable positions for Li atoms are presented. Throughout this chapter, ovalene ($C_{32}H_{14}$) is used as a model structure of a-C.

2. Method of Calculation

MO calculations were performed with the modified neglect of diatomic overlap (MNDO) method [15]. This method has been extensively employed for organolithium compounds because a systematic study on methyllithium [16] suggested that the MNDO method gives quite reasonable results. Moreover, the MNDO method has been successfully applied to structural analyses of organolithium compounds [17]. We used the GAUSSIAN 94 MO program package [18] to perform MO calculations.

As a model carbon structure, ovalene was employed in this study, as mentioned above, because molecules possessing D_{6h} symmetry such as coronene and circumcoronene, which seem to be appropriate for model structures of a-C materials, are technically difficult to treat, due to their degenerate MOs [13]. The geometry of ovalene was fixed within D_{2h} symmetry; all the C—C and C—H bonds were fixed as 1.40 and 1.08 Å, respectively, and all the bond angles as 120°. The [H]/[C] molar ratio, which determines various properties of a-C materials, is 0.44 for ovalene. This value corresponds to that of PAS materials which are heat-treated at 530 °C [19]. All the systems calculated contain even numbers of Li atoms because of the restricted Hartree-Fock method used in this study. Favorable positions for dopant Li were analyzed for various structures in terms of heat of formation (ΔH_f). The net charge of Li atoms was obtained from Mulliken's population analysis [20].

3. Results and Discussion

3.1. Favorable Li positions. Let us first examine favorable positions for dopant Li, using two-Li models with different geometrical structures. Figure 1 indicates seven kinds of Li positions calculated.

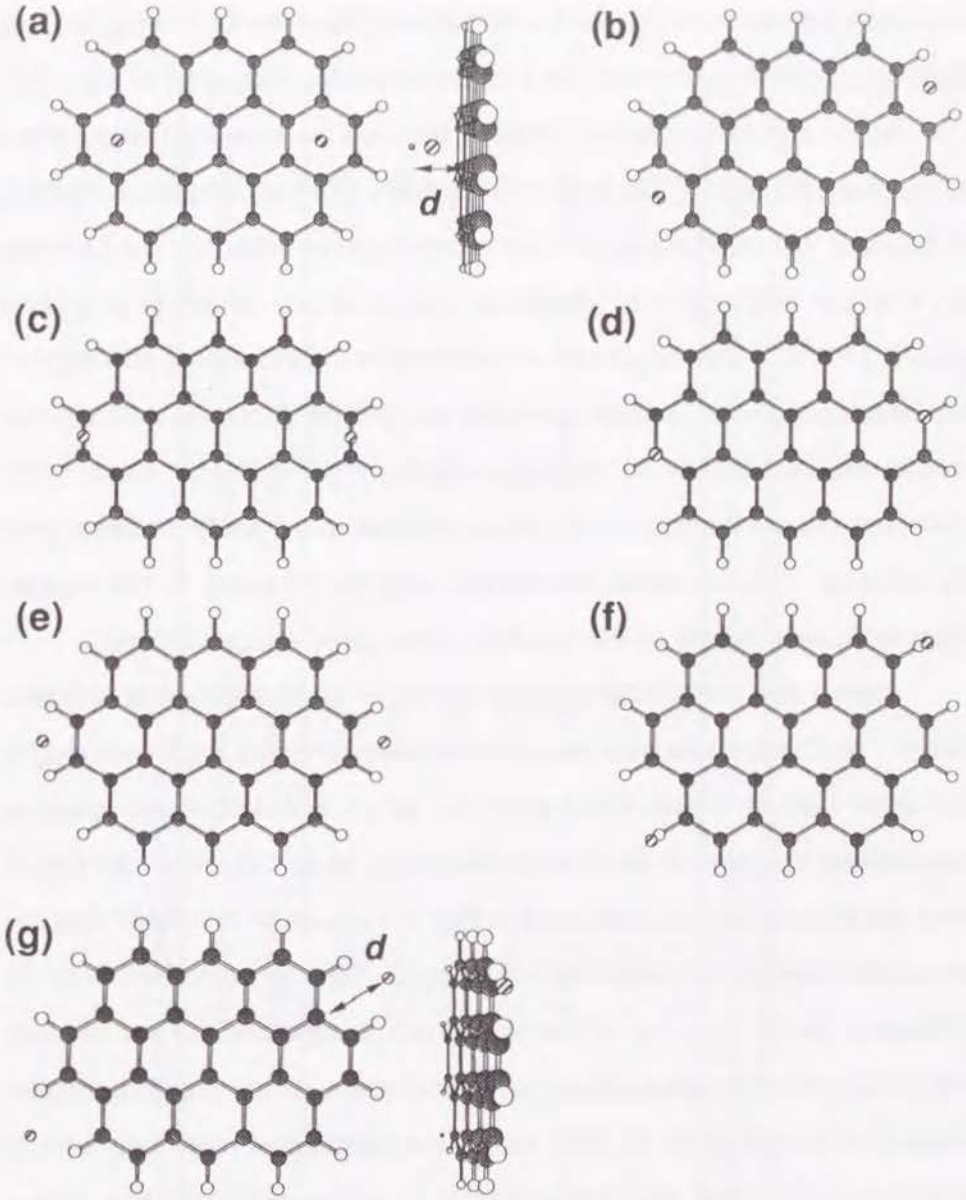

Figure 1. Configurations of two-Li-doped ovalene systems. The Li atoms are located over (a)center of benzene ring (ring-over site), (b)acene-edge (acene-edge site), (c)C-C bond (bond-over site), (d)C atom (atom-over site), (e)phenanthrene-edge (phenanthrene-edge site), and (f)the line on the C—H bond (C—H bond-over site). The vertical distance, *d*, between the Li and the ovalene sheet was optimized. In configuration (g), the Li atoms are located on the same plane with ovalene and the distance between the edge carbon was optimized.

Geometry optimization just for the distance (d) between Li and the ovalene layer was carried out, except for a coplanar model, indicated in Fig. 1(g). Only in this coplanar model, the distance between the Li and the edge carbon atoms was optimized. The heats of formation, relative energies, optimized distances d, and net charges of Li are summarized in Table 1. The Li atoms are found to be completely ionized as a form of Li^{+1} at this doping level ([Li]/[C] = 6%). The calculated overestimation of Li charge is attributed to Mulliken's population analysis since this analysis partitions the two centered atomic orbital (AO) bond population equally for different atoms [20]. However, this does not cause a serious problem in the analyses throughout this chapter. The electrons transferred from the Li atoms to the ovalene sheet are located mainly on the 2pπ-AOs of the carbons near Li atoms.

From Table 1 we can see several interesting characteristics, as indicated below. (i) The position over the center of a benzene ring (ring-over site) is the most favorable site for dopant Li, as is well-known in graphite intercalation compounds such as the first stage of Li-GIC [6]. (ii) For Li ions, the acene-edge site, indicated in Fig. 1(b), is more favorable than the phenanthrene-edge site, indicated in Fig. 1(e). This can be derived from the difference in the number of carbon atoms around the Li ion because negatively charged carbon atoms can stabilize the Li ion electrostatically. There is in general large LUMO (the lowest unoccupied molecular orbital) amplitude in the acene-edge site so that the Li ion is greatly stabilized in this region. (iii) The position over the C—C bond (bond-over site) is slightly more favorable for Li than the site just over the carbon atom (atom-over site). These relative energies per Li atom are approximately 0.5 eV compared with that of the most favorable ring-over site. Note that this value is qualitatively consistent with *ab initio* values, 0.3-0.4 eV, obtained for one Li atom sandwiched between two circumcoronene layers [14]. (iv) A proposed

Table 1. Calculated results of two-Li doped ovalene systems.

Location of Li atoms[a]	Heat of formation (eV)	Relative energy[b] (eV)	Optimized distance, d (Å)	Li charge[c]
(a) ring-over site	6.934	0.0	1.867	1.05
(b) acene-edge site	7.635	0.701	1.713	1.00
(c) bond-over site	7.939	1.005	2.023	0.98
(d) atom-over site	7.980	1.046	2.017	0.98
(e) phenanthrene-edge site	8.842	1.908	1.701	0.97
(f) C–H bond-over site	9.263	2.329	1.703	0.98
(g) coplanar site	9.724	2.790	2.841[d]	1.03

[a]Locations of lithium atoms are shown in Figure 1. [b]Positive value indicate unstable state. [c]Determined by Mulliken population analysis. [d]Distance from the carbon atom indicated by the arrow in Figure 1.

Li—C—H interaction model in Ref. 3 seems not to play an important role in the Li storage mechanism because configuration Fig. 1(f) is quite unstable. The interaction between the Li and H atoms is repulsive, due to the electrostatic repulsion between the Li ion and positively charged H atom (ca. +0.1). We think that the obtained linear relationship between the capacity and the [Li]/[C] ratio [3] is a consequence of some indirect effects such as size and alignment of carbon layers. (v) The coplanar model is also unrealistic because stabilization effect through electrostatic attraction between carbon π-electrons and a Li ion is quite weak.

Some of the results described above can be understood qualitatively by electrostatic interactions between the delocalized π-electrons on the ovalene sheet and a positively charged Li nucleus (attractive) and also the 1s electrons remaining in Li^{+1} (repulsive), though the 1s electrons are not explicitly included in the semiempirical MNDO method. It is found that the favorable Li position is a direct consequence of electrostatic interactions.

The optimized distance *d* shown in Table 1 is 1.867 Å at the ring-over position (Fig. 1(a)), and this value agrees fairly well with the observed distance of the first stage Li-GIC (*d* changes from 1.675 Å to 1.853 Å as a result of Li intercalation) [21]. On the other hand, the *d* values at the bond-over and atom-over positions (indicated in Fig. 1(c) and (d), respectively) are larger than 2 Å, which shows these types of interactions not to be attractive. Thus, the ring-over site is energetically favored for dopant Li.

To get more information about the favorable position for dopant Li, the change in ΔH_f was examined as a function of Li···Li distance by using models indicated in Fig. 2. We fixed one Li atom on a terminal benzene ring and moved another Li atom from the phenanthrene- or acene-edge site to the nearest neighboring benzene ring. We kept the Li···ovalene nonbonded distance to be 2 Å. As we see in Fig. 2 (a), the position of Li at site B is

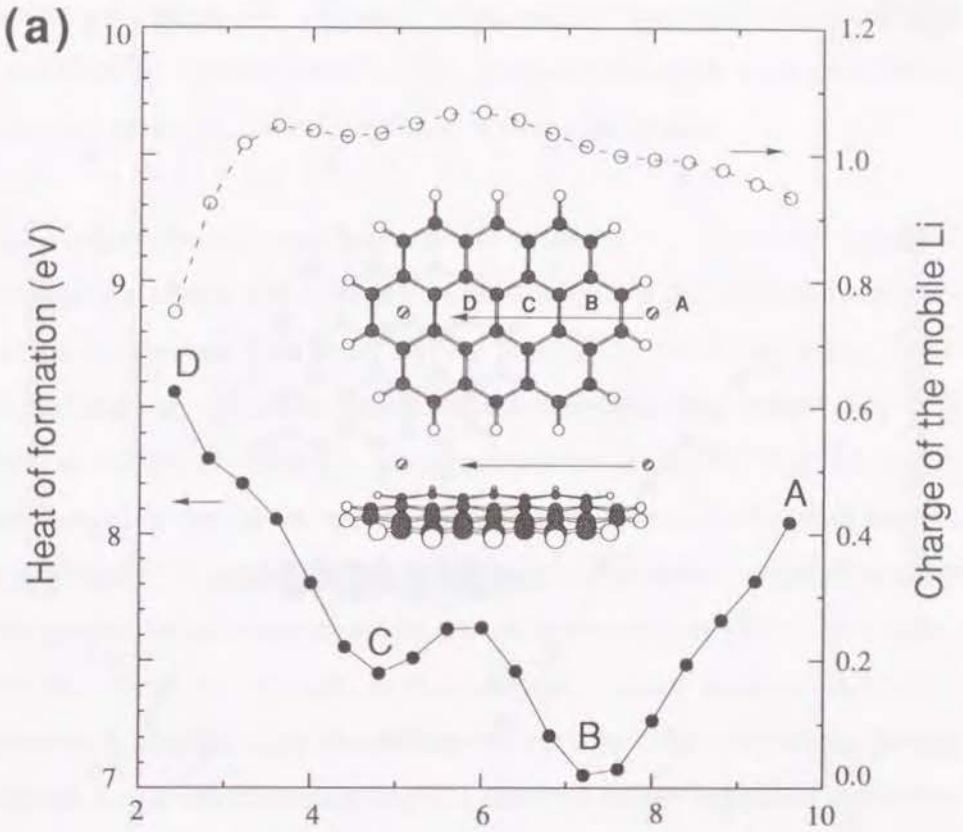

Figure 2. The energy profiles of the two-Li-doped systems with regard to the Li position. One Li atom is fixed at the center of the ring, and another Li atom is moved from (a)the phenanthrene-edge, and (b)the acene-edge. The heat of formation (closed circle) and the charge of the moved Li (open circle) are plotted as a function of Li—Li distance.

much more stable than the phenanthrene-edge site, A. It is important to note that the migration of Li from site A to site B has no cost of activation energy. This suggests that Li can enter very easily between the carbon layers. Further approach to the fixed Li makes the system energetically unstable, due to the electrostatic repulsion between the Li ions. Although Li can be located

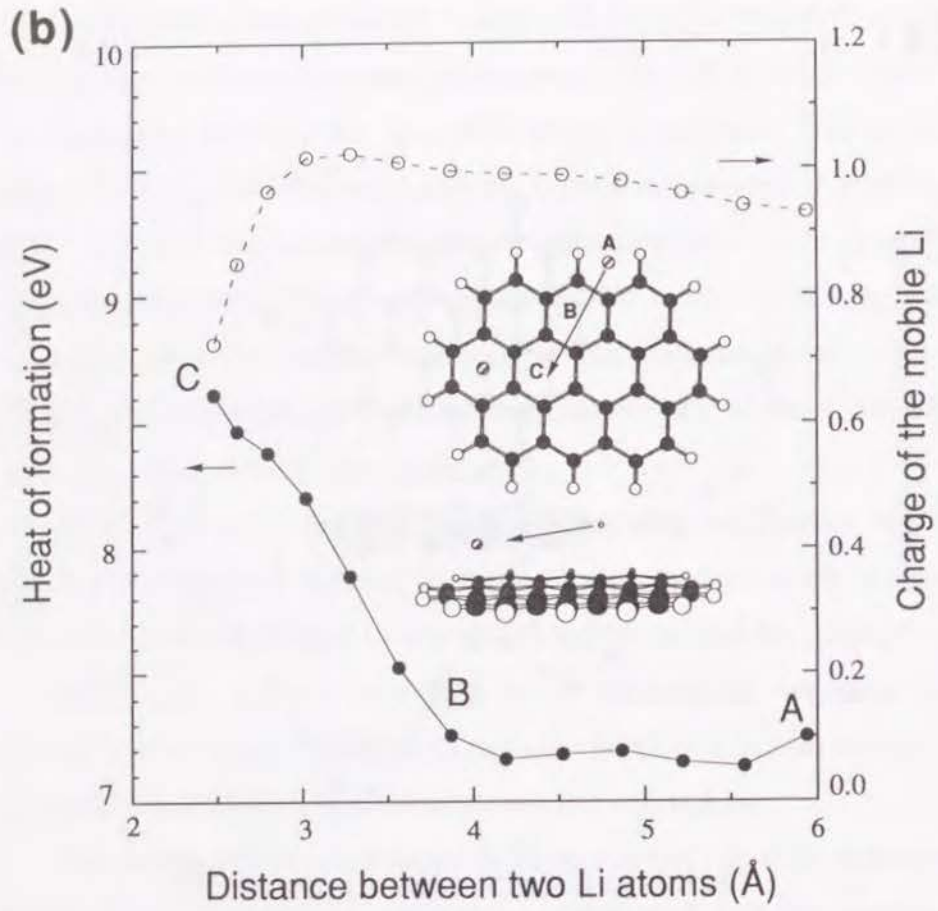

Figure 2. continued.

on site C, the occupation of the nearest neighbor site D is very difficult as a result of strong electrostatic repulsion.

The migration from the acene-edge was also investigated, as shown in Fig. 2(b). We see that acene-edge site A is quite favorable for Li, compared with phenanthrene-edge site; interestingly, the stability at site A is at the same level of that of ring-over site B. However, when site C is occupied by dopant Li, strong electrostatic repulsion works, and as a consequence, the system becomes energetically unstable. From the great stability at site B in Fig. 2(b), we can see that the C_6Li configuration can be formed without

electrostatic repulsion. An observed remarkable decrease in the Li charge at site D in Fig. 2(a) and site C in Fig. 2(b) (~+0.75) would be derived from a decrease in the electrostatic repulsion between the Li ions.

3.2. Intercalation and adsorption models. Having described favorable positions for dopant Li, in this section it is described the properties of model systems consisting of two dopant Li and two ovalene sheets. Figure 3 shows two model structures and their ΔH_f. One model (Fig. 3(a)) has two dopant Li inside the two layers, and the other (Fig. 3(b)) has two Li atoms outside the layers; we call them intercalation and adsorption models, respectively. A great stabilization energy is found in the intercalation model compared with the adsorption one, due to the structure of Li ions sandwiched by two negatively charged ovalene sheets. Thus, in an actual doping process in graphite or a-C materials, we infer the following doping process occurs; In the initial doping stage Li adsorbed on the outside of the carbon layers immediately migrates into the layers, and the adsorbed Li remain after

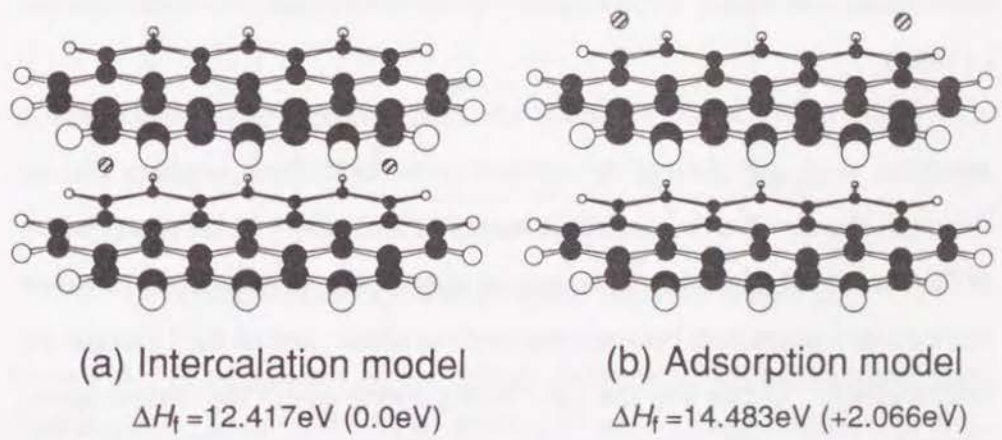

Figure 3. Comparison of the heat of formation of the two Li atoms in (a)intercalation and (b)adsorption models. In the parenthesis the relative energy is indicated.

filling the interlayer sites. An observation [22] that in disordered coke carbon materials a change in interlayer distance is larger in a low doping stage would support this result.

The most interesting problem is how many Li atoms can coexist with the two ovalene sheets. The difference in the energy profiles between intercalation and adsorption models was studied by using two models shown in Fig. 4(a) and (b), where the interlayer distance is fixed at 4.0 Å and all the Li···ovalene distance is kept at 2.0 Å. Assuming first the C_6Li configuration, energy profiles were examined with respect to the positions of newly added two dopant Li in the intercalation and adsorption models. In these models, [Li]/[C] ratio is 22 % which is larger than that of C_6Li state (17 %). When two Li atoms intercalate from the phenanthrene-edges simultaneously (Fig. 4 (a)), the ΔH_f of the system increases largely after passing the peripheral C—C bond. This result shows that the ratio of intercalating Li atoms cannot exceed that of the C_6Li configuration. In this process, the Li charge of approximately 1.0 does not decrease, so that this destabilization is clearly a consequence of the electrostatic repulsion between Li atoms.

Since newly added Li atoms are fully ionized, strong electrostatic repulsion work and prevent the occupation at the nearest neighbor site, as shown in Fig. 2. We find that the charges of intercalant Li are independent of the number of adsorbing Li as well as the number of intercalant Li atoms (ten Li atoms intercalate between two ovalene sheets, and all the Li atoms are fully ionized). In this way the C_2Li configuration *within the carbon layers* cannot be expected from our calculations. The fact that the C_2Li state with an intercalation structure can be formed only under an extreme condition of 50 kbar and 280 °C [23] supports our result. The transferred electrons are

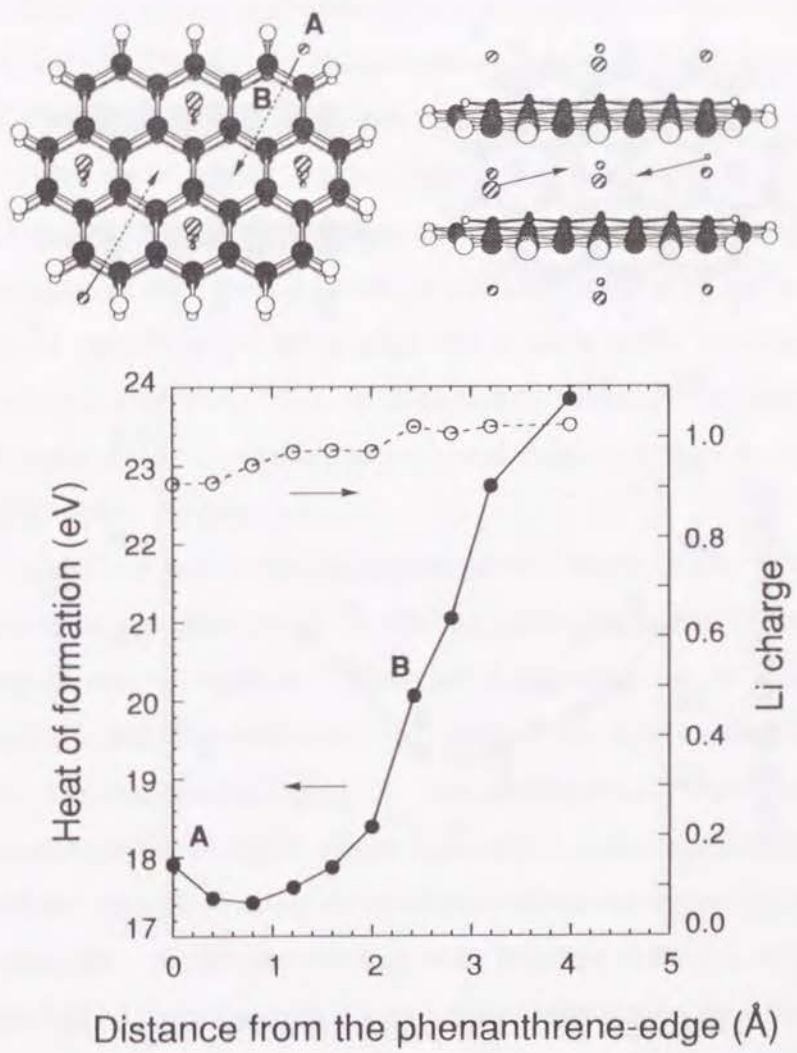

Figure 4. Comparison of the energy profiles of (a)intercalation and (b)adsorption. In the 12 Li doped systems (4 and 8 Li atoms intercalate and adsorb, respectively), extra two Li atoms (a)intercalate and (b)adsorb as indicated by the arrow. Closed and open circles show the heat of formation and charge of the extra Li, respectively.

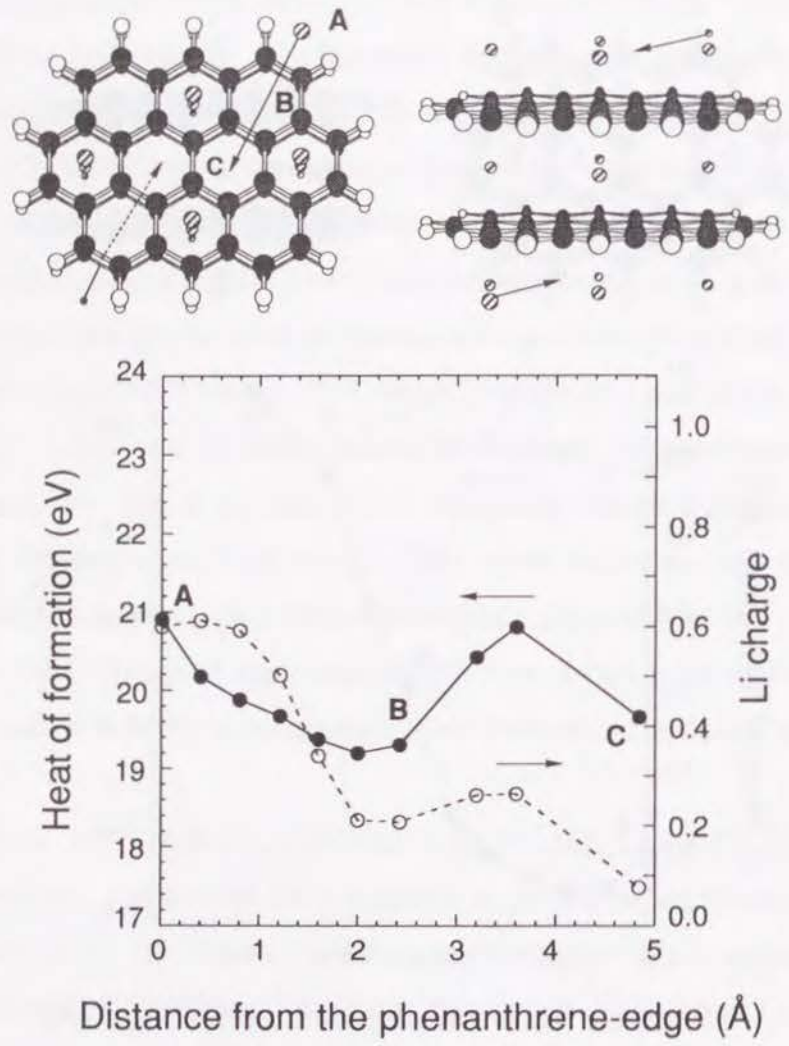

Figure 4. continued.

found to spread on the carbon atoms of two ovalene sheets, especially on the carbons near the Li atoms.

We look in detail at the change of ΔH_f in Fig. 4(a). The calculated local minimum of ΔH_f at distance of 0.8 Å suggests possible existence of loosely trapped Li ions at the phenanthrene-edge site. This is an interesting result because it shows that Li ions can exist in the periphery of carbon clusters after the so-called C_6Li sites, indicated in **1**, are fully occupied. The occupation at the acene-edge site sandwiched by the two carbon layers can also occur even after the C_6Li configuration is completed. As mentioned above, Li trapped at the acene-edge site is more stable than that at the phenanthrene-edge site. Thus, we think that the observed high doping level in a-C materials can be ascribed to such local trapping sites in the peripheral region of carbon clusters.

Let us next look at the adsorption model, shown in Fig. 4(b). Two local minima are clearly seen in the ΔH_f curve (at B and C sites), after passing the outer C—C bond. Thus, site B and site C can be occupied by dopant Li. It is noteworthy that the charge of the newly added Li is less positive than that of intercalating Li. The calculated Li charge is in contrast to the results shown in Fig. 3, where intercalant Li ions are stabilized greatly by both the upper and lower carbon layers which are negatively charged. The adsorption profile provides us with possible existence of partially charged Li, and it also suggests a possibility of high doping level than that of the C_6Li state in graphite. We consider that these partially charged Li atoms should form molecular clusters, as discussed below. It is noted that the adsorption of Li atoms on the carbon layer was already confirmed in corannulene [24]. We suppose that very high capacity of a-C materials can be derived from the adsorption on the carbon layer. The limit of adsorption will be discussed later.

3.3. Intercalation mechanism. Intercalant concentration higher than that of C_6Li state is not realistic, as shown in the previous section except for the edge sites. The next question is whether or not extra Li atoms can exist if D is larger than 4.0 Å. This question arises from the observed large interlayer separation in PAS materials which can contain extremely high dopant Li concentrations [8]. The relation between the interlayer separation and dopant concentration was evaluated using a model containing six Li atoms sandwiched by the two ovalene sheets, as shown in Fig. 5. The obtained energy curve suggests that there are three different regions as a function of D.

When $D > 7$ Å, the electrostatic attractions between the upper (lower) Li and the upper (lower) carbon layer are supposed to be dominant. This state can be regarded as two isolated adsorption models. In the second region of $5.4 < D < 7$ Å, the electrostatic repulsion between the upper Li and lower Li atoms are stronger than those in $D > 7$ Å. When $5.4 < D < 7$ Å, the charge of upper Li atoms are decreased as D decreases. This behavior occurs in order to reduce the electrostatic repulsion between the positively charged Li atoms. In the third region of $D < 5.4$ Å, a remarkable decrease in ΔH_f occurs with increasing Li charge. An important factor in this region is the electrostatic attractions between Li ions and two carbon layers (upper and lower), providing the most stable state though we considered in the previous section such a state is unrealistic. It is found that separation of layers up to 7 Å is required for realization of the both-side adsorption in one layer. Since formation of such a structure is actually difficult, we think that a "house of cards" structure proposed by Dahn et al. [25] and a cyclophane-type structure proposed by us, indicated in the left and right illustrations of **2**, respectively, are more realistic models.

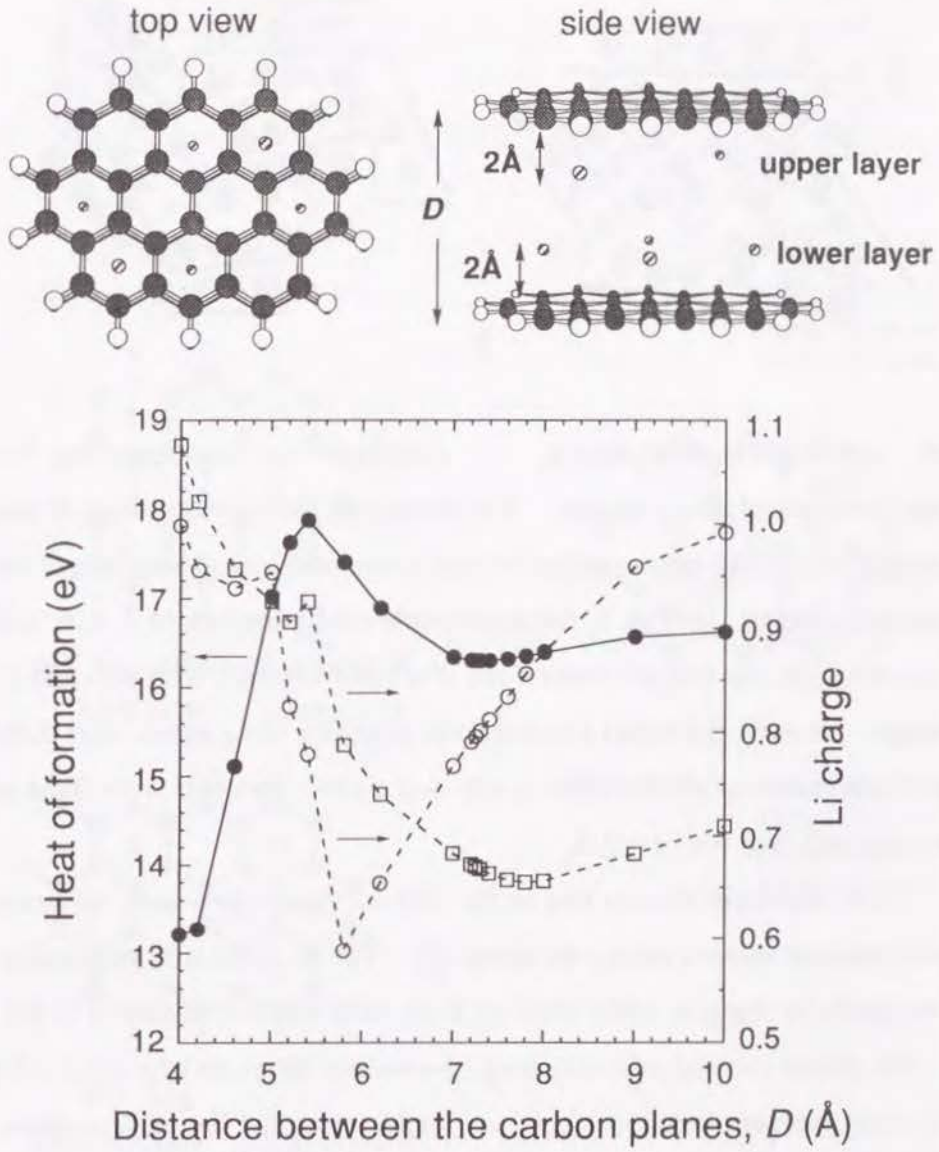

Figure 5. The energy profile plotted vs. the interlayer distance, D, of the six-Li-intercalated system. The distance between the upper (lower) Li and the upper (lower) ovalene is fixed as 2.0 Å. The ΔH_f, the average charge of the upper and lower Li atoms are shown by closed circles, open circles, and open squares, respectively.

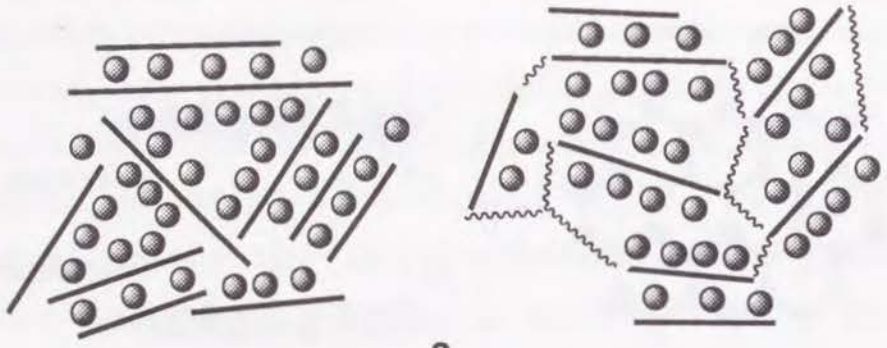

2

3.4. Adsorption mechanism. Adsorption is an interesting but very complicated phenomenon. We showed in the previous section that partially charged Li atoms can be formed theoretically on the surface of the adsorption model. In Fig. 6, the most stable configurations of 2, 4, 6, and 8 Li atoms on one side of ovalene are displayed together with ΔH_f and Li charges. In two- and four-Li systems the positions of Li atoms were fully optimized, whereas the positions in six- and eight-Li systems were fixed at the ring-over sites with $d = 2$ Å.

It is important to note that in the four-Li system two quite different configurations showed almost the same ΔH_f. The Li atoms in configuration A are partially charged, while those of B are fully ionized, as shown in Fig. 6. The former showed relatively long Li···ovalene distances ($d = 2.1$-2.3 Å) indicating weaker interactions between the Li atoms and the ovalene sheet. The latter has a shorter Li···ovalene distance of 1.84 Å as a consequence of strong electrostatic attractions between the Li atoms and the ovalene sheet.

These two four-Li systems are characterized well by MO interaction diagrams shown in Fig. 7. No orbital mixing was observed in the both configurations. This result shows that a dominant factor in Li-doped carbon materials is electrostatic interactions which come from a charge-transfer

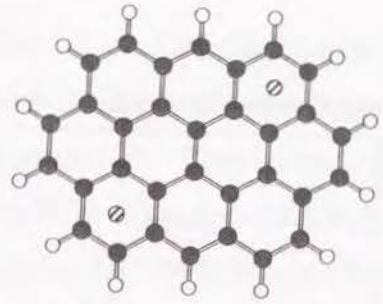

(a) Li_2

ΔH_f=6.944eV charge 1.00

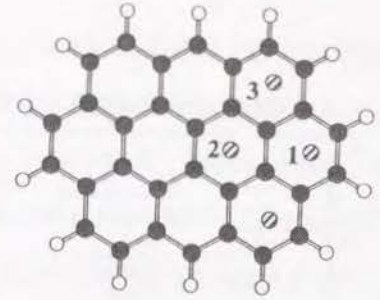

(b) Li_4 configuration A

ΔH_f=8.214eV charge (1) 0.30
charge (2) 0.26
charge (3) 0.70

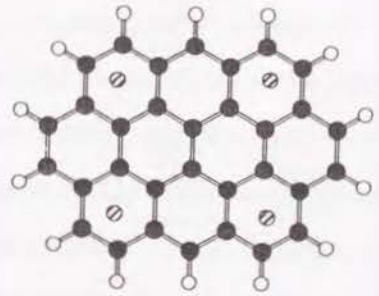

(c) Li_4 configuration B

ΔH_f=8.217eV charge 0.98

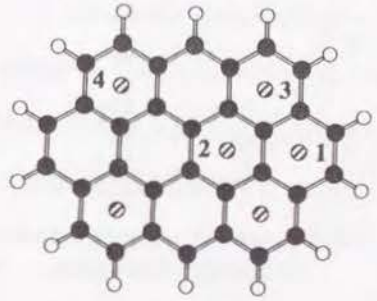

(d) Li_6

ΔH_f=10.037eV charge (1) 0.37
charge (2) 0.23
charge (3) 0.68
charge (4) 0.96

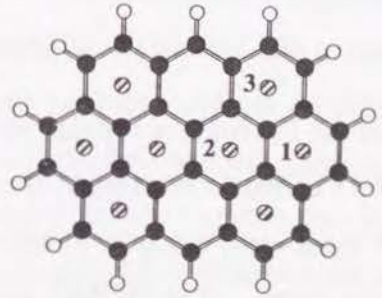

(e) Li_8

ΔH_f=12.377eV charge (1) 0.32
charge (2) 0.34
charge (3) 0.68

Figure 6. The most stable configurations of 2, 4, 6, and 8 Li-atoms adsorbed ovalene system. For the two and four Li systems, the positions of Li atoms are fully optimized, while those of six and eight Li systems are fixed at the center site keeping $d = 2$ Å. In the four Li doped system, two quite different configurations, A and B, with almost the same energies were obtained.

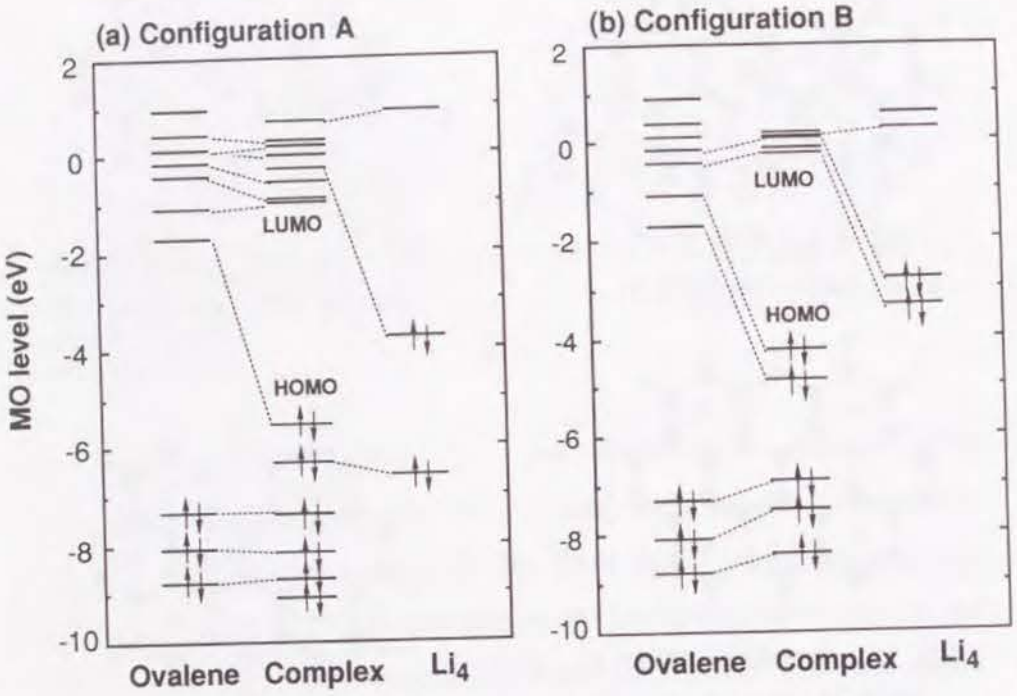

Figure 7. Calculated MO diagram of the four Li adsorbed ovalene systems with configurations (a)A and (b)B.

reaction. In configuration A, the electrons of the Li atoms occupying the next highest occupied MO (next HOMO; HOMO-1) remain unchanged after the interactions, whereas in configuration B significant electron transfer occurs from the four Li atoms to the ovalene sheet. The HOMO and (HOMO-1) of the complex in configuration B are composed of the ovalene's (LUMO+1) and LUMO, respectively. On the other hand, the (HOMO-1) of the complex in configuration A comes from the Li AOs. This remarkable difference stems from the large stability of the next HOMO in model A. In other words, in configuration A a stable Li_4 molecule is formed.

Small Li clusters with 2-30 atoms have been extensively studied [26-28] from the viewpoints of quantum size effects [29] and magic numbers

[30]. From these theoretical studies, it has been clarified that planar Li clusters with 2-10 atoms favor a hexagonal structure rather than a square structure [26]. The nearest neighbor atomic distance of a neutral hexagonal cluster is 2.7-3.0 Å [26] and oxidation of such clusters is supposed to lengthen the Li—Li bonds. On the basis of these calculation results, one can expect the formation of small Li (cation) clusters on the carbon layers. Because the Li cluster is commensurate with the carbon lattice, only several atoms can cohere to keep the Li—Li bond length of ~3 Å. Note that the Li—Li bond length of the clusters is 2.7-3.0 Å while the distance between the nearest neighbor ring-over sites in graphite is 2.424 Å. It has been reported that Li clusters commensurate with the graphite lattice are formed on the graphite surface by injection of Li atoms and that heating up to 200 °C leads to the formation of incommensurate Li clusters with a diameter of ~100 Å [31].

We can see coexistence of ionized and clustered Li species in the most stable six-Li system. In actual Li-doped a-C materials, Li clusters and Li ions probably coexist on the surface of the carbon layer. From ESR analyses, the spin-orbit coupling of conduction electrons was enhanced by Li doping, which suggests that the charge of dopant Li decreases as doping proceeds [32]. Although the absolute stability of eight-Li system in Fig. 6(e) cannot be confirmed, we suppose this configuration to be unrealistic due to its commensurate structure. The deposition of Li on the carbon layer is one of the key factors in order to clarify a high capacity of a-C materials.

3.5. Discharging mechanism. Lithium loss in the first charging-discharging cycle is a serious problem in a-C materials used in Li ion rechargeable battery because the loss reduces its reversible capacity. For instance, the irreversible capacity of PAS material is 250mAh/g which

corresponds to 29% of the total reversible capacity (850mAh/g) [7]. Discharging process is carried out by removing electrons from the negatively charged carbon materials, releasing Li^{+1} ions simultaneously into electrolyte. Therefore Li loss would originate from the formation of still unknown Li species possessing considerably high ionization potential. In this section, the reversibility of Li-doped ovalene systems is discussed on the basis of two characteristic models indicated in Fig. 6 (b) and (c).

In four-Li-doped ovalene system with configuration B, four 2s electrons of Li atoms transferred to ovalene, as shown in Fig. 7(b). It is therefore possible to remove the four electrons from the negatively charged ovalene, that is, all the Li^{+1} ions of configuration B can be undoped. Similar discharging process will occur in the intercalation models because the intercalating Li atoms are fully ionized. On the other hand, in the complex with configuration A, two 2s electrons remained on the *Li molecule* and the corresponding MO level (HOMO-1) is relatively low, as shown in Fig. 7(a). However, in this case, at least two electrons transferred to the ovalene sheet can be removed with releasing two Li^{+1} ions, resulting in two-Li adsorbed complex. We think that the highly-charged two Li atoms on site 3 of configuration A should be undoped first. As is already discussed in Fig. 2, the two remaining Li atoms will be fully ionized and separated well, followed by release of the remaining two electrons and the two Li^{+1} ions. These stepwise undoping process of the configuration A would cause a large hysteresis in the electrode potential vs. capacity profile [8].

We consider that the observed Li loss does not come from the adsorbing Li atoms nor from the intercalating Li species. As suggested in literature [32,33], we think that stable states such as the formation of Li-C covalent bonds and still unknown side-reactions of electrolytes are the causes of the irreversible capacity loss in Li ion rechargeable battery.

3.6 Heteroatomic effects. Let us finally look at heteroatomic effects on the doping mechanism in a-C materials. So-called heterographite, in which a part of carbon atoms are substituted by heteroatoms with various atomic ratios, *i.e.*, BC_3, BC_2N, and C_5N have been synthesized so far using chemical vapor deposition (CVD) techniques [34,35]. The changes in the electronic properties of graphite caused by heteroatom substitution are of great interest for graphite-intercalation compounds [36-38]. Several kinds of heterographite such as BC_2N have been tested as an anode material of battery, but remarkable capacity enhancement has not been observed so far [39]. For the design of a new type of a-C materials, it is important to examine the Li storage mechanism in heteroatomic systems from a theoretical viewpoint.

MO calculations were performed on ovalene-based heteroatomic systems, $B_8C_{24}H_{14}$ and $C_{24}N_8H_{14}$. The calculated MO levels as well as those of non-substituted ovalene are shown in Fig. 8. Since a boron atom has only three valence electrons, its electron deficiency largely stabilizes the MO levels in the frontier orbital region, as indicated in Fig. 8(b). These changes in such MO levels, especially low-lying unoccupied levels, would enhance the ionization of intercalating Li atoms. On the other hand, a nitrogen atom offers two electrons for 2pπ-AO and thus destabilizes the MO levels in the frontier orbital region, as seen in Fig. 8(c). Thus, the nitrogen substitution would suppress the ionization of intercalating Li atoms.

We first examined the intercalation model for heteroatomic systems by using models similar to Fig. 4(a). The obtained energy profiles gave a result similar to the nonsubstituted system (Fig. 4(a)) which contains fully ionized intercalating Li atoms. An observed difference is the position of the local minimum of ΔH_f. The most preferred position for newly added Li was 1.6Å and 0.4Å apart from the phenanthrene-edge for the boron- and

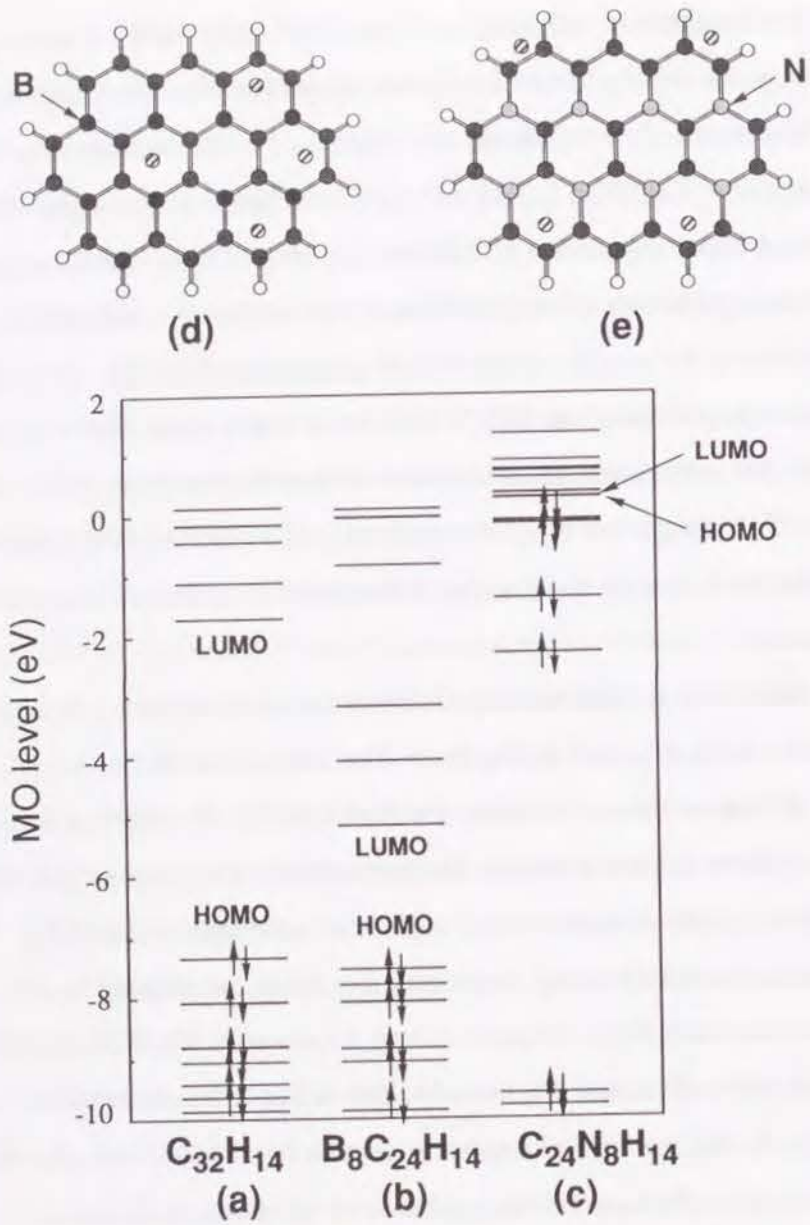

Figure 8. Comparison of MO levels of neutral (a)ovalene, (b)boron substituted ovalene, and (c)nitrogen substituted ovalene systems. The positions of the heteroatoms are indicated by arrows in (d) and (e). The optimized geometry of the four-Li-doped boron-substituted system obtained from configuration A is shown in (d). In (e), the optimized geometry of the four Li doped nitrogen substituted system obtained from configuration B is shown.

nitrogen-substituted systems, respectively, while that of the non-substituted system is 0.8Å (see Fig. 4(a)). Thus, the local trapping site for Li described in Fig. 4(a) exists also in these heteroatomic systems. Difference in the local minimum position among the non-, boron- and nitrogen-substituted ovalenes can be explained from a difference in the π-electron densities.

In case of adsorption, the commensuration of Li clusters limits the growth of larger clusters. The barriers found in the bond-over and atom-over positions would originate from the π-electrons of the carbon layer. Therefore reduction of the π-electron density occurring in boron substitution is expected to weaken the commensuration. Optimized geometries of boron-substituted ovalene of configuration A and nitrogen-substituted one of configuration B are shown in Fig. 8 (d) and (e), respectively. Although we tried to optimize the geometry of configuration A for boron-substituted ovalene, one of the Li atoms moved to the nearest neighboring ring-over site. Because the boron substitution enhances the ionization of dopant Li (+0.81~+0.98), the electrostatic repulsion between Li atoms are stronger in boron-substituted ovalene. This effect would lead to the formation of smaller Li clusters, as seen in Fig. 8(d). On the other hand, when we tried to optimize configuration B for nitrogen-substituted ovalene, two Li atoms moved out of the ovalene sheet. This is because the unoccupied levels of nitrogen-substituted ovalene are very much destabilized and as a result the system has no electron affinity enough for housing four Li ions.

On the basis of the results obtained in these calculations, we cannot expect a higher capacity in heteroatomic a-C materials. Furthermore, odd numbers of heteroatoms will bring an unpaired electron like PAHs with odd numbers of carbon atoms [40], resulting in a covalent-like bond with Li. Hence heteroatomic system would increase amount of the irreversible Li atoms.

4. Conclusion

The geometric and electronic structures of Li-doped carbon materials have been studied using ovalene as a basic carbon structure on the basis of semiempirical MO analyses. It is found that the ring-over site is most favorable for dopant Li and that the activation energy for the migration of Li ion to the neighboring ring-over site is about 0.5 eV. We have examined two kinds of Li states which are classified into intercalation and adsorption. Intercalant Li which is almost completely ionized is stabilized well by both the negatively-charged upper and lower carbon layers, which results at most in the formation of the C_6Li configuration. On the other hand, adsorbing Li atoms on the carbon layer can form small Li cation clusters concomitant with fully ionized Li atoms. Very small Li clusters are allowed to exist only on the carbon layer surface because of the restriction of the Li—Li distance of such clusters. Heteroatomic substitutions are found not to enhance a doping level from a theoretical aspect. Two major guiding principles for preparing high-capacity a-C materials are indicated below. (i) For a higher doping level, the acene-edge is more favorable than the phenanthrene-type. (ii) The interlayer distance of the carbon layers should be separated well to make Li clusters on the both sides of a single carbon layer. However, it is unrealistic to separate the carbon layers up to 7 Å, as mentioned above. We think that the two models with "house of cards" and cyclophane-type structures, indicated in **2**, are possible structures.

References

[1] T. Kitamura, T. Miyazaki, and K. Kawagoe, *Synth. Met.*, **18**, 537 (1987).

[2] K. Tanaka, S. Yata, and T. Yamabe, *Synth. Met.*, **71**, 2147 (1995).

[3] J. R. Dahn, T. Zheng, Y. Liu, and J. S. Xue, *Science*, **270**, 590 (1995).

[4] K. Tanaka, M. Ata, H. Kimura, and H. Imoto, *Bull. Chem. Soc. Jpn.*, **67**, 2430 (1994).

[5] D. Guyomard and J. M. Tarascon, *Adv. Mater.*, **6**, 408 (1994).

[6] (a) N. A. W. Holzwarth, S. Rabii, and L. A. Girifalco, *Phys. Rev.*, **B18**, 5190 (1978). (b) N. A. W. Holzwarth, L. A. Girifalco, and S. Rabii, *Phys. Rev.*, **B18**, 5206 (1978).

[7] S. Yata, Y. Hato, H. Kinoshita, N. Ando, A. Anekawa, T. Hashimoto, M. Yamaguchi, K. Tanaka, and T. Yamabe, *Synth. Met.*, **73**, 273 (1995).

[8] S. Yata, H. Kinoshita, M. Komori, N. Ando, T. Kashiwamura, T. Harada, K. Tanaka, and T. Yamabe, *Synth. Met.*, **62**, 153 (1994).

[9] K. Sato, M. Noguchi, A. Demachi, N. Oki, and M. Endo, *Science*, **264**, 556 (1994).

[10] Y. Matsumura, S. Wang, and J. Mondori, *Carbon*, **33**, 1457 (1995).

[11] T. Zheng, J. S. Xue, and J. R. Dahn, *Chem. Mater.*, **8**, 389 (1996).

[12] C. S. Bahn, W. J. Lauderdale, and R. T. Carlin, *Int. J. Quant. Chem.*, **29**, 533 (1995).

[13] K. Nagata, H. Ago, K. Yoshizawa, and T. Yamabe, *Proc. Annu. Meet. Chem. Soc. Jpn.*, 1PC029, Tokyo, March (1996).

[14] D. J. Hankinson and J. Almlöf, *J. Mol. Struc., THEOCHEM*, in press.

[15] M. J. S. Dewer and W. Thiel, *J. Am. Chem. Soc.*, **99**, 4899 (1977).

[16] E. Kaufmann, K. Raghavachari, A. E. Reed, and P. R. Schleyer, *Organometallics*, **7**, 1597 (1988).

[17] L. A. Paquette, W. Bauer, M. R. Sivik, M. Bühl, M. Feigel, and P. R. Schleyer, *J. Am. Chem. Soc.*, **112**, 8776 (1990).

[18] M. J. Frisch and J. A. Pople *et al.*, GAUSSIAN 94, Gaussian Inc., Pittsuburgh, Pennsylvania, PA (1995).
[19] K. Tanaka, T. Koike, T. Yamabe, J. Yamauchi, Y. Deguchi, and S. Yata, *Phys. Rev.*, B**35**, 8368 (1987).
[20] R. S. Mulliken, *J. Chem. Phys.*, **23**, 1841 (1955).
[21] D. Guerard and A. Herold, *Carbon*, **13**, 337 (1975).
[22] Y. Mori, T. Iriyama, T. Hashimoto, S. Yamazaki, F. Kawakami, H. Shiroki, and T. Yamabe, *J. Power Sources*, **56**, 205 (1995).
[23] J. Conard, V. A. Nalimova, and D. Guerard, *Mol. Crys. Liq. Cryst.*, **245**, 25 (1994).
[24] M. Baumgarten, L. Gherghel, M. Wagner, A. Weitz, M. Rabinovitz, P. C. Cheng, and L. T. Scott, *J. Am. Chem. Soc.*, **117**, 6254 (1995).
[25] Y. Liu, J. S. Xue, T. Zheng, and J. R. Dahn, *Carbon*, **34**, 193 (1996).
[26] S. Quassowski and K. Hermann, *Phys. Rev.*, B**51**, 2457 (1995).
[27] (a) B. K. Rao, S. N. Khanna, and P. Jena, *Phys. Rev.*, **B36**, 953 (1987). (b) P. Jena, B. K. Rao, and R. M. Nieminen, *Solid State Commun.*, **59**, 509 (1986).
[28] Y. Ishii, S. Ohnishi, and S. Sugano, *Phys. Rev.*, **B33**, 5271 (1986).
[29] J. C. Boettger and S. B. Trickey, *Phys. Rev.*, **B45**, 1363 (1992).
[30] W. D. Knight, K. Clemenger, W. A. Heer, W. A. Saunders, M. Y. Chou, and M. L. Cohen, *Phys. Rev. Lett.*, **52**, 2141 (1984).
[31] Z. P. Hu and A. Ignatiev, *Phys. Rev.*, **B30**, 4856 (1984).
[32] K, Tanaka, H. Ago, Y. Matsuura, T. Kuga, T. Yamabe, S. Yata, Y. Hata, and N. Ando, *Synth. Met.*, submitted.
[33] For instance, R. Fong, U. Sacken, and J. R. Dahn, *J. Electrochem. Soc.* **137,** 2009 (1990).
[34] J. Kouvetakis, R. B. Kaner, M. L. Sattler, and N. Bartlett, *J. Chem. Soc., Chem. Comm.*, 1758 (1986).
[35] A. W. Moore, S. L. Strong, G. L. Doll, M. S. Dresselhaus, I. L. Spain, C. W. Bowers, J. P. Issi, and L. Piraux, *J. Appl. Phys.*, **65**, 5109 (1989).
[36] M. O. Watanabe, S. Itoh, K. Mizushima, and T. Sasaki, *J. Appl. Phys.*, **78**, 2880 (1995).

[37] P. Saalfrank, W. Rümler, H. U. Hummel, and J. Ladik, *Synth. Met.*, **52**, 1 (1992).
[38] J. P. LaFemina, *J. Phys. Chem.*, **94**, 4346 (1990).
[39] (a) M. Ishikawa, T. Nakamura, M. Morita, Y. Matsuda, S. Tsujioka, and T. Kawashima, *J. Power Sources*, **55**, 127 (1995). (b) M. Morita, T. Hanada, H. Tsutsumi, Y. Matsuda, and M. Kawaguchi, *J. Electrochem. Soc.*, **139**, 1227 (1992).
[40] K. Yoshizawa, K. Okahara, T. Sato, K. Tanaka, and T. Yamabe, *Carbon*, **32**, 1517 (1994).

GENERAL CONCLUSION

In this thesis, the author has studied electronic properties of functional organic systems on the basis of quantum chemistry and solid state physics, in order to search their new possibilities and to develop the applications. The focus has been put on polymers and pyrolyzed polymers because they are appropriate to practical use on account of their processibility, easiness of large surface manufacturing, light weight, and stability.

In Part I, the electronic and magnetic properties of the copolymer, poly[disilanylene(thienylene)$_n$] (n=1-5), have been investigated. From crystal orbital calculations, it is suggested that the planar structure is the most stable and that there is only a slight hyperconjugation of Si 3p orbital suggesting rather weak π-σ interaction. By using this large cut-off effect of the silicon unit, we have proposed the concept of a modified polaronic ferromagnet, in which the polaronic spin is generated in each oligothienylene unit and these spins interact ferromagnetically through silicon sp^3-hybridized orbital working as the through-space coupler. From the experiment of p-type doped polymers, the nature of the spin has been found to change with respect to the number of thiophene rings of the thienylene unit, and the polaronic spin has been confirmed in the polymers including ter-, quater-, and quinquethienylene units. However, the spin concentration was considerably small and no magnetic interaction was observed. This small spin concentration has been inferred to come from the aggregation of oligothienylene units around the acceptor. Although the interaction between spins was not observed, the author supposes the present concept provides the new possibility for the organic ferromagnetic polymer.

In Part II, two characteristic narrow-gap polymers have been studied. First, the electronic structures of the poly(thienothiadiazole) and copolymers containing thienothiadiazole and thiophene with the ratio of 1:1 and 1:2 have been explored. The copolymer with 1:2 ratio possesses a very small band gap. From *ab initio* crystal orbital calculations, an interesting transition of the electronic structure has been confirmed in poly(thienothiadiazole). It has been found that the narrow-gap nature of the copolymer with 1:2 ratio is substantially originates in the nonbonding molecular orbitals of tetramethyleneethane and that the π-conjugation is not developed in all the polymers. Second, the effect of a magnetic field on the electronic property of polyacene, which is predicted to have a considerably small band gap, has been studied based on the Hückel Hamiltonian by introducing the vector potential. It has been clarified that the band gap and total energy of polyacene change periodically with increasing a magnetic field.

In Part III, the electronic structure and the Li-doping mechanism of the amorphous carbon, polyacenic semiconductor (PAS) material, have been researched. From the electron spin resonance (ESR) spectra, the spin-orbit interaction as well as metallic transition have been confirmed. The former suggests the possible migration of a conduction electron to a Li dopant through a certain activation process. By using the decomposition reaction of a series of alkali azide, the PAS material has been successfully doped with alkali metals. The observed linear dependency of the ESR linewidth upon the atomic number of dopant manifests the spin-orbit interaction. The ^{7}Li nuclear magnetic resonance (NMR) analysis showed Knight shift up to 9 ppm. This result has been understood in terms of the Fermi contact interaction between a Li nucleus and a conduction electron. It has also been suggested that a Li dopant can move more freely compared with that in

graphite. The microporous structure of the PAS material has been studied through the adsorption of Xe atoms using ^{129}Xe NMR. It becomes clear that the PAS material contains a great number of micropores with the diameter of 7.7±1.6 Å. Moreover, we have firstly investigated the change in the microporous structure brought about by the Li-doping, and found that almost all of the micropores are filled with the solvent molecules. From the semiempirical molecular orbital calculations, two interesting new findings have been obtained. The first one is the possibility of forming Li small cationic cluster on the surface of the carbon layer and the second is the large difference in the stability of Li dopants with respect to the edge-structure of a carbon layer. Based on the result, the author can propose two promising carbon structures. The author believes that the present new findings will provide the valuable information on the Li-storage mechanism and the precious clues to design of the high capacity anode material.

It has become clear that some synthetic metals exhibit superior functions to inorganic compounds. However, there are a few successful applications of synthetic metals, for the reasons of the endurance, stability, reliability, and cost. Therefore, it is the time to reconsider the peculiarity of synthetic metals compared with inorganic compounds, like quantum effect and quantum nanowire. Moreover, the cooperative effect between 2pπ-electrons and s- or d-electrons would become an interesting subjects, this attempts is beginning in the design of ferromagnetic molecules.

Finally, the author wishes this thesis will contribute for further development of functional organic materials and material science.